UNIVERSITY OF CANTERBURY

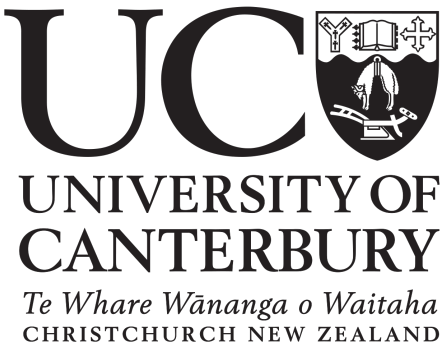

PHD THESIS

Strong Gravitational Lensing and its Applications in Cosmology

---

Author:
Christopher J. HARVEY-HAWES

Supervisor:
David L. WILTSHIRE

A thesis submitted in fulfilment of the requirements
for the degree of PhD in Mathematical Physics

in the

School of Physical and Chemical Sciences

July 25, 2025

"I'm 27 years old. I've no money and no prospects. I'm already a burden to my parents. And I'm frightened."

Charlotte Lucas, Pride and Prejudice (2005)

Acknowledgements

I would like to thank David Wiltshire for his guidance and advice throughout my PhD. In particular, I would like to thank him for his trust and patience throughout my off-shore start during the COVID pandemic. His experience and insights have fundamentally changed the way I view physics, for which I am incredibly grateful, and I have enjoyed our many debates.

As much as it pains me to say this, the work in this thesis would not have been possible without the constant pestering of Marco Galoppo. I reluctantly thank him for our seemingly endless discussions on physics, philosophy, and food - of which he still has lots to learn. I would like to thank Zachary Lane, without whom half of my code would not run and I have greatly benefitted from his knowledge of observational astronomy. I wish to thank Pierre Mourier for diligently reading my thesis and providing many useful comments that have greatly improved the work, as well as for his general advice and intuition. I would also like to thank the many people who have influenced and aided the process of completing this thesis, including: Ryan Ridden-Harper, John Forbes, Chris Stevens, Orlon Petterson, Jenny Wagner, Pavel Kroupa, and the UC Gravity group.

The last few years have been made significantly more enjoyable thanks to the solidarity in suffering of those in the fifth floor offices, particularly Morag Hills, Shreyas Tiruvaskar, Emma Johnson, Marco Galoppo, Zachary Lane, Michael Williams, Manon Van Zyl, and Rudeep Gaur (who I consider an honorary member along with Sylvie and Jess).

I wish to thank those who have housed me over the last few months: Shreyas Tiruvaskar and Nora Michels, Alice Carter-Champion, Lizzy Harvey-Hawes, and those at Athol Terrace. In particular, Nicolas Davey and Keiko Rayner, who have put up with me throughout my time in Aotearoa New Zealand. Finally, I would like to thank Levi Evans, and the postdocs in the Royal Holloway University of London physics offices for enabling my trespassing and encouraging me to keep writing mid-spiral.

Abstract

In this thesis, we use strong gravitational lensing to investigate the underlying assumptions of the standard model of cosmology: the spatially flat Friedmann-Lemaître-Robertson-Walker background, dark energy, and dark matter. Strong gravitational lens catalogues are typically used to constrain a combination of cosmological and empirical power-law lens mass model parameters, often introducing additional empirical parameters and constraints from high resolution imagery. We investigate these lens models using Bayesian methods through a novel alternative that treats spatial curvature via the non-Friedmann-Lemaître-Robertson-Walker timescape cosmology. We apply Markov Chain Monte Carlo methods using a catalogue of 161 lens systems in order to constrain both lens and cosmological parameters for: (i) the standard ΛCDM model with zero spatial curvature; and (ii) the timescape model. We then generate large mock data sets to further investigate the choice of cosmology on fitting simple power-law lens models. In agreement with previous results, we find that without additional information from follow-up high resolution imagery or introducing further free parameters to fit, no combination of lens and cosmological model return reliable physical estimates of cosmological parameters. Regardless of cosmology, unphysical distance ratios are given from power-law lens models resulting in a poor goodness of fit. We extend this work to systems with additional time-delay data as an exploratory analysis and find the further constraints were still unable to produce physical cosmological parameters. However, individually fitting lens models to a select number of systems - from the *H0LiCOW* program - returns realistic parameter values and finds timescape statistically indistinguishable from the standard model of cosmology. With larger datasets soon available, separation of cosmology and lens models must be addressed.

The parametrisation of lens models best fit to observations not only informs on the nature of dark matter, but also enables investigations of alternative theories of gravity. In this regard, disc galaxies represent a promising laboratory for the study of gravitational physics, including alternatives to dark matter, owing to the possibility of coupling rotation curves' dynamical data with strong gravitational lensing observations. In particular, Euclid, DES and LSST are predicted to observe hundreds of thousands of gravitational lenses. In chapter 5, we investigate disc galaxy strong gravitational lensing in the MOND framework. We employ the concept of equivalent Newtonian systems within the quasi-linear MOND formulation to make use of the standard lensing formalism. We derive the phantom dark matter distribution predicted for realistic disc galaxy models and study the impact of morphological and mass parameters

on the expected lensing. We find purely MONDian effects dominate the lensing and generate non-trivial correlations between the lens parameters and the lensing cross section. Moreover, we show that the standard realisation of MOND predicts a number count of disc galaxy lenses of one order of magnitude higher than the dark matter-driven predictions, making it distinguishable from the latter in upcoming surveys. Thus, we propose future work to predict the number of disc galaxy lenses using dark matter lens profiles and in MOND, in anticipation of the vast amounts of data expected to arrive from upcoming and ongoing surveys such as the Vera Rubin Legacy Survey of Space and Time, Euclid, and the Dark Energy Survey. Finally, we show that disc galaxy gravitational lensing can be used to strongly constrain the interpolating function of MOND.

Table of Contents

Acknowledgements **ii**

Abstract **iii**

1 Cosmology **1**

1.1 The Λ Cold Dark Matter Model 2

1.1.1 The Cosmological Principle 2

1.1.2 The FLRW Solution 3

1.1.3 Dark Matter 5

1.1.4 Dark Energy 7

1.2 Distances in the Standard Model 8

1.2.1 Cosmological Redshift 9

1.2.2 Proper and Comoving Distance 10

1.2.3 Parallax Distance 11

1.2.4 Luminosity Distance 12

1.2.5 Angular Diameter Distance 13

1.3 Challenges to the Standard Paradigm 14

1.3.1 The Hubble Tension 14

1.3.2 S_8 Tension 15

1.3.3 Dipoles and Anisotropies in Cosmic Source Populations 18

1.4 Resolving Tensions with New Physics 18

1.4.1 wCDM and Dynamical Dark Energy 19

1.4.2 Early Dark Energy 20

1.4.3 Interacting Dark Energy 21

1.4.4 Modified Theories of Gravity 21

1.5 Inhomogeneous Cosmology 22

1.5.1 Exact Inhomogeneous Solutions of Einstein's equations 22

1.5.2 Coarse-graining and Backreaction . . . 24
1.5.3 Buchert's Averaging Scheme . . . 27
1.5.4 Timescape . . . 29
Distances in the Timescape Model . . . 36
1.6 Modified Newtonian Dynamics . . . 37

2 Lensing Overview **40**
2.1 A Very Brief History of Gravitational Lensing . . . 40
2.2 Lensing Formalism . . . 41
2.2.1 Deflection Angle . . . 41
2.2.2 Lens Equation . . . 43
2.2.3 Convergence . . . 45
2.2.4 Einstein Radius . . . 46
2.2.5 Magnification and Distortion . . . 48
2.2.6 Critical and Caustics Curves . . . 49
2.2.7 Image Types . . . 50
2.2.8 The Mass-Sheet Degeneracy . . . 51
2.3 Strong Lensing - a Series of Acronyms . . . 53
2.3.1 Cluster Scale Lensing . . . 53
2.3.2 Time-Delay Cosmography . . . 54
2.3.3 Dark Matter Haloes . . . 56

3 Power-law lens models for strong lensing in cosmology **58**
3.1 Introduction . . . 58
3.2 Timescape Model Overview . . . 61
3.3 Catalogue, Observables and Lens Models . . . 64
3.3.1 Catalogue Data . . . 64
3.3.2 Lens Models . . . 66
Extended Power-Law Model . . . 67
Spherical Power-Law Model . . . 68
Singular Isothermal Sphere Model . . . 68
3.4 Parameter Determination and Model Preference Results . . . 69
3.4.1 Discussion of Results . . . 70
3.5 Mock Catalogues and Parameter Fitting . . . 74

3.5.1 Methodology . . . 74
3.5.2 Simulation Results and Discussion . . . 75
3.6 Conclusions . . . 78

4 Time Delay Lensing as a Test of Cosmological model 86
4.1 Introduction . . . 86
4.2 Population Statistics . . . 88
4.2.1 Methodology . . . 88
Time-delay Formalism . . . 88
MCMC Set Up . . . 89
4.2.2 Data . . . 90
4.2.3 Results and Discussion . . . 91
4.3 H0LiCOW-style analysis . . . 91
4.3.1 Lens sample . . . 93
4.3.2 Lens Modelling . . . 95
4.3.3 Analysis . . . 96
4.3.4 H0LiCOW results . . . 97
4.4 Conclusions . . . 99

5 Gravitational Lensing By Disc Galaxies in MOND 100
5.1 Introduction to Spiral Galaxy Lensing . . . 100
5.2 Strong Gravitational Lensing . . . 104
5.3 Matter density profiles . . . 105
5.3.1 Analytical baryonic matter density modelling . . . 106
5.3.2 Realistic disc galaxy model parameters . . . 107
5.3.3 Equivalent Newtonian system . . . 107
5.4 Results . . . 109
5.5 Conclusions . . . 114

6 Conclusions 122

Bibliography 125

Chapter 1

Cosmology

At the time of writing, the field of cosmology is entering the most exciting period in its history. The standard model of cosmology, the Λ Cold Dark Matter (ΛCDM) model or "concordance" cosmology, has prevailed for two and a half decades as a relatively simple model based on the tenets of: *(i)* cosmic inflation in the very early universe ($t < 10^{-9}$s), *(ii)* dark matter, *(iii)* dark energy, and *(iv)* a spatially flat Friedmann-Lemaître-Robertson-Walker (FLRW) background. However, as the precision of our cosmological measurements has steadily improved, tensions within the standard model have grown. Many of these tensions are now irreconcilable at beyond a 5σ disagreement, signalling a possible requirement of new physics and a revisiting of our fundamental assumptions [1].

Previously, cosmological analyses investigating these tensions and alternative models have been severely limited by the lack of observational data. However, in the next few years we are expecting a dramatic increase in the quantity of high quality data through surveys such as *Euclid* [2], *Vera Rubin (LSST)* [3], *Dark Energy Spectroscopic Instrument (DESI)* [4, 5], *Dark Energy Survey (DES)* [6, 7], and many more. Additionally, space telescopes such as the *James Webb* [8] and *Nancy Grace Roman* projects [9] will enable extreme precision in high-resolution follow-up imagery. This vast amount of data will enable detailed analyses of the standard model and give us the opportunity to make comparisons otherwise not possible. Furthermore, we are now in the era of multimessenger astronomy, enabled by gravitational wave detectors such as the Laser Interferometer Gravitational-wave Observatory (LIGO) [10], Virgo [11, 12], and KAmioka GRAvitational-wave detector (KAGRA) [13], as well as neutrino detectors such as the IceCube Observatory [14] and Super-Kamiokande detector (Super-K) [15]. These programs, amongst others, allow us to combine data from a range of different signals to tightly constrain astrophysics and cosmology.

In this chapter, we review the foundations of ΛCDM, describe the distance measures it produces, and discuss various extensions and alternatives to the standard paradigm.

1.1 The Λ Cold Dark Matter Model

1.1.1 The Cosmological Principle

The cosmological principle is one of the foundational assumptions from which modern cosmology is built upon. Whilst the precise definition is often debated, the generally accepted interpretation is that the Universe is both statistically homogeneous and isotropic over large scale averages. This statement is obviously false when only considering the local universe on scales[1] below $\lesssim 100\,h^{-1}$ Mpc, where it is defined by a cosmic web of over-dense filaments – which are themselves comprised of galaxy groups and clusters – and under-dense voids. However, if we look to larger scales, we can identify a *scale of statistical homogeneity* (SSH). For averages over large enough domains, the Universe does look the same in all directions on the sky. Hence, we say the universe is isotropic.

According to the Copernican principle, there should be no privileged positions within the universe. Thus, if all typical observers see a statistically isotropic universe, this implies statistical homogeneity and each observer will see a universe with the same average matter density beyond the SSH.

However, what constitutes the "large scales" required for the cosmological principle to hold? The SSH is generally found to be at least beyond 60 - 80 h^{-1} Mpc using the 2-point galaxy correlation function [16–19], though the scale at which statistical homogeneity emerges varies significantly depending on the tracers used to determine it. In fact, studies of the SDSS quasar and luminous red galaxy samples find the SSH to be 150 h^{-1} Mpc and 230 h^{-1} Mpc, respectively [20]. Furthermore, empirically obtained scales often disagree with ΛCDM simulations, which find an upper limit of ∼260 h^{-1} Mpc for the SSH [21]. Upcoming galaxy surveys with large sky coverage will enable a refinement of this scale determined empirically from two-point (or N-point) galaxy correlations.

[1] where h is the dimensionless reduced Hubble constant, related to the Hubble constant by, $H_0 = 100\,h\,\mathrm{kms}^{-1}\mathrm{Mpc}^{-1}$.

1.1.2 The FLRW Solution

The Einstein field equations provide the leading theory that describes space-time and gravity, given with a cosmological constant Λ as

$$G_{\mu\nu} = R_{\mu\nu} - \frac{1}{2}R\, g_{\mu\nu} + \Lambda g_{\mu\nu} = \frac{8\pi G}{c^4} T_{\mu\nu}\,. \tag{1.1}$$

The ΛCDM cosmology is built upon the Friedmann-Lemaître-Robertson-Walker (FLRW) metric, a class of highly symmetric solutions to Eq. (1.1), given by

$$\mathrm{d}s^2 = -c^2\mathrm{d}t^2 + a(t)^2\left[\frac{\mathrm{d}r^2}{1-k\,r^2} + r^2(\mathrm{d}\theta^2 + \sin\theta^2\mathrm{d}\phi^2)\right], \tag{1.2}$$

where k gives the background constant spatial curvature and $a(t)$ is the scale factor from which we derive the global expansion rate[2] $H(t)$,

$$H(t) \equiv \frac{\dot{a}(t)}{a(t)}\,, \tag{1.3}$$

known as the Hubble parameter, and the Hubble constant is given as the present epoch[3] value $H_0 = H(t_0)$. The FLRW metrics are exact solutions of the Einstein field equations that, by construction, enforce the cosmological principle, for an observer comoving with the fluid introduced by the energy-momentum tensor. The FLRW solutions provide a powerful tool to perform cosmology with limited cosmological data. Observations that are only carried out on a small patch of the sky can be used to infer physical descriptions of the entire Universe.

On scales larger than the SSH, the small deviations from average FLRW expansion are treated perturbatively. Below the SSH, the formation of local small-scale structures enters the non-linear regime. This requires numerical simulations (typically Newtonian N-body) to effectively model within the standard framework [22, 23]. Fully general relativistic simulations have been developed over the past decade, and have the advantage of being directly able to constrain parameters such as the regional spatial curvature that the classical Newtonian approximations can only infer [24–26].

[2] Throughout this thesis, I adopt the convention that dotted characters indicate time derivatives with cosmic time t, or later Buchert average time.

[3] The subscript x_0 indicates the present epoch value of a parameter x throughout this thesis.

Although there are many observational and theoretical challenges to the cosmological principle (discussed in section 1.3), this foundational assertion is generally well supported by observations. This is particularly true in the early universe, where the Cosmic Microwave Background (CMB) radiation exhibits only minor deviations from isotropy. Temperature fluctuations around a near perfect blackbody spectrum of $T = 2.726$ K [27] are small and once the leading dipole component is removed – conventionally attributed to kinematics and our relative motion with respect to the CMB – the fluctuations are of order $\delta T/T \simeq 10^{-3}$ with further secondary perturbations of order $\sim 10^{-5}$ [28]. These relatively small variations from isotropy in the early universe are taken as strong evidence for the cosmological principle. However, observational constraints on the cosmological principle are much more nuanced in the late universe.

Assuming an FLRW metric with pressureless dust, additional radiation, and a cosmological constant Λ, the Einstein equations reduce to the Friedmann and Raychaudhuri equations

$$\left(\frac{\dot{a}}{a}\right)^2 + \frac{k\,c^2}{a^2} = \frac{8\pi}{3}\,G\,\rho\,, \tag{1.4}$$

$$2\frac{\ddot{a}}{a} + \left(\frac{\dot{a}}{a}\right)^2 + \frac{k\,c^2}{a^2} = -\frac{8\pi}{c^2}\,G\,p\,, \tag{1.5}$$

where ρ and p giving the total matter density and pressure, respectively. Eq. (1.5) can then be recast as the *sum rule*,

$$\Omega_M + \Omega_R + \Omega_k + \Omega_\Lambda = 1\,, \tag{1.6}$$

where the energy fractions of the universe are broken down into its constituent parts, Ω_M, Ω_R, Ω_k, and Ω_Λ. These parametrise the fraction of the total energy contribution given by pressureless matter (both baryonic and dark matter), radiation, spatial curvature and the cosmological constant (interpreted as dark energy), respectively,

$$\Omega_M = \frac{8\pi\,G\,\rho_M}{3H^2}\,, \tag{1.7}$$

$$\Omega_R = \frac{8\pi\,G\,\rho_R}{3H^2}\,, \tag{1.8}$$

$$\Omega_k = -\frac{k\,c^2}{a^2\,H^2}\,, \tag{1.9}$$

$$\Omega_\Lambda = \frac{\Lambda\,c^2}{3H^2}\,. \tag{1.10}$$

When fit to the Planck CMB data, the ΛCDM model returns a spatial curvature parameter, $k \approx 0$, very close to flatness. The present day energy distribution is then given by $\Omega_{M0} =$

0.3153 ± 0.0073 and $\Omega_\Lambda = 0.6847 \pm 0.0073$, with negligible contributions from radiation and curvature [28].

We can then define the critical density,

$$\rho_c = \frac{8\pi G}{3H^2}\,, \tag{1.11}$$

where the Hubble parameter can be expressed in terms of energy density, as

$$H = H_0\sqrt{\Omega_{R0}\,a^{-4} + \Omega_{M0}\,a^{-3} + \Omega_{k0}\,a^{-2} + \Omega_\Lambda}\,. \tag{1.12}$$

This critical density outlines the future expansion of the universe. If the overall density is greater than ρ_c, i.e. for $\Lambda = 0$ with $k > 0$, then the universe would collapse back in on itself and undergo the *Big Crunch*. Alternatively, if the overall density is less than the critical value, we get eternal expansion, $k \leq 0$.

1.1.3 Dark Matter

Of the present day energy budget of the Universe, only around 4% is contributed by baryonic matter [29]. The remaining $\sim$26% of matter is referred to as 'dark' as it does not interact via electromagnetic radiation. Since it has not been convincingly directly detected[4], there is as yet only indirect evidence for its existence, e.g., through the kinematics of luminous material in the universe.

One of the largest sources of evidence for dark matter[5] came through the rotation curves of disc galaxies [32–34]. Accounting for only the visible mass of stars and gas within a galaxy, and applying Newtonian approximations of a weak field limit of GR, is not sufficient to explain the flattening of the rotation curves observed. With purely baryonic matter, the expected quasi-Keplerian fall-off in the rotation with large radii suggest an additional source of gravity - thus dark matter was postulated. At present, dark matter has become a pillar of modern cosmology, with a large number of astrophysical phenomena requiring supplementary mass for a feasible explanation within the standard model, and non-relativistic (cold) dark matter essential for structure formation in ΛCDM [35].

[4]The DAMA collaboration claims to have made direct detections of dark matter particles [30]. However, this is yet to be confirmed with other experiments and detectors.

[5]The first evidence coming from the dynamics of galaxies and the application of the virial theorem to the Coma cluster, which Zwicky determined required *dark matter* [31].

The majority consensus within the scientific community has settled on dark matter as a solution to the *missing mass problem*, despite no viable candidate having been observed[6], so much so that the determination of the nature of dark matter has evolved into its own sector of high energy physics and cosmology.

Over recent decades, a plethora of dark matter candidates have been proposed that have had varying degrees of success in matching observations. In this section, I will give a brief description of some of the more notable classes of candidates:

- **MACHOs -** Massive compact halo objects were one of the first proposals to explain the missing mass problem. Essentially, the MACHO solution is that there exists a large number of ordinary mass objects which are faint enough not to meaningfully contribute to the luminous material we observe. MACHOs include brown dwarfs, faint stars, and stellar remnants, and are appealing because they do not require any additional exotic matter beyond the standard model of particle physics. However, microlensing along with other investigations have shown that MACHOs could not exist in an abundance high enough to explain the dynamics we observe in galaxies, and have been effectively ruled out as viable candidates [36, 37]. Alongside this, the relative abundances of light elements in the early universe are heavily dependent on the baryon to photon ratio at that epoch. Thus, for MACHOs to solely explain the mass discrepancy, there would have to be a far larger energy contribution of baryons around the epoch of Big Bang Nucleosynthesis. This is constrained by the ratio of light elements abundances in the oldest stars and by relative epochs of helium and hydrogen recombination in the early universe. Not only are the effects of MACHOs considered negligible, but baryonic matter cannot explain the missing mass problem without the modification of our law of gravitation / implementation of general relativity [38].

- **WIMPs -** Weakly interacting massive particles are natural candidates from particle physics [39]. WIMPs explain the dark matter phenomenon as thermal relics from the early universe. Interacting only weakly (via the weak force), these particles decoupled from thermal equilibrium in the early universe, which effectively fixes their relative abundance assuming minimal non-gravitational self-interaction [40]. There are many ongoing direct and indirect detection experiments being carried out, although so far there have been

[6] In section 1.6, an alternative of modified Newtonian dynamics is discussed, which attempts to explain the missing mass problem without dark matter.

no detection events. These tests have placed strong constraints on the WIMP-nucleon interaction cross-sections and have pushed searches towards lighter mass particles and alternative candidates such as axions [41–43].

- **Axions -** Axions are, at present, considered one of the most promising candidates for dark matter. They are an artefact of the Peccei-Quinn solution to the strong CP problem in quantum chromodynamics (QCD). Consquently, they are predicted to have small masses on the μeV - meV scale, but can be extended as low as $10^{-22}\,eV$ as *ultralight* dark matter [44–46]. Their main detection method is proposed to be through haloscopes and their bounds constrained by astrophysical observations. However, these bounds are continually getting tighter and no Axion signal has ever been detected.

There are, of course, many more candidates that are not mentioned here, including: boson-condensate stars, Kaluza-Klein particles, supersymmetric particles, *etc*., none of which have been directly observed.

1.1.4 Dark Energy

The general redshift of extragalactic objects observed (now known as just other galaxies) led to the understanding that the universe is expanding and the local linear relationship between the distance to an object and its recession velocity via Hubble law [47]. However, the universe is not only expanding, but that expansion appears to be accelerating, as inferred independently by the High-z Supernovae Search Team [48] and Supernovae Cosmology Project [49] from the analysis of type Ia Supernova in the late 20th century.

Now, the cosmological constant Λ, originally intended to balance the attractive effects of gravity to ensure a static universe [50], is reintroduced to explain the accelerating expansion. The extra geometric degree of freedom, given by the addition of the cosmological constant, can be interpreted as an effective energy contribution to the right-hand side of Eq. (1.1). As the name suggests, the corresponding effective density ρ_Λ is a constant and requires negative pressure to overcome gravitational collapse, such that the effective equation of state parameter is given as $w = -p_\Lambda/\rho_\Lambda = -1$. Alternative explanations for the acceleration beyond ΛCDM often give different parametrisations for this equation of state, but we broadly refer to the

energy driving cosmic expansion as 'dark energy' regardless of whether it is motivated by the cosmological constant or not.

If one does not assume a cosmological constant, then it is possible to construct a crude estimate for the vacuum energy density required from particle physics to provide an explanation for the accelerated expansion. However, these are massively discrepant with cosmological constraints, which predict a density 52 orders of magnitude smaller than the theoretical value [51], dubbed the *cosmological constant problem*. An explanation for the small but non-zero value for the energy density of dark energy has eluded the community, so much so that many are satisfied to simply leave its value up to the anthropic principle [52] – that if the dark energy contributions were larger, no structures could form, or smaller and there would be no expansion.

A plethora of studies have since made attempts to constrain the equation of state of dark energy w, which confirm the apparent accelerating expansion of the universe. Over the past two decades, survey precision and depth has improved greatly, such that high precision measurements of w are now possible. Examples of surveys that attempt this, include: the Equation of State Supernova Cosmic Expansion survey (ESSENCE) [53, 54], the Pantheon+ supernova survey [55], the Dark Energy Survey (DES) [56], the Supernova Legacy Survey (SNLS) [57], the Sloan Digital Sky Survey (SDSS) [58], and the Pan-STARRS Medium deep survey [59]. The most recent surveys are now capable of producing strong constraints on the evolution of the equation of state with redshift [4]. These advancements enable investigations into this modification of ΛCDM, named wCDM, which is discussed in section 1.4.1.

1.2 Distances in the Standard Model

Distances in cosmology are not directly observable. The majority of distances inferred to an object within the universe are derived from the physical properties of the electromagnetic radiation observed – e.g., from the spectra, intensity or periodicity of light – and a cosmological model. Whilst an exact metric distance between objects can be derived in any given spacetime, it is of no practical use in observational astronomy. This distinction is important, as the basis for cosmological tensions within ΛCDM is founded on our definitions and calibrations of distances. In astronomy, our estimates for cosmological distances are calibrated with previous, more local measurements i.e, parallax distances are used to calibrate the luminosity distances

to nearby stars or Cepheid variables to supernova type Ia [60]. This technique for establishing the distance-redshift relation is known as the cosmic distance ladder, as each 'step' on the ladder is used to calibrate the next.

What follows is a brief discussion of some of the standard distance measures used in modern cosmology.

1.2.1 Cosmological Redshift

We define the redshift of an object as the difference in the wavelength of light between emission and when it is observed, which can be written generally as

$$1 + z_{\text{obs}} = \frac{\lambda_{\text{obs}}}{\lambda_{\text{em}}} = \frac{E_{\text{em}}}{E_{\text{obs}}} = \frac{-\mathbf{U}_{\text{em}} \cdot \mathbf{k}}{-\mathbf{U}_{\text{obs}} \cdot \mathbf{k}} = \frac{U^{\mu}_{\text{em}}\, k_{\mu}}{U^{\nu}_{\text{obs}}\, k_{\nu}}\,, \tag{1.13}$$

where λ and E are the respective wavelength and energies measured in the local frames of the observer and emitter, identified by the corresponding subscript, with associated 4-velocites $\mathbf{U}$, and $\mathbf{k}$ represents the 4-momentum of the photon.

In the local universe, it is assumed that the observer and emitter are sufficiently close to one another for the effects of the geometric background to be neglected and only special relativistic effects applied. Then the observed redshift can be attributed solely to a radial Lorentz boost with relative velocity v between the observer and emitter

$$1 + z_{\text{obs}} = \sqrt{\frac{c+v}{c-v}} \approx 1 + \frac{v}{c} + \mathcal{O}\left(\frac{v^2}{c^2}\right)\,. \tag{1.14}$$

Whilst we know that general relativity is even relevant on scales as small as the solar system, this special relativistic formulation is used throughout modern cosmology as the basis for the Hubble–Lemaître law.

We can further split the general redshift relation of Eq. (1.13) into 3 parts via local Lorentz transformations at observer and source positions as

$$1 + z_{\text{obs}} = \frac{\mathbf{U}_A \cdot \mathbf{k}}{\mathbf{U}_{\text{obs}} \cdot \mathbf{k}} \frac{\mathbf{U}_B \cdot \mathbf{k}}{\mathbf{U}_A \cdot \mathbf{k}} \frac{\mathbf{U}_{\text{em}} \cdot \mathbf{k}}{\mathbf{U}_B \cdot \mathbf{k}} \tag{1.15}$$

$$= (1 + z_{\text{pec, obs}})\, \frac{g_{\mu\nu}\, U^{\mu}_B\, k^{\nu}|_{x_B}}{g_{\alpha\beta}\, U^{\alpha}_A\, k^{\beta}|_{x_A}}\, (1 + z_{\text{pec,src}})\,. \tag{1.16}$$

Here, the first and third terms give the redshift that corresponds to the relative peculiar velocities for an ideal model observer in the frame of measurement and the frame of earlier emission respectively. These can further be broken up into components corresponding to the motions

of the Earth relative to the Sun, the solar system relative to our galaxy and our galaxy relative to the barycentre of the local group, if one chooses. The second factor corresponds to the cosmological term, which for ideal observers at rest (i.e., in comoving coordinates), gives

$$1 + z_{\cos} = \frac{g_{\mu\nu}\, U_B^\mu\, k^\nu|_{x_B}}{g_{\alpha\beta}\, U_A^\alpha\, k^\beta|_{x_A}} = \frac{g_{00}\, U_B^0\, k^0|_{x_B}}{g_{00}\, U_A^0\, k^0|_{x_A}}\,. \tag{1.17}$$

This cosmological term can be split further into

$$(1 + z_{\cos}) = (1 + z_{\phi,A})\,(1 + \bar{z})\,(1 + z_{\phi,B})\,, \tag{1.18}$$

where $(1 + z_{\phi,A}) \equiv 1/(-g_{00}U_A^0)|_{x_A}$ and $(1 + z_{\phi,B}) \equiv 1/(-g_{00}U_B^0)|_{x_B}$ are interpreted as the gravitational redshifts with respect to the background expansion, which has its own corresponding redshift contribution

$$(1 + \bar{z}) \equiv \frac{k^0(\mathbf{x}_B)}{k^0(\mathbf{x}_A)}\,. \tag{1.19}$$

In the ΛCDM model, with enforced homogeneity and isotropy through an FLRW background, the corresponding 4-momentum associated to the expansion gives $k^0 = 1/a(t)$. Therefore, we recover the typical cosmological redshift expected in the standard model,

$$1 + \bar{z} = \frac{a(t_A)}{a(t_B)}\,, \tag{1.20}$$

where the scale factor is often normalised to $a(t_A) \equiv 1$ for an observer at the present cosmic time. The gravitational redshift components are often overlooked in conventional cosmology. However, even small gravitational redshifts can have a noticeable impact on the best-fit cosmological parameters [61, 62].

1.2.2 Proper and Comoving Distance

By applying the corresponding scaling relations Eqs. (1.7)–(1.10) for the various energy density contributions in ΛCDM, from Eqs. (1.11), (1.12) the Hubble parameter can be written as

$$H(z) = H_0\sqrt{\Omega_{R0}\,(1+z)^4 + \Omega_{M0}\,(1+z)^3 + \Omega_{k0}\,(1+z)^2 + \Omega_\Lambda}\,. \tag{1.21}$$

Often in the literature, the dimensionless parameter $E(z)$ is defined for convenience by

$$H(z) \equiv H_0\, E(z)^{1/2}\,. \tag{1.22}$$

Starting with the initial FLRW metric, Eq. (1.2), the proper distance between two comoving observers connected by radial geodesics relative to an observer at the origin, is obtained by integrating

$$\mathrm{d}s^2 = a^2(t)\,\frac{\mathrm{d}r^2}{1-k\,r^2}\,, \tag{1.23}$$

so that

$$s = \int_0^s \mathrm{d}s' = a(t)\int_0^r \frac{\mathrm{d}r}{\sqrt{1-k\,r^2}}\,. \tag{1.24}$$

The solutions to Eq. (1.24), are dependent on the choice of spatial curvature in our FLRW model, as

$$s(t) = a(t)\begin{cases} |k|^{-1/2}\sinh^{-1}\sqrt{|k|}\,r & \text{if } k<0\,, \\ r & \text{if } k=0\,, \\ |k|^{-1/2}\sin^{-1}\sqrt{|k|}\,r & \text{if } k>0\,, \end{cases} \equiv a(t)\,\chi\,, \tag{1.25}$$

where χ is the respective comoving distance for various choices of k, and r is the coordinate distance. The proper distance s describes the physical distance in an expanding FLRW spacetime at any given instant in cosmic time and will therefore vary with cosmic expansion, as determined by the scale factor, $a(t)$.

1.2.3 Parallax Distance

For very local measurements within our own galaxy, parallax is an effective tool for establishing the distance to nearby objects. The parallax distance is the displacement of an object's angular position on the sky relative to very distant 'fixed' sources, arising from the variations of the relative positions of the observer and object. This is most easily understood in day-to-day life as the slight variation in position with respect to the background when looking at a nearby object, such as an outstretched thumb, with each of your eyes alternately. This technique is analogously applied to determine the distance to nearby luminous objects, by comparing their apparent deviation in position against the background of distant stars and galaxies, when observed at different points of the Earth's orbit around the Sun, reaching a maximum every 6 months.

Traditionally, parallax distances have been used as the first rung on the cosmic distance ladder to calibrate the empirical period–luminosity relation of Cepheid variable stars, which are observed in galaxies out to greater distances at which parallaxes are no longer detectable. The Cepheid variables have then been used to calibrate other distance indicators, building up the

distance ladder. Naturally a recalibration of any rung of the ladder can have a major impact. The recent Gaia-ESO survey has had a major impact in not only vastly improving the precision and volume of parallax distances within our galaxy, but also radial velocities as well as other data products [63].

1.2.4 Luminosity Distance

In a static universe with Euclidean geometry, the luminosity distance is defined to satisfy the relation

$$D_L = \left(\frac{L}{4\pi F} \right)^{1/2} , \tag{1.26}$$

with absolute bolometric luminosity L and measured bolometric flux F. This can be generalised to an FLRW universe as

$$D_L = \frac{c\,(1+z)}{H_0 \sqrt{|\Omega_{k0}|}}\, S_k \left(\sqrt{|\Omega_{k0}|} \int_0^z \frac{\mathrm{d}z'}{E(z')} \right) , \tag{1.27}$$

where

$$S_k(x) = \begin{cases} \sin(x) & \text{for } k > 0\,, \\ x & \text{for } k = 0\,, \\ \sinh(x) & \text{for } k < 0\,. \end{cases} \tag{1.28}$$

Unlike angular diameter distances, which require *standard rulers*, the luminosity distance needs *standard candles* with known luminosity for calibration. In astronomy, the apparent magnitude m of an object's brightness is the observable quantity measured and can be related to the absolute magnitude M through an empirical relation via the luminosity distance. This expression is known as the distance modulus

$$\mu \equiv m - M = 5 \log_{10} \left(\frac{D_L}{\mathrm{Mpc}} \right) + 25\,. \tag{1.29}$$

In practice, there are no true standard candles in astronomy but *standardisable candles*. SNe Ia – whose standarisation is based on empirical relations first discovered in the 1990s [64] – make up some of the most precise luminosity distance indicators in cosmology, and are well sampled out to redshifts $z \simeq 1$, and somewhat beyond.

1.2.5 Angular Diameter Distance

This measure of distance is based on the idea of a *standard ruler*, where the object's proper length is known, in Euclidean space. The *angular diameter distance*, D_A, is then defined as the ratio of an object's physical (proper) size, ℓ_θ, to the angular size, δ on the sky as it appears to an observer

$$D_A \equiv \ell_\theta / \delta \,, \tag{1.30}$$

which for an FLRW universe can be rewritten as

$$D_A(z) = \frac{c}{\sqrt{|\Omega_{k0}|}\, H_0\, (1+z)} S_k \left(\sqrt{|\Omega_{k0}|} \int_0^z \frac{\mathrm{d}z'}{E(z)^{1/2}} \right) . \tag{1.31}$$

We can then relate angular diameter distances to luminosity distances via the Etherington reciprocity relation [65],

$$D_L = (1+z)^2\, D_A \,. \tag{1.32}$$

Possibly the best known examples of objects of fixed proper length are optical water masers in the accretion discs of near edge on active galactic nuclei. Their Keplerian orbital parameters can be used to define an absolute proper length scale of the accretion disc, which can be compared to the angle subtended on the sky. The best known example is NGC4258 which is used as an anchor to calibrate the distance ladder [66], which bypasses parallax distances. NGC4258 is not gravitationally bound to our Local Group, but is relatively close in the filament at a distance $D = 7.58 \pm 0.11\,\mathrm{Mpc}$ [67].

In Euclidean space more distant objects of fixed proper size will always appear smaller. However, in an expanding spacetime the angle an object subtends on the sky eventually reaches a minimum value, corresponding to the maximum angular diameter distance. Thus, the angular diameter distance is not continuously increasing with redshift/lookback time. This can be explained via

$$\delta = \frac{\ell_\theta}{D_A} = \frac{(1+z)^2\, \ell_\theta}{D_L} \,, \tag{1.33}$$

where as D_L generally increases, the angle subtended by the object decreases, until $(1+z)^2$ begins to grow faster than D_L. The redshift of this turning point corresponds to an object's maximum D_A or minimum apparent diameter δ. Therefore, objects beyond this scale counter-intuitively appear larger on the sky. Consequently, angular diameter distances do not necessarily sum simply, i.e., $D_A^{ol} + D_A^{ls} \neq D_A^{os}$, as the distance inferred is related to the proper size

of the object when the light observed was emitted. Angular diameter distances are used frequently in gravitational lensing analysis, therefore, it is important to have an expression for the distance between lens and source objects, D_A^{ls}. Using Eq. (1.31), the distance[7] between the lens and source objects can be expressed, for $\Omega_k \geq 0$, as

$$D_A^{ls} = \frac{1}{1+z_s}\left[(1+z_s)\, D_A^{os}\sqrt{1+\Omega_k\,(1+z_l)^2\, D_A^{ol\,2}} - (1+z_l)\, D_A^{ol}\sqrt{1+\Omega_k\,(1+z_s)^2\, D_A^{os\,2}}\right] \tag{1.34}$$

The Baryon Acoustic Oscillation (BAO) scale represents a completely different type of standard ruler, since its source is not a fixed proper length. Rather, it corresponds to a slight excess of galaxies generated from the first acoustic peak in the spectrum of primordial density perturbations, which remained frozen in when the electromagnetic pressure support among baryons dissipated at recombination. The absolute BAO scale is still growing with cosmic expansion. Hence, the combination of CMB anisotropies and the BAO scale determined from late epoch galaxy clustering statistics, provides an incredibly powerful constraint on the expansion history of the universe.

1.3 Challenges to the Standard Paradigm

1.3.1 The Hubble Tension

The present value for the expansion rate H_0 provides the most discussed tension in modern cosmology [68]. This tension arises when estimates of H_0 inferred from early universe measurements of the CMB anisotropies by the *Planck* collaboration[8][9] are compared to late universe, low redshift probes. Fig. 1.1, from the large collaboration and review of Abdalla *et al*. [1], shows the many H_0 estimates from a plethora of different direct and indirect probes. As the precision of our cosmological measurements has improved, the statistical significance of this late and early universe disagreement has increased. Most notably, the Cepheid calibrated supernova type Ia differ by more than 5σ from their *Planck* CMB inferred counterparts [28]. Other independent estimates such as the tip of the red giant branch method [71–73], gravitational

[7] Often throughout this thesis, when later discussing gravitational lensing, we drop the subscript A unless when dealing with multiple types of distance measures simultaneously.

[8] There are other teams and experiments that constrain H_0 from CMB measurements, such as the *Atacama Cosmology Telescope* [69] and the *South Pole Telescope* [70]. However, the *Planck* satellite measurements are widely considered to be the ultimate standard in cosmological measurements.

[9] It is important to once again acknowledge what is being measured here, as the *Planck* CMB power spectrum is measured with a high level of precision but the constraints on cosmology inferred are model-dependent. Indeed, often a fiducial ΛCDM cosmology with set parameter values is assumed in the analysis when reducing data but before fitting for cosmology. This is equally true of late universe probes, where the measurement is typically of spectroscopic redshifts and a cosmological model is applied to determine H_0.

wave standard sirens [74–76], galaxy-clustering [77, 78], masers [79], X-ray observations of the Sunyaev-Zeldovich effect in clusters [80–83], Balmer line L-σ relation of HII galaxies [84–86], and many more, fail to solve this discrepancy. Some of these estimates, such as those from gravitational waves, return values in agreement with both high and low redshift data [87]. However, this is suspected to only be due to the large uncertainties associated with their measurement, and crucially cannot explain why the tension persists in the remaining probes.

This begs the question: can systematics resolve this tension alone or are new physical theories required? Systematic error may easily build up in the cosmic distance ladder. Whilst any systematic errors shared between early and late-epoch calibrations could in principle resolve the Hubble tension, the increasing precision and volume of data coupled with the growing significance of the discrepancy motivates new physics and the reevaluation of fundamental assumptions. Furthermore, direct distance measurements which avoid the distance ladder are of incredible value. This is one of the major advantages of strong gravitational lensing, later discussed in chapter 2.

1.3.2 S_8 Tension

Another notable tension within the ΛCDM model is the S_8 tension [1]. This arises in the clustering of matter within the universe, parametrised by $S_8 = \sigma_8\sqrt{\Omega_{M0}/0.3}$, where σ_8 is the root-mean-square of the amplitude of matter perturbations, smoothed over $8\,h^{-1}$ Mpc scales. The tension in the S_8 parameter, much like the Hubble tension, is caused by a mismatch in observations of low redshift data compared with the expectation from the evolution of structure determined from high redshift measurements and the CMB perturbations. Low redshift measurements determining the distribution of matter and galaxy clustering in the late universe ($z \leq 0.5$–1) show a much “smoother" distribution, and therefore a lower S_8 value, than compared with the standard ΛCDM evolution of CMB fluctuations [88].

A large number of low redshift estimates for S_8 are presented by Abdalla *et al* [1] in Fig. 1.2. These include probes from weak lensing [78, 89–92], galaxy-clustering [93–96], galaxy clusters [97], CMB lensing tomography [98–101], and the combination and joint analysis of each [56, 102–104]. The magnitude of the tension from these measurements gives a 2-3 σ disagreement from model predictions.

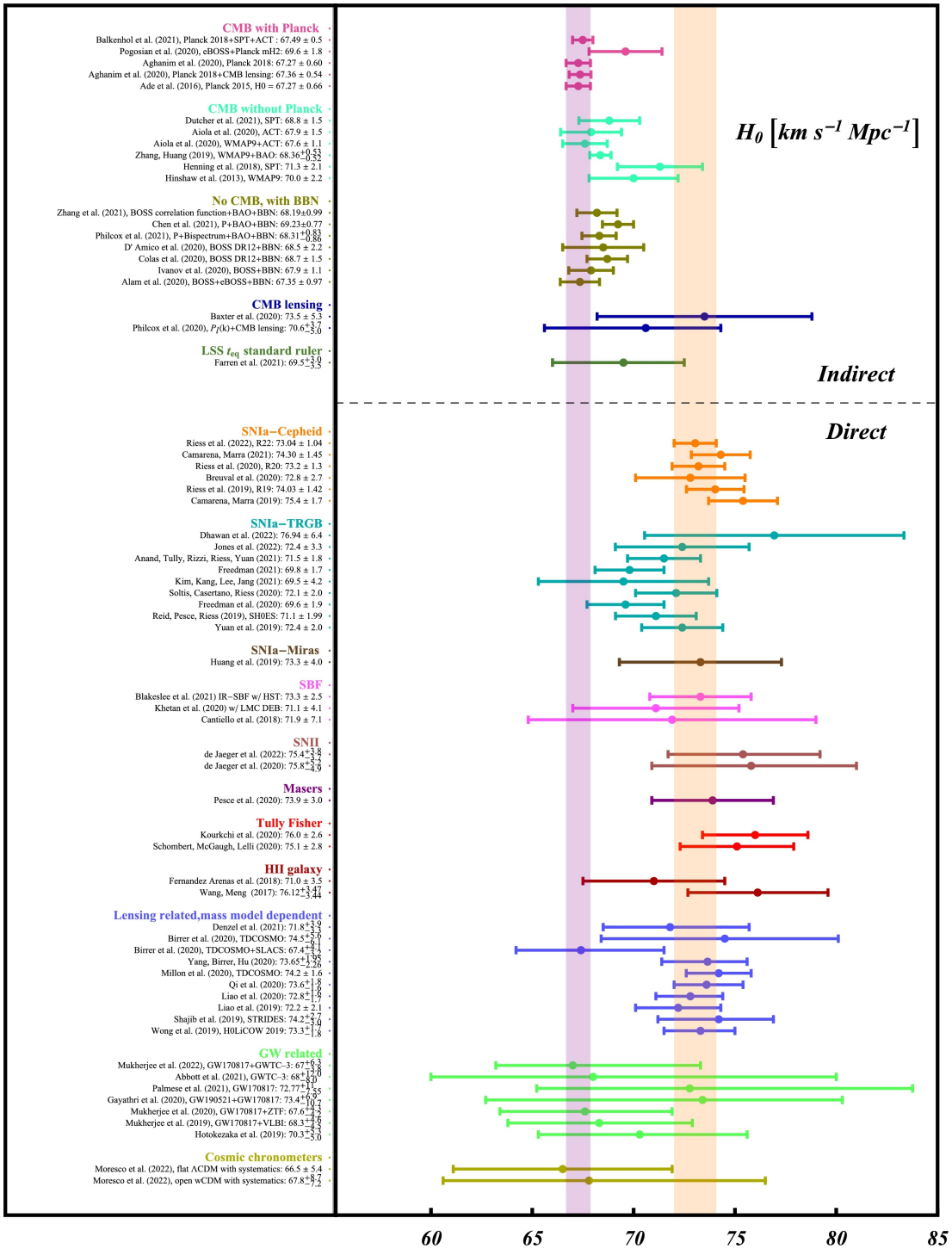

Figure 1.1: The 68% confidence level regions on H_0 constraints from numerous different cosmological probes. The original figure and reference therein are compiled in [1].

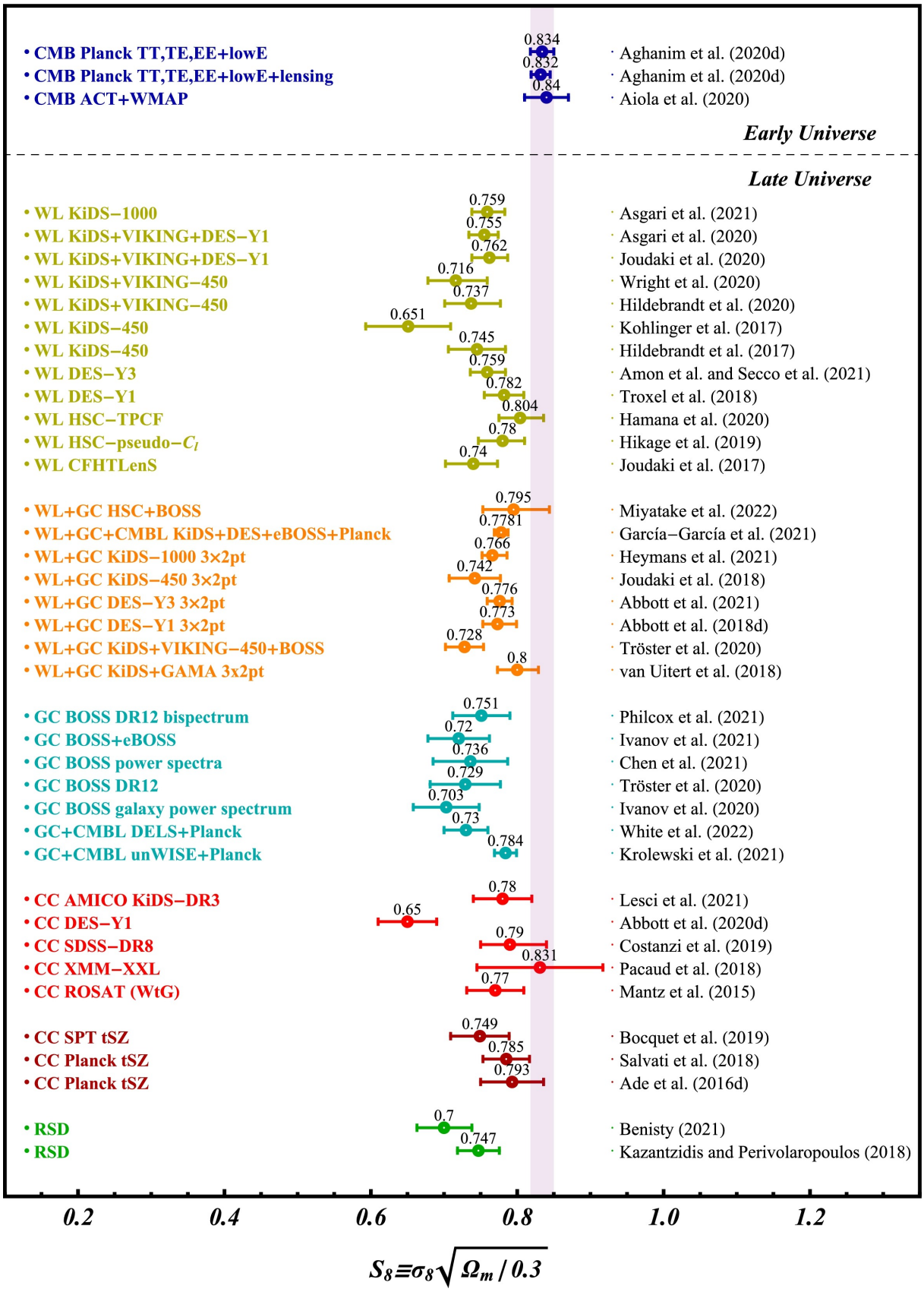

Figure 1.2: The 68% confidence level regions on S_8 constraints from numerous different cosmological probes. The original figure and reference therein are compiled in [1].

1.3.3 Dipoles and Anisotropies in Cosmic Source Populations

Once the galactic plane of the CMB is removed, there is a remaining dipole that, when attributed purely to a special relativistic boost, is understood as a result of the Sun's velocity of $v = 369.82 \pm 0.11 \text{km s}^{-1}$ with respect to the CMB rest frame, towards RA = 168°, DEC = $-7°$ [105]. This relative motion may also be inferred from the modulation and aberration effects in high-redshift ($z > 1$) radio galaxy counts, as noted by Ellis and Baldwin [106]. The Ellis–Baldwin test is incredibly valuable, as it provides a simple model-independent consistency check of FLRW cosmologies [107]. The size of current surveys is already large enough to enable this test. The analysis of combined surveys of the NRAO VLA Sky Survey (NVSS) [108] and the Sydney University Molongo Sky Survey [109, 110] catalogues by Colin *et al.* [111] yields an estimate of the relative velocity of $v = 1729 \pm 187 \text{km s}^{-1}$, towards RA = $149° \pm 2°$, DEC = $-17° \pm 12°$. Whilst this dipole is roughly aligned with that of the CMB, it is substantially larger than expected. Such a large dipole seems to rule out local clustering as an explanation and presents a challenge to the cosmological principle [112].

Furthermore, it is not just radio galaxies that can be used as tracers. In recent years, the CatWISE survey released their all-sky quasar dataset which, after masking out the galactic plane and poor quality data, has a final count of over 1.3 million sources[10] [114]. Analysis of this catalogue also yields a deviation from the expected dipole at 4.9σ [115], and when combined with the NVSS catalogue, one may reject a kinematic dipole at 5.1σ [116]. In Fig. 1.3 from Aluri *et al*. [112], we show the various directions of anisotropy inferred on the sky from multiple different sources.

1.4 Resolving Tensions with New Physics

In the following, I briefly describe some of the alterations to ΛCDM that are considered potential solutions to cosmological tensions. In general, no proposed solution exists (to the author's knowledge) that satisfactorily solves all the cosmological tensions between early and late universe measurements and includes dark energy of some kind, without introducing new tensions in different areas of cosmology [117].

[10]The Zwicky Transient Facility has recently released a catalogue of over 5 million quasars [113]. However, the associated kinematic dipole has yet to be calculated from this sample.

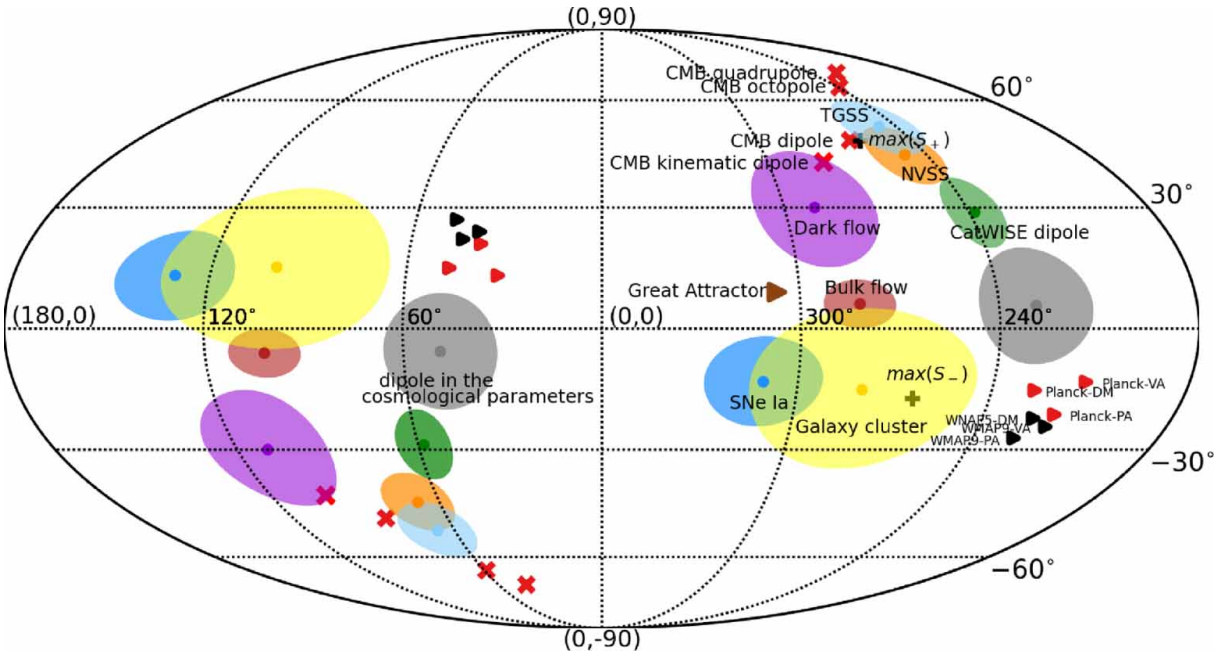

Figure 1.3: The various directions of anisotropies in the Universe, as compiled in Aluri *et al*. [112] with references therein.

1.4.1 wCDM and Dynamical Dark Energy

In general, we refer to any perfect fluid that violates the strong energy condition as dark energy. For an equation of state, $-1 \leq w \leq -1/3$, the fluid will obey the dominant energy condition but not the strong energy condition – which is required for gravitational attraction to allow matter to coalesce into structures [118]. Allowing the equation of state parameter of dark energy to be a free parameter fit to cosmological data, such that $w \neq -1$, is one of the immediate potential solutions to the Hubble tension, and has the appeal of being a simple extension to ΛCDM by an additional free constant. Beyond this, there are more nuanced (yet often ad hoc) parametrisations of the equation of state parameter that vary with cosmic time/redshift, $w(z)$ [119]. These classes of solutions are known as dynamical dark energy models; the most commonly investigated being given by the Chevallier–Polarski–Linder (CPL) [120, 121] form:

$$w(z) = w_0 + w_a \frac{z}{1+z} \,. \tag{1.35}$$

Whilst Eq. (1.35) does not fall out of a more fundamental theory, the choice of parametrisation is well motivated in the local universe. The CPL form neatly breaks down into the present equation of state parameter w_0 and its time evolution w_a, so if ΛCDM or wCDM is correct, either can be returned as a limit of the CPL parametrisation through best fit parameters of $w(z) = -1$ or $w_a = 0$, respectively.

Due to the cosmological tensions previously discussed, the nature of dark energy is a subject of ongoing investigation. The Union 3 joint analysis of supernovae Ia, BAO, and CMB data show an agreement of wCDM and ΛCDM with $w \approx -1$ [122]. However, this same analysis found 1.7–2.6 σ evidence in favour of a thawing dark energy as compared to ΛCDM. The most recent DESI BAO results have also shown a preference for the CPL dark energy parametrisation over "vanilla" ΛCDM or wCDM. In doing so, the equation of state parameter crosses the 'phantom' line, as shown in Fig. 1.4 (originally compiled by the DESI collaboration [5]). This violates the dominant energy condition for a perfect fluid and can lead to conventionally unphysical phenomena such as faster-than-light mass-energy flows [119, 123]. Given how recent this latest result is, its confirmation from upcoming surveys such as Euclid and LSST are eagerly awaited with the expectation that they may confirm a deviation from dark energy driven by a cosmological constant, in favour of dynamical dark energy.

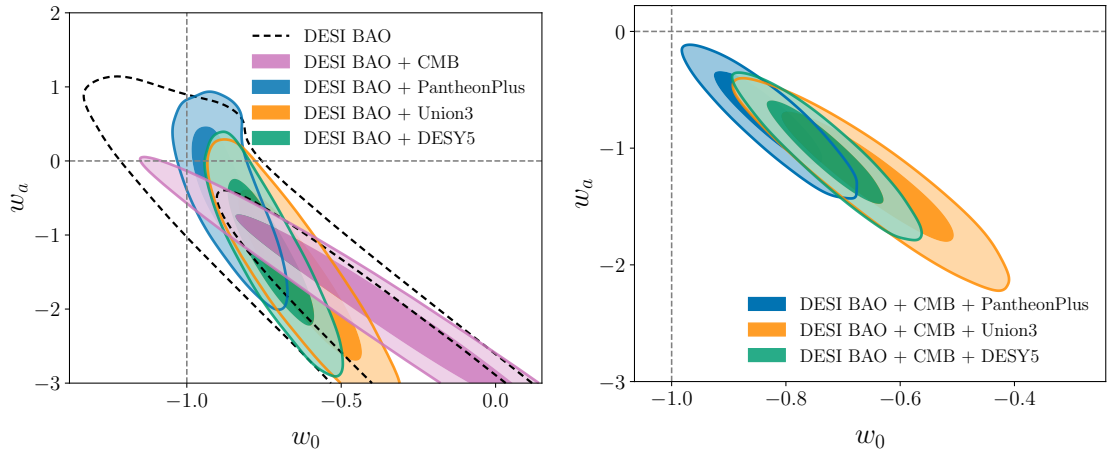

Figure 1.4: *Left Panel*: 1σ and 2σ marginalised posterior constraints in the spatially flat w_0w_aCDM from a combination of DESI BAO and CMB or supernova datasets. *Right Panel*: 1σ and 2σ marginalised posterior constraints in the spatially flat w_0w_aCDM from a combination of DESI BAO, CMB and supernova data. For the Pantheon+, Union3 and DES Y5 datasets a significant tension with ΛCDM was found at 2.5σ, 3.5σ and 3.9σ respectively. Both of these plots were originally compiled by the DESI collaboration [5].

1.4.2 Early Dark Energy

Early dark energy behaves like the cosmological constant Λ at high redshifts, $z \gtrsim 3000$, and then decays away at lower redshifts, faster than the energy density of radiation [124]. This class of models addresses the Hubble tension by reducing the scale of the sound horizon at the time of decoupling, thus a larger H_0 expansion rate is inferred from the CMB which may match estimates from late-universe probes. There are many forms of early dark energy theorised [1],

typically involving scalar fields and associated *ad hoc* potentials[11].

However, it has been shown that early dark energy is not capable of relieving both H_0 and S_8 tensions simultaneously [125]. This is due, in part, to the large degeneracies present between the value of H_0 inferred and the dark matter density contribution to Ω_{M0} required to explain the CMB acoustic peak heights [126]. Nonetheless, there is a slight preference for early dark energy in the recent analysis of ACT and SPT ground based data [127–130].

1.4.3 Interacting Dark Energy

Interacting dark energy models are a class in which dark energy and dark matter are coupled so as to share interactions that are not exclusively gravitational [1]. These models introduce an additional free parameter ξ that mediates the flow of energy from dark matter to dark energy and vice versa. When assuming an equation of state, $w = -1$, corresponding to a cosmological constant a strong preference is found for a non-zero dark energy – dark matter interaction at 5σ significance, when fit to *Planck* CMB data [131]. This is capable of resolving the Hubble tension between estimates from early and late-universe measurements to less than 1σ. However, when combined with other probes in a joint analysis such as *Planck+Pantheon* or *Planck+BAO*, the results weaken and no-longer are capable of resolving the Hubble tension [132–134].

There are other realisations of interacting dark energy – namely, models with $w < -1$ where there is a flow of energy from dark energy to dark matter, and those with $w > -1$ in which energy flows from dark matter to dark energy. Indeed, this form has shown promise in the possibility of resolving the S_8 tension, without affecting the current tension in H_0 [135].

1.4.4 Modified Theories of Gravity

The inclusion of dark energy and dark matter in the standard model of cosmology is only a requirement, given the cosmological principle and the implementation of general relativity on different scales. The ΛCDM model adds dark matter to make gravitational interactions stronger on smaller scales and dark energy to make gravity weaker on large scales, in order to explain the accelerated cosmic expansion. Alternatively, rather than the inclusion of mysterious mass/energy contributions, one might seek to retain the cosmological principle while modifying the Einstein–Hilbert action of general relativity.

[11] There is often a 'two birds and one stone' approach to early dark energy models, as they often also attempt to explain the initial inflation of the universe.

There are a large number of modified gravity models in which the features of gravity vary with scale, in an attempt to resolve the Hubble tension with varying degrees of success (for a review of many prominent theories, see Clifton *et al* [136]). Some examples of which are: emergent gravity [137, 138], $f(R)$ gravities [139], fractional gravity [140, 141], Lanczos–Lovelock gravity [142], modified gravity (MoG) [143, 144], postquantum classical gravity [145, 146], and rainbow gravity [147]. One of the more successful theories in predicting astrophysical phenomena, Modified Newtonian Dynamics (MOND), is discussed in section 1.6.

1.5 Inhomogeneous Cosmology

Modelling the inhomogeneous distribution of matter on scales smaller than the SSH is important not only for correctly understanding the astrophysics of matter sources, but also for foundational questions in general relativity related to the emergence of statistical isotropy and homogeneity. Many of these questions are summarised in the *fitting problem* [148, 149]: given the non-linear nature of the Einstein equations the problem of fitting one geometry inside other another described by an effective dust or perfect fluid source is non-trivial. Related mathematical and theoretical issues have a history going back to the 1930s, and are discussed extensively in related monographs [150, 151] and texts [152].

1.5.1 Exact Inhomogeneous Solutions of Einstein's equations

Exact solutions of Einstein's equations for irrotational pressureless dust sources[12] with fewer symmetries than the FLRW models have been investigated as model cosmologies beginning with the pioneering spherically symmetric solutions of Lemaître [155] and Tolman [156] in the 1930s. The properties of these models and their geodesics were further investigated in detail by Bondi in 1947 [157], and are consequently known as either the Lemaître–Tolman or Lemaître–Tolman–Bondi (LTB) solutions. They are used in a variety of circumstances in general relativity, including the problem of gravitational collapse. As toy models of the universe having a preferred centre they violate the *Copernican principle* – that there is no special observer with a privileged position in the universe. They are therefore difficult to reconcile with physical models for the early universe and are not regarded as serious contenders to the FLRW

[12] We focus on dust sources here, but there exists inhomogeneous perfect fluid solutions as well [153, 154].

solutions. Nonetheless, since they exhibit the phenomenon of non-kinematic differential expansion[13], they provide a simple alternative for the modelling of cosmic dipoles as compared to FLRW models plus local special relativistic boosts.

Large Void Lemaître-Tolman-Bondi Solutions – Although spherically symmetric LTB models with a central overdense hump provide a good fit to some cosmological datasets [158], typical LTB constructions involve a large central underdense void surrounded by an overdense shell that with an appropriate choice of functions asymptotes to an FLRW background. Cosmic dipoles are then generated for off-centre observers along an axis joining them to the void centre. The LTB line element can be written as[14]

$$\mathrm{d}s^2 = -\mathrm{d}t^2 + B^2(t,r)\mathrm{d}r^2 + R^2(t,r)(\mathrm{d}\theta^2 + \sin^2\theta\mathrm{d}\phi^2)\,, \tag{1.36}$$

where the functions $B(t,r)$ and $R(t,r)$ are arbitrary functions that have both spatial and temporal dependence and are assumed positive. The FLRW limiting case is found via letting

$$B(t,r) \longrightarrow \frac{a(t)}{\sqrt{1-kr^2}}, \qquad R(t,r) \longrightarrow r\,a(t)\,. \tag{1.37}$$

Whilst this choice of model is clearly an unreasonable one upon which to build a fully realistic cosmological model, the LTB solutions exhibit relativistic effects that FLRW solutions cannot and may prove to be useful tools in modelling small scale structure. A notable feature is that the 'bang time' – cosmic time from the big bang to the present – is not universal for positions in space. This does not mean the universe started at different times for different observers, but that time runs faster for observers in underdense regions so that they measure a universe much older than an observer in an overdense region. This is in stark contrast with the always synchronous observers of an FLRW universe.

Szekeres Solutions - The Szekeres solutions [159, 160] are Petrov type-D solutions with intrinsically built-in inhomogeneities. In the general case, whilst the metric has a particular form which enables the construction of exact solutions, the Szekeres models have no global symmetry groups generated by Killing vectors. The Szekeres class of solutions are seen to generalise not only the LTB models, but also other exact solutions: the homogeneous but anisotropic Kantowski–Sachs solution [161] and the planar symmetric Eardley–Liang–Sachs models [162]. One advantage of the Szekeres models is that they can be used to construct spacetimes which

[13] For generic, off-centre observers.

[14] In this section, unless otherwise stated, we work in natural units with $c = 1$ and $G = 1$.

are asymptotically FLRW at large distances but with strong inhomogeneities for expanding regions close to the observer. In the general case, the line element in spherical coordinates is given as

$$\begin{aligned} \mathrm{d}s^2 = &-\mathrm{d}t^2 + \frac{1}{\epsilon - K}\left[R' + \frac{R}{S}(S'\cos\theta + N\sin\theta)\right]^2 \mathrm{d}r^2 + R^2(\mathrm{d}\theta^2 + \sin^2\theta \mathrm{d}\phi^2) \\ &+ \left(\frac{R}{S}\right)^2 \left\{[S'\sin\theta + N(1-\cos\theta)]^2 + [(\partial_\phi N)(1-\cos\theta)]^2\right\} \mathrm{d}r^2 \\ &- 2\left(\frac{R}{S}\right)^2 [SS'\sin\theta + SN(1-\cos\theta)]\mathrm{d}r\mathrm{d}\theta + 2\left(\frac{R}{S}\right)^2 (\partial_\phi N)\, S\sin\theta\,(1-\cos\theta)\mathrm{d}r\mathrm{d}\phi\,, \end{aligned} \tag{1.38}$$

where $N(r,\phi) \equiv P'\cos\phi + Q'\sin\phi$, $\epsilon = 0, \pm 1$, and S, P, Q, R, and K are arbitrary functions of r with $K(r) \leq \epsilon$ [163]. Here, the prime index denotes the partial derivative $' \equiv \partial/\partial r$. The choice of ϵ determines the type of solution implemented: ($\epsilon = 0$) quasi-planar, ($\epsilon = -1$) quasi-hyperbolic, or the most often employed for cosmology the ($\epsilon = +1$) quasi-spherical solution. The quasi-spherical solution can be thought of a series of non-concentric shells with a density dipole formed between them due to the relative shifting and rotation between the shells.

Bianchi Solutions - The Bianchi exact solutions are homogeneous but not necessarily isotropic due to differential expansion. The simplest type, Type I [164], are a generalisation of the FLRW solutions with coordinate-specific scale factors as

$$\mathrm{d}s^2 = -\mathrm{d}t^2 + a_x(t)^2\,\mathrm{d}x^2 + a_y(t)^2\,\mathrm{d}y^2 + a_z(t)^2\,\mathrm{d}z^2\,. \tag{1.39}$$

These solutions can be used to attempt to model the local anisotropic expansion of the universe due to nearby structures. However, numerical studies applying Bianchi models to investigate the effects of Laniakea, the local supercluster the Milky Way is contained within, have not been able to resolve the Hubble tension [134].

1.5.2 Coarse-graining and Backreaction

Many of the tensions already discussed, such as the Hubble tension, cannot be resolved by simple extensions to the ΛCDM model without incurring new tensions in cosmological parameters or heightening preexisting ones. The cosmological principle states that the universe is statistically homogeneous and isotropic when dealing with *large scale* averages, and assumes one particular notion of such averages — that of an FLRW geometry. Combining the Copernican principle and the isotropy of the observed mean CMB temperature, we find that at the

epoch of last scattering the early universe must be close to FLRW to a high precision. However, the application of a single global FLRW metric from last scattering until the present epoch potentially neglects important non-linear effects of local structures and inhomogeneities. At redshifts $z \lesssim 0.7$ the distribution of galaxies begins to trace an increasingly complex cosmic web. The fact that the onset of this complexity coincides roughly with apparent onset of cosmic acceleration in the standard cosmology, (c.f., [165], Fig. 8), has led a number of cosmologists to question [166] whether this coincidence may replace the standard cosmic coincidence problem of FLRW models. The latter is usually phrased as: "why is the magnitude of the cosmological constant, Λ, such that the expansion of the universe was decelerating for much of its history and only began accelerating in the relatively recent past?". In standard cosmology, some theorists favour a dynamical solution to this coincidence [167], rather than appealing to anthropic arguments [52].

One potential explanation for the requirement of dark energy within the standard framework is an improper accounting for the average effects of inhomogeneities on the expansion of the universe. However, the manner in which we take cosmological averages is not a trivial question. In the FLRW universe, we implicitly coarse-grain over structures and remove their corresponding degrees of freedom in order to construct the fluid description utilised in the standard cosmology. Coarse-graining in this manner is a standard practice in many areas of physics and up until the scale of galaxies with stellar systems as dust particles, it is considered appropriate and highly effective depending on what you are investigating. For example, it is not considered important to have a description of every atom of a football to be able to predict how it rolls along a field.

In the standard cosmology we coarse-grain over a hierarchy of structures choosing the domain to be of the SSH scale, but as a consequence, lose the subtleties of the long-range, non-linear gravitational interaction between objects below this scale. Furthermore, we assume that there must exist a well-defined global average that is itself an exact solution to the Einstein field equations with averaged sources — this is the FLRW solution,

$$\langle g_{\mu\nu} \rangle = g^{\text{FLRW}}_{\mu\nu} \,, \tag{1.40}$$

where angle brackets $\langle\ \rangle$ indicate an unspecified averaging procedure. However, this assumption is not necessarily true, there need not be an average solution that satisfies the Einstein equations, nor does it necessarily have to be FLRW in nature.

More generally, is possible to represent the metric $g_{\mu\nu}$ of a general inhomogeneous universe as an average metric $\langle g_{\mu\nu}\rangle$ (potentially $\neq g^{\text{FLRW}}_{\mu\nu}$) plus a term describing the deviations from homogeneity,

$$g_{\mu\nu} = \bar{g}_{\mu\nu} + \delta g_{\mu\nu}\,, \tag{1.41}$$

where the bar denotes averaged quantities as $\bar{g}_{\mu\nu} \equiv \langle g_{\mu\nu}\rangle$. Using solely the average metric component of the general metric, we can construct a connection $\bar{\Gamma}^{\lambda}_{\mu\nu} \equiv \Gamma^{\lambda}_{\mu\nu}(\langle g_{\mu\nu}\rangle)$, curvature tensor $\bar{R}^{\mu}{}_{\nu\lambda\rho} \equiv R^{\mu}{}_{\nu\lambda\rho}(\langle g_{\mu\nu}\rangle)$, and Ricci tensor $\bar{R}_{\mu\nu} \equiv R_{\mu\nu}(\langle g_{\mu\nu}\rangle)$. The differences in the connection and curvature tensors between general and averaged geometries define *backreaction* terms that represent the effect of inhomogeneities on the average geometry

$$\delta\Gamma^{\lambda}_{\mu\nu} \equiv \langle\Gamma^{\lambda}_{\mu\nu}(g_{\mu\nu})\rangle - \bar{\Gamma}^{\lambda}_{\mu\nu}\,, \tag{1.42}$$

$$\delta R^{\mu}{}_{\lambda\nu\rho} \equiv \langle R^{\mu}{}_{\lambda\nu\rho}(g_{\mu\nu})\rangle - \bar{R}^{\mu}{}_{\lambda\nu\rho}\,, \tag{1.43}$$

$$\delta R_{\mu\nu} \equiv \langle R_{\mu\nu}(g_{\mu\nu})\rangle - \bar{R}_{\mu\nu}\,. \tag{1.44}$$

Similarly, an Einstein tensor $\bar{G}_{\mu\nu}$ can be constructed for the average metric which will not in general be equivalent to the average Einstein tensor of the inhomogeneous metric, $\langle G_{\mu\nu}(g_{\mu\nu})\rangle \neq \bar{G}_{\mu\nu}$. The Einstein field equations can then be written in terms of the average and backreaction Einstein tensors, as

$$\bar{G}_{\mu\nu} + \delta G_{\mu\nu} = \frac{8\pi G}{c^4}\langle T_{\mu\nu}\rangle\,, \tag{1.45}$$

showing how the Einstein tensor of the homogeneous (average) metric is not sourced only by the averaged energy-momentum.

Backreaction is then defined as the difference between the evolution of the average metric (most often assumed to be FLRW) and the average evolution of a general inhomogeneous metric. The impact of backreaction in cosmology is still a subject of broad debate. In the standard cosmology, the global FLRW metric is assumed to apply to averages on all spatial scales larger than the SSH, with perturbations remaining small, namely in the *linear regime* of perturbation theory. These assumptions work to the extent that ΛCDM successfully passes many independent observational tests, with the provison that it now faces the increasing challenges outlined in section 1.3. Perturbation theory must then break down on scales somewhat below the SSH, where we enter the *non-linear regime* of structure formation. However, it remains possible that such non-linear effects below the SSH feed back on the large-scale average evolution due to the

coupling of scales in non-linear dynamics, causing the average to deviate from the expected FLRW evolution. Some models—including the timescape cosmology discussed later in this section—result in an order-unity relative deviation with respect to the FLRW evolution associated with the averaged sources; they are accordingly called '*strong backreaction*' models. Such a description must be background-free, i.e., it should not assume *a priori* a global FLRW background. Other, so-called '*weak backreaction*' models produce deviations from the average FLRW evolution which are large enough to affect cosmological observables but only at the level of a few percent relative to their FLRW-inferred values. However, even small backreaction terms of this magnitude can have a meaningful impact on the expansion history of the universe [168, 169].

1.5.3 Buchert's Averaging Scheme

There are many different formalisms developed for constructing cosmological averages (for a review see [168]), but the approach developed by Thomas Buchert [170–173] is the most well studied. Rather than averaging tensorial quantities—which is not uniquely defined and requires extra mathematical structures—the Buchert formalism takes spatial averages of the scalar quantities associated with the Einstein equations arising from the fluid flow within a specific domain, including its density ρ, expansion θ, and shear scalar σ. The averages are taken over a fluid-comoving domain $\mathcal{D}$ on global spatial hypersurfaces Σ within a 3+1 Arnowitt–Deser–Misner (ADM) [174, 175] spacetime foliation, choosing synchronous coordinates and a restriction to irrotational and pressureless flows[15]. Angle brackets now denote the spatial volume average of a scalar, e.g., for any scalar quantity Ψ,

$$\langle \Psi \rangle \equiv \frac{1}{\mathcal{V}(t)} \int_{\mathcal{D}} \mathrm{d}^3x \, \sqrt{\det({}^3g)} \, \Psi(t, \vec{x}) \,, \tag{1.46}$$

with $\mathcal{V}(t) \equiv \int_{\mathcal{D}} \mathrm{d}^3x \, \sqrt{\det({}^3g)}$ being the volume of the domain $\mathcal{D}$ contained on the hypersurface Σ with spatial metric ${}^3g$. The domain propagation between consecutive spatial slices is specified by requiring it to be comoving with the fluid flow. This ensures that there is no transfer of mass or of fluid elements across the boundaries of the averaging domain, and thus that the total rest mass within it is preserved over its evolution.

[15] A generalisation of the averaging formalism to include vorticity scalars and dynamical backreaction terms was introduced in 2019 by Buchert, Mourier and Roy [172]. However, Buchert's original 2000 scheme [170], which we present here, already contains the terms relevant to the timescape cosmology phenomenology.

Scalar projections of the Einstein equations can then be averaged to give the Buchert equivalent of the Friedmann, Raychaudhuri, and continuity equations:

$$3\frac{\dot{\bar{a}}^2}{\bar{a}^2} = 8\pi G\langle\rho\rangle - \frac{1}{2}c^2\langle\mathcal{R}\rangle - \frac{1}{2}\mathcal{Q}\,, \tag{1.47}$$

$$3\frac{\ddot{\bar{a}}}{\bar{a}} = -4\pi G\langle\rho\rangle + \mathcal{Q}\,, \tag{1.48}$$

$$\frac{\partial\langle\rho\rangle}{\partial t} + 3\frac{\dot{\bar{a}}}{\bar{a}}\langle\rho\rangle = 0\,, \tag{1.49}$$

where the overdot represents a derivative with respect to the coordinate time[16] t, and $\mathcal{Q}$ is the kinematical backreaction given by

$$\mathcal{Q} \equiv \frac{2}{3}\langle(\theta - \langle\theta\rangle)^2\rangle - 2\langle\sigma^2\rangle = \frac{2}{3}(\langle\theta^2\rangle - \langle\theta\rangle^2) - 2\langle\sigma^2\rangle\,, \tag{1.50}$$

where θ is the trace of the expansion tensor Θ_{ij} of the fluid flow, and the shear scalar σ is written in terms of σ_{ij}, the trace-free symmetric shear tensor, as $\sigma^2 = \frac{1}{2}\sigma^{ij}\sigma_{ij}$. The scale factor $\bar{a}$ in Eqs. (1.47)–(1.49) is not given by a particular choice of underlying geometry. It is an average quantity defined by the ratio of the domain volume at a given time to its initial volume,

$$\bar{a}(t) \equiv \left(\frac{\mathcal{V}(t)}{\mathcal{V}(t_i)}\right)^{1/3}. \tag{1.51}$$

Analogously to the FLRW equivalent, the Hubble parameter can be expressed in terms of the volume-averaged expansion scalar,

$$\bar{H}(t) \equiv \frac{\dot{\bar{a}}}{\bar{a}} = \frac{1}{3}\langle\theta\rangle\,. \tag{1.52}$$

The first Buchert equation, Eq. (1.47), for a two component fluid with matter density, ρ_M, and radiation density, ρ_R, may then be rewritten analogously to the ΛCDM sum rule, Eq. (1.6), as

$$\Omega_M + \Omega_k + \Omega_R + \Omega_{\mathcal{Q}} = 1 \tag{1.53}$$

where[17] $\Omega_M = 8\pi G\langle\rho_M\rangle/(3\bar{H}^2)$, $\Omega_R = 8\pi G\langle\rho_R\rangle/(3\bar{H}^2)$, $\Omega_k = -c^2\langle\mathcal{R}\rangle/(6\bar{H}^2)$ and $\Omega_{\mathcal{Q}} = -\mathcal{Q}/(6\bar{H}^2)$.

Finally, the non-commutativity of Buchert's averaging procedure with evolution in time is expressed precisely by

$$\partial_t\langle\Psi\rangle - \langle\dot{\Psi}\rangle = \langle\Psi\,\theta\rangle - \langle\theta\rangle\langle\Psi\rangle \tag{1.54}$$

[16] Later referred to as the volume-averaged time in the context of the timescape model.

[17] Since we include an explicit radiation source we denote the average curvature term Ω_k rather than $\Omega_{\mathcal{R}}$ to avoid potential confusion.

for any scalar Ψ. For an in-depth description of the derivation and applications of the Buchert's averaging scheme, we encourage the reader to see [168, 170–172].

The magnitude and relevance of backreaction in cosmology has been the subject of much debate for the past two decades, beginning with early debates on the effects of structures as perturbations about an FLRW background [148], with proponents for [176] and against [177] the effects being important. Particular criticisms of the Buchert scheme were made by Ishibashi and Wald [178], who questioned (i) the magnitude of the backreaction term, $\Omega_{\mathcal{Q}}$; (ii) the physical interpretation of the time parameter in the Buchert equations; and (iii) the relationship of its statistical quantities to physical observables. The Buchert equations are underdetermined and one additional integrability condition is required for their closure. Different implementations of the closure condition are associated with different possible physical interpretations of the statistical averages. Wiltshire proposed the timescape cosmology in 2007 to directly address the criticisms of Ishibashi and Wald.

In 2010, Green and Wald proposed an alternative backreaction formalism [179], which differs fundamentally from that of Buchert by assuming that the global average evolution is well described by an exact solution of Einstein's equations at any scale of averaging. In the Green–Wald scheme the backreaction terms yield a small effective traceless energy-momentum tensor term representing a gravitational wave background. The Green-Wald scheme provides a mathematical self-consistency check on the standard ΛCDM cosmology [180], but has been refuted as not mathematically general enough to capture the essential nonlinear effects found in averages of the Einstein equations [181]. This conclusion has been further explicitly demonstrated thorough studies of exact solutions to the EFE for inhomogeneous dust-filled cosmologies [182]. Whereas Buchert's averaging scheme is found to give a faithful way of interpreting the large-scale expansion of space and its deviations from the FLRW geometry, the Green–Wald formalism does not appear to yield any information about the large-scale properties of a given inhomogeneous spacetimes but is entirely dependent on the choice of a background which is not uniquely specified for any given inhomogeneous spacetime. This would appear to limit the applicability of the Green–Wald formalism to the real universe [182].

1.5.4 Timescape

The timescape model of cosmology is a two scale solution to the Buchert averaged Einstein field equations, sourced by irrotational, shearless dust, that seeks to explain the accelerated

expansion of the universe as an apparent effect, without the need for dark energy. Here, we present a brief description of the foundations of the model. For original details see [183–185] and for a review see [166].

The basic setup is that the present epoch horizon volume consists of a statistical ensemble of wall and void regions given by exact solutions of the EFEs, of which we later take the Buchert average. Assuming that null geodesics follow those of the statistical volume average Buchert geometry, they are then conformally matched to null geodesics of the local regional geometry on the timelike bounding surface of the wall regions, finite infinity, *fi*. Finite infinity is defined by the time evolution of the critical density scale from last scattering to the present epoch: its geometry is that of the spatially flat FLRW model. Unlike standard FLRW models which take this to be the global geometry for the whole universe, in timescape the $k_w = 0$ FLRW metric prescribes the local asymptotic geometry for realistic sources and observers. Since all known astrophysical sources formed from initial perturbations that were greater than critical density, finite infinity demarcates between gravitationally bound overdense structures and underdense expanding space.

In the timescape model, the domain of coarse-graining in the Buchert averaging scheme is taken to match the SSH of $100\,h^{-1}$ Mpc, so that the flow of energy and matter between coarse-grained cells can be neglected. The void and wall regions are each defined by locally homogeneous and isotropic FLRW solutions with their own respective scale factors a_v and a_w, which are combined as a disjoint union to form the Buchert volume-average scale factor,

$$\bar{a} = f_{vi}\, a_v^3 + f_{wi}\, a_w^3\,, \tag{1.55}$$

where f_{vi} and f_{wi} correspond to the initial fraction of void and wall regions by volume in the universe. Note that,

$$f_{wi} = 1 - f_{vi}\,, \tag{1.56}$$

$$f_v(t) + f_w(t) = 1\,, \tag{1.57}$$

where $f_w(t) = f_{wi}\, a_w^3/\bar{a}^3$ and $f_v(t) = f_{vi}\, a_v^3/\bar{a}^3$ are the wall and void volume fractions, respectively. The volume averaged (or *bare*) Hubble parameter can then be defined as

$$\bar{H} \equiv \frac{\dot{\bar{a}}}{\bar{a}} = f_w H_w + f_v H_v\,, \tag{1.58}$$

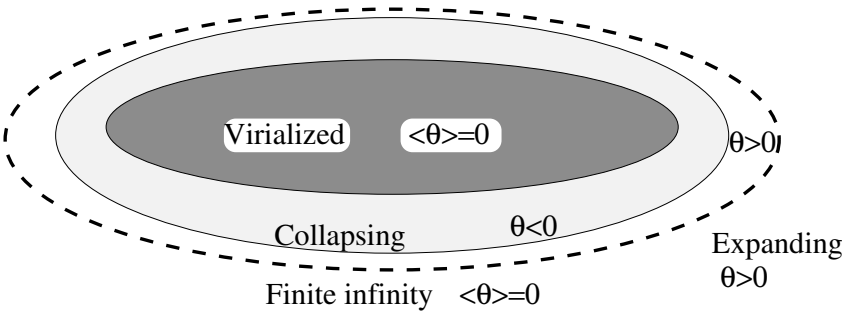

Figure 1.5: A finite infinity region is one over which the average expansion is zero [183]. It contains virialized subregions which are not expanding, surrounded by a region collapsing inward. The finite infinity boundary lies in the expanding region outside, containing some expanding regions which balance out the collapsing regions in the average.

where $H_w \equiv \dot{a}_w/a_w$ is the wall Hubble parameter and $H_v \equiv \dot{a}_v/a_v$ is the void Hubble parameter as determined by a volume-average observer.

Walls are required to be spatially flat when averaged, $\langle \mathcal{R} \rangle_w = 0$ and $k_w = 0$, so that $\langle \theta \rangle_w = 0$. Since there are always flows of matter into gravitationally bound structures, i.e., regions within walls for which $\theta < 0$, this means that finite infinity surface itself expands outwards encompassing regions with $\theta > 0$ that bound the collapsing regions so that the net regional average is zero. such that they are non-expanding: see Fig. 1.5. The void regions have negative average spatial curvature $\langle R \rangle_v = 6k_v/a_v^2$ where $k_v < 0$. The total volume average curvature can then be written as

$$\langle \mathcal{R} \rangle = \frac{6k_v\, f_v}{a_v^2}\,. \tag{1.59}$$

Although Buchert's formalism allows for more complexity, Wiltshire's 2007 timescape construction assumes no kinematical backreaction within walls and voids through Eq. (1.50), as their homogeneous and isotropic construction enforces $\langle \sigma^2 \rangle = 0$ and $\langle \theta^2 \rangle = \langle \theta \rangle^2$. However, the ensemble of their solutions will produce backreaction, given as

$$\mathcal{Q} = \frac{2\,\dot{f}_v^2}{3f_v(1-f_v)}\,. \tag{1.60}$$

The Buchert equations, Eqs. (1.47) and (1.48), can be now written as

$$\frac{\dot{\bar{a}}^2}{\bar{a}^2} + \frac{\dot{f}_v^2}{9f_v(1-f_v)} + \frac{k_v f_{vi}^{2/3}\, f_v^{1/3}}{\bar{a}^2} = \frac{8\pi G}{3}\left(\bar{\rho}_{M0}\,\frac{\bar{a}_0^3}{\bar{a}^3} + \bar{\rho}_{R0}\,\frac{\bar{a}_0^4}{\bar{a}^4}\right)\,, \tag{1.61}$$

$$\ddot{f}_v + \frac{\dot{f}_v^2\,(2f_v-1)}{2f_v\,(1-f_v)} + 3\frac{\dot{\bar{a}}}{\bar{a}}\dot{f}_v + \frac{3k_v\, f_{vi}^{2/3}\, f_v^{1/3}\,(1-f_v)}{2\bar{a}^2} = 0\,, \tag{1.62}$$

after solving the continuity equation, Eq. (1.49), with $\langle \rho_M \rangle = \rho_{M0}\,\bar{a}_0^3/\bar{a}^3$ and $\langle \rho_R \rangle = \rho_{R0}\,\bar{a}_0^4/\bar{a}^4$.

The sum rule, Eq. (1.53), for bare quantities now applies where

$$\bar{\Omega}_M = \frac{8\pi G\,\bar{\rho}_{M0}\,\bar{a}_0^3}{3\bar{H}^2\,\bar{a}^3}\,, \tag{1.63}$$

$$\bar{\Omega}_R = \frac{8\pi G\,\bar{\rho}_{R0}\,\bar{a}_0^4}{3\bar{H}^2\,\bar{a}^4}\,, \tag{1.64}$$

$$\bar{\Omega}_k = \frac{-k_v f_v}{a_v^2\,\bar{H}^2}\,, \tag{1.65}$$

$$\bar{\Omega}_{\mathcal{Q}} = \frac{-\dot{f}_v^2}{9 f_v\,(1-f_v)\,\bar{H}^2}\,, \tag{1.66}$$

and the overbar indicates an average over the present epoch particle horizon volume. Of course it is also possible to include a cosmological constant Λ in the Einstein field equations and derive its corresponding bare density parameter $\bar{\Omega}_\Lambda = \Lambda/(3\bar{H}^2)$. However, as an aim of the timescape model is to explain the accelerated expansion of the universe without dark energy, we exclude this term.

The statistical ensemble of wall and void regions is not the full description of the timescape model. This volume-averaged statistical geometry, for which we can assume the spherically symmetric form as an ansatz,

$$\mathrm{d}\bar{s}^2 = -c^2\mathrm{d}t^2 + \bar{a}^2(t)\mathrm{d}\bar{\eta}^2 + \mathcal{A}(\bar{\eta},t)\mathrm{d}\Omega^2\,, \tag{1.67}$$

is matched to the local wall geometry, where $\mathcal{A}$ satisfies $\int_0^{\eta_H}\mathrm{d}\bar{\eta}\,\mathcal{A}(\bar{\eta},t) = \bar{a}^2(t)\mathcal{V}_i(\eta_H)/(4\pi)$. The wall geometry is itself comprised of a collective of *finite infinity* regions used to describe bound structures with the local average metric,

$$\mathrm{d}s_{\mathit{fi}}^2 = -c^2\mathrm{d}\tau_w^2 + a_w^2(\tau_w)[\mathrm{d}\eta_w^2 + \eta_w^2\,\mathrm{d}\Omega_2^2]\,. \tag{1.68}$$

Void regions are described by the negatively curved $k=-1$ (open) FLRW geometry

$$\mathrm{d}s_v^2 = -c^2\mathrm{d}\tau_v^2 + a_v^2(\tau_v)[\mathrm{d}\eta_v^2 + \sinh^2(\eta_v)\,\mathrm{d}\Omega_2^2]\,. \tag{1.69}$$

The key ingredient in the timescape model is its physical interpretation of the closure relation in the Buchert scheme. This arises from a generalisation of the Strong Equivalence Principle to cosmological averages in the form of a Cosmological Equivalence Principle [186]. On scales at which regionally isotropic motion of comoving particles at rest in an expanding space is operationally indistinguishable from the equivalent isotropic motion of particles in an empty space the regional metric is the $k=0$ FLRW metric. This applies at the finite infinity scale in

wall regions and on scales much smaller than the curvature radius within voids. One can then define a notion of uniformity of expansion deep within the non-linear regime at the expense of recalibrating rulers and clocks in the presence of spatial curvature gradients. The voids and walls are combined in the Buchert averages by the *quasi-local uniform bare Hubble flow* condition,

$$\bar{H} = \frac{1}{a_w}\frac{\mathrm{d}a_w}{\mathrm{d}\tau_w} = \frac{1}{a_v}\frac{\mathrm{d}a_v}{\mathrm{d}\tau_v}\,, \tag{1.70}$$

so that the regional Hubble parameters with walls and voids are equal to the volume averaged parameter.

We rewrite Eq. (1.67) in terms of the wall time using the lapse function

$$\bar{\gamma}_w = \frac{\mathrm{d}t}{\mathrm{d}\tau_w} \tag{1.71}$$

so that

$$\mathrm{d}\bar{s}^2 = -\bar{\gamma}_w^2(\tau_w)c^2\mathrm{d}\tau_w^2 + \bar{a}(\tau_w)\mathrm{d}\bar{\eta}^2 + \mathcal{A}(\bar{\eta},\tau_w)\mathrm{d}\Omega_2^2\,. \tag{1.72}$$

Then, we conformally match radial null geodesics between Eq. (1.68) and (1.72) to obtain the relation

$$\mathrm{d}\eta_w = \frac{f_{wi}^{1/3}\,\mathrm{d}\bar{\eta}}{\bar{\gamma}_w\,(1-f_v)^{1/3}} \tag{1.73}$$

Using this relation and its integral, the local finite infinity geometry of Eq. (1.68) can be extended to obtain the *dressed* statistical metric

$$\mathrm{d}s^2 = -c^2\mathrm{d}\tau_w^2 + a^2(\tau_w)[\mathrm{d}\bar{\eta}^2 + r_w^2(\bar{\eta},t)\,\mathrm{d}\Omega_2^2]\,, \tag{1.74}$$

with

$$r_w \equiv \bar{\gamma}_w\,(1-f_v)^{1/3}\,f_{wi}^{-1/3}\,\eta_w(\bar{\eta},\tau_w)\,, \tag{1.75}$$

and $a \equiv \bar{\gamma}_w^{-1}\,\bar{a}$. This metric in Eq. (1.74) represents an extension of the local regional geometry to cosmological scales parametrized by the volume-average conformal time $\bar{\eta}$. It is spherically symmetric, but since it is not a global exact solution of the EFE, it is not a LTB geometry.

The timescape interpretation is that when we fit a global spherically symmetric metric to cosmological observations on scales larger than the SSH, Eqs. (1.74) and (1.75) are the effective metric we apply, with wall time τ_w being close to our own proper time. It is then this dressed geometry that is used when making comparisons between timescape and the ΛCDM cosmology as cosmological parameters we infer beyond the SSH will not be the volume average *bare*

parameters as we are not observers with clocks corresponding to the volume-average time.[18] Beyond the SSH we instead infer the *dressed* parameters,

$$H \equiv \frac{1}{a}\frac{\mathrm{d}a}{\mathrm{d}\tau_w} = \frac{1}{\bar{a}}\frac{\mathrm{d}\bar{a}}{\mathrm{d}\tau_w} - \frac{1}{\bar{\gamma}_w}\frac{\mathrm{d}\bar{\gamma}_w}{\mathrm{d}\tau_w} = \bar{\gamma}_w\bar{H} - \frac{\mathrm{d}\bar{\gamma}_w}{\mathrm{d}t} \tag{1.76}$$

and

$$\Omega_M = \bar{\gamma}_w^3\,\bar{\Omega}_M\,. \tag{1.77}$$

Whilst full numerical simulations and the inclusion of a radiation fluid are required to fully describe the radiation dominated epoch (see [185] for the addition of radiation), during the matter dominated era an exact solution of the Buchert equations can be found [184] which approaches a '*tracker*' limit. This is typically applied to give a simple analytic form for cosmological distances that is very accurate on scales $z < 10$ and is considered valid up to $z \approx 40$. The tracker solution corresponds to walls expanding an Einstein-de Sitter model in volume-average time, with $a_w = a_{w0}\,t^{2/3}$, and voids as empty Milne universes, $a_v = a_{v0}\,t$, so that

$$h_r = \frac{H_w}{H_v} = \frac{2}{3}. \tag{1.78}$$

The tracker solution to the Buchert equations is then given by

$$\bar{a} = \frac{\bar{a}_0\,(3\bar{H}_0\,t)^{2/3}}{2+f_{v0}}[3f_{v0}\,\bar{H}_0\,t + (1-f_{v0})(2+f_{v0})]^{1/3} \tag{1.79}$$

$$= \frac{\bar{a}_0\,(3\bar{H}_0\,t)}{2+f_{v0}}\left(\frac{f_{v0}}{f_v}\right)^{1/3}, \tag{1.80}$$

where

$$f_v(t) = \frac{3f_{v0}\,\bar{H}_0\,t}{3f_{v0}\,\bar{H}_0\,t + (1-f_{v0})(2+f_{v0})}\,. \tag{1.81}$$

The present void fraction f_v gives a method of writing typical defining cosmological parameters in simple forms as [187]

$$\bar{H} = \frac{(2+f_v)}{3t}\,, \tag{1.82}$$

$$\bar{\Omega}_M = \frac{4(1-f_v)}{(2+f_v)^2}\,, \tag{1.83}$$

$$\bar{\gamma}_w = \frac{1}{2}(2+f_v)\,. \tag{1.84}$$

[18] The volume-average time, t, represents a local proper time only for those observers whose local spatial curvature matches that of the Buchert average over the entire present particle horizon volume. Such a location is in a void but not the void centres, where the local proper time is τ_v.

From Eq. (1.82) the volume-average age of the universe is given by

$$t_0 = \frac{2 + f_{v0}}{3\bar{H}_0}\,, \tag{1.85}$$

although the age inferred for an ideal isotropic observer[19] will depend on their local cosmological environment, i.e., within a wall or void. The relation between the wall time and volume-average time is given by

$$\tau_w = \frac{2}{3}t + \frac{4\Omega_{M0}}{27 f_{v0}\bar{H}_0}\ln\left(1 + \frac{9 f_{v0}\bar{H}_0 t}{4\Omega_{M0}}\right)\,, \tag{1.86}$$

which, due to the substantial difference in present epoch clock rates, leads to a universe in which a wall observer will infer an age of the universe billions of years younger than a volume-average or void observer. However, a large cumulative variance in clock rates only applies where gradients in the kinetic energy of expansion are large: between bound structures and extremely underdense voids. For wall regions within non-expanding gravitationally bound clusters of galaxies, as long as gravitational fields are weak, it is assumed that the clock rates of ideal observers will not differ significantly from those at the finite infinity boundaries.

An effective bare deceleration parameter $\bar{q} \equiv -\ddot{a}/(\bar{H}^2\bar{a})$ can be assigned to a volume-average isotropic observer. In the tracker solution, this then becomes

$$\bar{q} = \frac{2(1 - f_v)^2}{(2 + f_v)^2}\,, \tag{1.87}$$

which decreases monotonically from an initial Einstein–de Sitter value $\bar{q} \simeq \frac{1}{2}$ as the void fraction grows from the initial $f_v \simeq 0$, but is always positive and thus, no cosmic acceleration will be inferred. However, a physical observer is a wall observer who measures the dressed deceleration parameter [184],

$$q = -\frac{1}{H^2 a}\frac{\mathrm{d}^2 a}{\mathrm{d}\tau_w^2} = -\frac{(1 - f_v)(8 f_v^3 + 39 f_v^2 - 12 f_v - 8)}{(4 + f_v + 4 f_v^2)^2}\,. \tag{1.88}$$

where the dressed Hubble parameter, H, is related to the bare Hubble parameter by $H = \bar{H}(4 + f_v + 4f_v^2)/[2(2 + f_v)]$ for the tracker solution. The dressed deceleration parameter again starts out at $q \simeq \frac{1}{2}$ when $f_v \simeq 0$, but becomes negative when the void fraction reaches $f_v \simeq 0.587$, at a zero of the cubic term in Eq. (1.88). This occurs at a relatively late epoch when voids have grown to dominate the universe by volume.

[19] For this purpose an ideal observer at any location is one who measures a CMB temperature with the greatest degree of isotropy, modulated only by the primordial anisotropies and structure dipoles from local inhomogeneities on scales of the order of the SSH.

The accelerated expansion of space is now interpreted as an apparent effect, which is explained as a consequence of the cumulative difference in clock rates between wall and volume-average observers. This neatly solves the cosmic coincidence problem as the epoch of void dominance coincides with the emergence of large structures in the cosmic web [165]. Therefore, there is no requirement for dark energy in the timescape model.

The dressed deceleration parameter has a global minimum value $q_{\rm min} \simeq -0.043$ at $f_v \simeq 0.774$, and in the far future $q \to 0$ as $f_v \to 1$. Thus in contrast to the ΛCDM model, with a deceleration parameter $q_{\Lambda CDM} = \frac{3}{2}(1-\Omega_\Lambda) - 1 \simeq -0.53$, in the timescape model the apparent acceleration has a much smaller amplitude and its future is close to that of a global Milne universe, rather than ever continuing acceleration of cosmic expansion.

Distances in the Timescape Model

Using the tracker solution described above, relations for equivalents of the standard distance measures used in cosmology can be derived which will be parametrised by the present void fraction f_{v0} and $\bar{H}_0$. The dressed luminosity distance relation is given as

$$d_L = a_0(1+z) r_w \,, \tag{1.89}$$

where the effective comoving distance r_w is given by

$$r_w = \bar{\gamma}_w (1-f_v)^{1/3} \int_t^{t_0} \frac{c\,{\rm d}t'}{\bar{\gamma}_w(t')(1-f_v(t'))^{1/3}\,\bar{a}(t')} \,. \tag{1.90}$$

The cosmological redshift relation satisfies,

$$z+1 = \frac{\bar{a}_0\,\bar{\gamma}_w}{\bar{a}\bar{\gamma}_{w0}} = \frac{(2+f_v)\,f_v^{1/3}}{3 f_{v0}^{1/3}\,\bar{H}_0\,t} = \frac{2^{4/3}\,t^{1/3}(t+b)}{f_{v0}^{1/3}\,\bar{H}_0\,t\,(2t+3b)^{4/3}} \,. \tag{1.91}$$

where

$$b = \frac{2(1-f_{v0})(2+f_{v0})}{9 f_{v0}\,\bar{H}_0} \,. \tag{1.92}$$

The integral in Eq. (1.91) can be used to express angular diameter distance d_A as

$$d_A = c\,t^{2/3} \int_t^{t_0} \frac{2\,{\rm d}t'}{(2+f_v(t'))\,(t')^{2/3}} \,, \tag{1.93}$$

$$= c\,t^{2/3}\,(\mathcal{F}(t_0) - \mathcal{F}(t)) \,, \tag{1.94}$$

where

$$\mathcal{F}(t) = 2t^{1/3} + \frac{b^{1/3}}{6} \ln\left(\frac{(t^{1/3}+b^{1/3})^2}{t^{2/3}-b^{1/3}\,t^{1/3}+b^{2/3}}\right) + \frac{b^{1/3}}{\sqrt{3}} \tan^{-1}\left(\frac{2t^{1/3}-b^{1/3}}{\sqrt{3}\,b^{1/3}}\right). \tag{1.95}$$

This gives the tools required to make cosmological inferences comparable to ΛCDM. If one takes a spatially flat FLRW model with negligible contributions from radiation to the energy fraction in the late universe, then both the ΛCDM and timescape expansion histories can be parametrised by two parameters - Ω_{M0} and H_0 in ΛCDM, and f_{v0} and $\bar{H}_0$ in timescape. This makes them ideal for statistical comparisons, the nuances of which are discussed in Chapter 3.

1.6 Modified Newtonian Dynamics

MOdified Newtonian dynamics (MOND) presents an alternative solution to the *missing mass problem* on galactic scales, in which the Newtonian description of gravity or inertia is altered, rather than requiring additional mass in the form of dark matter. Originally motivated by the failure of Newtonian physics to explain the galactic rotation curves of spiral galaxies with purely luminous matter, Milgrom postulated a modification to Newton's second law for very small accelerations such that the flattened rotation curves could be explained [188–190]. In doing this, the MOND paradigm introduces a new fundamental constant in the acceleration scale $a_0 \approx 1.2 \times 10^{-10}\,\mathrm{ms}^{-1}$, below which MONDian effects dominate[20]. This is the central tenet of all MOND formulations.

For large accelerations, standard Newtonian dynamics are returned as

$$a \gg a_0\,, \qquad \mathbf{a} = \mathbf{a}_N = -\nabla\phi_N\,, \tag{1.96}$$

where $\mathbf{a}$ is the true (or MONDian) gravitational acceleration and $\mathbf{a}_N$ is the standard acceleration as calculated in the Newtonian regime with the potential, ϕ_N. However, for accelerations smaller than the acceleration scale, the deep-MOND (dMOND) limit applies

$$a \ll a_0\,, \qquad a = \sqrt{|\mathbf{a}_N|\,a_0}\,, \tag{1.97}$$

It is then trivial to show how the dMOND limit returns flat rotation curves as, in the weak acceleration limit for circular orbits,

$$\frac{v^2}{r} = a_N = \frac{GM}{r^2}\,, \tag{1.98}$$

[20]Depending on context, it can be useful to define a MOND length scale, l_0, as a proxy for the acceleration scale, $l_0 \equiv c^2/a_0$, and a MOND mass $M_0 \equiv c^4/(a_0\,G)$.

therefore in the dMOND limit,

$$v^2 = \sqrt{a_0\, G\, M}\,, \tag{1.99}$$

which is independent of radius so asymptotes to a constant value. Note that, Eq. (1.99) is the MOND equivalent of the empirical Tully-Fisher relation between the mass of a galaxy (derived from its luminosity) and its asymptotic rotation velocity.

Although there is no agreed upon, final theory of MOND [191], all formulations developed are based on the nonrelativistic tenets described above. How each MOND formulation transitions between the Newtonian and dMOND limits is dependent upon the choice of formulation and of its interpolating function, μ. Milgrom's law can be written as follows:

$$\mu\left(\frac{a}{a_0}\right)\mathbf{a} = \mathbf{a}_N \tag{1.100}$$

where the interpolating function has the limits

$$\mu(x) \longrightarrow \begin{cases} 1\,, & \text{for } x \gg 1\,, \\ x\,, & \text{for } x \ll 1\,, \end{cases} \tag{1.101}$$

and where $x = a/a_0$. Alternatively, Eq. (1.100) is often inverted to be written as

$$\mathbf{a} = \nu\left(\frac{a_N}{a_0}\right)\mathbf{a}_N \tag{1.102}$$

with

$$\nu(y) \longrightarrow \begin{cases} 1\,, & \text{for } y \gg 1\,, \\ y^{-1/2}\,, & \text{for } x \ll 1\,, \end{cases} \tag{1.103}$$

where $y = a_N/a_0$, which is often more convenient.

The choice of interpolating function is somewhat *ad hoc*, and for the majority of observations inconsequential as astrophysical phenomena often comfortably fit entirely within the Newtonian or dMOND limits. This is partially why only limitted progress has been made distinguishing between the many MOND formulations. Two major non-relativistic formulations, the AQUAadratic Lagrangian (AQUAL) and QUasi-linear MOND (QUMOND) descriptions of MOND, are discussed in the introduction of Chapter 5. As yet none of the non-relativistic theories have been found as a limit of GR and the artificial nature of the choice of interpolating function implemented, leads many to view MOND as an effective empirical theory for many astrophysical phenomena rather than something more fundamental. In fact, the definition of a

universal acceleration scale breaks the strong equivalence principle of GR by implying an absolute inertial frame; bringing further questions as to whether there exists a fundamental MOND theory.

Relativistic theories incorporating MOND have been developed with varying success. Rather than modifying the Poisson equation in the Newtonian case, these extensions modify the Einstein-Hilbert action such as the Tensor-Vector-Scalar (TeVeS) formulation of Bekenstein [192] and then Generalised TeVeS theory [193], Bimetric MOND [194–196], or MOND adaptions of Einstein-Aether theories [197].

Despite the absence of an appropriate theoretical framework, MOND has been incredibly successful in making predictions at the galactic scale. Not only has MOND been able to well-constrain a large number of rotation curves [191, 198, 199], but is effective at constraining the kinematics of galaxies [191, 200], dynamics of wide binary stars [201, 202], radial acceleration relation of galaxies [RAR, 203, 204], orbital velocity of interacting galaxy pairs [205], early-universe galaxy and cluster formation [206], and galaxy-scale gravitational lensing [207, 208]. However, MOND fails at modelling larger structures such as on the galaxy cluster scale [209, 210] where some dark matter is still required to explain the observed mass to temperature relation for intra-cluster gas.

Chapter 2

Lensing Overview

2.1 A Very Brief History of Gravitational Lensing

Gravitational lensing refers to the deflection of the path of light rays due to their passage through a gravitational field. Whilst conventional wisdom understands this effect through the theory of general relativity, gravitational lensing was first conceptualised well in advance of Einstein's theories. Sir Isaac Newton considered the deflection of light due to gravity in 'Opticks' 1704. In this work he assumes a corpuscular theory of light with photons of a discrete (but small) mass, resulting in the deflection angle α being given as

$$\hat{\alpha} = \frac{2G\,M}{c^2\,\xi}\,, \tag{2.1}$$

where G, M, c and ξ indicate Newtons gravitational constant, the mass of the lens object, the speed of light, and the impact parameter respectively. It turns out Eq. (2.1) returns precisely half the value for the deflection angle as predicted by Einstein through GR,

$$\hat{\alpha} = \frac{4G\,M}{c^2\,\xi}\,. \tag{2.2}$$

This difference between the Newtonian deflection angle of Eq. (2.1) and that of GR, Eq. (2.2), provided an early test for Einstein's theories.

In 1919, the first experimental test of a prediction of general relativity – the lensing effect – was made on Eddington's expedition to observe the deflection of starlight by the Sun during a solar eclipse. This pioneering observation confirmed the deviation from a Newtonian deflection angle to Eq. (2.2) and was the first step in developing the astrophysical tool used today.

Following Eddington's expedition, the theory and formalism of gravitational lensing was

expanded. Soon after, the formation of multiple images, rings, and magnifications was theorized (although initially still focused on the lensing of stars). It was not until 1937, that Zwicky proposed that the mass of extragalactic nebulae, which we now know as other galaxies, could be determined using gravitational lensing. Then around another 30 years until Refsdal and Shapiro, individually but in the same year, consider the time-delay between the multiple images produced by strong gravitational lensing of supernovae as a potential way to infer the Hubble constant, H_0.

The first detection of a multiply imaged gravitational lensing candidate was made in 1979 by D. Walsh *et al.*[211] of the doubly imaged quasar system 0957+561 from a radio survey. Some time later, due to the variable name of QSOs, the first time-delay between images was determined for 0957+561. This was the first real confirmation of Refsdal and Shapiro's prediction [212, 213] that gravitational lensing could be used for cosmology, and provided the first stepping stone on the way to the current high precision research ongoing to date.

At the time of writing, several thousand strong gravitational galaxy-galaxy scale lenses have been discovered and hundreds of them have corresponding follow-up imagery [2, 214, 215]. We now have multiple lensed supernova, some of which are sufficiently well constrained in order to provide precise estimates of H_0, in SN Refsdal [216], SN H0pe [217], SN Encore [218] and more. Cosmology from strong gravitational lensing has traditionally been limited by the quantity and quality of available data. However, with the next generation of surveys and space telescopes being launched, this is expected to change over the next few years.

2.2 Lensing Formalism

In this section, we provide a brief description of the standard lensing formalism of geometric optics used for gravitational lensing. There are many textbooks and reviews that lay out this approach, see any of the following for more comprehensive detail [219–225].

2.2.1 Deflection Angle

In order to derive the standard lensing formalism, we make various assumptions. Firstly, we assume weak fields, $|\Phi|/c^2 \ll 1$, and that the motion of the lens is small with respect to the system of the observer and source. We also neglect the expansion of space as the region of space in which we consider deflection by a Newtonian perturbation is considered small enough that

it will not be affected by the expansion. Thus, we begin to describe the deflection caused by a lens by assuming a Minkowski metric[1]

$$\mathrm{d}s^2 = \eta_{\mu\nu}\mathrm{d}x^\mu \mathrm{d}x^\nu \,, \tag{2.3}$$

$$= -c^2\mathrm{d}t^2 + \mathrm{d}\mathbf{x}^2 \,, \tag{2.4}$$

which is then perturbed by the Newtonian potential of our lens as

$$\mathrm{d}s^2 = -c^2\left(1+\frac{2\Phi}{c^2}\right)\mathrm{d}t^2 + \left(1-\frac{2\Phi}{c^2}\right)\mathrm{d}\mathbf{x}^2 \,. \tag{2.5}$$

When we consider null geodesics, with $\mathrm{d}s^2 = 0$, we can write the effective coordinate velocity of light in the gravitational field of the lens as

$$c' = \frac{|\mathrm{d}\mathbf{x}|}{\mathrm{d}t} = c\,\frac{\sqrt{1+2\Phi/c^2}}{\sqrt{1-2\Phi/c^2}} \approx c\left(1+\frac{2\Phi}{c^2}\right) \,, \tag{2.6}$$

taking a first-order Taylor expansion by our original assumption of $\Phi/c^2 \ll 1$. By treating the gravitational lenses in the same manner as in conventional optics, we can define an effective refractive index n as

$$n = \frac{c}{c'} = 1 - \frac{2\Phi}{c^2} \,, \tag{2.7}$$

and see that, for $\Phi \leq 0$ such that $n \geq 1$, the effective speed of light c' diminishes in the presence of the lens' gravitational field.

By applying Fermat's principle which states that the path a light ray follows is extremal between two fixed points, A and B, so that it takes the path corresponding to the least travel time

$$\delta\tau = \delta\int_A^B n[\mathbf{x}(l)]\mathrm{d}l = 0 \,, \tag{2.8}$$

where l parametrises the position along the curved path [227]. We can reparametrise $\mathrm{d}l$ with a curve parameter λ as

$$\mathrm{d}l = \left|\frac{\mathrm{d}\mathbf{x}}{\mathrm{d}\lambda}\right|\mathrm{d}\lambda \,, \tag{2.9}$$

such that we can define the Lagrangian

$$L(\mathbf{x}, \dot{\mathbf{x}}, \lambda) \equiv n[\mathbf{x}(\lambda)]\left|\frac{\mathrm{d}\mathbf{x}}{\mathrm{d}\lambda}\right| . \tag{2.10}$$

[1]It is possible to derive the lens equation and associated expressions, starting with an FLRW metric [226] or Schwarschild solution [219] of the Einstein field equations. However, for simplicity, the following argument will suffice.

By solving the resulting Euler-Lagrange equations, we find the total deflection angle to the gradient of the potential perpendicular to the light ray, integrated across the path as

$$\hat{\boldsymbol{\alpha}} = -\frac{2}{c^2} \int \nabla_\perp \Phi \, \mathrm{d}\lambda \,. \tag{2.11}$$

Note that as $\nabla_\perp \Phi$ points away from the centre of the lens, the deflection angle, α, does also.

Since we have implemented the weak field assumption, we can also expect the deflection angles to be small. Indeed, typical deflection angles are of the order of arc seconds. Therefore, we apply the Born approximation where the light path can be approximated by straight lines, with the entire deflection happening in the lens's plane. For a point mass M at the origin, $\Phi = -GM/r$, where $r = \sqrt{x^2 + y^2 + z^2}$. If the light ray propagates along the z-axis passing the lens with an impact parameter $\xi = \sqrt{x^2 + y^2}$, then the deflection angle is written as

$$\hat{\alpha} = \frac{4GM}{\xi^2 \, b} \,. \tag{2.12}$$

2.2.2 Lens Equation

We also approximate the lens mass distribution as projected onto a plane, this is because the lens width is thin in comparison to the large distances involved in the system. If we take the *thin lens approximation*, then we can derive the *lens equation* from geometric arguments. From Fig. 2.1, it is easily shown using small angle approximations that

$$\boldsymbol{\eta} = \frac{D_s}{D_l} \boldsymbol{\xi} - D_{ls} \, \hat{\alpha}(\boldsymbol{\xi}) \,, \tag{2.13}$$

which can be transformed using $\boldsymbol{\eta} = D_s \, \boldsymbol{\beta}$, and $\boldsymbol{\xi} = D_l \, \boldsymbol{\theta}$ as

$$\boldsymbol{\beta} = \boldsymbol{\theta} - \frac{D_{ls}}{D_s} \, \hat{\boldsymbol{\alpha}}(D_l \boldsymbol{\theta}) \,, \tag{2.14}$$

where D_s, D_l, and D_{ls}, denote the angular diameter distances from the source to observer, lens to observer, and source to lens, respectively. We can then define the *reduced* or *scaled* deflection angle $\boldsymbol{\alpha}$ as

$$\boldsymbol{\alpha} \equiv \frac{D_{ls}}{D_s} \, \hat{\boldsymbol{\alpha}} \,, \tag{2.15}$$

so that the lens equation is now written simply as

$$\boldsymbol{\beta} = \boldsymbol{\theta} - \boldsymbol{\alpha} \,. \tag{2.16}$$

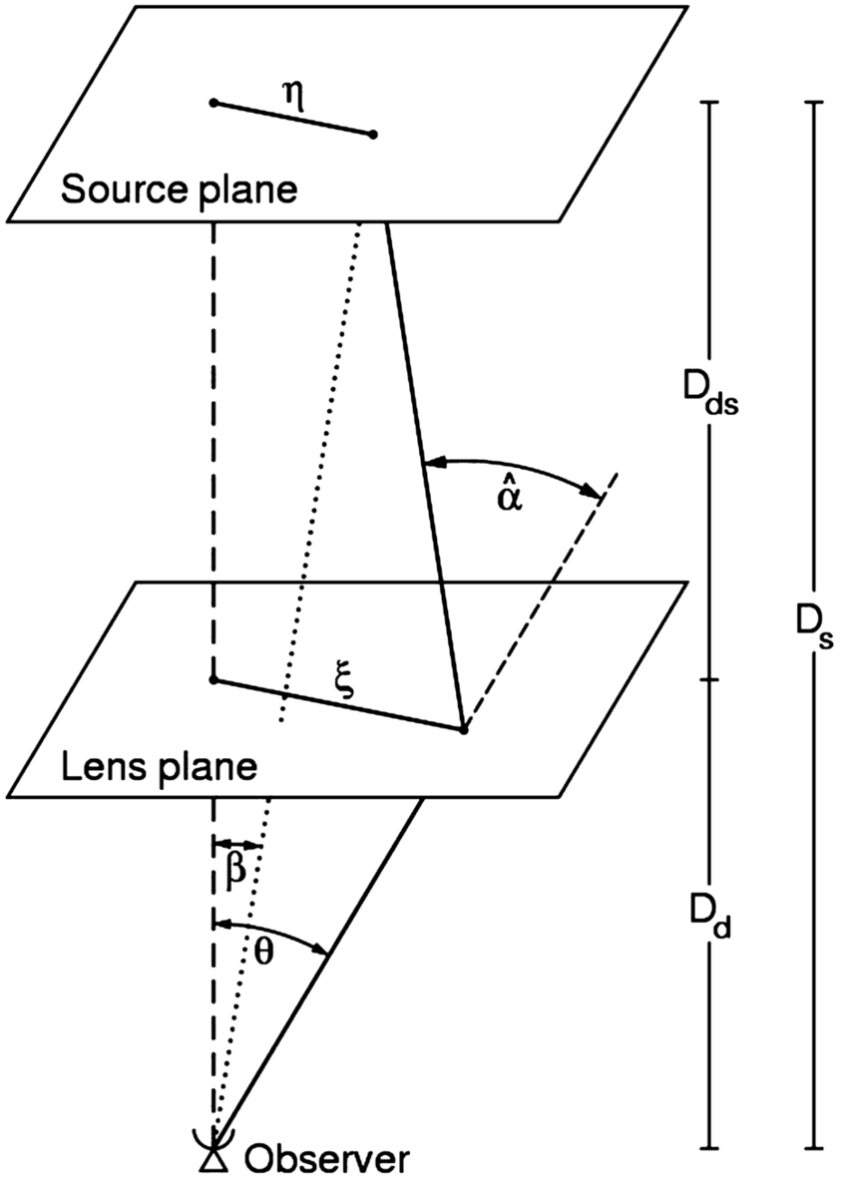

Figure 2.1: The set-up for the standard strong gravitational lensing formalism is shown, where β is the angular position of the source, θ is the angular position of the corresponding image, and $\hat{\alpha}$ is the deflection angle. Light is emitted from a point on the source plane with position η where it intersects with the lens plane at position ξ, before being deflected to the observer.

For a true source position with angular coordinates β, an observer will see images produced with angular coordinates θ that satisfy the lens equation. For strong lensing, the lens equation can be multivalued, producing many images for one source position. We can express the reduced deflection angle as

$$\boldsymbol{\alpha} = \nabla_{\perp} \left[\frac{2}{c^2} \frac{D_{ls}}{D_s} \int \Phi \mathrm{d}z \right] . \tag{2.17}$$

If we rewrite the perpedicular gradient in terms of a gradient in θ, the reduced delection angle is expressed as in terms of a 2D *lensing potential* on the lens plane

$$\boldsymbol{\alpha} = \nabla_{\theta} \, \psi \, , \tag{2.18}$$

where

$$\psi = \frac{2}{c^2} \frac{D_{ls}}{D_s \, D_l} \int \Phi \, \mathrm{d}z \, . \tag{2.19}$$

2.2.3 Convergence

If we further take the divergence of Eq. (2.18) and insert Possions equation for the resulting Laplacian, we find

$$\nabla^2 \psi = \frac{8\pi G}{c^2} \frac{D_l \, D_{ls}}{D_s} \Sigma \, , \tag{2.20}$$

where Σ is the projected surface mass density of the lens on the lens plane,

$$\Sigma(x, y) \equiv \int \rho(x, y, z) \mathrm{d}z \, . \tag{2.21}$$

The projected mass density can be related to a dimensionless surface mass density or *convergence*, κ,

$$\kappa(\boldsymbol{\theta}) = \frac{\Sigma(D_l \boldsymbol{\theta})}{\Sigma_{\mathrm{crit}}} \quad \text{with} \quad \Sigma_{\mathrm{crit}} = \frac{c^2}{4\pi G} \frac{D_s}{D_l \, D_{ls}} \, , \tag{2.22}$$

where Σ_{crit} is the critical surface mass density. Σ_{crit} is the minimum mass required for strong lensing to produce multiple images; a mass distribution with $\Sigma \geq \Sigma_{\mathrm{crit}}$ or equivalently $\kappa \geq 1$ exhibits the strong lensing.

We can rewrite Eq. (2.20) as[2]

$$\nabla_{\theta}^2 \, \psi = 2\kappa \, . \tag{2.23}$$

[2]After this point, we drop the subscript θ on the gradient.

Therefore, we can now express both the scaled deflection angle and lensing potential in terms of the convergence as

$$\boldsymbol{\alpha}(\boldsymbol{\theta}) = \frac{1}{\pi}\int \mathrm{d}^2\theta'\, \kappa(\boldsymbol{\theta'})\, \frac{\boldsymbol{\theta}-\boldsymbol{\theta'}}{\left|\boldsymbol{\theta}-\boldsymbol{\theta'}\right|^2}\,, \tag{2.24}$$

$$\psi(\boldsymbol{\theta}) = \frac{1}{\pi}\int \mathrm{d}^2\theta'\, \kappa(\boldsymbol{\theta'})\, \ln\left|\boldsymbol{\theta}-\boldsymbol{\theta'}\right|. \tag{2.25}$$

It will also be useful to define the *Fermat potential*

$$\tau(\boldsymbol{\theta};\boldsymbol{\beta}) = \frac{1}{2}(\boldsymbol{\theta}-\boldsymbol{\beta})^2 - \psi(\boldsymbol{\theta})\,, \tag{2.26}$$

for which we can write an equivalent expression for the lens equation

$$\nabla\tau(\boldsymbol{\theta};\boldsymbol{\beta}) = 0\,. \tag{2.27}$$

The Fermat potential is incredibly useful in the classification of multiple images and quantifying the delay in the arrival time of light between different lensed images, A and B, as

$$\Delta t = \frac{D_{\Delta t}}{c}[\tau(\boldsymbol{\theta}_A) - \tau(\boldsymbol{\theta}_B)]\,, \tag{2.28}$$

where $D_{\Delta t}$ is the 'time-delay distance' defined as

$$D_{\Delta t} \equiv (1+z_l)\frac{D_l\, D_s}{D_{ls}}\,. \tag{2.29}$$

This is useful for time-delay cosmography as each constituent angular diameter distance is inversely proportional to the Hubble constant, thus $D_{\Delta t} \propto H_0^{-1}$. However, in practice, no lens is completely isolated and the effects of external structures along the line of sight will influence the inferred time-delay distance. Thus, we typically parametrise the effects of external structures by fitting an external convergence κ_{ext} parameter when attempting to constrain cosmological parameters as

$$D_{\Delta t} = \frac{D_{\Delta t}^{\text{model}}}{1-\kappa_{\text{ext}}}\,. \tag{2.30}$$

2.2.4 Einstein Radius

If one considers a point mass at the origin, its convergence may be expressed as

$$\kappa(\boldsymbol{\theta}) = \pi\,\theta_E^2\,\delta(\boldsymbol{\theta})\,, \tag{2.31}$$

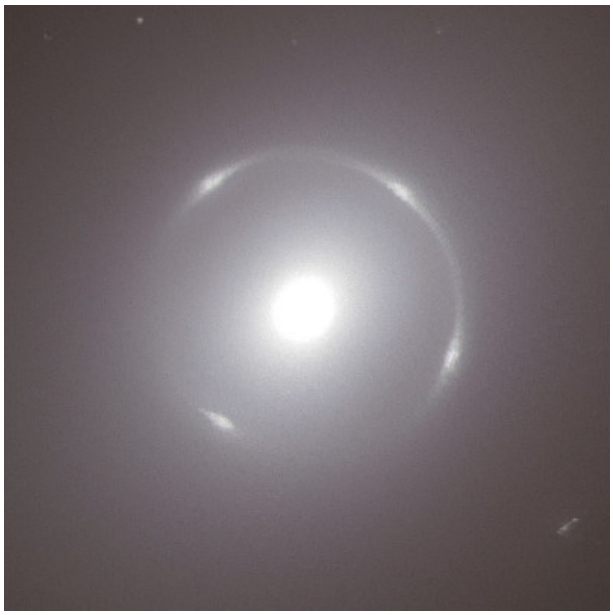

Figure 2.2: An example of an Einstein ring formed by an elliptical galaxy NGC 6505, found by the Euclid telescope. Its Einstein radius is $\theta_E = 2.5''$ [228].

where θ_E is an as yet undefined constant. For this mass distribution, the lens equation is then given as

$$\boldsymbol{\beta} = \left(1 - \frac{\theta_E^2}{|\theta|^2}\right) \boldsymbol{\theta}\,. \tag{2.32}$$

If a source lies directly along the line of sight, such that $\beta = 0$, we find that

$$|\boldsymbol{\theta}| = \theta_E\,, \tag{2.33}$$

and the image produced will be stretched out into a ring - the *Einstein ring* - with an angular radius θ_E - the *Einstein radius*. A recent example found by the Euclid telescope, presented in Fig. 2.2, shows a near perfect Einstein ring formed by the lowest redshift lens galaxy detected so far in NGC 6505 at $z = 0.042$ [228].

We can extend this definition to more general mass distributions, where the Einstein radius defines a region in which the mean enclosed convergence is $\kappa = 1$. The corresponding mass for this convergence is $\pi\,\theta_E^2\,\Sigma_{\rm crit}$, so by applying Eq. (2.22) we find

$$\theta_E^2 = \frac{4GM}{c^2}\frac{D_{ls}}{D_s\,D_l}\,, \tag{2.34}$$

or alternatively

$$\theta_E = \frac{4GM}{c^2\xi}\frac{D_{ls}}{D_s}\,. \tag{2.35}$$

2.2.5 Magnification and Distortion

For point sources, the images locations are determined by the solutions of θ to the lens equation. However, for extended sources, such as the host galaxies of the lensed quasars, the images produced will be distorted and magnified as there is differential deflection between light rays propagating from different regions of the source. Therefore, the shape and position of the images produced involves solving the lens equation for all points within the extended source.

However, if we are dealing with a source much smaller than the scale of the deflection angle, then the angular separation from the centre to the edge of the source, $\delta\boldsymbol{\beta}$, can be approximated by a first-order Taylor expansion of the lens equation,

$$\delta\boldsymbol{\beta} \approx \mathcal{A}\,\delta\boldsymbol{\theta}\,. \tag{2.36}$$

Here, $\mathcal{A}$ is the Jacobian matrix that describes the lens mapping and distortion of images

$$\mathcal{A}(\boldsymbol{\theta}) = \frac{\partial\boldsymbol{\beta}}{\partial\boldsymbol{\theta}} = \left(\delta_{ij} - \frac{\partial^2\psi(\boldsymbol{\theta})}{\partial\theta_i\,\partial\theta_j}\right) = \begin{pmatrix} 1-\kappa-\gamma_1 & -\gamma_2 \\ -\gamma_2 & 1-\kappa+\gamma_1 \end{pmatrix}, \tag{2.37}$$

where γ_1 and γ_2 are the components of shear $\gamma \equiv \gamma_1 + i\,\gamma_2$. These components can be expressed through derivatives of the lensing potential as

$$\gamma_1 = \frac{1}{2}(\psi_{,11} - \psi_{,22})\,, \qquad \gamma_2 = \psi_{,12}\,, \tag{2.38}$$

where the $x_{,12}$ subscript indicates a partial derivative with respect to the following indices. It can be convenient to write the Jacobian as

$$\mathcal{A} = (1-\kappa)\begin{pmatrix} 1 & 0 \\ 0 & 1 \end{pmatrix} - |\gamma|\begin{pmatrix} \cos 2\varphi & \sin 2\varphi \\ \sin 2\varphi & \cos 2\varphi \end{pmatrix}, \tag{2.39}$$

where the first term, dependent on the convergence, only modifies the size of the image and the second shear term quantifies the change of shape. However, as the original image shape is not typically observed, it is useful to invert the Jacobian to transform from image coordinates to source coordinates[3],

$$\mathcal{A}^{-1} = \frac{1}{\det\mathcal{A}}\begin{pmatrix} 1-\kappa+\gamma_1 & \gamma_2 \\ \gamma_2 & 1-\kappa-\gamma_1 \end{pmatrix}. \tag{2.40}$$

[3]Often the inverse Jacobian is referred to as the magnification tensor $M(\boldsymbol{\theta})$.

We can then define the magnification, μ, from the ratio of fluxes of the lensed and unlensed source, which corresponds to the prefactor in Eq. (2.40) as

$$\mu = \frac{1}{\det \mathcal{A}} = \frac{1}{(1-\kappa)^2 - \gamma^2}\,. \tag{2.41}$$

2.2.6 Critical and Caustics Curves

Critical curves are closed, smooth curves on which the determinant of the Jacobian equals zero, $\det \mathcal{A} = 0$. *Caustic curves* correspond to the mapping of critical curves back onto the source plane via the lens equation; these curves are not necessarily smooth and may exhibit various types of cusped features. To show this, if we parametrise the critical curve as $\boldsymbol{\theta}(\lambda)$ and the corresponding caustic as $\boldsymbol{\beta}(\lambda)$, we can then write the derivative along the caustic as

$$\frac{\mathrm{d}\boldsymbol{\beta}(\boldsymbol{\theta}(\lambda))}{\mathrm{d}\lambda} = \frac{\partial \boldsymbol{\beta}}{\partial \boldsymbol{\theta}} \frac{\mathrm{d}\boldsymbol{\theta}}{\mathrm{d}\lambda} = \mathcal{A}(\boldsymbol{\theta}(\lambda)) \frac{\mathrm{d}\boldsymbol{\theta}}{\mathrm{d}\lambda}\,. \tag{2.42}$$

Therefore, the tangent vector along the caustic will vanish if the tangent vector to the critical curve is parallel to the non-zero eigenvector of $\mathcal{A}$. In this case, the caustic curve is not smooth but displays a cusp.

The position of a source object relative to these caustic curves will determine the lensed properties of the images produced, such as their multiplicity and magnification. A naïve interpretation of the magnification would be that a source object situated directly on a caustic curve, would experience infinite magnification as μ diverges. However, this is of course not physically possible, as there are no point sources in reality. As the size of a source object becomes increasingly close to being point like, the geometric optics description used to build the lensing formalism breaks down, and we must apply wave optics instead. Despite this, very high magnifications are still possible for sources positioned very close to caustic lines.

A source crossing a caustic curve either creates or destroys 2 images, depending on the direction of crossing. We label the side with a high multiplicity of images, the inner side, and the two images produced when crossing over in this direction will appear on either side of the corresponding critical line. These critical curves split the lens plane into regions of magnification ($\mu > 0$) and demagnification ($\mu < 0$), so one image produced will always be magnified whilst the other is demagnified.

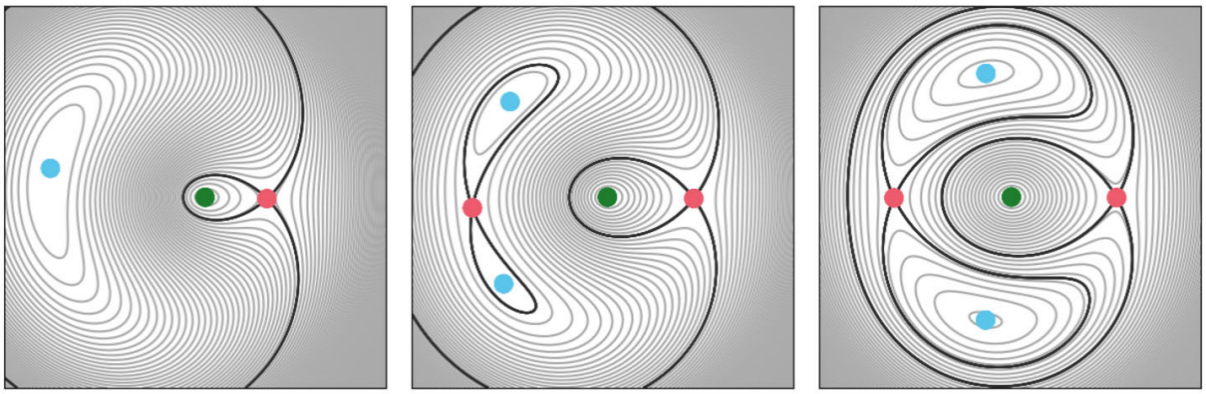

Figure 2.3: Contour plots of the fermat potential τ, varying the source position $\boldsymbol{\beta}$ but keeping a constant lensing potential ψ. Image positions that correspond to maxima, minima and saddle points are marked in green, light-blue and pink, respectively. The figure was originally compiled by Saha *et al.* [222]

2.2.7 Image Types

The images we observe are conveniently classified by the types of stationary points of the Fermat potential $\tau(\boldsymbol{\theta};\boldsymbol{\beta})$, which defines 2D arrival time surface. Images are produced at $\boldsymbol{\theta}$ which correspond to the source object lying on either a minimum, maximum or saddle point value of τ. As we can write the Jacobian as the hessian of the Fermat potential, we can determine which type of stationary point an image corresponds to by the two eigenvalues, the determinant and/or trace of $\mathcal{A}$.

- Minimum point: Both eigenvalues of the Jacobian are positive. Therefore, the determinant and trace are both positive as well, $\det \mathcal{A} > 0$ and $\mathrm{Tr}(A) > 0$.
- Maximum point: Both eigenvalues of the Jacobian are negative. Therefore, the determinant is positive but the trace is negative, so $\det \mathcal{A} > 0$ and $\mathrm{Tr}(A) < 0$.
- Saddle point: The eigenvalues have alternate signs, so that $\det \mathcal{A} < 0$.

As the trace of the Jacobian is dependent on the convergence of the lens,

$$\mathrm{Tr}(A) = 2(1-\kappa)\,, \tag{2.43}$$

then the maxima will correspond to image positions where $\kappa > 1$ and the minima where $\kappa < 1$. Fig. 2.3 and Fig. 2.4, originally compiled by Saha *et al.* [222], displays the three types of images that can be produced by varying the source position for a fixed lensing potential of a psuedo-isothermal ellipitcal mass distribution.

Therefore, strong gravitational lenses are often defined as a lens in which $\kappa > 1$ for any point $\boldsymbol{\theta}$. The logic being that any image corresponding to the point where $\kappa(\boldsymbol{\theta}) > 1$, will be a maxima

point and thus, at least one additional image must appear at the corresponding minima point. However, a more complete criterion for the requirement of multiply images sources is that there must exist a point $\boldsymbol{\theta}$ where $\det \mathcal{A} < 0$, as if a lens has an image corresponding to a saddle point, then according to the Odd-number theorem [229], there must be at least two more images corresponding to the minima and maxima of the Fermat potential.

2.2.8 The Mass-Sheet Degeneracy

One of the major complications with using gravitational lensing (particularly strong gravitational lensing) for cosmology is the *mass-sheet degeneracy*. As the lensing properties of an object with a given lensing potential are defined by gradients of the surface density and potential, we can transform many of the standard lensing expressions by a multiplicative factor of λ. This rescaling is equivalent to adding a sheet of mass into the lens plane that will affect the time-delays measured, but will leave all other observables unchanged. If we transform the convergence as,

$$\kappa_\lambda(\boldsymbol{\theta}) = (1-\lambda) + \lambda\kappa(\boldsymbol{\theta})\,, \tag{2.44}$$

then the first term corresponds to adding a sheet of dimensionless surface mass density to the lens mass distribution and then the λ coefficient on the second term will describe the rescaling of the original mass distribution. From henceforth, the subscript λ indicates the scaled parameters.

The lens equation will now read as

$$\boldsymbol{\beta} = \boldsymbol{\theta} - \boldsymbol{\alpha}_\lambda(\boldsymbol{\theta})\,, \tag{2.45}$$

where

$$\boldsymbol{\alpha}_\lambda(\boldsymbol{\theta}) = (1-\lambda)\,\boldsymbol{\theta} + \lambda\,\boldsymbol{\alpha}(\boldsymbol{\theta})\,. \tag{2.46}$$

The lensing potential is also scaled as

$$\psi_\lambda(\boldsymbol{\theta}) = \frac{1-\lambda}{2}\,|\boldsymbol{\theta}|^2 + \lambda\,\psi(\boldsymbol{\theta})\,, \tag{2.47}$$

which allows the lens equation to be expressed as

$$\frac{\boldsymbol{\beta}}{\lambda} = \boldsymbol{\theta} - \boldsymbol{\alpha}(\boldsymbol{\theta})\,, \tag{2.48}$$

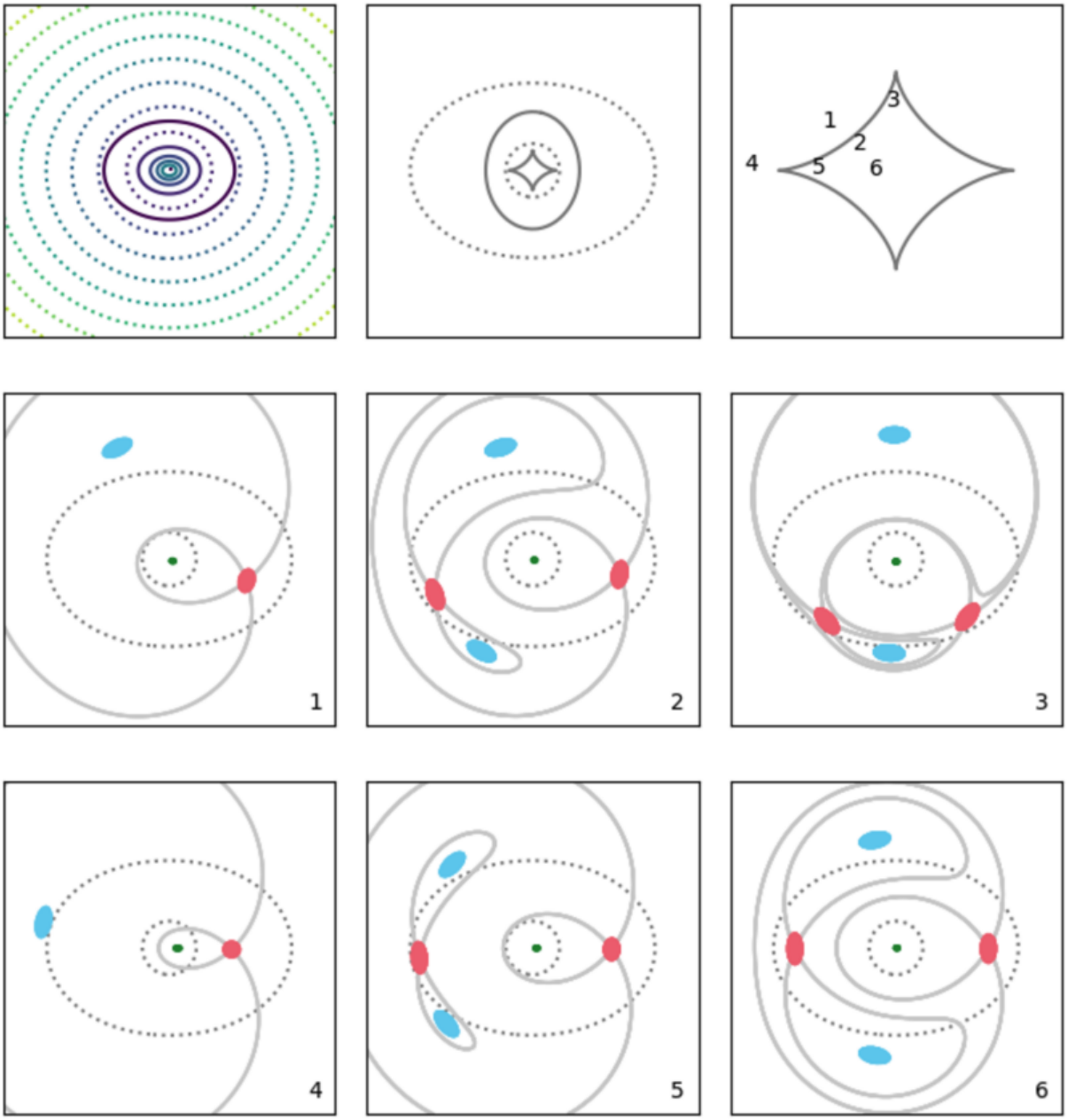

Figure 2.4: Lens and Image properties for a psuedo-isothermal elliptical mass distribution. The upper left panel displays the convergence and lensing potential with solid and dotted curves respectively. The upper middle panel shows the caustic and critical curves, solid and dotted respectively. The upper right panel denotes the source positions relative to the caustic lines, corresponding to each of the image configurations in the middle and lower panels. In each of the other panels, the dotted curves indicate the critical curves and the coloured markers show mamima (green), minima (light-blue), and saddle points (pink). This figure is originally compiled by Saha *et al.* [222].

which is just the original lens equation of Eq. (2.16) but with a $1/\lambda$ coefficient. Following this, the Jacobian and magnification can be described as

$$\mathcal{A}_\lambda = \lambda\,\mathcal{A}\,, \qquad \text{and} \qquad \mu_\lambda = \frac{\mu}{\lambda^2}\,. \tag{2.49}$$

It is important to note that whilst the Jacobian is rescaled, the reduced shear and thus the ellipticity of the images produced are unaffected. As the original brightness of a source is not typically known, it is not possible to use the magnification to constrain the mass-sheet degeneracy either. Crucially, the critical and caustic lines corresponding to $\kappa = 1$, remain unchanged, thus the image positions are also unaffected by the transformation. The only difference to an observable is in the Fermat potential, which transforms as

$$\tau_\lambda(\boldsymbol{\theta};\boldsymbol{\beta}) = \frac{1}{2}(\boldsymbol{\theta}-\boldsymbol{\beta})^2 - \psi_\lambda(\boldsymbol{\theta}) = \lambda\,\tau(\boldsymbol{\theta};\boldsymbol{\beta}/\lambda) + C(\beta)\,, \tag{2.50}$$

where $C(\beta)$ is a constant depending on β. Due to the nature of the mass-sheet degeneracy only affecting the time-delay between images, it adds a layer of complexity when attempting to fit a lens model to observations in order to constrain cosmology. However, if one assume a value of H_0, then the degeneracy is broken, and it is possible to determine the absolute surface mass density of the lens. In order to break the mass-sheet degeneracy for cosmological purposes, further information about the lens mass distribution must be gathered alongside strong lensing observables, such as the velocity dispersion of the lens [230].

2.3 Strong Lensing - a Series of Acronyms

As previously discussed, strong gravitational lensing is classified by the producing of multiple images, arcs, or rings, of a background source object due to the intermediary gravitational field of a lens object. In this section, we provide a summary of the major applications of strong lensing and discuss ongoing projects in the field.

2.3.1 Cluster Scale Lensing

Throughout the work in this thesis, we focus on galaxy scale lens objects, mostly due to their simplicity to model. However, cluster lenses have a great potential for cosmological applications. Clusters act as a cosmic magnifying glasses, enabling us to observe high-redshift, low-luminosity objects that might not otherwise have been possible [231]. This makes them

incredibly useful for the study of the evolution of astrophysical objects, and ongoing projects include:

- The Hubble space telescope Frontier Fields program (HFF) - This is a deep-field imaging campaign using the Hubble telescope to obtain observations of six strong lensing clusters to detect and study faint high redshift galaxies and provide insights into their evolution [232, 233]. This is built upon its predecessor, the Cluster Lensing And Supernova survey with Hubble (CLASH) [234]. The six cluster lenses observed by the HFF are: Abell 370, MACS J0717.5+3745, MACS J0416.1-2403, Abell S1063, Abell 2744, and MACS J1149.5+2223 [235]. These clusters cover a redshift range of $0.3 < z < 0.55$ and will allow detection of galaxies up to redshift $z \sim 9$ [233].
- The REionization LensIng CLuster Survey (RELICS) is a survey using Hubble and Spitzer space telescope observations of 41 massive galaxy clusters [236]. From these clusters, over 300 lensed galaxies have been discovered in the redshift range $6 < z < 8$ [237]. The RELICS survey expects to confirm lensed candidates at redshift $z \sim 10$ with follow-up imagery from JWST [238].
- The Beyond Ultra-deep Frontier Fields And Legacy Observations (BUFFALO) project is an extension of the HFF survey designed to learn about early galaxy assembly and prepare targets for JWST imagery [239].

Cluster lenses are difficult to model as their mass distributions are complex. However, one galaxy cluster can have numerous background source objects that it lenses. Therefore, there is a large amount of data that can be used to constrain the lens model, in contrast to galaxy scale lenses. Effective lens modelling is one of the greatest challenges for using strong gravitational lensing for cosmology. Cosmological parameters we infer are heavily dependent on the choice of parametrisation used, thus simpler objects such as elliptical galaxies are preferred for time-delay cosmography.

2.3.2 Time-Delay Cosmography

Probably the most well-known use of strong gravitational lensing is to estimate the Hubble constant H_0 from the time-delay between images caused by the different path lengths and gravitational potentials traversed for each image. To do this, one needs accurate lens models to describe the lensing potential and precise measurements of the time-delay between transient images.

Supernova present ideal candidates for this technique, as measuring a time-delay between multiply imaged type Ia or type II supernova is relatively simple due to their well-defined light curve peaks. This was originally suggested by Refsdal [212], hence the first lensed supernova is named "SN Refsdal" [240, 241]. Since this first detection, only a handful of further lensed supernova have been detected [242, 243]. Lensed Type Ia supernova have been detected in SN H0pe and SN Encore, which are well constrained enough to enable the first estimates of H_0 from these lenses [216, 217, 244, 245]. Whilst these objects are incredibly powerful astrophysical tools, they are heavily limited by the amount of data available. However, the next generation of surveys predict to see hundreds of lensed supernova from LSST [3]. The Highly Optimised Lensing Investigations of Supernovae, Microlensing Objects, and Kinematics of Ellipticals and Spirals (HOLISMOKES) collaboration, besides having the best acronym of any group in astrophysics, investigates the use of lensed supernova for cosmological purposes [246].

A far more abundant transient source is that of quasars or quasi-stellar objects (QSOs Quasars are close to an ideal source for lensing observations as in general they have a high luminosity, making them easily detectable, and their intrinsic variability makes time-delay cosmography possible. However, measuring the time-delay between images is far more laborious than for supernova as quasar light curves are far more complex. The COSmological MOnitoring of GRAvItational Lenses (COSMOGRAIL) program [247] is a campaign aiming to precisely measure the time-delays between lensed quasars to a minimum of 3% accuracy in order to provide tight constraints on H_0. This is a time-consuming process, and the most recent measurements of 18 lensed quasars required up to 15 years of monitoring in order to return well constrained time-delays [248]. Whilst this process is improving, it does provide a heavy limiting factor to cosmological analysis from our sample of lensed quasars.

COSMOGRAIL has expanding into further projects in the 'H_0 Lenses in COsmograil's Wellspring' (H0LiCOW) [249–253] and the 'Strong Lensing Insights into the Dark Energy Survey' (STRIDES) programs [254]. The H0LiCOW collaboration has found a value of H_0 consistent with other late-universe estimates of $H_0 = 73.3^{+1.7}_{-1.8}\,\mathrm{kms}^{-1}\mathrm{Mpc}^{-1}$, when combining measurements from six quasars and assuming a spatially flat ΛCDM model and a choice of lens mass model [249]. STRIDES added another quasar which finds a Hubble value in agreement with the H0LiCOW result [255] of $H_0 = 74.2^{+2.7}_{-3.0}\,\mathrm{kms}^{-1}\mathrm{Mpc}^{-1}$. These projects fall under the umbrella collaboration of the Time-Delay COSMOgraphy (TDCOSMO) organisation which investigates the systematic effects present with lensing analyses [256–259].

2.3.3 Dark Matter Haloes

Instead of choosing a lens model and fitting for cosmology, one can fix the parameters of the standard ΛCDM model to be inline with other late-universe probes and investigate the mass distribution of the lens. The Strong-lensing High Angular Resolution Programme (SHARP) aims to study the nature of dark matter via strong gravitational lensing using adaptive optics imaging [252, 260]. The improved imaging precision adaptive optics demonstrates allows for the analysis of small-separation lenses that otherwise could not be resolved. The determination of the mass distribution of the dark matter halo of lens objects, informs not only on the evolution of the lens object itself, but the nature of dark matter and large scale structure formation. Project Dinos attempts to investigate the mass distribution of elliptical type galaxies specifically, and find they are consistent with a power-law profiles [261].

There are many parametrisations of dark matter halo used to model lens galaxies effectively. Typical choices include the singular isothermal ellipsoid [262], elliptical power-law models [215], and the combination Navarro-Frenk-White (NFW) profile [263, 264] and luminous matter description (e.g. a Sérsic profile mapped with a mass to luminosity ratio). However, there is a seemingly endless list of different lens models one can choose from - each with their own accronym - that can be confusing to those unfamiliar with the field. The python package LENSTRONOMY provides a list of many lens models and their respective lensing potentials [265]. Overall, there is no major preference between power-law models and NFW profiles when fitting to data [257], but the NFW profiles are motivated by cold dark matter simulations in a ΛCDM universe, whereas power-law models are chosen as an empirical model with enough freedom to effectively describe lensing systems.

Note that the density profiles for the singular isothermal sphere

$$\rho(r) = \frac{\sigma_v}{2\pi G}\frac{1}{r^2}\,, \tag{2.51}$$

the Navarro-Frenk-White profile

$$\rho(r) = \frac{\rho_s}{(r/r_s)(1+r/r_s)^2}\,, \tag{2.52}$$

and general power-law models

$$\rho(r) \propto r^{-\gamma}\,, \tag{2.53}$$

display a central density divergence or cusp in their density profile[4] as $r \to 0$. These halos are inline with cosmological N-body simulations but differ from the types of profiles inferred in lower mass galaxies, such as those required to match rotation curves in disc galaxies - like the Burkert profile [266, 267]. This is known as the core-cusp problem, and whilst there are already several proposed solutions - including baryonic feedback or self-interacting dark matter - strong gravitational lensing provides another avenue to investigate this. The Sloan WFC Edge-on Late-type Lens Survey (SWELLS) catalogues low mass spiral galaxies and finds at least 16 lenses of this type [223, 268, 269].

[4]Here, σ_v is the velocity dispersion of the lens, r_s and ρ_s are the characteristic scale and density of the dark matter halo, and γ is a free parameter that defines the density profile.

Chapter 3

Power-law lens models for strong lensing in cosmology

This chapter has been published as 'Revisiting the effect of lens mass models in cosmological applications of strong gravitational lensing' by Christopher Harvey-Hawes and David L. Wiltshire in the *Monthly Notices of the Royal Astronomical Society*, Volume 534, Issue 4, November 2024, Pages 3364–3376, DOI: 10.1093/mnras/stae2306.

3.1 Introduction

Strong gravitational lensing (SGL) occurs when the light path from a distant source is warped around an intermediary lens body on its way to an observer, producing several images, arcs or rings. Over the last couple of decades, strong gravitational lenses have been observed with an increased number. The current largest compilation of all strong gravitational lenses which can be used viably for constraining lens properties and cosmological parameters consists of 161 systems [215]. The number of such strong gravitational lenses is set to increase by orders of magnitude over the coming decade: the Rubin Observatory Large Synoptic Survey Telescope (LSST) and Euclid are projected to observe 1.2×10^6 and 1.7×10^6 galaxy-galaxy scale lenses respectively [270]. Since the standard cosmology faces increasing challenges [112, 271, 272] it is important to understand the interplay of lens models and cosmological models. In this paper, we will test such assumptions using the existing catalogue of Chen *et al.* [215].

It is possible to constrain the properties of the lens galaxies given an assumed background cosmology, typically using the standard spatially flat Λ Cold Dark Matter (ΛCDM) model with Planck value parameters [28]. Alternatively, one can constrain the parameters of the assumed

cosmological model given a particular choice of lens mass density profile. Attempts to simultaneously fit both the lens density profile and cosmological parameters have been conducted [215, 273], inevitably running into degeneracies that require further observational data to resolve.

There are several different methods to perform statistical cosmological analysis with strong gravitational lenses. Time-delay cosmography as pioneered by Refsdal [212] is the most sensitive to cosmological parameters and deals with each system individually rather than trying to deal with an 'average' ideal lens model. This method is particularly useful in determining the Hubble constant, $H_0 \equiv H(t_0)$, as the measured time-delay between multiply imaged events can be used to determine their different path lengths, and thereby a value for the Hubble expansion [249, 256]. Despite time-delay cosmography being a powerful technique, only a small fraction of the observed lensing systems have well-defined time-delays, thus limiting the potential application of this approach. The vast increase in available lens systems from the next generation of telescopes is now set to overcome this hurdle.

To date most observed galaxy-scale lensing systems involve distant quasars sources. As compared to observations of smaller numbers of lensed Sne Ia, the uncertainties in time-delay measurements of quasars are significantly larger. Given the paucity of data available for accurate time-delay cosmography, alternate approaches should be considered to make full use of the observed lens systems.

This paper will focus in particular on the distance ratio

$$\frac{d_{ls}}{d_s} = \sqrt{1 - k\, d_l^2} - \frac{d_l}{d_s}\sqrt{1 - k\, d_s^2} \quad , \tag{3.1}$$

introduced in the distance sum rule test of Räsänen *et al.*[274]. Here d_s, d_l and d_{ls} denote the dimensionless comoving distances, $d(z_l, z_s)$, from the source to observer, lens to observer and source to lens respectively. The comoving distance is related to the angular diameter distances, D_A, and dimensionless luminosity distance, D_L by

$$d = \frac{H_0}{c} D_A (1+z) = \frac{H_0}{c}\frac{D_L}{1+z} \tag{3.2}$$

$$= \frac{1}{\sqrt{\Omega_{\mathrm{k0}}}} \sinh \sqrt{\Omega_{\mathrm{k0}}} \int_1^{1+z} \frac{\mathrm{d}x}{\sqrt{\Omega_{\Lambda 0} + \Omega_{\mathrm{k0}}\, x^2 + \Omega_{\mathrm{M0}}\, x^3}}, \tag{3.3}$$

where $\Omega_{\mathrm{k0}} = -kc^2/H_0^2 = 1 - \Omega_{\mathrm{M0}} - \Omega_{\Lambda 0}$, and Ω_{M0} and $\Omega_{\Lambda 0}$ are the present epoch matter and cosmological constant density parameters. In this paper, we will focus on spatially flat FLRW

models where $\Omega_{\mathrm{k0}} = 0$ and thus Eq. (3.3) becomes

$$d = \int_1^{1+z} \frac{\mathrm{d}x}{\sqrt{(1-\Omega_{\mathrm{M0}}) + \Omega_{\mathrm{M0}}\, x^3}}\,. \tag{3.4}$$

and the distance ratio is given as

$$\mathcal{D} \equiv \frac{d_{ls}}{d_s} = \frac{d_s - d_l}{d_s}\,. \tag{3.5}$$

The relation Eq. (3.1) provides an exact expression for the ratio of two observed angular distances in the case of a FLRW metric with constant spatial curvature k. It is then typically used as a self-consistency check of the standard FLRW cosmology, or to constrain the global spatial curvature of some assumed FLRW universe [275, 276]. However, any cosmological model – whether FLRW or not – can be substituted on the r.h.s. of Eq. (3.1) provided the model has a suitable definition of the distance ratio in terms of its underlying parameters.

For a specific lensing system, it is also possible to compute its respective distance ratio purely from a given lens model and its corresponding observables and parameter values, independent of cosmology. Therefore, we can compare values for the distance ratio derived from cosmological angular diameter distance measurements to values determined from an assumed lens model, thus, allowing for constraints on both lens and cosmological parameters. This can be extended to a comparison of different cosmological models through Bayesian inference [277]. Such Bayesian analysis might involve two FLRW models with different priors on cosmological parameters, or alternatively an FLRW model compared to a non-FLRW model such as the timescape [187].

The distance ratio is independent of the Hubble parameter, and therefore sidesteps the issue of its current epoch value $H_0 = H(t_0)$. This is a major advantages of this technique, as the Hubble tension continues to pose a significant challenge to the ΛCDM model [278]. Furthermore, since SGL bypasses the cosmic distance ladder, it directly allows us to infer cosmological parameters without relying on other astronomical distance measures and the systematics they depend upon.

While the distance ratio has been used to test the self-consistency of FLRW models, to date it has not been applied to non-FLRW metrics. This paper will fill that gap by revisiting the analysis of Chen *et al.* [215] and extending it to include the timescape model. We will perform a Bayesian comparison between the spatially flat FLRW model and the timescape model, and determine the corresponding best fit cosmological parameters. In addition, we investigate three

different parametrisations of the lens galaxies mass profile and their effect on cosmological fits. Strong gravitational lensing is heavily dependent on the choice of lens model, as well as the background cosmology the systems are embedded within. Therefore, it is vital that lens galaxies are well modelled in advance of new observations by the next generation of telescopes.

An overview of the paper is as follows. In section 3.2, we will briefly review the timescape model. In section 3.3 we will discuss the different lens models used in this paper, as well as provide a description of the catalogue of lensing systems, identifying the uncertainties involved and model biases. Section 5.4 outlines the methodology for determining cosmological parameters within a given lens model and gives the results of the fitting procedure. Section 3.5 presents the results of simulations of mock data generated from the catalogue data with randomly added noise. In section 5.5 we discuss our results and the conclusions that can be drawn.

3.2 Timescape Model Overview

Standard ΛCDM cosmology, and indeed all FLRW models, are based upon the cosmological principle that on average the universe is both spatially homogeneous and isotropic. While some notion of spatial homogeneity and isotropy certainly holds for whole sky averages of very distant objects, the universe is inhomogeneous on scales $< 100\ h^{-1}$ Mpc [17, 279, 280] where it is dominated by a cosmic web of over-dense filaments and under-dense voids. The standard cosmology has been incredibly successful. Nonetheless, challenges to the ΛCDM model remain unresolved despite of the growth of available data and increased observational precision ([112, 271, 272]).

The timescape model assumes that cosmology should not invoke a single global reference background with a unique split of space and time [183, 184, 281]. To model the universe effectively, we have to account for *backreaction of inhomogeneities*, namely deviations from average FLRW evolution at the present epoch. This is due to structure formation of filaments and voids and the resulting cosmic web, which grows in complexity in the late universe. Timescape makes use of Buchert spatial averages [171] to provide the average evolution of the Einstein equations with backreaction.

The interpretation of Buchert's formalism has been much debated; critics pointed out that as a fraction of the averaged energy density, a term Buchert denotes the "kinematical backreaction" $\bar{\Omega}_{\mathcal{Q}}$, should be small [178]. A universal feature of all viable backreaction proposals is that,

unlike FLRW, average spatial curvature does not scale as a simple power of the average cosmic scale factor $\bar{a}$, $\bar{\Omega}_K \neq -k/(\bar{a}^2\bar{H}^2)$, where k is constant and $\bar{H}$ an average expansion rate. In the timescape model, in particular, $\bar{\Omega}_K \propto f_{\rm v}^{1/3}/(\bar{a}^2\bar{H}^2)$, where the variable *void volume fraction*, $f_{\rm v} \to 0$ at early times but is significant in the late epoch universe. This means that conclusions about spatial curvature derived from CMB data in FLRW models are not relevant for backreaction models: when fit to the angular diameter distance of the CMB (with $\Lambda = 0$) it is curvature, $\bar{\Omega}_K$, that dominates in the late epoch universe, [185, Fig. 1]. Furthermore, while the average energy-density parameters for matter, radiation, curvature and kinematical backreaction satisfy a simple sum rule

$$\bar{\Omega}_M + \bar{\Omega}_R + \bar{\Omega}_K + \bar{\Omega}_{\mathcal{Q}} = 1\,, \tag{3.6}$$

the quantities appearing in Eq. (3.6) are *statistical* volume average quantities, not directly related to *local* observables. Consequently, conclusions about apparent cosmic acceleration do not follow simply from determining the magnitude of $\bar{\Omega}_{\mathcal{Q}}$. The timescape ansatz fixes the relationship of these quantities to local observables, resulting in a viable phenomenology with $\bar{\Omega}_K \sim 0.86$, $\bar{\Omega}_M \sim 0.17$, $\bar{\Omega}_{\mathcal{Q}} \sim -0.03$ at present, $z = 0$.

Since the local geometry varies dramatically depending on the position of an observer in the cosmic web, local geometry is generally very different to the global volume average. Local structure not only affects the average evolution of the Einstein equations, but also the calibration of distance and time measures relative to the volume average[1] observer. Timescape allows for variation of the calibration of regional clocks relative to one another due to the gravitational energy cost of the gradients in spatial curvature between filaments and voids. Ideal observers, who see a close to isotropic CMB, in different local environments would age differently, hence the name timescape.

The accelerated expansion of the universe is now an apparent effect derived from fitting an FLRW model with constant spatial curvature and global cosmic time to an inhomogeneous non-FLRW universe. An ideal void observer not gravitationally bound to any structure will not infer a cosmic acceleration at all, whereas an observer in a bound structure such as galaxy will use a different time parameter and will infer an accelerated expansion at late cosmic epochs. The timescape model can eliminate the need for dark energy entirely and does so without introducing new ad hoc scalar fields or modifications to the gravitational action; rather it revisits

[1] A volume average observer in the timescape model represents an observer whose local spatial curvature coincides with that of the largest spatial averages. Such an observer is necessarily at an average position by volume - in a void - and systematically different from observers in bound structures. A typical location by volume is not a typical location by mass.

averaging procedures that build upon Einstein's general relativity.

Since the ΛCDM has been so successful in diverse cosmological tests, any phenomenologically viable model must yield similar predictions, particularly with regard to large scale averages for distances beyond the scale of inhomogeneity. For over a decade, timescape has consistently given fits to type Ia supernovae which are essentially statistically indistinguishable from ΛCDM by Bayesian comparison [282–284]. The most recent analysis of the Pantheon+ catalogue shows, furthermore, that timescape predictions for cosmic expansion below ~ 100 scales are consistent with observations in a manner which may provide a self-consistent resolution of the Hubble tension [285]. The difference between the distance–redshift relations of the timescape model and those of *some* ΛCDM model with fixed Ω_{M0}, $\Omega_{\Lambda 0}$, is only 1–3% over a small range of redshifts, but timescape effectively interpolates between ΛCDM models with different parameters over larger redshift ranges – which is why it can resolve the Hubble tension in a natural fashion. Of course, this must be tested with completely independent cosmological tests.

Among the many different definitions of distance in the timescape model, here we focus on the matter dominated era, where a simple 'tracking solution' is found to apply. Instead of the parameters $\Omega_{\rm M0}$ in a spatially flat FLRW model, distances are instead parameterised in terms of the present epoch void fraction $f_{\rm v0}$. The *effective comoving distances* directly comparable to those in the distance sum rule Eq. (3.1) are[2]

$$\begin{cases} d_s = H_0 t_s^{2/3}[\mathcal{F}(t_0) - \mathcal{F}(t_s)](1+z_s) \\ d_l = H_0 t_l^{2/3}[\mathcal{F}(t_0) - \mathcal{F}(t_l)](1+z_l) \\ d_{ls} = H_0 t_s^{2/3}[\mathcal{F}(t_l) - \mathcal{F}(t_s)](1+z_s) \end{cases} \tag{3.7}$$

where

$$\mathcal{F}(t) = 2\,t^{1/3} + \frac{b^{1/3}}{6}\ln\left(\frac{(t^{1/3}+b^{1/3})^2}{t^{2/3} - b^{1/3}\,t^{1/3} + b^{2/3}}\right) + \frac{b^{1/3}}{\sqrt{3}}\arctan\left(\frac{2t^{1/3}-b^{1/3}}{\sqrt{3}\,b^{1/3}}\right), \tag{3.8}$$

$$b = \frac{2\,(1-f_{\rm v0})(2+f_{\rm v0})}{9\,f_{\rm v0}\,\bar{H}_0}, \tag{3.9}$$

[2]Care must be taken with choices of units. With an explicit factor c, b and $\mathcal{F}$ must have dimensions of t and $t^{1/3}$ respectively, which is different to a convention often assumed for timescape [166].

and H_0 and $\bar{H}_0$ are the *dressed* and *bare* Hubble constants respectively.[3] The Buchert volume averaged time parameter t has been interpreted in different ways in different backreaction models. For the timescape tracker solution, observers in gravitationally bound systems measure a time parameter related to volume-average time according to

$$\tau = \frac{2}{3}t + \frac{2(1-f_{\rm v0})(2+f_{\rm v0})}{27 f_{\rm v0}\bar{H}_0}\,\ln\left[1+\frac{9 f_{\rm v0}\bar{H}_0}{2(1-f_{\rm v0})(2+f_{\rm v0})}\right]. \tag{3.10}$$

The volume-average time parameter is related to our observed redshift by

$$z+1 = \frac{2^{4/3}\,t^{1/3}\,(t+b)}{f_{\rm v0}^{1/3}\,\bar{H}_0\,t\,(2t+3b)^{4/3}}\,, \tag{3.11}$$

[286]. The distance ratio is then given as

$$\mathcal{D}^{\rm Time} \equiv \frac{d_{ls}}{d_s} = \frac{\mathcal{F}(t_l)-\mathcal{F}(t_s)}{\mathcal{F}(t_0)-\mathcal{F}(t_s)}\,. \tag{3.12}$$

Further details on the motivation and derivation of these equations is given by [166, 187]. It is now simple to make comparisons between timescape and spatially flat FLRW models, as they have the same number of free parameters: f_{v0} and Ω_{M0} are direct analogues due to their effect on distance measurements. Any dependence on the dressed or bare Hubble constant is cancelled due to the nature of the distance ratio, hence there is only one defining cosmological parameter for each model.

3.3 Catalogue, Observables and Lens Models

3.3.1 Catalogue Data

The data set used in this investigation is taken from the catalogue of 161 strongly lensed systems of Chen *et al.* [215]. It is the largest catalogue compiled to date, and is itself built upon a previous catalogue of 118 systems from Cao *et al.* [273]. This catalogue is a compilation of multiple surveys consisting of the LSD [287–290], SL2S [291–294], SLACS [295–297], S4TM [298, 299], BELLS [300] and BELLS Gallery surveys [301, 302]. From these surveys, the following

[3]The bare or volume average Hubble parameter is defined by the average volume expansion - not a global scale factor - and uses a time parameter relative to an idealised volume average observer. This time parameter differs systematically from that of observers in bound systems. The bare Hubble parameter is found to be related to the dressed Hubble parameter by

$$H(t) = \frac{[4f_{\rm v}^2(t)+f_{\rm v}(t)+4]\bar{H}(t)}{2(2+f_{\rm v}(t))}\,.$$

and $f_{\rm v0} \equiv f_{\rm v}(t_0)$ etc denote present epoch values.

observables are listed: spectroscopic lens and source redshift z_l and z_s, Einstein radius θ_E, half-light radius of the lens galaxy $\theta_{\rm eff}$, aperture radius $\theta_{\rm ap}$ and the central velocity dispersion of the lens galaxy $\sigma_{\rm ap}$. Spectroscopic measurements are provided by Sloan Digital Sky Survey (SDSS), W. M. Keck-II Telescope and Baryon Oscillation Spectroscopic Survey (BOSS) spectroscopic instruments depending on survey. Follow-up imagery from the Hubble Space Telescope (HST) Advanced Camera for Surveys is then used for the determination of θ_E and $\theta_{\rm eff}$.

Each of these surveys has differing instrumental parameters and thus has different uncertainties in the measurement of the central velocity dispersions[4] of the lens galaxies, which contributes the largest portion of the uncertainty in this method. Velocity dispersions of lens galaxies are measured spectroscopically within a given aperture radius $\theta_{\rm ap}$. However, the shape and size of the aperture used in each survey differs and thus an aperture correction formula is applied so that velocity dispersions are determined as if they were found with a normalized typical circular aperture σ_0 [303]. To transform rectangular apertures into an equivalent circular aperture for comparison, the following formula is used,

$$\theta_{\rm ap} \approx 1.025\sqrt{\frac{\theta_x\theta_y}{\pi}}\,, \tag{3.13}$$

where θ_x and θ_y are the width and height of the rectangular aperture respectively. Since aperture radii vary even within the class of circular apertures, the following normalization is also applied along the line of sight,

$$\sigma_{\parallel} \equiv \sigma_0 = \sigma_{\rm ap}\left(\frac{\theta_{\rm eff}}{2\theta_{\rm ap}}\right)^{\eta}\,, \tag{3.14}$$

where $\theta_{\rm eff}$ corresponds to the half-light radius of the lens galaxy as $\theta_{\rm eff} = R_{\rm eff}/D_l$. The value of η is taken from Cappellari *et al.* [304] of $\eta = -0.066 \pm 0.035$ is found empirically via fitting to individual galaxy profiles and is in agreement with other values determined by Jorgensen *et al.* [303] and Mehlert *et al.* [305] of $\eta = -0.04$ and $\eta = -0.06$ respectively.

The uncertainty in η is the greatest source of uncertainty in the distance ratio inferred from gravitational lensing. In addition, Eq. (3.14) contains a statistical error in $\sigma_{\rm ap}$ as quoted in the surveys, and a further systematic error source. The latter is understood as the effect of interfering matter along the line of sight and whilst the surveys are restricted to isolated systems, the sytematic error is estimated at 3% in all cases [306]. The combined total error budget is then

[4]This is obtained by converting the redshift dispersion from spectroscopic measurements around the galaxy using the radial special relativistic formula $z = \sqrt{(c+v)/(c-v)} - 1$.

given by,

$$\Delta\sigma_0^{\rm tot} = \sqrt{(\Delta\sigma_0^{\eta})^2 + (\Delta\sigma_0^{\rm sys})^2 + (\Delta\sigma_0^{\rm stat})^2}\,. \tag{3.15}$$

No uncertainty in the Einstein radius or associated redshifts is quoted within the catalogue data set. Thus, it is assumed these uncertainties are included within the systematic uncertainty of σ_0, although this is most likely an underestimation of the errors present in the data. A uniform error could be applied across the data set to θ_E, but is omitted to stay consistent with the work of Chen *et al.* We find that changing the magnitude of the errors present in our parameters does not significantly effect our conclusions throughout this paper.

Further cuts were also applied in compiling the catalogue. Not only did systems have to be isolated and have no significant substructure, but lens galaxies must also be early-type galaxies, either elliptical (E) or lenticular (S0).

3.3.2 Lens Models

When modelling lens mass distributions individually for use in time-delay cosmography, one of two descriptions are used: (i) power-law models that take into account both baryonic and dark matter simultaneously; and (ii) a combination of a luminous baryonic mass profile with a Navarro-Frank-White dark matter halo [307, 308]. Constraints on the value of H_0 from either class of model are very similar and statistically consistent with one another [256]. However, to model a statistically average lens galaxy within large catalogues, more general power-law models are used [309].

In this section, we review the three power-law models applied to the Chen *et al.* catalogue, commonly used to model the matter distribution of elliptical lens galaxies: Extended Power-Law (EPL), Spherical Power-Law (SPL) and Singular Isothermal Sphere (SIS).

All three lens models discussed in this paper rely upon the assumption that while galaxies may differ in shape, when taking averages the dominant component of the matter density is spherically symmetric. However, the angular structure of a lens galaxies mass distribution is very significant to the image separation produced. In fact, quadruply imaged sources are not possible with spherically symmetric mass distributions. Since the luminous matter in individual galaxies is not spherically symmetric, whether the angular component of all matter in each lens galaxy can be averaged out in this fashion is an assumption which can be tested in future.

Solving the radial Jeans equation, following the procedure given in Appendix 3.6, the distance ratio for the most general Extended Power Law (EPL) model is found to be

$$\mathcal{D}^{\rm obs} \equiv \frac{d_{ls}}{d_s} = \frac{c^2\theta_E}{2\sqrt{\pi}\sigma_0^2}\left(\frac{\theta_{\rm eff}}{2\theta_E}\right)^{2-\gamma} F(\gamma,\delta,\beta_s)\,, \tag{3.16}$$

where θ_E is the Einstein radius of the system. $F(\gamma,\delta,\beta_s)$ depends on the total mass density slope, γ, the luminous matter denisty slope, δ, and the stellar orbital anisotropy, β_s.

In deriving Eq. (3.16) several physical assumptions have been made, viz.:

1. The creation, destruction and collisions of stars are neglected.
2. The thin lens approximation applies as the distances from observer to lens and lens to source are far larger than the width of the lens object itself. A projected mass density can then be defined in the lens plane that is responsible for the deflection of light.
3. The system is stationary, i.e., $\partial_t = 0$. The properties of the lens galaxy vary insignificantly over the short periods in which lensed images are observed.
4. The weak field limit of general relativity applies (linearized gravity) with an asymptotically flat (Minkowski) background. For the vast majority of lensing scenarios one assumes $\Phi/c^2 \ll 1$.
5. Angles of deflection due to gravitational lensing are small, so that the small angles approximation is invoked.
6. The Born approximation applies as the deflection angle is small. The gravitational potential along the deflected and undeflected light paths can be considered to be approximately the same.

Extended Power-Law Model

For the EPL model [309], the most nuanced and complex model considered in this paper, the function F in Eq. (3.16) takes the form

$$F(\gamma,\delta,\beta_s) = \frac{3-\delta}{(\xi-2\beta_s)(3-\xi)} \times \left[\frac{\Gamma\left(\frac{\xi-1}{2}\right)}{\Gamma\left(\frac{\xi}{2}\right)} - \beta_s\frac{\Gamma\left(\frac{\xi+1}{2}\right)}{\Gamma\left(\frac{\xi+2}{2}\right)}\right]\left[\frac{\Gamma\left(\frac{\gamma}{2}\right)\Gamma\left(\frac{\delta}{2}\right)}{\Gamma\left(\frac{\gamma-1}{2}\right)\Gamma\left(\frac{\delta-1}{2}\right)}\right], \tag{3.17}$$

where $\xi = \gamma + \delta - 2$.

Through a specific choice of γ, δ and β_s, which parameterise the total mass density profile ρ, the luminous mass density profile ν and the stellar orbital anisotropy β_s,

$$\rho(r) = \rho_0 (r/r_0)^{-\gamma}\,, \tag{3.18}$$

$$\nu(r) = \nu_0 (r/r_0)^{-\delta}\,, \tag{3.19}$$

$$\beta_s \ = 1 - \sigma_\theta^2/\sigma_r^2\,, \tag{3.20}$$

simpler models are recovered. Both $\gamma = \gamma_0$ and

$$\gamma = \gamma_0 + \gamma_z z_l + \gamma_s \log \tilde{\Sigma} \tag{3.21}$$

parameterisations are considered for the total matter density profile where the normalised surface mass density $\tilde{\Sigma} \propto \sigma_0^2 / R_{\rm eff}$.

Spherical Power-Law Model

If both $\delta = 2$ and $\beta_s = 0$ are fixed, the SPL model is obtained. In this spherically symmetric model, the only free parameter is the total mass density (dark matter halo) profile, γ, and

$$F := F(\gamma, 2, 0) = \frac{1}{\sqrt{\pi}} \frac{1}{\gamma(3-\gamma)}\,. \tag{3.22}$$

The SPL model is often generalized further to allow for the variation of γ with redshift or surface brightness density of the lens galaxy. For our investigation, we limit γ to a constant value, γ_0. However, Chen *et al.*[215] explore different parametrizations of γ, which are discussed in section 3.4.1.

Singular Isothermal Sphere Model

The SIS model is the simplest discussed, where $\gamma = \delta = 2$, $\beta_s = 0$, and

$$F := F(2, 2, 0) = \frac{1}{2\sqrt{\pi}}\,. \tag{3.23}$$

It assumes that the halo mass of the lens galaxy is in isothermal equilibrium, with gravitational attraction balanced entirely by the pressure associated with the constituent stars' interactions. The total mass density relation is then

$$\rho(r) = \frac{\sigma^2}{2\pi G r^2}\,, \tag{3.24}$$

which leads to the distance ratio,

$$\frac{d_{ls}}{d_s} = \frac{c^2\theta_E}{4\pi\sigma_0^2}\,. \tag{3.25}$$

3.4 Parameter Determination and Model Preference Results

From Eqs. (3.4) and (3.5), or Eq. (3.12), with Eq. (3.16) we find a value of σ_0 that depends purely on model parameters, redshifts z_s and z_l, and the Einstein radius θ_E. We can then compare these values with the observationally determined ones via an MCMC sampling procedure, to constrain the defining parameters of both lens and cosmological models.

The likelihood of the combined lens and cosmological models is determined via

$$\chi^2 = \sum_{i=1}^{161} \frac{\left(\sigma_0 - \sigma_0^{\text{model}}(z_l, z_s, \theta_E, \mathbf{p})\right)^2}{\Delta\sigma_0^2}\,, \tag{3.26}$$

where $\mathbf{p}$ are the defining parameters for a specific lens model i.e., γ, δ and β_s as well as cosmological parameters Ω_{M0} and f_{v0}. σ_0^{model} is given by the combination of lens and cosmological models.

We initially take wide uniform priors for all parameters to avoid biases in the values determined.The stellar orbital anisotropy β_s of all lens galaxies in the catalogue is not measured, so we assume a 2σ Gaussian prior $\beta_s = 0.18 \pm 0.26$, established from a study of nearby elliptical galaxies and adopted by Chen *et al.*[215]. A full list of the priors involved in our MCMC sampling is given in table 3.4.

To obtain the results given in Figs. 3.1 and 3.2, the MCMC sampler ran for 50,000 steps with 32 walkers and a *burn-in* phase discarding the first 20% of the samples. These were created using the EMCEE PYTHON package.

To distinguish between the spatially flat FLRW and timescape models, which have the same number of free parameters, a straightforward Bayes factor, B, can be calculated by integrating the likelihoods $\mathcal{L} \sim e^{-\chi^2/2}$ over the 2σ priors $f_{\text{v0}} \in (0.5, 0.799)$, $\Omega_{\text{M0}} \in (0.143, 0.487)$ [284, 310]and corresponding lens model parameters. The cosmological parameter priors are determined using non-parametric fits of the Planck CMB data [311] constrained by estimates of the angular BAO scale from the BOSS survey data and Lyman alpha forest statistics [312, 313]. Following Dam *et al.*[284] we use wide priors for both models so as not to unfairly disadvantage ΛCDM. The priors usually adopted for ΛCDM, including a precise estimate

Bayes Factors (B)		
Lens Model	B	$\lvert\ln B\rvert$
EPL	0.4928	0.7077
SPL	9.38×10^{-7}	13.9
SIS	3.28×10^{-3}	5.72

Table 3.1: Bayes factors Eq. (3.27), where $B < 1$ favours the spatially flat FLRW model.

$\Omega_{\mathrm{M0}} = 0.315 \pm 0.007$ [28], arise from constraints on perturbation theory on an FLRW background. A timescape equivalent has yet to be developed to constrain the equivalent free parameter, f_{v0}. We take the luminosity density profile δ to have priors informed by profiles fitted to Hubble Space Telescope imagery, giving $2.003 < \delta < 2.343$. The full list of priors used for Bayesian comparison are given in table 3.5.

We adopt the Jeffrey's scale for the Bayes factor

$$B = \frac{\int \mathcal{L}^{\mathrm{timescape}}\, \mathrm{d}f_{\mathrm{v0}}\, \mathrm{d}\gamma\, \mathrm{d}\delta\, \mathrm{d}\beta_s}{\int \mathcal{L}^{\mathrm{FLRW}}\, \mathrm{d}\Omega_{\mathrm{M0}}\, \mathrm{d}\gamma\, \mathrm{d}\delta\, \mathrm{d}\beta_s} \tag{3.27}$$

so that values of $B > 1$ will indicate preference for timescape and $B < 1$ for FLRW. By the standard interpretation, evidence with $|\ln B| < 1$ is 'not worth more than a bare mention' or 'inconclusive', while $1 \leq |\ln B| < 3$, $3 \leq |\ln B| < 5$ and $|\ln B| \geq 5$ indicate 'positive', 'strong' and 'very strong' evidences respectively [314, 315].

3.4.1 Discussion of Results

The Bayes factors favour a spatially flat FLRW model over the timescape model in all cases but with varying degrees of strength, as shown in table 3.1. For the SIS and SPL lens models, the preference is a strong. However, both FLRW and timescape have a minimum χ^2 per degree of freedom ~ 2, which shows in both cases the fit could be improved, specifically within the choice and parametrisation of the lens model. It is important to note that the Bayes factors of table 3.1 should not be interpreted naïvely, as lower χ^2 for FLRW models comes at the expense of an unphysical matter density at the extremes $\Omega_{\mathrm{M0}} \simeq 0$ or $\Omega_{\mathrm{M0}} \simeq 1$. By contrast, the values of f_{v0} predicted are within the 2σ priors $f_{\mathrm{v0}} \in (0.5, 0.799)$ for timescape and remain physically plausible for the majority of lens model parametrisations.

Chen *et al.* [215] already noted that $\Omega_{\mathrm{M0}} \simeq 0$ for specific lens models. However, by considering

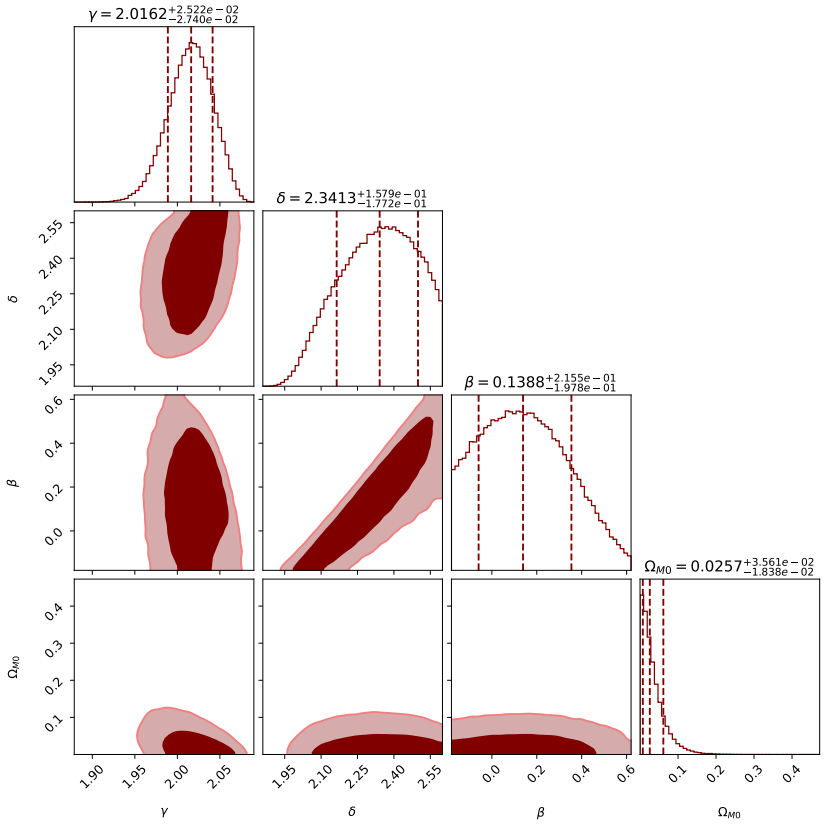

(a) $k = 0$ FLRW

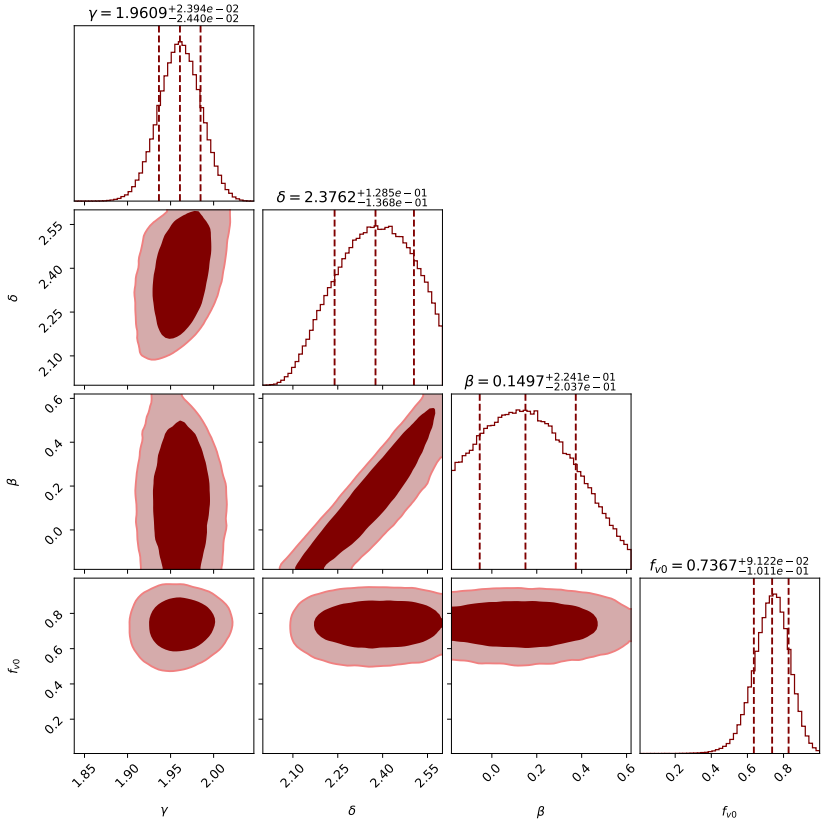

(b) Timescape

Figure 3.1: Parameter probability distributions of the EPL lens model for both spatially flat FLRW and timescape models, constrained using 161 lensing systems. Dashed lines representing the 2σ bounds and median value of MCMC samples.

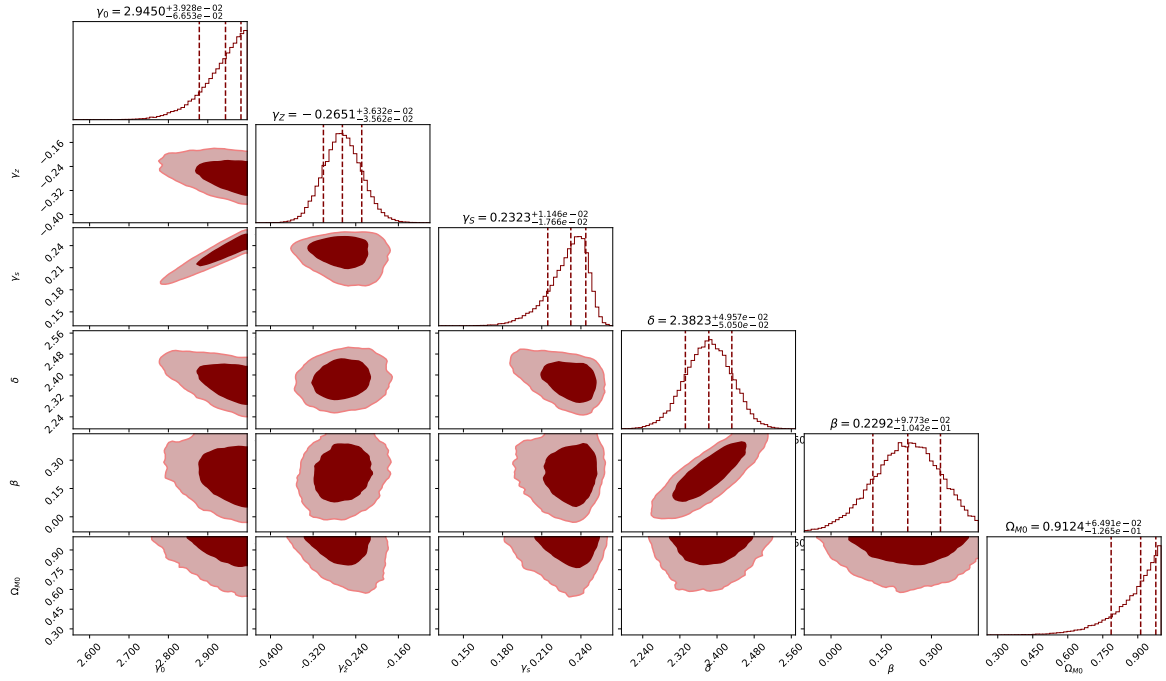

(a) $k = 0$ FLRW

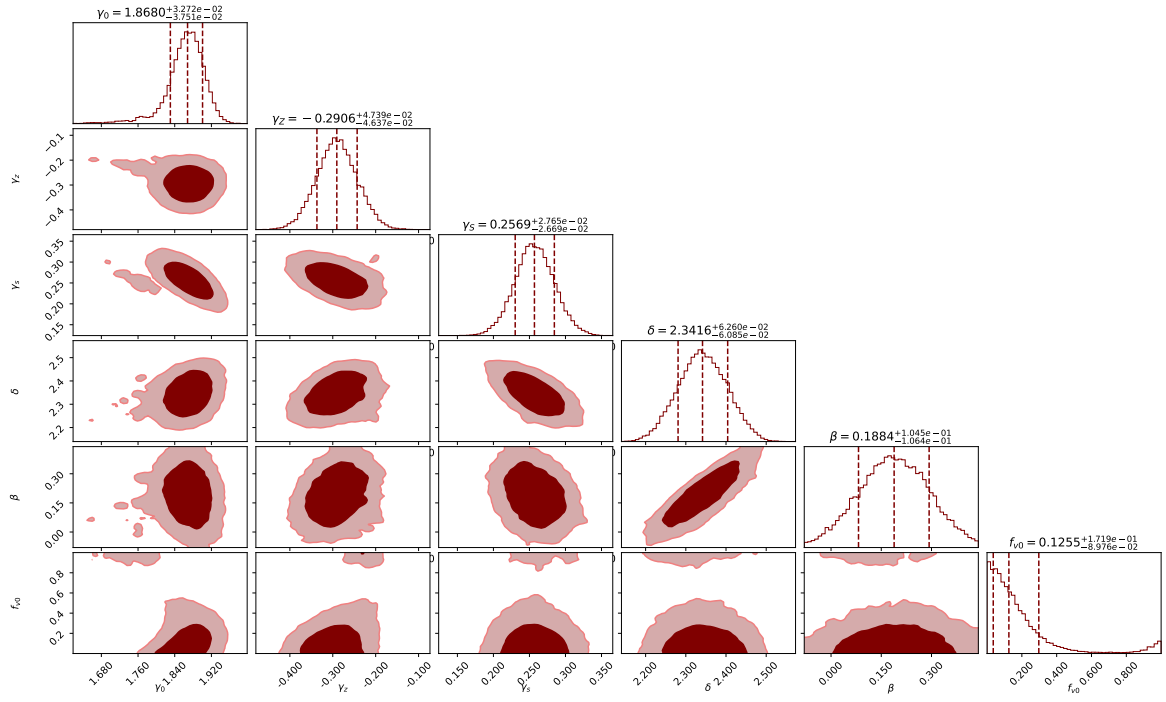

(b) Timescape

Figure 3.2: Parameter probability distributions of the fully extended EPL lens model for both spatially flat FLRW and timescape models, constrained using 161 lensing systems.

FLRW ($k = 0$)				
Lens Model	β_s	δ	γ	Ω_{M0}
EPL (full parametrisation)*	$0.2292^{+9.773\times10^{-2}}_{-1.042\times10^{-1}}$	$2.3823^{+4.947\times10^{-2}}_{-5.050\times10^{-2}}$	$\gamma_0 = 2.9450^{+3.928\times10^{-2}}_{-6.653\times10^{-2}}$ $\gamma_z = -0.2651^{+3.632\times10^{-2}}_{-3.562\times10^{-2}}$ $\gamma_s = 0.2323^{+1.146\times10^{-2}}_{-1.766\times10^{-2}}$	$0.9124^{+6.491\times10^{-2}}_{-1.265\times10^{-1}}$
EPL ($\gamma = \gamma_0$)	$0.1388^{+2.155\times10^{-1}}_{-1.978\times10^{-1}}$	$2.3413^{+1.579\times10^{-1}}_{-1.722\times10^{-1}}$	$2.0162^{+2.522\times10^{-2}}_{-2.740\times10^{-2}}$	$0.0257^{+3.561\times10^{-2}}_{-1.838\times10^{-2}}$
SPL	–	–	$1.9306^{+1.707\times10^{-2}}_{-1.844\times10^{-2}}$	$0.0188^{+2.317\times10^{-2}}_{-1.319\times10^{-2}}$
SIS	–	–	–	$0.0036^{+5.00\times10^{-3}}_{-2.70\times10^{-3}}$

Table 3.2: Ideal parameter values obtained from MCMC sampling of velocity dispersions obtained using FLRW distances and one of the listed lens models.

Timescape				
Lens Model	β_s	δ	γ	f_{v0}
EPL (full parametrisation)*	$0.2292^{+9.773\times10^{-2}}_{-1.042\times10^{-1}}$	$2.3823^{+4.947\times10^{-2}}_{-5.050\times10^{-2}}$	$\gamma_0 = 2.9450^{+3.928\times10^{-2}}_{-6.653\times10^{-2}}$ $\gamma_z = -0.2651^{+3.632\times10^{-2}}_{-3.562\times10^{-2}}$ $\gamma_s = 0.2323^{+1.146\times10^{-2}}_{-1.766\times10^{-2}}$	$0.9124^{+6.491\times10^{-2}}_{-1.265\times10^{-1}}$
EPL ($\gamma = \gamma_0$)	$0.1497^{+2.241\times10^{-1}}_{-2.037\times10^{-1}}$	$2.3762^{+1.285\times10^{-1}}_{-1.368\times10^{-1}}$	$1.9609^{+2.394\times10^{-2}}_{-2.740\times10^{-2}}$	$0.7367^{+9.122\times10^{-2}}_{-1.011\times10^{-1}}$
SPL	–	–	$1.8837^{+6.20\times10^{-3}}_{-6.20\times10^{-3}}$	$0.6751^{+1.73\times10^{-2}}_{-1.73\times10^{-2}}$
SIS	–	–	–	$0.7044^{+3.780\times10^{-2}}_{-3.859\times10^{-2}}$

Table 3.3: Ideal parameter values obtained from MCMC sampling of velocity dispersions obtained using timescape distances and one of the listed lens models.

1. an alternate parametrisation of γ to include a dependency on redshift and normalised surface mass density of each lens galaxy, $\gamma = \gamma_0 + \gamma_z z_l + \gamma_s \log \tilde{\Sigma}$; and
2. δ as an observable for each lens galaxy

more realistic values of Ω_{M0} are inferred. One can only fit δ given high-resolution imagery of a lens galaxy; for the Chen *et al.*[215] catalogue this reduces the sample of lensing systems from 161 to 130. Future surveys are predicted to observe several orders of magnitude more lensing systems. The requirement of follow up high resolution imaging will therefore face significantly greater challenges on account of the vast increase of data volume. When fitting a global value for δ in the EPL model, we find values consistent with 2σ priors informed by HST imagery of $2.003 < \delta < 2.343$ as shown in Figs. 3.1 and 3.2.

Physically plausible values of Ω_{M0} for FLRW have only been found when steps (i) and (ii) are applied to the further parametrised EPL model. If δ is not constrained for each system in the EPL model, then $\Omega_{\mathrm{M0}} \simeq 1$, the other unphysical extreme. Timescape also returns the physically implausible extreme value for $f_{\mathrm{v0}} \simeq 0$ which corresponds exactly to the Einstein de Sitter universe ($\Omega_{\mathrm{M0}} = 1$) for the full paramaterisation of γ.

3.5 Mock Catalogues and Parameter Fitting

3.5.1 Methodology

The unphysical cosmological parameter values found through MCMC sampling, in particular of Ω_{M0}, motivate further investigation. Thus, we generate mock catalogues to gauge how sensitive the fitting procedure is on cosmological parameters. We generate mock catalogues using the following procedure:

1. Using the catalogue data for the 161 lensing systems, we apply the relation for the simplest case lens model SIS, Eq. (3.25), in combination with distance ratios found from cosmology (see Eqs. (3.4) and (3.5) or Eq. (3.12)) to find the *model ideal* values of σ_0. This requires an initial seed value of Ω_{M0} or f_{v0}, which we hope to later recover when fitting.
2. Gaussian noise is then added to σ_0 for each of the 161 lens galaxies.
3. We then use Eq. (3.25) with the catalogue data and the velocity dispersion, with added noise, to find a new value of the distance ratio d_{ls}/d_s.

4. The mock distance ratio and the value determined from either the timescape or spatially-flat FLRW models can then be compared through the χ^2 test

$$\chi^2 = \sum_{i=1}^{161} \left(\frac{\mathcal{D}_i^{\rm model}(\mathbf{q}) - \mathcal{D}_i^{\rm mock}(\mathbf{q}^{\rm seed})}{\Delta \mathcal{D}_i} \right)^2 , \tag{3.28}$$

   where $\mathbf{q} = \{\Omega_{\rm M0}, f_{\rm v0}\}$ depending on cosmology.

5. The $\Omega_{\rm M0}$ and $f_{\rm v0}$ parameters are varied, the best fit values corresponding to the minimized χ^2 value.

6. We repeat this for 10^4 mock samples, with the best fit parameters for each cosmology being binned into a histogram for each individual mock. We then determine whether the original seed parameters of $\Omega_{\rm M0}$ and $f_{\rm v0}$ are recovered from the fitting procedure.

A wide variety of seed values are chosen with parameters in the range $\Omega_{\rm M0} \in \{0.1, 0.9\}$ for spatially flat FLRW, and similarly $f_{\rm v0} \in \{0.1, 0.9\}$ for timescape. We find that regardless of the initial input values of the cosmological parameters, this procedure always lowers $\Omega_{\rm M0}$ significantly for FLRW. For timescape, a value of $f_{\rm v0} \simeq 0.73$ is returned irrespective of the input value.

3.5.2 Simulation Results and Discussion

The histograms produced from the mock data provide interesting results, shown in Fig 3.3. Naïvely, one would assume that if the cosmological model plays a significant role in the pipeline then the generated cosmological parameters would match the input values. However, this is only the case when the uncertainty in the velocity dispersion is set artificially low.

The timescape fit finds values of $f_{\rm v0} \approx 0.73$ which are consistent with the model expectation based on constraints from Sne Ia distances, CMB, etc [185]. In fact, this is still true for timescape fits of the FLRW mocks. The FLRW mocks have a significantly wider cosmological parameter spread, as shown in Fig. 3.4.a as compared to Fig. 3.4.b. Furthermore, the FLRW model yields an $\Omega_{\rm M0}$ more in-line with the expected value of $\Omega_{\rm M0}$ from the Planck CMB data [28] when it is fit against data generated with the timescape model. For FLRW the maximum likelihood of $\Omega_{\rm M0}$ is found to increase as the input $\Omega_{\rm M0}$ is lowered, resulting in an overall maximum likelihood $\Omega_{\rm M0} \to 0$, corresponding to an unphysical Milne universe. For timescape the maximum likelihood increases for seed values close to $f_{\rm v0} \simeq 0.73$.

Both the data and mock catalogues produce some outlying unphysical distance ratios $\mathcal{D} > 1$

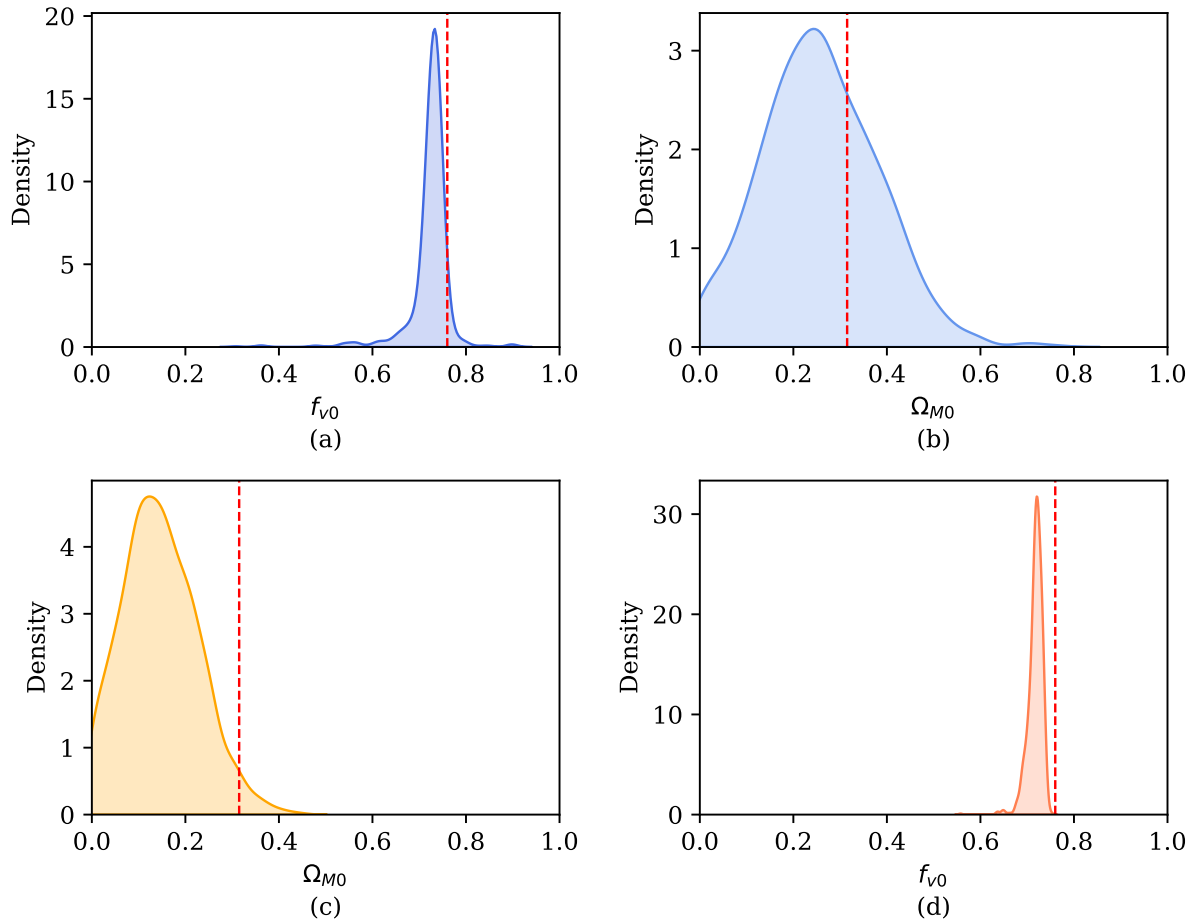

Figure 3.3: Kernel density estimate plots of the best fit parameters for: (a) timescape fit to timescape data, (b) FLRW fit to timescape data, (c) FLRW fit to FLRW data and (d) timescape fit to FLRW data. The dashed vertical red line indicates the initial parameter value used to generate the mock data, $f_{\rm v0} = 0.76$ and $\Omega_{\rm M0} = 0.315$ for timescape and FLRW models respectively.

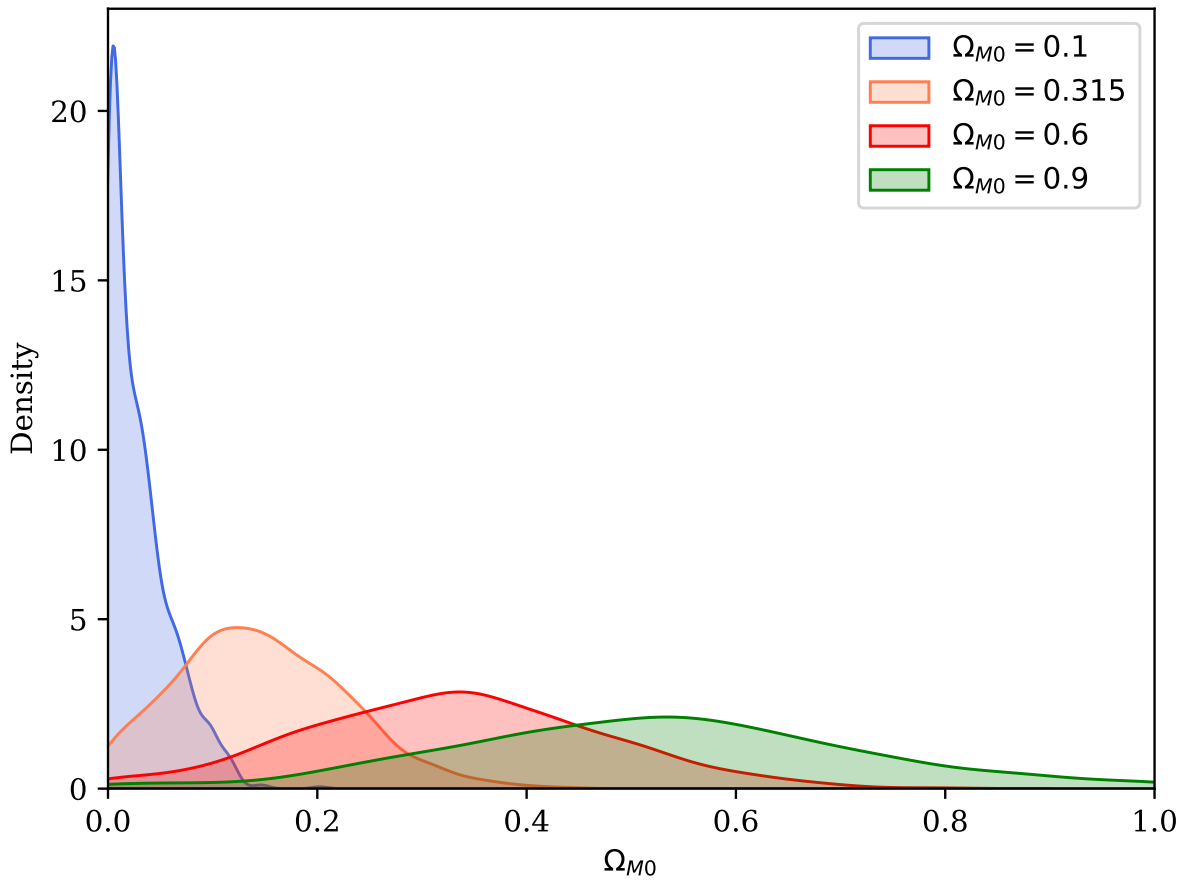

(a) FLRW

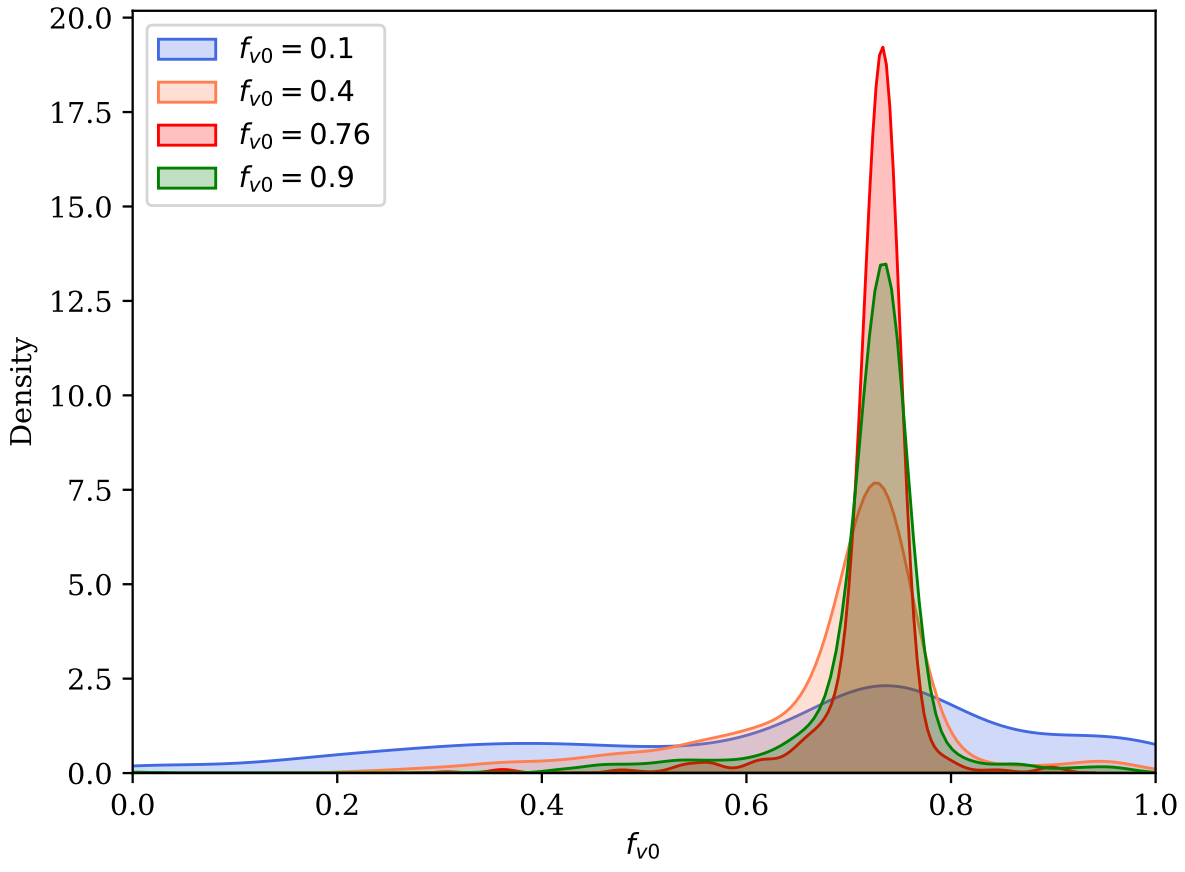

(b) Timescape

Figure 3.4: Kernel density estimate plots showing the best fit cosmological parameters for both FLRW (a) and timescape (b) models fit against data generated with varying initial parameter values.

with closer source than lens to observer (see Fig. 3.5). This is an artefact of choosing a global power-law lens model and fitting to a data set with high variations in the observed velocity dispersions. Some systems are not well described by the lens model choice, and thus produce abnormally high distance ratios that skew the distribution. Fitting any curve $D(\sigma)$ to the data of Fig. 3.5 will be skewed by the unphysical values.

The implications can by understood by considering Fig. 3.6.a and Fig. 3.6.b where distance ratios $\mathcal{D}^{\text{FLRW}}$ and $\mathcal{D}^{\text{Time}}$ are shown for particular fixed source and lens redshifts, z_s and z_l. Varying z_s and z_l we see that while the distance ratio generally increases with increasing z_s, the maximum is always found at $\Omega_{\text{M0}} \simeq 0$ for FLRW and $f_{\text{v0}} \simeq 0.73$ for timescape. With a high enough uncertainty in the velocity dispersion, much larger distance ratios are possible in the simulations. Therefore, the fitting of cosmological parameters is forced towards the values that enable the highest possible distance ratios.

Whilst our simulations were performed using a SIS lens model, the entire class of lens models in our investigation return unphysical distance ratios, $\mathcal{D} \geq 1$, when using the ideal parameters determined by MCMC sampling. Even the EPL model with the full parametrisation, Eq. (3.21), which enables a slight variation of the power law model between systems, often yields unphysical distance ratios.

3.6 Conclusions

In order to increase the goodness of fit of power-law lens models, additional empirical parameters are often added to the lens models along with constraints from high resolution imagery. The simplest parametrisations of these models, in combination with the standard spatially flat FLRW cosmology, have already been shown to produce poor fits to data without additional observationally determined luminosity density profiles [215]. We find that all choices of power-law model investigated naïvely prefer a spatially flat FLRW cosmology, but as a consequence delegate all the mass along the line of sight to the lens galaxy, resulting in $\Omega_{\text{M0}} \simeq 0$. For the full parametrisation, Eq. (3.21), of the EPL model the fits return an Einstein de Sitter universe with $\Omega_{\text{M0}} = 1$, which is also clearly unphysical.

The timescape cosmology gives void fraction values of $0.68 \leq f_{\text{v0}} \leq 0.74$ consistent with constraints from independent tests [185, 285] in all cases except that of Eq. (3.21) when it also returns the same unphysical Einstein de Sitter universe ($f_{\text{v0}} = 0$). Simulations with a fixed SIS lens model consistently return values of $f_{\text{v0}} \simeq 0.73$, regardless of the input seed value. Our

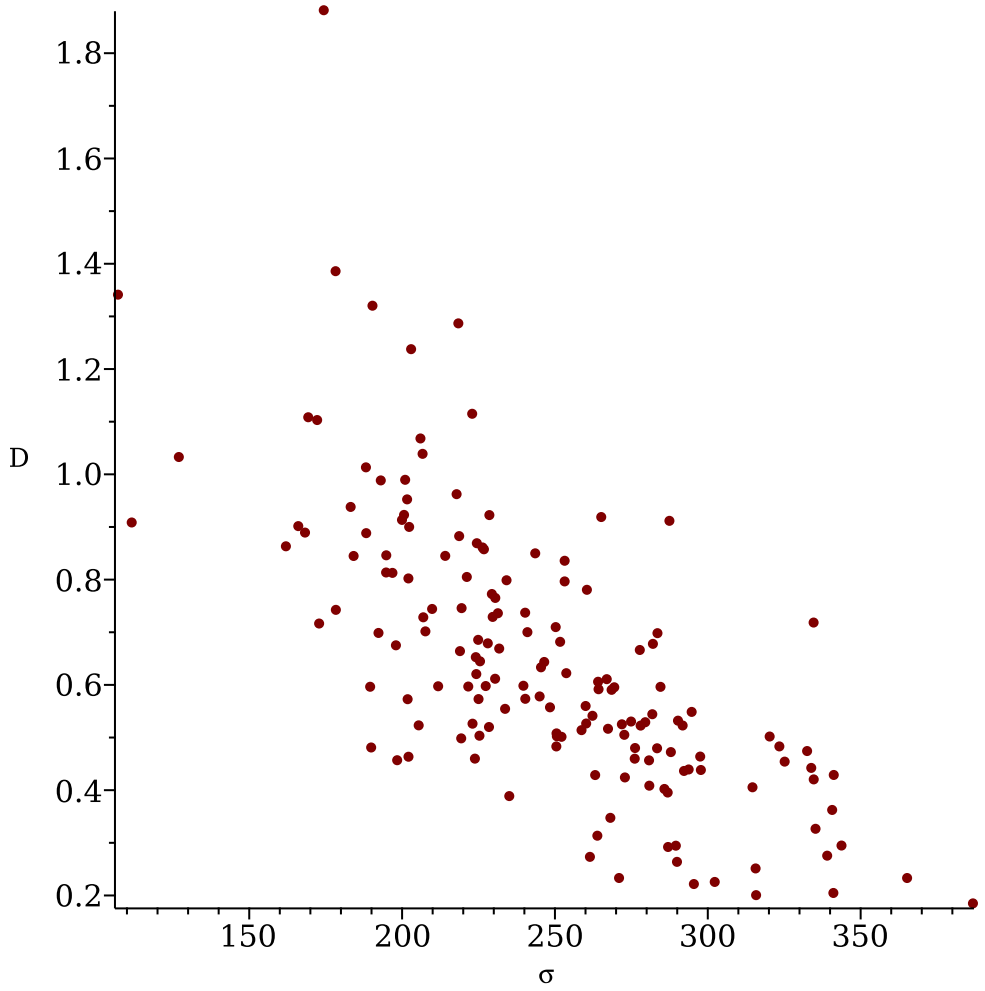

Figure 3.5: Distance ratios against velocity dispersion (kms^{-1}) for a Single Isothermal Sphere lens model using catalogue data for 161 systems.

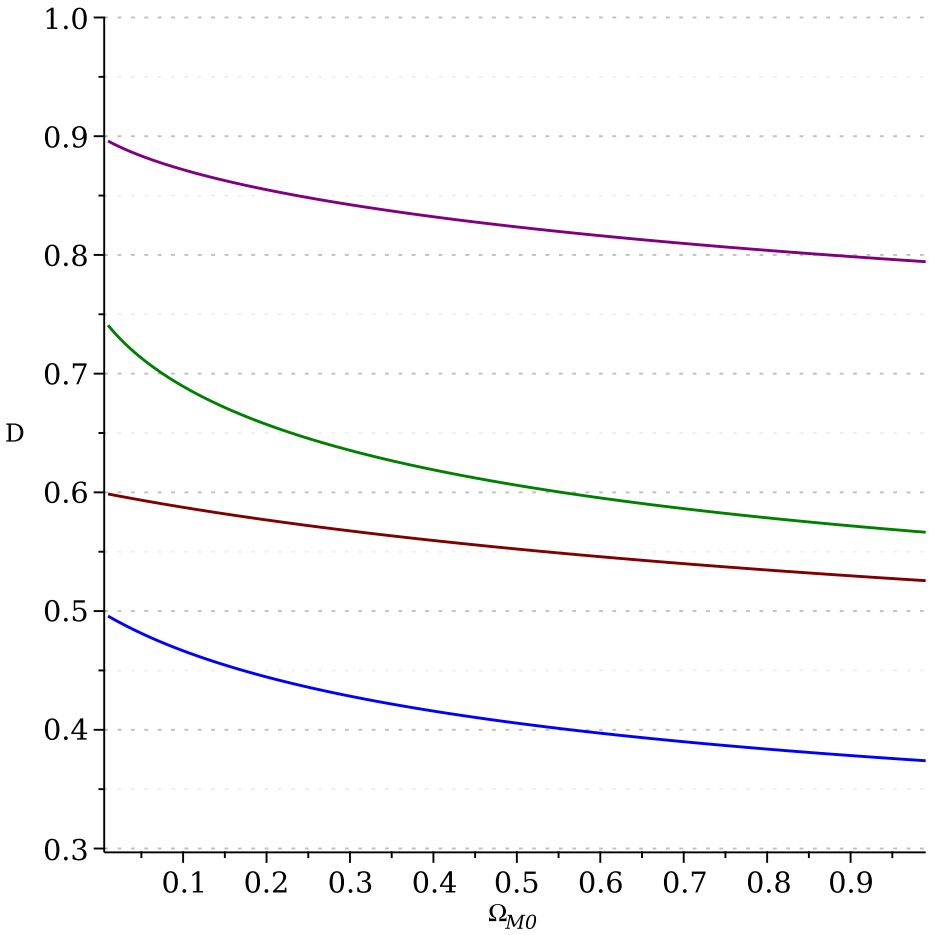

(a) FLRW

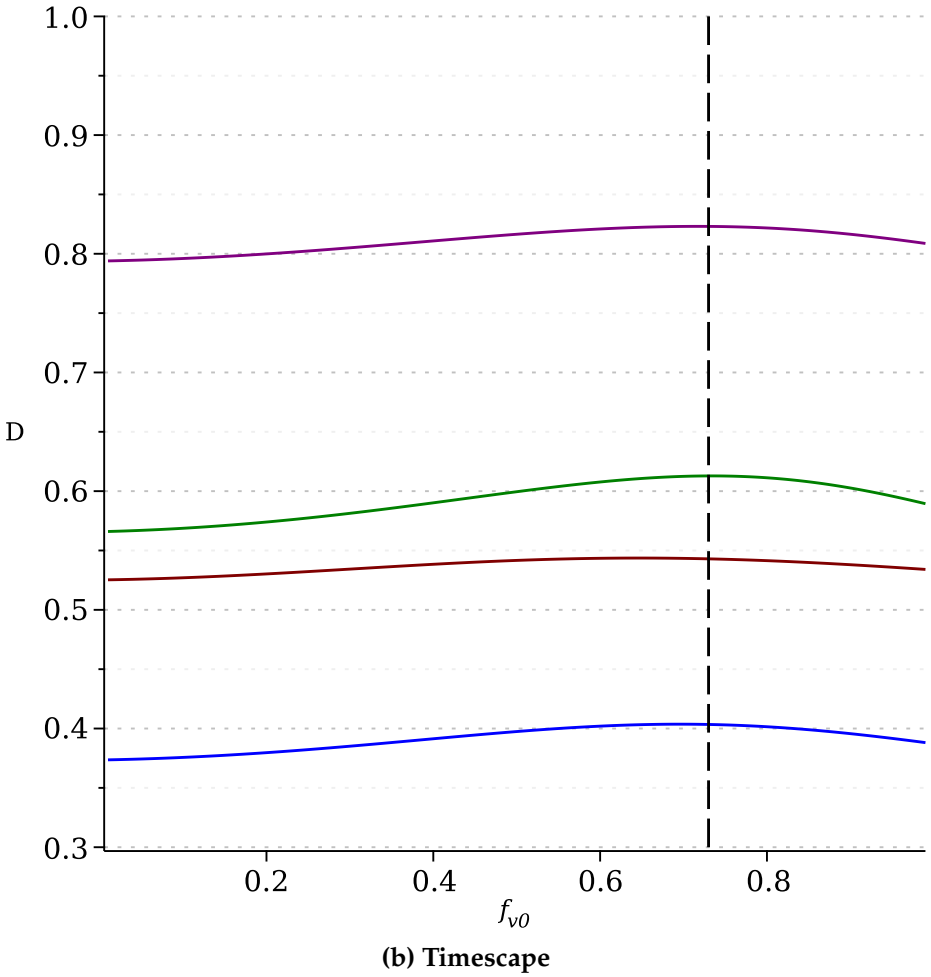

(b) Timescape

Figure 3.6: Distance ratios for fixed lens and source redshifts in both spatially flat FLRW and timescape models with varying Ω_{M0} and f_{v0} respectively.

results highlight the imperative of exploring alternatives to the standard ΛCDM cosmology. Even if any particular non-FLRW cosmology is incorrect, such comparisons may give insight into breaking the many degeneracies present in SGL analyses to date.

It is clear that either

1. power-law models cannot be applied globally to large surveys of lensing systems as they make unphysical predictions of the distance ratios, or,
2. our measurements of the velocity dispersions of lens galaxies are not currently at a high enough accuracy and precision to enable this kind of analysis.

Navarro-Frenk-White profiles are generally taken as the standard for modelling the dark matter haloes of elliptical galaxies, rather than the power-law models used here for large SGL catalogues. The use of a general lens model across all systems in the catalogue, assuming that on average they will be well-defined, is evidently not the case. Many lens galaxies have large uncertainties in their respective velocity dispersion measurements, leading to unphysical distance ratios for many lensing systems regardless of the choice of power-law used.

Systems that deviate from these power-law models negatively skew the distribution of distance ratios, leading to biasing in the determination of cosmological parameters. In fact, even an individualised EPL model, with the full parametrisation of γ, fails to produce physically plausible distance ratios for all systems. What results is that the 'best fit' cosmological parameters found are those which can produce the highest possible distance ratios to match the unphysical predictions of the lens models.

Without additional imaging data, the technique of using distance ratios as a test statistic is weak at constraining cosmological parameters. However, it has the advantage of a far larger dataset than that of using time-delay distances. With the next generation of telescopes (JWST, Euclid, LSST etc) predicted to observe even more lensing systems, it is of paramount importance that appropriate lens models are determined in advance of the upcoming catalogues if one aims to use strong lensing for robust statistical constraints in cosmology.

Time-delay cosmography is able to constrain the lens mass distribution with far greater precision than the distance sum rule test. This arises from the extra constraints given by the magnification and time-delay between each of the images. In addition, time-delay cosmography models lensing systems individually, whereas the distance ratio technique fits global lens models to large catalogues of highly variable systems. At present, despite the smaller number of

systems available, time-delay cosmography may present the only viable way to use strong gravitational lensing to constrain both cosmological models and lens matter models with the precision of measurements available in ongoing surveys.

Appendix

Priors

The priors used for the MCMC sampling procedure and Bayesian analysis are listed in table 3.4 and table 3.5.

Model derivation and explanation of parameters

In this section we will discuss the various assumptions that go into the extended power-law model of Koopmans [309] for elliptical galaxies as gravitational lenses. The extended power-law model, as well as variants SPL and SIS, are derived from the radial Jeans equation here given in spherical coordinates (r, θ, ϕ):

$$\frac{\mathrm{d}}{\mathrm{d}r}[\nu(r)\,\sigma_r^2] + \frac{2\beta_s}{r}\,\nu(r)\,\sigma_r^2 = -\nu(r)\frac{\mathrm{d}\Phi}{\mathrm{d}r}\,, \tag{3.29}$$

where

$$\frac{\mathrm{d}\Phi}{\mathrm{d}r} = \frac{GM(r)}{r^2} \tag{3.30}$$

Here, the velocity dispersion σ_r is defined as follows with f being the distribution function of the stars within the galaxy.

$$\sigma_r^2 = \frac{1}{\nu}\int v_r f \mathrm{d}^3 v \tag{3.31}$$

The Jeans equation looks at the average motion of the distribution of stars defined by the luminous matter density distribution $\nu(r)$ within a Newtonian gravitational potential created by the total matter density $\rho(r)$, including dark matter. The parameter $\beta_s(r)$ denotes the anisotropy of the stellar velocity dispersion and is also known as the stellar orbital anisotropy. These are parametrised as such for the extended power-law,

$$\rho(r) = \rho_0(r/r_0)^{-\gamma} \tag{3.32}$$

$$\nu(r) = \nu_0(r/r_0)^{-\delta} \tag{3.33}$$

$$\beta_s(r) = 1 - \sigma_\theta^2/\sigma_r^2\,, \tag{3.34}$$

MCMC Priors						
Lens Model	γ	γ_z	γ_s	β_s	δ	f_{v0}/Ω_{M0}
EPL (full)	(1.0, 3.0)	(-1, 1)	(0,1)	$\mathcal{N}$(-0.08, 0.44)	(1.8, 2.6)	(0, 1)
EPL ($\gamma = \gamma_0$)	(1.8, 2.2)	–	–	$\mathcal{N}$(-0.08, 0.44)	(1.8, 2.6)	(0, 1)
SPL	(1.8, 2.2)	–	–	–	–	(0, 1)
SIS	–	–	–	–	–	(0, 1)

Table 3.4: Priors assumed for MCMC sampling. In general wide uniform priors are taken, with the except of the stellar orbital anisotropy parameter β_s, which is assumed to have a Gaussian distribution.

Bayes Factors Priors					
Lens Model	γ	δ	β_s	f_{v0}	Ω_{M0}
EPL	(1.2, 2.8)	(2.003, 2.343)	$\mathcal{N}$(-0.08, 0.44)	(0.5, 0.799)	(0.143, 0.487)
SPL	(1.2, 2.8)	–	–	(0.5, 0.799)	(0.143, 0.487)
SIS	–	–	–	(0.5, 0.799)	(0.143, 0.487)

Table 3.5: Priors used for establishing Bayes factors between cosmological models.

where σ_θ and σ_r are the tangential and radial velocity dispersions respectively. With $\beta_s(r) \neq 0$, we can account the average orbits of stars deviating from circular paths, however the total mass density will remain spherical - it does not disrupt the spherical dark matter halo of the galaxy.

In order to solve the Jeans equation, numerous assumptions are made:

- the system is static i.e., $\partial_t = 0$. This feels like a reasonable assumption to make as the structure of the elliptical galaxy should not be expected to change over the course of lensing measurements.
- the stress tensor σ_{ij} is diagonal, such that $\langle v_i v_j \rangle = 0$ if $i \neq j$.
- spherical symmetry applies such that $\sigma^2_{r\phi} = \sigma^2_{r\theta} = 0$ and ρ and ν only depend on r with no angular component.
- collisionless matter. The Jeans equation is originally derived from the collisionless Boltzman equation and as such does not permit interactions between the constituent stars within galaxies.

After making these assumptions, the radial Jeans equation can be solved for the radial velocity dispersion in terms of the luminous matter distribution and the total mass inside a sphere of radius r,

$$\sigma_r^2(r) = \frac{G \int_r^\infty \mathrm{d}r' r'^{2\beta_s - 2} \nu(r') M(r')}{r^{2\beta_s} \nu(r)} \,. \tag{3.35}$$

We can then define the mass contained within a cylinder of radius R_E, the Einstein radius, which quantifies the mass of the lens galaxy,

$$M_E = \int_0^{R_E} \mathrm{d}R \, 2\pi R' \Sigma(R') \,, \tag{3.36}$$

where $\Sigma(R)$ is the mass density projected into the lens plane,

$$\Sigma(R) = \int_{-\infty}^{\infty} \mathrm{d}Z \, \rho(r) = \int_{-\infty}^{\infty} \mathrm{d}Z \, \rho_0 \, r_0^\gamma (Z^2 + R^2)^{-\gamma/2} \,, \tag{3.37}$$

$$\Sigma(R) = \sqrt{\pi} \, R^{1-\gamma} \frac{\Gamma((\gamma-1)/2)}{\Gamma(\gamma/2)} \rho_0 \, r_0^\gamma \,. \tag{3.38}$$

Here R is the radius of the galaxy in the lens plane and Z is the distance along the line of sight perpendicular to the lens plane, r is the spherical radius as previous such that $r^2 = R^2 + Z^2$.

The mass contained inside the Einstein radius is therefore,

$$M_E = 2\pi^{3/2} \, \frac{R_E^{3-\gamma}}{3-\gamma} \frac{\Gamma((\gamma-1)/2)}{\Gamma(\gamma/2)} \rho_0 \, r_0^\gamma \,. \tag{3.39}$$

The total mass within a sphere of radius r can also be calculated,

$$M(r) = \int_0^r \mathrm{d}r' 4\pi\, r'^2\, \rho(r') = 4\pi\, \rho_0\, r_0^\gamma \frac{r^{3-\gamma}}{3-\gamma} \tag{3.40}$$

which can be written in terms of the mass M_E contained within the cyclinder as

$$\sigma_r^2(r) = \frac{2}{\sqrt{\pi}} \frac{GM_E}{R_E} \frac{1}{\xi - 2\beta_s} \frac{\Gamma((\gamma-1)/2)}{\Gamma(\gamma/2)} \left(\frac{r}{R_E}\right)^{2-\gamma} \tag{3.41}$$

where $\xi = \gamma + \delta - 2$. The velocity dispersion from observation is the component of the luminosity weighted average along the line of sight and pver the effective spectroscopic aperture R_A. This can be written as:

$$\sigma_\parallel^2(\leq R_A) = \frac{\int_0^{R_A} \int_{-\infty}^{\infty} \mathrm{d}R\, \mathrm{d}Z\, 2\pi R\, \sigma_r^2(r) \left(1 - \beta_s \frac{R^2}{r^2}\right) \nu(r)}{\int_0^{R_A} \int_{-\infty}^{\infty} \mathrm{d}R\, \mathrm{d}Z\, 2\pi\, R\, \nu(r)}\,. \tag{3.42}$$

By substituting in the expression for σ_r^2 and the power-law of $\nu(r)$ we arrive at

$$\sigma_\parallel^2(\leq R_A) = \frac{2}{\sqrt{\pi}} \frac{GM_E}{R_E} \frac{3-\delta}{(\xi - 2\beta_s)\,(3-\xi)} \left[\frac{\Gamma\left(\frac{\xi-1}{2}\right)}{\Gamma\left(\frac{\xi}{2}\right)} - \beta_s \frac{\Gamma\left(\frac{\xi+1}{2}\right)}{\Gamma\left(\frac{\xi+2}{2}\right)}\right] \times \frac{\Gamma\left(\frac{\gamma}{2}\right)\Gamma\left(\frac{\delta}{2}\right)}{\Gamma\left(\frac{\gamma-1}{2}\right)\Gamma\left(\frac{\delta-1}{2}\right)} \left(\frac{R_A}{R_E}\right)^{2-\gamma}. \tag{3.43}$$

Using the deflecting mass found from the lensing equation

$$M_E = \frac{c^2\,\theta_E}{4G} \frac{D_s\, D_l}{D_{ls}}\,, \tag{3.44}$$

$R_A = D_l \theta_A$ and $R_E = \theta_E D_l$ we get,

$$\sigma_\parallel^2(\leq R_A) = \frac{2}{\sqrt{\pi}} \frac{D_s\,\theta_E\, c^2}{D_{ls}} \frac{3-\delta}{(\xi - 2\beta_s)(3-\xi)} \left[\frac{\Gamma\left(\frac{\xi-1}{2}\right)}{\Gamma\left(\frac{\xi}{2}\right)} - \beta_s \frac{\Gamma\left(\frac{\xi+1}{2}\right)}{\Gamma\left(\frac{\xi+2}{2}\right)}\right] \times \frac{\Gamma\left(\frac{\gamma}{2}\right)\Gamma\left(\frac{\delta}{2}\right)}{\Gamma\left(\frac{\gamma-1}{2}\right)\Gamma\left(\frac{\delta-1}{2}\right)} \left(\frac{\theta_A}{\theta_E}\right)^{2-\gamma}, \tag{3.45}$$

which is the expression we call the extended power-law. The use of the lens equation also is built upon several assumptions:

- the weak field limit of general relativity applies and that $\Phi/c^2 \ll 1$,
- small deflection angles,
- the Born approximation applies.

Chapter 4

Time Delay Lensing as a Test of Cosmological model

This chapter contains the natural extension to chapter 3, attempting to use strong gravitational lensing for statistical cosmology with additional time-delay data.

4.1 Introduction

The inconsistency in the current expansion rate of the universe, H_0, inferred from early and late universe measurements, known as the Hubble tension, presents one of modern cosmology's greatest challenges. Late-universe results from the *SH0ES* collaboration of $H_0 = 73.04 \pm 1.04\,\mathrm{km\,s^{-1}Mpc^{-1}}$ are in a $\approx 5\sigma$ tension with values inferred from the *Planck* CMB data of $H_0 = 67.4 \pm 0.5\,\mathrm{km\,s^{-1}Mpc^{-1}}$ [28, 68]. This disagreement has motivated research to determine the value of H_0 from a variety of different astrophysical phenomena [73]. Ultimately, the tension has only grown greater in magnitude as the precision of data has increased and the systematic and statistical uncertainty has reduced. This does not mean there cannot be an underlying systematic common to each early or late universe measurement that is unaccounted for, nor does it rule out a series of unaccounted systematics. However, the tendency for cosmological tensions to increase in recent years provides motivation for new physics or the revisiting of fundamental assumptions in cosmology [316].

Strong gravitational lensing (SGL) presents a relatively recent (at least in cosmological terms!) alternative method to determine H_0 and constrain cosmological models. Requiring a specific configuration of lens and source object (e.g. an elliptical galaxy and quasar source, respectively), SGL results in multiple images being produced of the source object. For transient sources, with generally different travel times for emitted light to the observer, an associated

time-delay distance difference can be inferred, from which an estimate of H_0 can be calculated [212]. This technique is known as time-delay cosmography. Despite the vast increase in the number of observed lensing systems, only around 30 have precise time-delay measurements [248, 317]. Regardless, a value for H_0 can be inferred for each individual system, assuming a sufficiently accurate lens model. Hence, only a few systems are enough to achieve comparable precision to analyses of thousands of supernovae [249].

A major advantage of time-delay cosmography is that it is independent of the cosmic distance ladder and thus, has an entirely separate set of systematics to other methods of estimating H_0 [256]. This one-step method provides an important tool for cross-checking other local distance measures and investigating their systematics. The *H0LiCOW* collaboration has successfully constrained the Hubble constant to 2.4% precision using time-delay cosmography, finding $H_0 = 73.3^{+1.7}_{-1.8}\,\mathrm{km\,s^{-1}Mpc^{-1}}$, in agreement with other late universe probes and in a 3.1σ tension with the *Planck* values [249], depending on the lens model used. This result further contributes to the tension, elevating it to 5.3σ when applied in combination with distance ladder results.

In chapter 3 we performed statistical cosmological analyses built upon the relations derived from the distance ratio between lens and source objects alone. These studies show that without additional observational data or without fitting an individual lens model to each distinct system, the use of spherically symmetric power-law lens models cannot accurately constrain cosmological parameters in population level statistical analyses. The further inclusion of time-delay data adds additional constraints on the lens models, with the aim of returning physically plausible values when fitting for cosmology.

Here, we first perform an initial assessment of whether the application of spherically symmetric lens models with the inclusion of additional time-delay data can effectively constrain cosmological parameters. We then complete an exploratory analysis of the timescape cosmology by extending the work of the H0LiCOW collaboration [249]. This more refined analysis involves individually fitting more nuanced lens models to each system and, therefore, does not 'wash out' the information lost by assuming spherically symmetric lens models. However, it has the limitation of a much smaller dataset.

In this chapter, section 4.2.1 describes the formalism of TD cosmography and gives the methodology used to fit for cosmological parameters. Section 4.2.2 gives the data set used and the method for generating mock data where required. Section 4.2.3 provide the results

of the analysis of the entire time delay catalogue. The H0LiCOW lens sample is described in section 4.3.1 and the corresponding lens modelling and analysis in sections 4.3.2 and 4.3.3, respectively. In section 4.3.4 we discuss the results of this analysis. In section 4.4, we discuss our conclusions.

4.2 Population Statistics

4.2.1 Methodology

Time-delay Formalism

We follow the typical formalism described by Schneider, Kochanek and Wambsganss [219]. For a given lens mass distribution and image configuration, the time of arrival of a particular image can be expressed as

$$t(\theta, \beta) = \frac{D_{\Delta t}}{c} \left[\frac{(\theta - \beta)^2}{2} - \psi(\theta) \right], \tag{4.1}$$

where θ, β, and ψ, are the image position, source position, and lensing potential, respectively. $D_{\Delta t}$ is defined as a ratio of angular diameter distances referred to as the time-delay distance,

$$D_{\Delta t} \equiv (1 + z_l) \frac{D_l \, D_s}{D_{ls}}, \tag{4.2}$$

where z_l is the spectroscopic lens redshift. The time-delay between two images, θ_i and θ_j, of the same source is then simply expressed by the difference of arrival times,

$$\Delta t_{ij} = \frac{D_{\Delta t}}{c} \left[\frac{(\theta_i - \beta)^2}{2} - \frac{(\theta_j - \beta)^2}{2} - \psi(\theta_i) + \psi(\theta_j) \right], \tag{4.3}$$

where the values of θ are determined empirically from observations to a high degree of precision. However, the lensing potential, ψ, is dependent on the choice of lens model and is necessary in order to solve the lens equation to determine the unperturbed source position, β. In this work, we assume spherical symmetry on average. Any effect due to the ellipticity of the *elliptical* galaxies is assumed to average out with a large enough sample size, and thus can be ignored [215, 273]. Whilst chapter 3 brings this assumption into question, we now investigate whether the addition of time-delay constraints enables the use of these lens models in this manner. For spherically symmetric power-law lenses, the lensing potential can be well described by[317–319]

$$\psi(\theta) = \frac{\theta_E^2}{3 - \gamma} \left(\frac{\theta}{\theta_E} \right)^{3-\gamma}, \tag{4.4}$$

where θ_E is the Einstein radius. The case of $\gamma = 2$ returns the familiar singular isothermal sphere result,

$$\psi(\theta) = \theta\,\theta_E\,. \tag{4.5}$$

Combining Eqs. (4.3) and (4.5), and by applying $(\theta_i + \theta_j)/2 = \theta_E$, leads to an expression for the time-delay between the two images for the singular isothermal sphere model

$$\Delta t_{ij} = \frac{D_{\Delta t}}{2c}(\theta_i^2 - \theta_j^2)\,. \tag{4.6}$$

For generic spherical power-law models an equivalent relation is found using the deflection angle and lens equation for a two-image configuration of a power-law lens [320],

$$\Delta t_{ij} = \frac{D_{\Delta t}}{c}\,\theta_E^2\,\left[\frac{1}{2}\left\{\left(\frac{\theta_E}{\theta_i}\right)^{2\gamma-4} - \left(\frac{\theta_E}{\theta_j}\right)^{2\gamma-4}\right\} + \frac{1}{3-\gamma}\left\{\left(\frac{\theta_E}{\theta_j}\right)^{\gamma-3} - \left(\frac{\theta_E}{\theta_i}\right)^{\gamma-3}\right\}\right], \tag{4.7}$$

where

$$\theta_E^{\gamma-1} = \frac{\theta_i + \theta_j}{\theta_i^{2-\gamma} + \theta_j^{2-\gamma}}\,. \tag{4.8}$$

For systems with accurate velocity dispersion and luminosity density profile measurements, a further extension to the EPL lens model is possible. However, for the majority of lens galaxies in our sample this data was not available. A future extension would be to assume that the time-delay lenses are a subset of the wider lens population (and elliptical galaxy population more generally), and thus share the correlations between velocity dispersion, half-light radius, and luminosity density profile motivated by the empirical fundamental plane relation.

MCMC Set Up

In our analysis we assume wide priors as not to unfairly bias the MCMC sampling in favour of the timescape model. If the narrow range in uncertainty in H_0 and Ω_{M0} taken from *Planck* CMB data were used as uniform priors, it would unfairly weight the Bayes factor comparison in favour of timescape as the equivalent precise parametric fits to CMB data have not yet been developed in the timescape cosmology. Thus, we take wide uniform priors as $0 < \Omega_{M0} < 1$ and $0 < f_{v0} < 1$ in cosmological parameters. For our initial analysis, we assume a value of the Hubble constant (or dressed Hubble constant in the timescape model) of $H_0 = 70\,\mathrm{km\,s^{-1}Mpc^{-1}}$. Priors on lens model parameters are chosen as in chapter 3, with the density profile exponent γ between $1.2 < \gamma < 2.8$. To carry out the MCMC analysis, we utilise the PYTHON package PYMULTINEST [321].

4.2.2 Data

Each lensing system consists of a multiply-imaged quasar being lensed by an elliptical galaxy. The catalogue of 31 lensing systems used in this chapter was compiled by Melia *et al.* [317] from a number of different surveys, predominantly made up of the COSMOGRAIL time-delay lensing sample [248]. COSMOGRAIL represents a 15-year-long effort to constrain the time-delays of transient light curves specifically for the purpose of time-delay cosmography. From this catalogue, spectroscopic redshifts of the lens and source z_l and z_s, image positions θ_i and θ_j, and time-delays $|\Delta t_{ij}|$ are obtained and given in table 4.1.

System	z_l	z_s	θ_i ($''$)	θ_j ($''$)	$\lvert\Delta t_{ij}\rvert$ (days)
FBQ0951+2635	0.26	1.246	0.886 ± 0.004	0.228 ± 0.008	16.0 ± 2.0
SDSS J1442+4055	0.284	2.593	1.385 ± 0.049	0.771 ± 0.028	25.0 ± 1.5
RXJ1131-1231	0.295	0.657	1.898 ± 0.015	1.922 ± 0.023	1.6 ± 0.7
PG1115+080	0.311	1.722	1.120 ± 0.014	0.950 ± 0.016	8.3 ± 1.5
QJ0158-4325	0.317	1.290	0.814 ± 0.038	0.410 ± 0.020	22.7 ± 3.6
Q0957+561	0.360	1.413	5.220 ± 0.006	1.036 ± 0.110	417.1 ± 0.1
HS0818+1227	0.390	3.113	2.219 ± 0.009	0.615 ± 0.003	153.8 ± 13.9
SDSS J0924+0219	0.393	1.523	0.878 ± 0.021	0.977 ± 0.072	2.4 ± 3.8
SDSS J1620+1203	0.398	1.158	2.277 ± 0.037	0.494 ± 0.010	171.5 ± 8.7
DES2325-5229	0.400	2.740	1.230 ± 0.050	1.790 ± 0.050	43.8 ± 4.3
HE0047-1756	0.407	1.678	0.894 ± 0.043	0.553 ± 0.027	10.4 ± 3.5
B1600+434	0.414	1.589	1.140 ± 0.075	0.250 ± 0.074	51.0 ± 4.0
J1001+5027	0.415	1.838	1.980 ± 0.080	0.930 ± 0.190	119.3 ± 3.3
SDSS J1335+0118	0.440	1.570	1.079 ± 0.031	0.489 ± 0.014	56.0 ± 5.9
WG0214-2105	0.450	3.240	1.018 ± 0.225	1.246 ± 0.275	7.5 ± 2.8
HE0435-1223	0.454	1.693	1.298 ± 0.008	1.168 ± 0.014	9.0 ± 0.8
Q0142-100	0.491	2.730	1.855 ± 0.002	0.383 ± 0.005	97.0 ± 15.8
SDSS J1650+4251	0.577	1.547	0.872 ± 0.027	0.357 ± 0.042	49.5 ± 1.9
DES J0408-5354	0.597	2.375	3.626 ± 0.342	3.053 ± 0.361	112.1 ± 2.1
HE2149-2745	0.603	2.033	1.354 ± 0.008	0.344 ± 0.012	72.6 ± 17.0
SDSS J1339+1310	0.609	2.231	0.580 ± 0.041	1.234 ± 0.106	47.0 ± 5.5
SDSS J0832+0404	0.659	1.116	1.560 ± 0.024	0.435 ± 0.008	125.3 ± 18.2
B0218+357	0.685	0.944	0.057 ± 0.004	0.280 ± 0.008	11.3 ± 0.2
Q1355-2257	0.702	1.370	0.959 ± 0.081	0.267 ± 0.023	81.5 ± 11.6
SBS1520+530	0.717	1.855	1.207 ± 0.004	0.386 ± 0.008	130.0 ± 3.0
HE1104-1805	0.729	2.319	1.099 ± 0.004	2.095 ± 0.008	152.2 ± 3.0
SDSS J1206+4332	0.742	2.054	1.676 ± 0.104	0.313 ± 0.019	210.2 ± 5.6
SDSS J1515+1511	0.748	1.789	1.870 ± 0.088	1.278 ± 0.097	111.0 ± 3.0
SBS0909+532	0.830	1.377	0.415 ± 0.126	0.756 ± 0.152	50.0 ± 3.0

System	z_l	z_s	θ_i ($''$)	θ_j ($''$)	$\lvert\Delta t_{ij}\rvert$ (days)
PKS1830-211	0.890	2.507	0.670 ± 0.080	0.320 ± 0.080	26.0 ± 5.0
WFI J2026-4536	1.040	2.230	0.673 ± 0.156	0.801 ± 0.184	18.7 ± 4.8

Table 4.1: The spectroscopic redshifts of the foreground deflector galaxy and background quasar source, image positions, and respective time delays are given for each system used in our time-delay analysis. The data for this table was originally compiled by Melia *et al.* [317].

4.2.3 Results and Discussion

We use the relation given by Eq. (4.7) to perform an MCMC sampling procedure with the likelihoods of the combined lens and cosmological models. These are generated with a simple χ^2 statistic,

$$\chi^2 = \sum_{i=1}^{31} \frac{(D_i^{\rm lens} - D_i^{\rm cosmo})^2}{\Delta D_i^2}\,, \tag{4.9}$$

where the likelihood is $\mathcal{L} \propto e^{\chi^2/2}$ and where ΔD_i is the uncertainty in the distance estimate. The original intention was to once again use the Jeffery's scale and evaluate the Bayes factor between timescape and FLRW models. However, as previously discussed in chapter 3, it is naïve to consider the Bayes factor when model parameters are constrained to unphysical values. We find that physically plausible values for cosmological parameters are not recovered regardless of the cosmological model used, and thus do not consider the Bayes factors between the models, which wildly swing between strong preferences for spatially flat FLRW models and timescape depending on the lens model parametrisation applied.

In Fig. 4.1, we see that with the inclusion of time-delay data, applying the SPL lens model, unphysical values of Ω_{M0} and f_{v0} are still recovered for the spatially flat FLRW and timescape models respectively. Specifically, fitting an FLRW model supports a matter dominated universe with $\Omega_{M0} \to 1$, whereas timescape supports a void dominated universe at the present epoch with $f_{v0} \to 1$. This differs to the results of the SPL model in chapter 3, where the FRLW model prefers an 'empty' universe. However, both analyses show that the same skewing of the lens model fits to observational data is occurring, as the distances are not being well-constrained by additional time-delay data. When fitting either cosmology, we find the density profile exponent γ to be lower than expected, inconsistent with average observations of $\gamma \gtrsim 2$ [322].

4.3 H0LiCOW-style analysis

Whilst the use of SGL for statistical cosmology has been unable to accurately constrain cosmological parameters to physical values in the case of a global fit with a single spherical model, time-delay cosmography has been very successful in constraining the value of H_0 to around 2.4% precision within the standard ΛCDM paradigm by individually fitting a lens model to each lensing system studied [249].

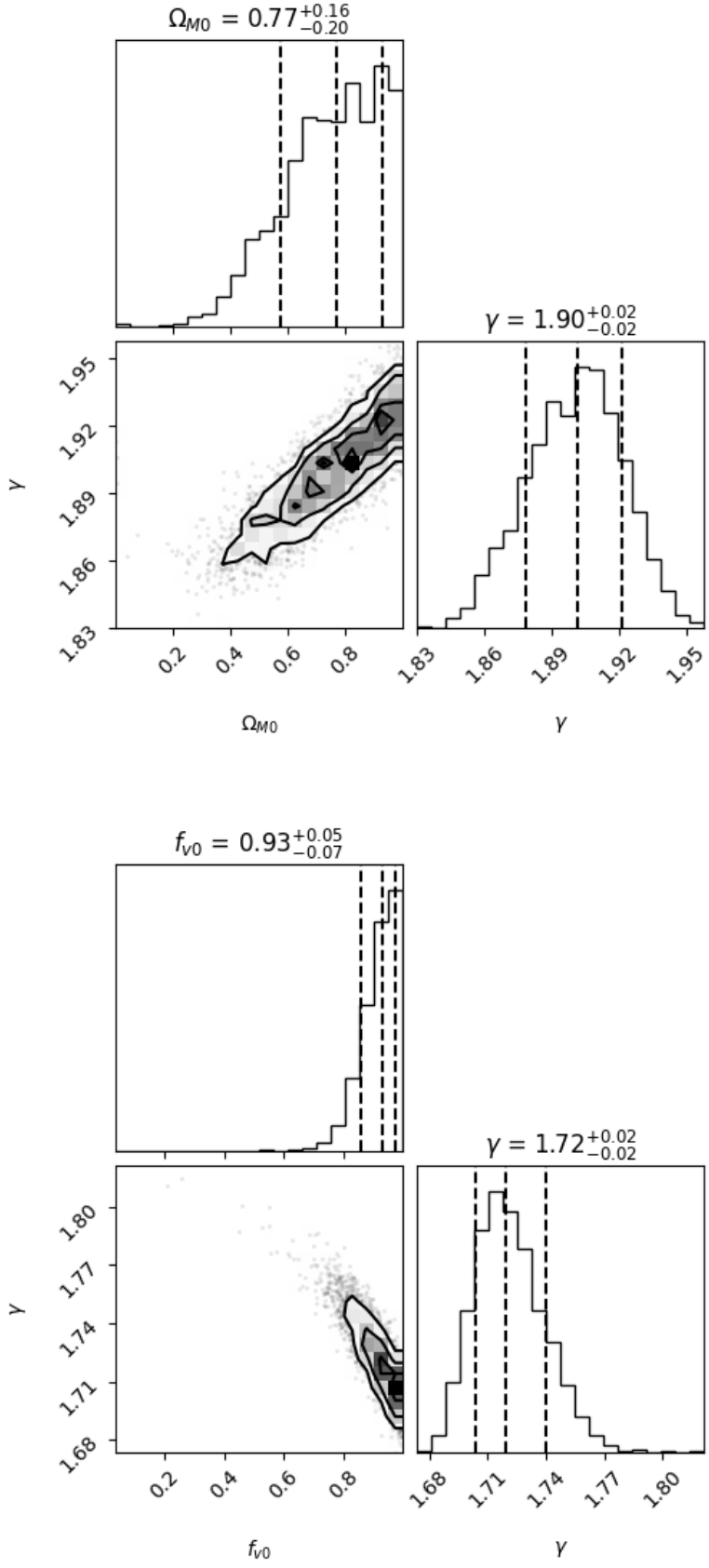

Figure 4.1: MCMC sampling results for a spatially flat FLRW cosmology (upper panel) and the timescape model (lower panel) using a spherical power-law lens model in Eq. (4.7).

This work has been expanded to include alternatives to ΛCDM, though consistently within cosmological models that assume a fixed global FLRW background [249]. Therefore, we use the same 6 lensing systems analysed by the H0LiCOW collaboration to constrain the equivalent H_0 in the timescape model, determine the dressed Hubble constant, and compare the BIC with previously studied ΛCDM variants. In this section, the distance posterior chains for each of the lenses are combined in the exact same joint analysis as in the work of Wong *et al.* [249] (referred to as H0LiCOW XIII henceforth), but with angular diameter distances given by the tracker solution of the timescape cosmology.

4.3.1 Lens sample

In line with the work of H0LiCOW XIII, the lens sample consists of 6 multiply imaged quasars by elliptical galaxies. The original 4 quad lenses are used from H0LiCOW I [250], with additional lenses SDSS 1206+4332 and PG 1115+080. Images of the lens sample used are presented in Fig. 4.2, taken directly from H0LiCOW XIII.

More recent studies such as in the TDCOSMO collaboration [257] include an additional lens to the H0LiCOW sample, DES 0408-5354. However, as H0LiCOW XIII provides the strongest constraints on H_0 and their analysis was easiest to adapt to include an equivalent timescape fit, we only consider the H0LiCOW sample. A further analysis for timescape including all known well-constrained time-delay lenses is warranted, but for this proof of concept, the 6 lenses given by H0LiCOW will be sufficient.

B1608+656

This is the first lensing system to have accurate time delays measured between each of the images to a high precision [323, 324]. It is the only lens in the H0LiCOW XIII sample with time delays measured independently of the COSMOGRAIL project. B1608+656 was discovered in the Cosmic Lens All-Sky Survey (CLASS) and is composed of two interacting lens galaxies [325]. The redshifts of the lens and source are $z_l = 0.6304$ and $z_s = 1.394$, respectively [326, 327]. The system shows a clear Einstein ring of the AGN host galaxy and whilst the individual images may not be apparent in the colour images produced in the optical and near-infrared observations from HST, they are clearly separable in the radio band. The two closely spaced images suggest that the strong lensing effect is due to the source object being positioned near a fold caustic, resulting in the observed quad configuration. The posterior distribution for the angular diameter distance to the lens galaxy are taken from Suyu *et al.* [325] and Jee *et al.* [328].

HE0435-1223

Wisotzki *et al.* [329] originally selected this system as a likely lensed quasar candidate from the Hamburg/ESO survey. The source quasar host galaxy aligns incredibly close to the line of sight through the lens object to give the familiar Einstein cross configuration, characteristic of (non-spherical) strong

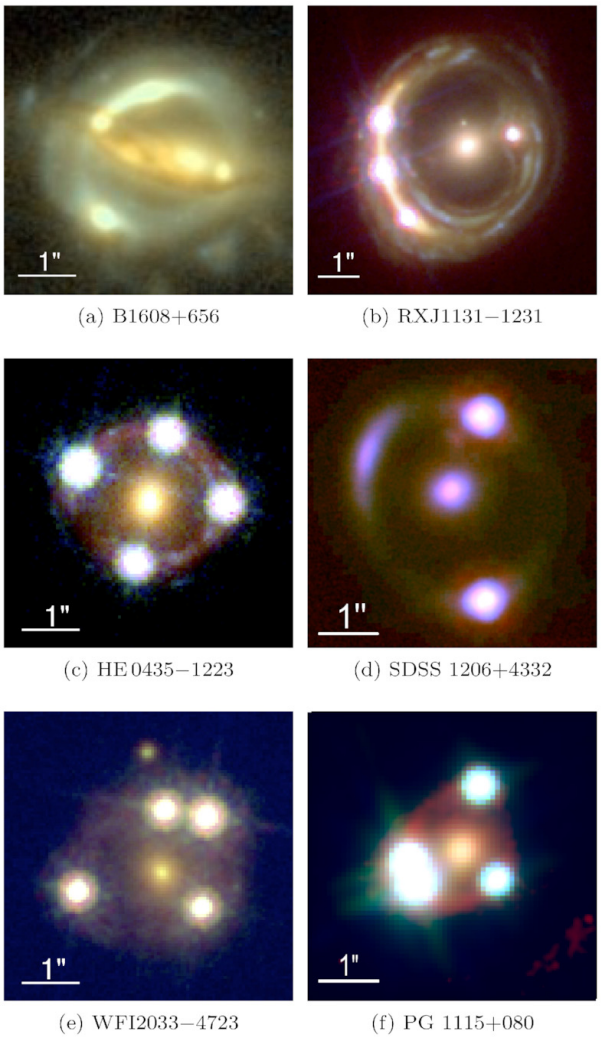

(a) B1608+656 (b) RXJ1131−1231

(c) HE 0435−1223 (d) SDSS 1206+4332

(e) WFI2033−4723 (f) PG 1115+080

Figure 4.2: Images of the six lensed quasars used in the H0LiCOW XIII analysis [249]. Images are created from observations from HST in the optical and near-infrared bands and/or with ground based adaptive optics data. The quad image configurations of B1608+656, HE0435-1223, RXJ1131-1231, and WFI2033-4723 are from the original H0LiCOW I sample [250].

gravitational lensing, where a clear elliptical ring is produced from the lensed quasar host galaxy. The lens and source objects are at redshifts $z_l = 0.454$ and $z_s = 1.693$, respectively [330, 331]. The distance posterior fit is given by Chen *et al.* [252] and Wong *et al.* [249].

PG1115+080

Originally discovered by Weymann *et al.* [332] as the second ever lensing system observed, follow-up observations with adaptive optics imaging from the Keck telescope and high resolution imagery from HST have been completed through the Strong lensing at High Angular Resolution Program (SHARP) so it could be included into later H0LiCOW analysis [252]. PG1115+080 is a quad lens system, exhibiting a fold configuration due to the image pair lying near the critical curve. The foreground lens is part of a galaxy group, with an individual redshift of $z_l = 0.3098$ [333]. The background source quasar and host

galaxy are at redshift $z_s = 1.722$ [333, 334]. The distance posterior distribution is taken from the work of Chen *et al.* [252] in the SHARP collaboration.

RXJ1131-1231

This system shows very clear multiply imaged quasars accompanying arclets of the lens host galaxy. The quad configuration observed from HST imagery displays a cusp configuration, identifiable from the three quasar images formed in close proximity. This system was first found by Sluse *et al.* [335] and the redshifts for lens and source objects identified as $z_l = 0.295$ and $z_s = 0.654$, respectively [335, 336]. Further studies of this system using adaptive optics were carried out to obtain the distance posteriors we use here from Chen *et al.* [252] and Suyu *et al.* [337].

SDSS 1206+4332

Oguri *et al.* [338] discovered this system in 2005. Through adaptive optics imagery using NIRC2 at the Keck Observatory, it was possible to constrain the lens to be a doubly-imaged quasar with a near-perfect Einstein ring. The redshift of the deflector galaxy was obtained via Keck-DEIMOS spectroscopy as $z_l = 0.745$ and the source quasar redshift as $z_s = 1.789$ [338, 339]. The distance posterior is given by Birrer *et al.* [253].

WFI2033-4723

This quad system was discovered by Morgan *et al.* [340] through a European Southern Observatory optical survey. The two images lying close to one another in the HST imagery indicate this is a fold lensing configuration. Multiple lens galaxies are found to be in the vicinity of the system, thus its lensing potential would be influenced by their presence. This is accounted for when considering the lens mass model of the foreground deflector galaxy, which is found at $z_l = 0.661$ [330]. The source quasar and associated host galaxy is found at redshift $z_s = 1.662$ [340]. The posterior distribution for the angular diameter distance is given by Chen *et al.* [252] and Rusu *et al.* [251].

4.3.2 Lens Modelling

The lens modeling identically follows the approach outlined in H0LiCOW XIII [249]. To fit the lens potential for each system, two parameterizations are used: the singular elliptical power-law model and a composite model. In the composite model, the dark matter halo is represented by an elliptical NFW profile, while the baryonic matter is mapped using the galaxy's luminosity profile and a mass-to-light ratio. The main codes implemented for lens modelling are GLEE [320], used for the majority of H0LiCOW lenses, and LENSTRONOMY for SDSS 1206+4332 [265].

The effect of line-of-sight perturbers on lensing is assessed using the "flexion shift" [341] influenced by mass, angular proximity to the lens, and redshift. For this reason, the analysis in H0LiCOW XIII

focuses on bright nearby galaxies found in spectroscopic surveys as contributing most to the external convergence affecting the lensing. Measurements of these perturbing galaxies' velocity dispersions are used to set priors on their associated Einstein radii. Alternatively, priors can be found from luminosity scaling. The spectroscopic data used in H0LiCOW XIII provides accurate redshifts for hundreds of galaxies spanning a wide area around the target lens object. This data is of additional use to determine galaxies' group and cluster membership, and define the effects from large significant structures along the line of sight (which are modelled as spherical NFW haloes). The galaxy number counts are compared with control surveys and ray tracing in the Millennium simulation [22, 342] to build a probability density function (PDF) of the external convergence. However, for the joint likelihood inference for the combined lens sample, non-cosmological parameters are marginalised as nuisance parameters.

4.3.3 Analysis

The posterior probability density function on model parameters is obtained by the product of the joint likelihood function and parameter priors. Using Bayes' theorem, we have

$$P(\boldsymbol{\xi}|\boldsymbol{d_{img}}, \boldsymbol{\Delta t}, \sigma, \boldsymbol{d_{los}}, \boldsymbol{A}) \propto P(\boldsymbol{d_{img}}, \boldsymbol{\Delta t}, \sigma, \boldsymbol{d_{los}}|\boldsymbol{\xi}, \boldsymbol{A})\, P(\boldsymbol{\xi}|\boldsymbol{A})\,, \tag{4.10}$$

where $\boldsymbol{\xi}$, $\boldsymbol{d_{img}}$, $\boldsymbol{\Delta t}$, σ, and $\boldsymbol{d_{los}}$ are the model parameters, imaging data, time delays, velocity dispersion, and line-of-sight information, respectively. $\boldsymbol{\xi}$ can be further broken down into cosmological parameters, $\boldsymbol{\pi}$, lens model parameters, $\boldsymbol{\nu}$, and further nuisance parameters of the external convergence, $\boldsymbol{\kappa_{ext}}$, and the anisotropic radius for stellar orbits, $\boldsymbol{\tau_{ani}}$. $\boldsymbol{A}$ represents the different modelling assumptions made in the set-up of the lens modelling, such as the precision of the reconstruction grid and the choice of deflector lensing potentials. These assumptions are varied to see their effect on $\boldsymbol{\xi}$, which is then incorporated into the weighting of different lens models in their inference.

The nuisance parameters are then marginalised over to give the posterior distribution of cosmological parameters alone,

$$P(\boldsymbol{\pi}|\boldsymbol{d_{img}}, \boldsymbol{\Delta t}, \sigma, \boldsymbol{d_{los}}) = \int \mathrm{d}\boldsymbol{\nu}\, \mathrm{d}\boldsymbol{\kappa_{ext}}\, \mathrm{d}\boldsymbol{\tau_{ani}}\, P(\boldsymbol{\xi}|\boldsymbol{d_{img}}, \boldsymbol{\Delta t}, \sigma, \boldsymbol{d_{los}})\,. \tag{4.11}$$

MCMC sampling is done to return the posterior distribution for each cosmological parameter with 32 walkers and 20000 samples. A full discussion of the analysis is given in the original H0LiCOW XIII article [249].

To compare cosmological models, we then find the maximum likelihood of the posterior distribution for each choice of cosmological parametrisation to compare with a Bayesian Information Criterion (BIC) as a test statistic,

$$\mathrm{BIC} = -2 \ln \mathcal{L}_{max} + k \ln n\,. \tag{4.12}$$

Here, $\mathcal{L}_{max}$ is the maximum likelihood, k is the number of model parameters, and n is the sample size,

which in our case is the number of lenses. The cosmologies investigated are listed in table 4.2 with their corresponding priors and BIC results.

Cosmology	**Description**	**Priors**	**BIC**	$\lvert\Delta\textbf{BIC}\rvert$
FΛCDM	Standard spatially flat ΛCDM	$H_0 \in (0, 150)$ $\Omega_{M0} \in (0.05, 0.5)$	135.39	2.32
Timescape	Timescape	$H_0 \in (0, 150)$ $f_{v0} \in (0.5, 0.99)$	135.18	2.11
oΛCDM	Open ΛCDM	$H_0 \in (0, 150)$ $\Omega_{M0} \in (0.05, 0.5)$ $\Omega_{k0} \in (-0.5, 0.5)$	134.15	1.08
FwCDM	Spatially flat wCDM	$H_0 \in (0, 150)$ $\Omega_{M0} \in (0.05, 0.5)$ $w \in (-2.5, 0.5)$	133.07	–
UΛCDM	ΛCDM with fixed Ω_{M0}	$H_0 \in (0, 150)$	133.40	0.33
w_0w_aCDM	Spatially flat w_0w_aCDM $w(z) = w_0 + w_a \frac{z}{1+z}$	$H_0 \in (0, 150)$ $\Omega_{M0} \in (0.05, 0.5)$ $w_0 \in (-2.5, 0.5)$ $w_a \in (-2, 2)$	134.77	1.70

Table 4.2: The BIC results and associated priors are presented for various cosmological models when fitting to the H0LiCOW dataset, following their analysis. In order, the cosmological models investigated are: spatially flat ΛCDM, timescape, open ΛCDM, spatially flat wCDM, spatially flat ΛCDM with a fixed $\Omega_{M0} = 0.3$ and dynamical dark energy w_0w_aCDM. The difference between BIC values and the best fit cosmology, FwCDM, are given in the furthest column right.

4.3.4 H0LiCOW results

When fitting a lens model individually to each system, taking into account the nuances of each system and the environment it is within, we find that physically plausible values of H_0 are found for both ΛCDM and timescape. In Fig. 4.3, we find the dressed Hubble parameter of the timescape model to be $H_0 = 76.9^{+2.9}_{-4.6}\,\mathrm{kms}^{-1}\mathrm{Mpc}^{-1}$; which is consistent with other late-universe probes within the standard cosmological paradigm. Nevertheless, comparisons between the two models based on parameters values are naïve, as whilst the dressed Hubble parameter is defined in such a way to emulate the ΛCDM counterpart, these parameters are not the same.

As seen in [249], the systems RXJ1131-1231 and PG 1115+080 give a higher probability to large H_0 values. However, it is difficult to make statements as to why with such a small sample size. In the original analysis, Bayes factors are found between each lens system in the sample by comparing their respective overlap in $D_{\Delta t}$ posteriors for a common set of cosmological parameters. It is found that the systems are consistent with one another and support the underlying hypothesis that they correspond to a realisation of the same set of cosmological parameters. We find that fitting solely a monopole in H_0 on the sky using these lenses is preferred to the addition of a dipole component. However, this is not statistically significant, with a $|\Delta\mathrm{BIC}| = 1.245$ in favour of the monopole fit. We would expect that local structure would cause variation in Hubble constant estimates across the sky though, as recent work

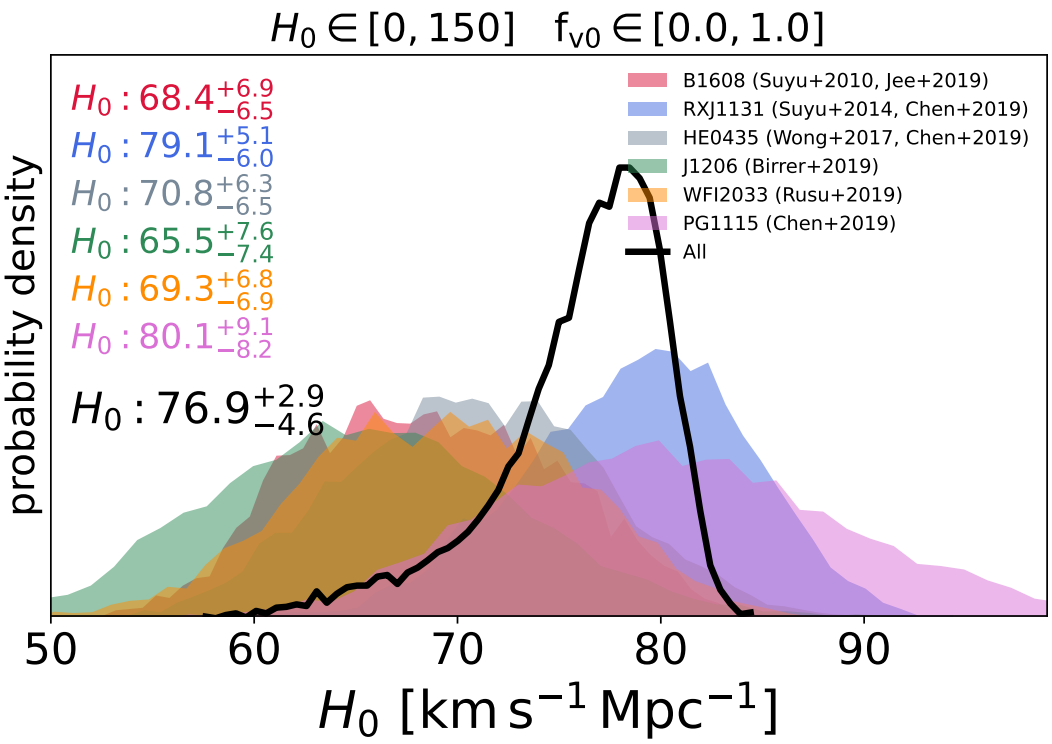

Figure 4.3: The dressed H_0 posterior distributions in the timescape model for each lensing system individually (the shaded and coloured regions), and combined as shown by the black line. Wide priors of $H_0 \in [0, 150]$ and $f_{v0} \in [0.0, 1.0]$ were applied.

from Williams *et al.* suggests [343], and it is interesting to note that the resulting dipole direction found is in line with many other cosmic dipoles, at $(278.7 \pm 24.9, 21.6 \pm 16.6)$ in galactic coordinates, (l,b). A full exploration of the variation of H_0 across the sky would require further well-constrained lenses with corresponding H_0 estimates to be able to understand the significance of the dipole (and quadrupole) derived from the distribution.

We compare the BIC between ΛCDM, timescape and other ΛCDM variants, which are listed in table 4.2. We see that spatially flat ΛCDM and timescape are statistically indistinguishable from one another, but, there is a weak preference for ΛCDM variants such as the spatially flat wCDM model (FwCDM), which gives the best fit to data. The best fit parameters of the FwCDM cosmology constrained by the H0LiCOW analysis are $w = -1.90^{+0.56}_{-0.41}$ and $H_0 = 81.6^{+4.9}_{-5.3}\,\mathrm{kms}^{-1}\mathrm{Mpc}^{-1}$ from time-delay cosmography alone; the full list of best parameter values is given in Table 6 of H0LiCOW XIII [249]. Other models have small $|\Delta\mathrm{BIC}|$ values compared to FwCDM, indicating no strong preference for one model over another. Higher precision data and a larger sample of lenses would be needed to statistically distinguish between them.

4.4 Conclusions

It is plain to see that fitting a global lens model to the entire catalogue of lensing systems leads to unphysical cosmological results that cannot be resolved by the extra inclusion of time-delay data. Whilst the number of systems with additional time-delay data is relatively small, the analysis presented in this chapter already shows clear convergence to unphysical cosmological parameters. Further extending the time-delay lens catalogue with more observed systems would likely not be sufficient to return plausible values, without addressing the implementation of the lens models across the variety of systems. Therefore, we find that it is not possible to use this technique to distinguish cosmological models and it cannot be applied to give evidence for one model over another in a self-consistent manner. Despite this, many studies apply globally fit spherically symmetric power-law lens models to entire catalogues of systems in their analyses [215, 273, 274, 276, 317, 344–351]. This is problematic as whilst these lens models may appropriately describe the average elliptical galaxies *mass distribution*, it is not necessarily true they represent the average *lensing effects*. Each individual galaxy will exhibit lensing properties that deviate dramatically from those of the average model, due to their ellipticity. For example, the quad image configuration of an Einstein cross cannot be produced by a spherically symmetric lens mass distribution alone.

However, TD cosmography has been very successful in constraining the value of H_0 to around 2.4% precision within the standard ΛCDM paradigm by individually fitting a lens model to each lensing system studied [249]. We find a more nuanced analysis of a select number of lens systems, with high resolution imagery, can well constrain the dressed Hubble parameter in the timescape cosmology, giving a value of $H_0 = 76.9^{+2.9}_{-4.6}\,\mathrm{km\,s^{-1}Mpc^{-1}}$. The maximum likelihood corresponding to the best fit cosmological parameters is used in a BIC comparison between multiple different cosmologies. The preferred cosmology is wCDM, the standard spatially flat FLRW background but with an equation of state parameter for dark energy $w \neq -1$. In fact, the preferred value found for the equation of state parameter is $w = -1.90^{+0.56}_{-0.41}$ which crosses the phantom line.

The preference for $wCDM$ is weak compared to other cosmologies studied. The timescape cosmology is found to be statistically indistinguishable from the standard spatially flat ΛCDM model. Given both lens and source objects are far beyond the scale of statistical homogeneity, it is unsurprising that both models return very similar results (see the Bayes factor comparison at different redshift cuts for the Pantheon+ supernova analysis [352]). Due to the small differences between timescape and ΛCDM, more data is required in order to separate them. However, we have shown that strong gravitational lensing has the potential to distinguish between cosmological models, when individually fitting the lens potential, rather than applying a global lens model across a catalogue of systems. Although this is more labour-intensive, it is necessary that each lens system has follow-up high resolution imagery and accurate time-delay measurements, in order to be used appropriately for cosmological purposes. Upcoming surveys (such as JWST and Roman) could soon make this a viable cosmological test in future.

Chapter 5

Gravitational Lensing By Disc Galaxies in MOND

The work in this chapter has been submitted to the *Astrophysical Journal* as 'A Novel Test for MOND: Gravitational Lensing by Disc Gaalxies' by Christopher Harvey-Hawes and Marco Galoppo.

5.1 Introduction to Spiral Galaxy Lensing

The dark matter (DM) hypothesis is an essential element of the standard cosmological model, Λ Cold Dark Matter (ΛCDM) [see e.g., 28]. DM was originally introduced to explain the observed rotation curves of disc galaxies [32–34]: both the lack of the expected quasi-Keplerian fall-off in the rotational velocity curve at large distances and the rotational velocity amplitudes pointed to an additional but invisible source of gravity, i.e., DM.

DM can successfully explain a plethora of astrophysical and cosmological observations, such as the cosmic microwave background power spectrum [29] and gravitational lensing by galaxies and galaxy clusters [see e.g., 223, 353]. In particular, DM halos are believed to dominate strong gravitational lensing (SGL) by galaxies [219].

However, the results of the many experiments aimed at the direct detection of DM particles are, to date, inconclusive [see, e.g., 354–356]. Furthermore, in the past two decades, the very nature of DM has become a point of strong debate within the scientific community [357, 358].

Various alternative explanations of astrophysical observations have been proposed in the form of novel theories of gravity: modified gravity [MoG, 143, 144], fractional gravity [140, 141], rainbow gravity [147], emergent gravity [137, 138], postquantum classical gravity [145, 146], $f(R)$ gravities [139], among others, as well as general relativistic models of disc galaxies [359–362].

Any viable alternative to DM must explain the phenomena naturally understood within the standard DM paradigm. Furthermore, observational procedures must be designed to differentiate between the many theories now present in the literature, and rule out those which do not match the observations. In

this regard, disc galaxies represent an ideal laboratory to design tests to investigate DM, and differentiate it from its alternatives. Indeed, we recall that in recent years the coupling of dynamics and SGL data in massive disc galaxies has already been used, on the few systems observed, to accurately probe the nature of DM [268, 320, 363].

In this work, we investigate inclination effects in disc galaxy SGL in the MOdified Newtonian Dynamics [MOND, 190] scenario (see e.g., [191], and [364] for reviews). To date, MOND represents the most widely studied alternative to the DM paradigm as it has been shown to successfully explain a plethora of astrophysical observations, such as kinematics of galaxies [191, 200], dynamics of wide binary stars [201, 202], radial acceleration relation of galaxies [RAR, 203, 204], orbital velocity of interacting galaxy pairs [205], early-universe galaxy and cluster formation [206], and galaxy-scale gravitational lensing [207, 208].

In the Lagrangian formulation of MOND by Bekenstein [365], referred to as AQUAL, the linear Poisson equation linking the Newtonian gravitational potential, $\Phi_{\rm N}$, to the matter density, ρ, i.e.,

$$\Delta\Phi_{\rm N} = 4\pi G\rho\,, \tag{5.1}$$

is replaced by the non-linear partial differential equation (PDE)

$$\boldsymbol{\nabla}\cdot(\mu(x)\boldsymbol{\nabla}\Phi_{\rm M}) = 4\pi G\rho\,, \tag{5.2}$$

where $x = ||\boldsymbol{\nabla}\Phi_{\rm M}||/a_0$, $a_0 \approx 1.2\times10^{-13}$ km/s^2 is the MOND universal acceleration scale [191], $\Phi_{\rm M}$ is the Milgromian gravitational potential and $\mu(x)$ is the MOND interpolating function, with the asymptotic limit behaviours

$$\mu(x) \approx \begin{cases} 1, & x \gg 1, \\ x, & x \ll 1. \end{cases} \tag{5.3}$$

Eqn. (5.3) then implies that for $||\boldsymbol{\nabla}\Phi_{\rm M}|| \gg a_0$, Eqn. (5.2) reduces to (5.1), and MOND recovers the standard Newtonian regime, whilst for $||\boldsymbol{\nabla}\Phi_{\rm M}|| \ll a_0$ one obtains the deep MOND (dMOND) regime, practically defined by

$$\boldsymbol{\nabla}\cdot(||\boldsymbol{\nabla}\Phi_{\rm M}||\,\boldsymbol{\nabla}\Phi_{\rm M}) = 4\pi G\rho\, a_0\,. \tag{5.4}$$

The extent to which MOND effects dominate an astrophysical system can be roughly gauged by evaluating [191, 364]

$$\kappa = \frac{GM}{r_c^2\, a_0}\,, \tag{5.5}$$

where M is the system mass and r_c is the typical scale length of the system. When $\kappa \gg 1$ the system is in a Newtonian regime, whilst for $\kappa \ll 1$ dMOND applies. In particular, we recall that for disc galaxies $\kappa \approx 1$, so that these require the full use of Eqn. (5.2) to be described within the MOND scenario.

We note that for every astrophysical system modelled through MOND, it is possible to construct

the equivalent Newtonian system (ENS), i.e., a system with the same baryonic matter density, $\rho_{\rm B}$, supplemented by an additional halo of phantom dark matter (PDM), with density profile $\rho_{\rm ph}$, such that $\Phi_{\rm N} = \Phi_{\rm M}$ throughout the physical system. In the AQUAL formulation of MOND, the construction of an ENS is a complex task due to the highly non-linear nature of Eqn. (5.2).

However, [366] constructed a different formulation of MOND which allows for a more direct approach to building ENS, i.e., quasi-linear MOND (hereafter QUMOND). QUMOND essentially relies on an approximation of Eqn. (5.2) in which $\Phi_{\rm M}$ is replaced by $\Phi_{\rm N}$. By this approach QUMOND involves only the solution of linear PDEs, with only non-linear algebraic steps. Indeed, in QUMOND, the Milgromian gravitational potential now solves for

$$\Delta\Phi_{\rm M} = 4\pi G \left[\rho_{\rm B} + \rho_{\rm ph}\right] , \tag{5.6}$$

where $\rho_{\rm ph}$ is given by

$$\rho_{\rm ph} = \frac{1}{4\pi G}\boldsymbol{\nabla}\cdot\left[\tilde{\nu}(y)\boldsymbol{\nabla}\Phi_{\rm N}\right] , \tag{5.7}$$

where $y = ||\boldsymbol{\nabla}\Phi_{\rm N}||/\,a_0$, and $\tilde{\nu}(y)$ has as asymptotic limiting behaviour

$$\tilde{\nu}(y) \approx \begin{cases} 0, & y \gg 1, \\ y^{-1/2}, & y \ll 1. \end{cases} \tag{5.8}$$

Therefore, within the QUMOND approach, given $\rho_{\rm B}$, the ENS is straightforwardly built by **(i)** first solving the classical Poisson equation for the baryonic matter, which becomes the source of $\rho_{\rm ph}$ via a non-linear algebraic procedure involving $\tilde{\nu}$; **(ii)** then by solving once more the Poisson equation for $\rho = \rho_{\rm B} + \rho_{\rm ph}$.

Here, we stress that the PDM is not constituted by real particles, and thus does not lead to dynamical dissipation or friction [191, 367, 368]. Furthermore, we note that the PDM density can become negative locally and, although it will respect the symmetries of the baryonic distribution, it can present shifts in its concentration peaks w.r.t. the former. In particular, for flattened matter distributions such as disc galaxies, the local positivity of $\rho_{\rm ph}$ is not assured, nor is the correspondence between the peak of baryonic density and of PDM [369–373]. Through the use of the ENS, one can study lensing of disc galaxies in MOND, whilst utilising the tools constructed for classical SGL within the ΛCDM paradigm. This allows us to bypass a series of difficulties in the study of SGL within MOND, e.g., the definition of the thin lens approximation, commonly employed for galaxy-scale SGL [374]. Furthermore, the ENS allows us to probe the Newtonian limit and "transition" regime of MOND in SGL, whilst naturally accounting for the impossibility of SGL in the dMOND limit [see e.g., 375].

In this paper, we investigate inclination effects on the observables of SGL for disc galaxies, e.g., SGL cross section, within the MOND scenario. We draw comparison to known results on disc galaxy lensing in ΛCDM, and we show that: **(i)** the number count of disc galaxy lenses predicted by MOND exceeds

the one expected in the DM scenario, and **(ii)** in MOND disc galaxy lensing the inclination effects are enhanced w.r.t. the DM halo paradigm. With the upcoming optical surveys, LSST, DES and Euclid, these differences in the inclination effects and overall lens number counts will become statistically detectable in SGL of disc galaxies, as these surveys are predicted to observe hundreds of thousands of galaxy-scale lenses [270, 376]. Thus, we propose that, in the next decade, statistical studies on the inclination and number of disc galaxy lenses will lead to an important direct test to differentiate cold DM from MOND.

Here, we focus on disc galaxies as isolated systems, assuming no interfering matter along the line of sight. This is a typical practice in studies of SGL on galaxy scales, where matter contributing to the lens effect from outside the lens galaxy is modelled by fitting an external convergence parameter, often in combination with weak lensing measurements [see e.g., 377, 378]. However, we note that due to external field effects (EFE) in the MOND paradigm the assumption of an isolated system is ultimately a stronger requirement than in the DM scenario [191, 364]. Indeed, due to the non-linear nature of the MOND field equation (cf., Eqs. (5.2) and (5.6)), the presence of external matter non-trivially influences the internal gravitational field of the lens itself. Therefore, our study will be directly applicable to highly isolated disc galaxies, whilst case-by-case corrections for EFE will have to be considered for SGL within clusters and more nuanced environments.

Throughout this paper, we assume a spatially flat ΛCDM cosmology, with matter density $\Omega_{\rm M0} = 0.3$ and Hubble constant $H_0 = 70\,{\rm km\,s^{-1}Mpc^{-1}}$, as a background cosmological model, with lens and source placed at redshift $z_{\rm L} = 0.5$ and $z_{\rm S} = 2.0$, respectively. We note that assuming a spatially flat ΛCDM cosmology is not at odds with a MOND description of disc galaxies. Indeed, even if MOND were to be ultimately correct, its relativistic extension would have to closely match the cosmological evolution predicted by the highly tested ΛCDM model. Therefore, employing ΛCDM as a cosmological model within a MOND scenario at the galactic scales can be directly understood as a good first-order approximation to the possible choice of a correct, and yet unknown, MOND cosmology [191, 364].

The rest of the paper is structured as follows. In Section 5.2 we recall the SGL fundamentals and derive the observables used to probe inclination effects in disc galaxy SGL. In Section 5.3 we define the analytic baryon density distribution for the disc galaxy models, and we derive the respective PDM distribution for realistic templates of such galaxies. In Section 5.4 we report our results, focusing on the effect of disc galaxy inclination on SGL cross sections and draw comparison to the DM scenario. Finally, Section 5.5 is dedicated to conclusions and future perspectives.

5.2 Strong Gravitational Lensing

For a given density distribution, in the weak-field limit of gravitational fields, the deflection angle of a light ray propagating perpendicular to the plane of the lens, $\vec{\hat{\alpha}}$, is defined as[1]

$$\vec{\hat{\alpha}}(\xi_1, \xi_2) := \frac{2}{c^2} \int_{-\infty}^{\infty} \mathrm{d}\xi_3 \, \vec{a}_{\perp}(\vec{\xi}) \,. \tag{5.9}$$

Here, $\vec{a}_{\perp}$ denotes the acceleration due to the gravitational potential of the lens object along the lens plane, i.e.,

$$\vec{a}_{\perp} = -\vec{\nabla}_{\perp} \Phi_{\mathrm{N}} \,, \tag{5.10}$$

with

$$\Phi_{\mathrm{N}}(\vec{\xi}) = G \iiint \frac{\rho(\vec{r})}{|\vec{\xi} - \vec{r}|} \, \mathrm{d}^3\vec{r} \,. \tag{5.11}$$

It is important to stress that the lens plane lies orthogonal to the line of sight from the observer to the lens and thus, it is not dependent on the inclination of the lens itself (see Fig. 5.1). Therefore, the inclination of a disc galaxy will have a large impact on its lensing, which is derived from the projection of its baryonic matter content onto the lens plane. Here, we note that in the presence of (almost) spherical DM halos, the inclination effects of disc lenses, although still clearly present, are partially suppressed by the role played by the DM in the lensing phenomena [379]. However, we do not expect such a situation in MOND, where no DM halos are present and the lensing is driven solely by the baryonic disc.

We note that by employing Eqns (5.9)-(5.11) coupled to the ENS of the disc galaxy's gravitational potential, SGL in MOND is then easily integrated into the usual lensing formalism, with Φ_{M} in place of the classical Newtonian potential Φ_{N}.

We can now follow the standard lensing formalism [see e.g., 219, 221] to define the lens equation

$$\vec{\beta} = \vec{\theta} - \frac{D_{LS}}{D_S} \vec{\hat{\alpha}} \, (\vec{\theta}) = \vec{\theta} - \vec{\alpha}(\vec{\theta}) \,, \tag{5.12}$$

where $\vec{\beta}$ and $\vec{\theta}$, respectively, describe the angular position w.r.t. to the lens centre of the source object and of the lensed images. Moreover, D_{LS} and D_S represent the angular diameter distances from the lens to the source and from the observer to the source. Fig. 5.1 depicts the lensing configuration under study. Then, from (5.12) we can define the Jacobian matrix $\mathcal{A}$,

$$\mathcal{A} = \frac{\partial \vec{\beta}}{\partial \vec{\theta}} = \mathbf{1} - \boldsymbol{\nabla} \vec{\alpha} \,. \tag{5.13}$$

The critical curves for the lens configuration are defined as the positions where the magnification, $\mu := 1/\det \mathcal{A}$, is formally infinite (for a point source). We note that it is, however, generally convenient to determine critical curves directly from the condition $\det \mathcal{A} = 0$. Then, we can use the lens equation

[1] Employing (5.9) implies a restriction on the possible choice of the a priori unknown relativistic MOND extension. Indeed, we are assuming that the lensing potential is twice the Newtonian potential in the weak-field regime, as in general relativity. See, e.g., [192] for such a theory.

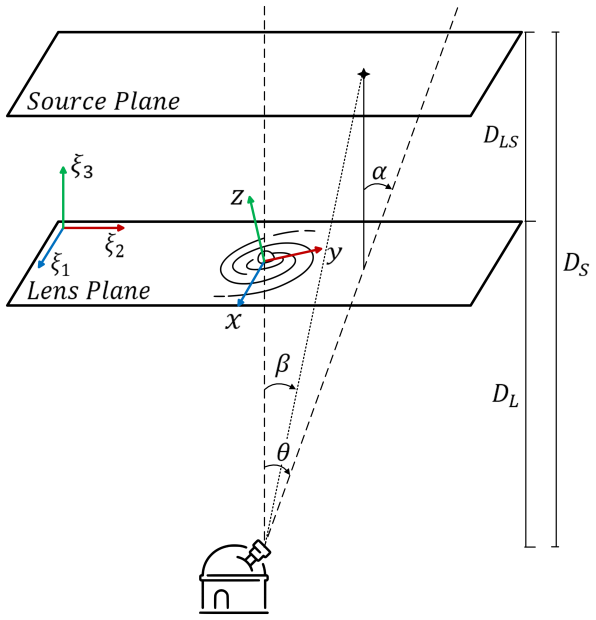

Figure 5.1: Lensing configuration for SGL by a disc galaxy. We report source, lens and observer positions, as well as the relevant angles and coordinate systems. Here, α is the deflection angle, β is the angular source position and θ is the angular image position.

(5.12) to project the critical curves back onto caustic curves on the source plane.

The position of a source object with respect to the caustic lines determines the number of images produced and their respective positions. Objects within caustic lines will produce multiple images, and thus, the area enclosed by caustic lines on the source plane defines the lensing cross section σ [219, 221]. We note that whilst the lensing cross section is a survey-independent quantity, the likelihood of observing SGL is not. The latter, although directly proportional to the former, will be influenced by the specific observations carried out [270, 380]. Therefore, to characterise the inclination effects of disc galaxies in MOND we only consider σ as an indirect measure of SGL likelihood and do not specialise to any specific surveys.

Finally, in this paper, we focus on point sources. Extended sources will have higher lensing likelihood, but for the purposes of determining the differences between lensing effects for different disc galaxy mass profiles and inclination effects, considering point-like sources is sufficient.

5.3 Matter density profiles

To describe the baryonic component of disc galaxies, we couple a thick exponential disc to a spherical bulge, such that $\rho_{\rm B} = \rho_{\rm b} + \rho_{\rm d}$, where $\rho_{\rm b}$ and $\rho_{\rm d}$ are the densities of the bulge and the disc, respectively.

5.3.1 Analytical baryonic matter density modelling

The spherical bulge component is well described by the Plummer density profile [381]

$$\rho_{\rm b}(r) = \frac{3r_{\rm b}^2 M_{\rm b}}{4\pi \left(r^2 + r_{\rm b}^2\right)^{5/2}}\,, \tag{5.14}$$

where r is the spherical radius, $r_{\rm b}$ is the scale parameter of the bulge and $M_{\rm b}$ is the total bulge mass. The baryonic disc matter distribution is conventionally taken as $\rho_{\rm d}(R,z) = \Sigma(R)\,Z(z)$, where R is the cylindrical radius and z is the axial coordinate. Then, the surface density of the disc is well approximated by the exponential profile [see e.g., 382]

$$\Sigma(R) = \frac{M_{\rm d}}{2\pi R_{\rm d}^2} e^{-R/R_{\rm d}}\,, \tag{5.15}$$

where $M_{\rm d}$ is the total disc mass and $R_{\rm d}$ is the scale length in the radial direction for the galactic disc. The distribution along z, such that $\int Z(z)\,{\rm d}z = 1$, can be defined as [382]

$$Z(z) = \frac{1}{2z_{\rm d}} e^{-|z|/z_{\rm d}}\,, \tag{5.16}$$

where $z_{\rm d}$ is the thickness scale length of the disc galaxy. In separating the density profile in this way, we have assumed that the disc has a scale height that is constant with radius, as is observed in the photometry of local edge-on disc galaxies [383, 384]. Thus, we have

$$\rho_{\rm d}(R,z) = \frac{M_{\rm d}}{2\pi R_{\rm d}^2 z_{\rm d}} e^{-R/R_{\rm d}} e^{-|z|/z_{\rm d}}\,. \tag{5.17}$$

We recall that in the pioneering work of [379] on SGL by disc galaxies within the ΛCDM paradigm, the baryonic disc component was approximated either by Mestel [385] or Kuzmin discs [386] within a softened, oblate isothermal DM halo[2]. Moreover, similar chameleon profiles were employed to combine dynamical and SGL data for disc galaxies in the more recent studies by [268] and [320], as well as in the first consideration of non-spherical lenses in MOND [389]. These profiles have been preferred to fully exponential mass distributions for the disc component due to their analytical properties in SGL computation [268, 320, 379, 389].

In MOND the lensing is entirely defined by the baryonic components of the galaxies, as no DM is required. Thus the morphological characteristics of the baryons in disc galaxies are more important in MOND than for cold DM scenarios. Furthermore, as already discussed by [379], Mestel and Kuzmin discs represent a poor fit for the vertical component of the baryonic disc and can only be a first approximation for the exponential radial profile. Hence, to avoid biases in the inclination effects in MOND, we chose to maintain a closer match to observational data for the mass density profile modelling of disc galaxies and implement a realistic exponential disc profile coupled to a spherical bulge.

[2]We note that in the papers by [387] and [388], uniform discs were considered for modelling the lens effect of a disc galaxy. However, due to the uniform assumption, and as noted by [379], these cannot produce realistic rotation curves and do not depict actual three-dimensional density profiles of disc galaxies.

5.3.2 Realistic disc galaxy model parameters

Once the baryonic mass profile has been defined, we have to pick meaningful values for the parameters so that the resulting disc galaxy models can be understood to be a good representation of observational data.

Following [379] we consider a massive spiral galaxy with a maximal disc, such that DM (or MOND) effects play a major role only in the outer kinematics of the galaxy. We therefore select a massive disc galaxy with $M_{\rm d} = 10^{11}\,{\rm M}_{\odot}$, and $R_{\rm d} = 3.5\,{\rm kpc}$. We then consider three possible values for $z_{\rm d}$, namely $z_{\rm d} \in \{0.35, 0.105, 0.035\}$ kpc, so that the ratio $z_{\rm d}/R_{\rm d} \in \{0.1, 0.03, 0.01\}$ as chosen by [379], thus facilitating comparisons.

We must also select appropriate values for $M_{\rm b}$ and $r_{\rm b}$. We note that correlations between $M_{\rm b}$, $r_{\rm b}$ and the disc parameters have been established in the literature [see, e.g., 390–392]. However, these are better understood for low-mass spirals and, given the plethora of disc galaxy morphologies, these correlations produce only weak constraints on the bulge parameters once the disc has been selected. Therefore, in our analysis, we selected $M_{\rm b}/M_{\rm d} \in \{0.01, 0.1, 0.2\}$ and $r_{\rm b}/R_{\rm d} \in \{0.03, 0.1, 0.2\}$.

Finally, we point out that our choice of following [379] in studying SGL by disc galaxies only in massive spirals is well justified by noting that the likelihood of SGL increases with the mass. Therefore, the low-mass spirals are not expected to significantly contribute to the population of disc galaxy lenses, even in the upcoming optical surveys.

5.3.3 Equivalent Newtonian system

To build the ENS corresponding to our choice of $\rho_{\rm B} = \rho_{\rm d} + \rho_{\rm b}$ we exploit the linearity of Poisson equation, so that

$$\Phi_{\rm N} = \Phi_{\rm N,d} + \Phi_{\rm N,b}\,, \tag{5.18}$$

where $\Phi_{\rm N,d}$ and $\Phi_{\rm N,b}$ are the Newtonian gravitational potentials generated by the exponential disc and the spherical bulge, respectively. We can directly calculate the two potentials by solving Eq. (5.1) with (5.14) and (5.17) as sources. We then obtain

$$\Phi_{\rm N,d}(R,z) = -GM_{\rm d}\int_0^\infty {\rm d}k \frac{J_0(Rk)\left(e^{-|z|k} - z_{\rm d}ke^{-|z|/z_{\rm d}}\right)}{\left(1+R_{\rm d}^2k^2\right)^{3/2}\left(1-z_{\rm d}^2k^2\right)}\,, \tag{5.19}$$

$$\Phi_{\rm N,b}(r) = \frac{GM_{\rm b}}{r_{\rm b}}\left(1 - \frac{r_{\rm b}}{\sqrt{r_{\rm b}^2+r^2}}\right)\,, \tag{5.20}$$

where J_0 is the Bessel function of the first kind. We can now directly calculate $\boldsymbol{\nabla}\Phi_{\rm N}$ and exploit Eq. (5.7) to obtain $\rho_{\rm ph}$ once we have chosen a functional form for the interpolating function $\tilde{\nu}$. In this work, we

implement the same functional form used in the Phantom of Ramses code for N-body and hydrodynamical simulations in the MOND scenario[3][393, 394], i.e.,

$$\tilde{\nu}(y) = -\frac{1}{2} + \sqrt{\frac{1}{4} + \frac{1}{y}}\,. \tag{5.21}$$

Here, it is important to note that whilst studies of disc galaxy rotation curves are quite robust w.r.t. the choice of interpolating function (due to the onset of the dMOND regime), in SGL this choice is highly non-trivial. Indeed, SGL effects probe the full spectrum of applicability of MOND and thus will be affected by the choice of $\tilde{\nu}$[4]. In this paper, we have chosen the widely adopted form of interpolating function of Eqn. (5.21) as it has been proven to give a MOND realisation able to pass a variety of observational tests [191], and it is widely employed in the study of in-galaxy dynamics within the MOND scenario [see e.g., 397, 398]. However, we caution that the results may change with different choices of the interpolating function, as already noted in previous SGL MOND studies [see, e.g., 399].

In Fig. 5.2 we show as an example, the distribution of PDM from an edge-on and face-on point of view for a disc galaxy with $M_{\rm d} = 10^{11}\,{\rm M}_{\odot}$, $R_{\rm d} = 3.5\,{\rm kpc}$, $z_{\rm d} = 0.35\,{\rm kpc}$, $M_{\rm b} = 10^{9}\,{\rm M}_{\odot}$, and $r_{\rm b} = 0.7\,{\rm kpc}$. For the same galaxy, in Fig. 5.3 we show the ratio of the baryon density to the PDM density, $\rho_{\rm B}/\rho_{\rm ph}$, along the radial direction on the equatorial plane, and the corresponding two-dimensional distribution in the $x - z$ plane within a scale height of the galactic disc. From Fig. 5.2 we note that the resulting PDM distribution follows the same symmetries of the underlying baryonic matter, as we should expect from Eqn. (5.7). We find it to be always positive definite and with no peak shift in its concentration w.r.t. the baryons. Moreover, we recover the superimposed disc-halo PDM morphology shown in previous studies [see e.g., 394].

Finally, from Fig. 5.3 we see that the PDM overtakes the baryonic matter as the dominant "matter", component within the very core of the galaxy (below the parsec level) and at large distances from the galactic centre (i.e., approximately at 15 kpc), precisely where we would expect MOND (or DM) effects to dominate the dynamics for this type of galaxy. The excess of the PDM over the baryons within the centre of the disc galaxy indicates the presence of a cusp in the PDM distribution. We note that such behaviour is not related to the specific choice of interpolating function, as the centre of the galaxy is in a dMOND regime, but relates to the interplay of the latter with the baryon density profile. This is can be shown analytically for the Plummer model of the bulge. From Eq. (5.21), we write

$$\lim_{r\to 0} \tilde{\nu} \approx y^{-1/2} = \left(\frac{|\partial_r \Phi_{N,b}|}{a_0}\right)^{-1/2}, \tag{5.22}$$

[3]Here, we have implemented an original routine to derive the PDM distribution and the SGL effect of the disc galaxies. The codes implemented are available at https://github.com/chrisharhaw/MOND_lensing.git. Moreover, we give a description of these codes in Appendix A.

[4]To test the dependence of our results on the choice of interpolating function, in Appendix B we show a comparison of our main results with those obtained with the RAR interpolating function [see e.g., 395, 396]. We find only marginal differences w.r.t. the results obtained for $\tilde{\nu}$ given in Eq. (5.21).

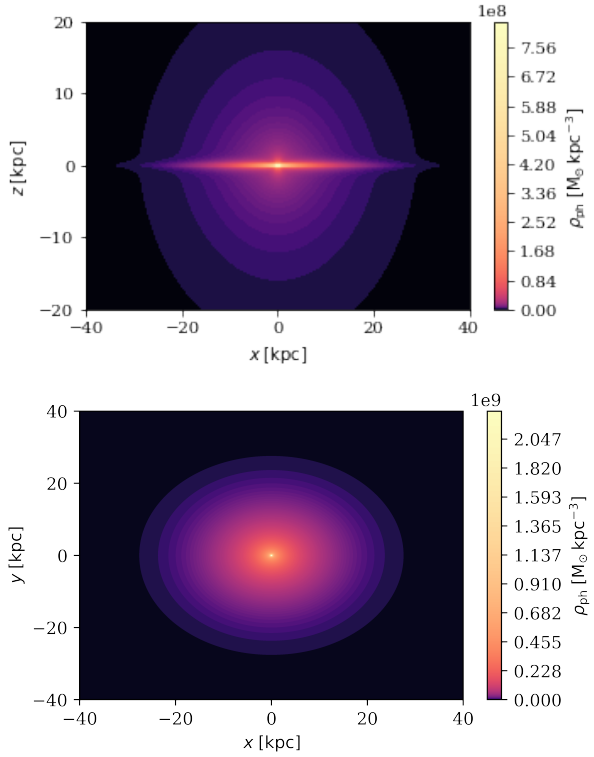

Figure 5.2: PDM density distribution on the $x-z$ plane (upper panel) and on the $x-y$ plane (lower panel) for a disc galaxy with $M_{\rm d} = 10^{11}\,{\rm M}_\odot$, $R_{\rm d} = 3.5\,{\rm kpc}$, $z_{\rm d} = 0.35\,{\rm kpc}$, $M_{\rm b} = 10^{9}\,{\rm M}_\odot$, and $r_{\rm b} = 0.7\,{\rm kpc}$. A log-scale is used for the density to highlight the morphology of the PDM distribution.

and from Eq. (5.20),

$$|\partial_r \Phi_{N,b}|_{|r\to 0} \approx \left(\frac{GM_{\rm b}}{r_{\rm b}^3}\right) r\,. \tag{5.23}$$

Therefore, by expanding Eq. (5.7) we find

$$\rho_{\rm ph,b}(r) = \frac{1}{4\pi G}\frac{d\tilde{v}}{dy}\left(\vec{\nabla} y\cdot\vec{\nabla}\Phi_{\rm N,b}\right) + \tilde{v}(y)\rho_{\rm b}(r)\,, \tag{5.24}$$

$$\rho_{\rm ph,b}(0) \approx -\frac{1}{8\pi G} y^{-3/2}\left(\vec{\nabla} y\cdot\vec{\nabla}\Phi_{\rm N,b}\right) + y^{-1/2}\rho_{\rm b}(0) \tag{5.25}$$

$$= -\frac{1}{8\pi\sqrt{r}}\left(\frac{a_0 M_{\rm b}}{G r_{\rm b}^3}\right)^{1/2} + \frac{3}{4\pi\sqrt{r}}\left(\frac{a_0 M_{\rm b}}{G r_{\rm b}^3}\right)^{1/2} \tag{5.26}$$

$$= \frac{5}{8\pi}\left(\frac{a_0 M_{\rm b}}{G r_{\rm b}^3}\right)^{1/2}\left(\frac{1}{\sqrt{r}}\right)_{|r\to 0} \longrightarrow +\infty\,, \tag{5.27}$$

taking $r \approx 0$ and employing Eq. (5.14). Thus, we see a central cusp in the PDM distribution which is a feature shared by any interpolating function which correctly encodes the dMOND limit.

5.4 Results

In Fig. 5.4 we show an example of the deflection angle magnitude, α, the magnification, μ, and the shear, γ, for the example of a massive disc galaxy with $M_{\rm d} = 10^{11}\,{\rm M}_\odot$, $R_{\rm d} = 3.5\,{\rm kpc}$, $z_{\rm d} = 0.35\,{\rm kpc}$,

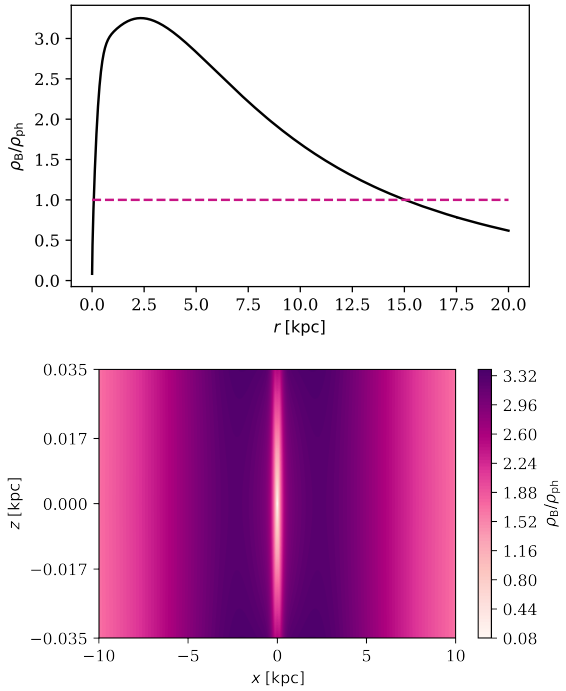

Figure 5.3: Ratio of the baryon density to the PDM density, ρ_B/ρ_{ph}, along the radial direction on the equatorial plane (top panel), and the corresponding two-dimensional distribution in the $x-z$ plane within a scale height of the galactic disc (bottom panel) for a disc galaxy with $M_d = 10^{11}\,M_\odot$, $R_d = 3.5\,\text{kpc}$, $z_d = 0.35\,\text{kpc}$, $M_b = 10^9\,M_\odot$, and $r_b = 0.7\,\text{kpc}$. The purple dashed line in the top panel highlights the point at which the two densities have the same value.

$M_b = 10^9\,M_\odot$, $r_b = 0.7\,\text{kpc}$ and $i = 0°$, $90°$. As expected, in the face-on case the geometry of the lensing agrees with that of an axisymmetric lens, and moreover gives physically plausible deflection angles. This is consistent throughout the array of inclination angles, as can be seen for the edge-on case, in which the maximum value of α approximately doubles w.r.t. to the face-on scenario. For $i = 90°$, the breaking of the circular symmetry of the projected matter density on the lens plane drastically changes the geometry of the lensing effects, already showing the importance of inclination for disc galaxy lensing in MOND.

In Fig. 5.5, for a fixed source position and lens parameters, we see that a wide variety of image configurations can be obtained by changing the inclination angle of the lens w.r.t. the observer. Indeed, we recover familiar image configurations – such as the Einstein cross quad-image configuration – already found in the previous studies on similar lensing systems. Here, we note that the tangential caustic curves of the lens do not develop butterfly features, even at high inclinations. This is in agreement with the results of [379] for disc galaxies within the DM paradigm, and differs from the findings of [387] and [388]. However, the density modelling employed by these studies presents unphysical features which might then influence the morphology of the tangential caustic curves. (See [400] for a discussion on exotic caustic curve morphologies.)

We find that changing the lens parameters, when restricted to realistic disc galaxy models, does not

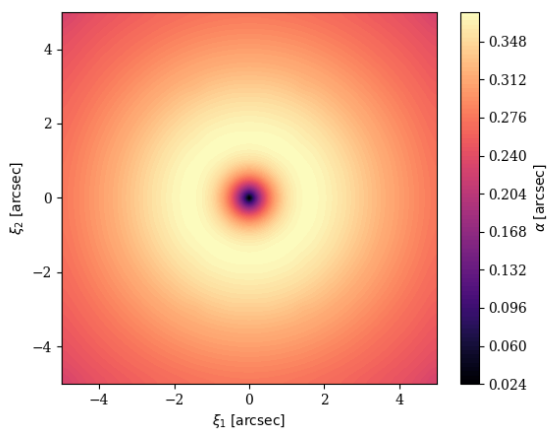

(a) Deflection angle, $i = 0$.

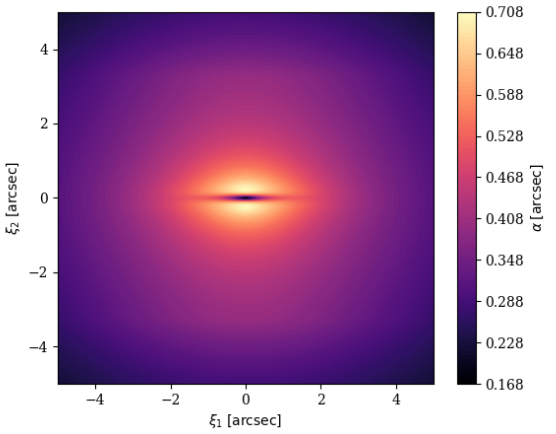

(b) Deflection angle, $i = \pi/2$.

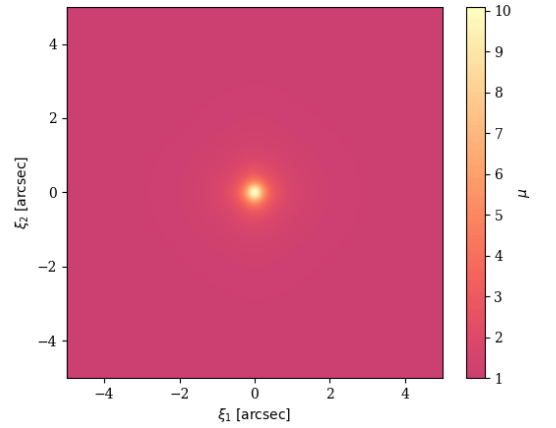

(c) Magnification, $i = 0$.

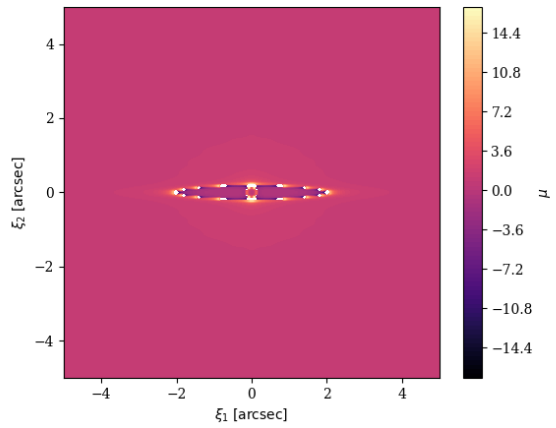

(d) Magnification, $i = \pi/2$.

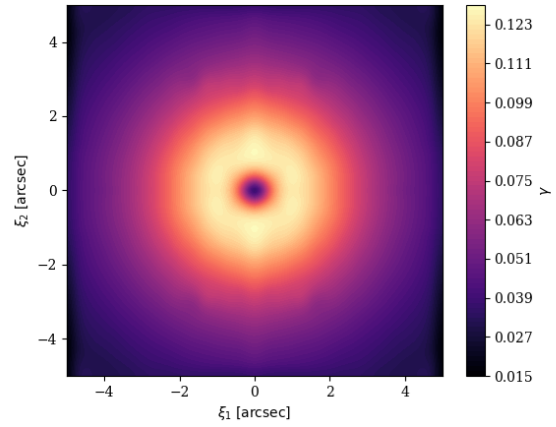

(e) Shear, $i = 0$.

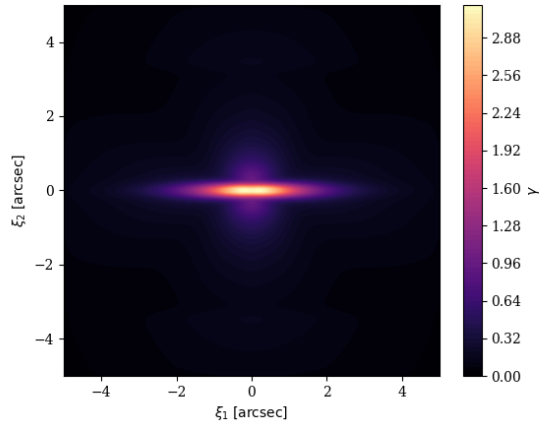

(f) Shear, $i = \pi/2$.

Figure 5.4: Examples of intrinsic lensing properties, namely the deflection angle (α), the magnification (μ), and the shear (γ), for a disc galaxy of inclinations $i = 0$ (left) and $i = \pi/2$ (right). The disc galaxy model is obtained by fixing $M_{\rm d} = 10^{11}\,{\rm M}_\odot$, $R_{\rm d} = 3.5\,{\rm kpc}$, $z_{\rm d} = 0.35\,{\rm kpc}$, $M_{\rm b} = 10^{9}\,{\rm M}_\odot$, and $r_{\rm b} = 0.7\,{\rm kpc}$.

significantly influence the shape of critical or caustic curves produced. However, varying the lens morphology and mass distribution in this way led to direct changes in the overall caustic area, as is shown in Fig. 5.6 and Fig. 5.7.

In Figs. 5.6-5.8 we show the lensing cross section with varying inclination angle and an ensemble of disc galaxy parameters. In these plots, due to the nature of calculating the SGL cross section via numerical methods on a grid, we assume a Poissonian error over the pixel count contained within the tangential caustic curves, i.e., the square root of the number of pixels (multiplied by the single-pixel area value).

Fig. 5.6 shows the effects of varying the disc thickness, $z_{\rm d}$, on the lensing cross section. Interestingly, no clear trend w.r.t. the disc thickness emerges, already indicating the non-trivial interplay between non-linear MONDian effects and lens parameters. Indeed, an increased lensing likelihood for more diffuse disc masses differs to the standard lensing expectations. In the weak-field limit of general relativity a more concentrated mass would produce stronger lensing effects.

In Fig. 5.7 the non-linear, non-Newtonian effects of MOND are more clearly captured. We see that an increased bulge mass negatively correlates with SGL cross section, within the mass range explored. Such a behaviour is in stark contrast to expectations from the standard weak-field SGL of disc galaxy [379]. This trend can be understood by noting that SGL encompasses the full breadth of MOND effects, as it probes the Newtonian limit, the dMOND regime and, most importantly, the transition acceleration scales. Therefore, an increased mass in the bulge, whilst increasing the Newtonian lensing effects, it is found to decrease the MONDian contribution to lensing (which is ultimately dominant in this case). Indeed, a greater mass induces larger Newtonian acceleration and hence decreases the onset of MONDian effects.

Finally, in Fig. 5.8 we present a comparison between the SGL cross section predictions for the same lens disc galaxy in the MOND scenario and the standard DM paradigm. The DM halo is assumed to be a conventional Non-Singular Isothermal Sphere [NSIS, see e.g., 262]

$$\rho_{\rm NSIS}(r) = \frac{\rho_0 r_0^2}{\left(r^2 + r_0^2\right)}\,, \tag{5.28}$$

with parameters taken to be $\rho_0 = 6.36 \cdot 10^7\,{\rm M}_\odot/{\rm kpc}^3$, and $r_0 = 3.44$ kpc, for the template disc galaxy with $M_{\rm d} = 10^{11}\,{\rm M}_\odot$, $R_{\rm d} = 3.5\,{\rm kpc}$, $z_{\rm d} = 0.35\,{\rm kpc}$, $M_{\rm b} = 10^9\,{\rm M}_\odot$, and $r_{\rm b} = 0.7\,{\rm kpc}$. The DM halo parameters are obtained by fitting the Newtonian rotation curve of the dark matter-baryon system to the MOND-derived rotation curve. In particular, we are "normalising" the DM model to obtain a rotation curve matching the MOND prediction. Here, to extrapolate the MONDian rotation curve on the galactic plane, $v_{\rm ROT}$, we directly employ the known algebraic MOND formula [401], i.e.,

$$v_{\rm ROT}(R,0) = \sqrt{R\,\left[1+\tilde{\nu}\left(y(R,0)\right)\right]\,\left|\partial_R \Phi_{\rm N}(R,0)\right|}\,, \tag{5.29}$$

Fig. 5.9 shows respectively, the MONDian rotation curve and the best fit for the chosen DM halo model,

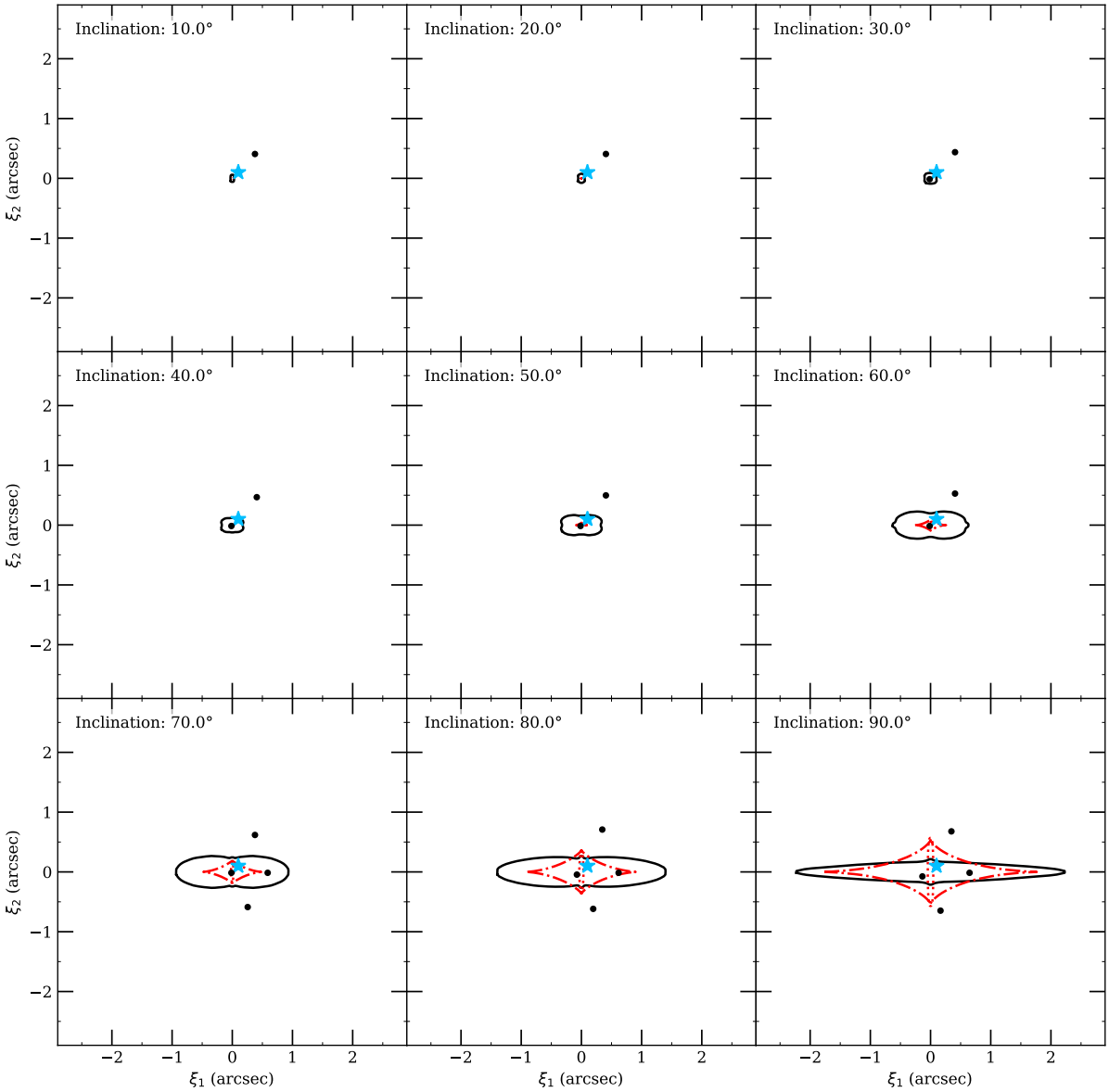

Figure 5.5: Example image configurations, caustic curves and critical curves for spiral galaxy MOND lenses with varying inclination and point source objects placed at a constant position relative to the lens centre. The solid black line, dotted red line and dashed-dotted red-line indicate the critical curve, radial caustic curve and tangential caustic curves respectively. The blue star represent the source image and black dots show the corresponding lensed images. The parameters of the lens galaxy are fixed to be $M_{\rm d} = 10^{11}\,{\rm M}_{\odot}$, $R_{\rm d} = 3.5\,{\rm kpc}$, $z_{\rm d} = 0.35\,{\rm kpc}$, $M_{\rm b} = 10^{9}\,{\rm M}_{\odot}$, and $r_{\rm b} = 0.7\,{\rm kpc}$. The lens and source are placed at redshift $z_{\rm L} = 0.5$ and $z_{\rm S} = 2.0$, respectively.

whilst Fig. 5.10 shows their corresponding cumulative mass functions. Fig. 5.8 shows the clear difference between the predictions of the two frameworks, with MOND SGL cross sections being distinctly larger than the DM alternative. Whilst in the DM paradigm inclination effects are present, these are increased in the MOND scenario, as we could expect from the presence of a "phantom dark disc" in the PDM distribution (see Fig. 5.2). Here we note that, a priori, a different choice of halo model, e.g., either the Navarro–Frenk–White profile [263, 264], or a Burkert halo [267, 402–404] could produce a different SGL effect. However, we find that changing the DM halo profile does not affect the lensing cross section significantly if we maintain a "normalisation" of the DM halo w.r.t. the expected MONDian rotation curve. Therefore, we conclude that disc galaxy SGL is able to differentiate between the two paradigms.

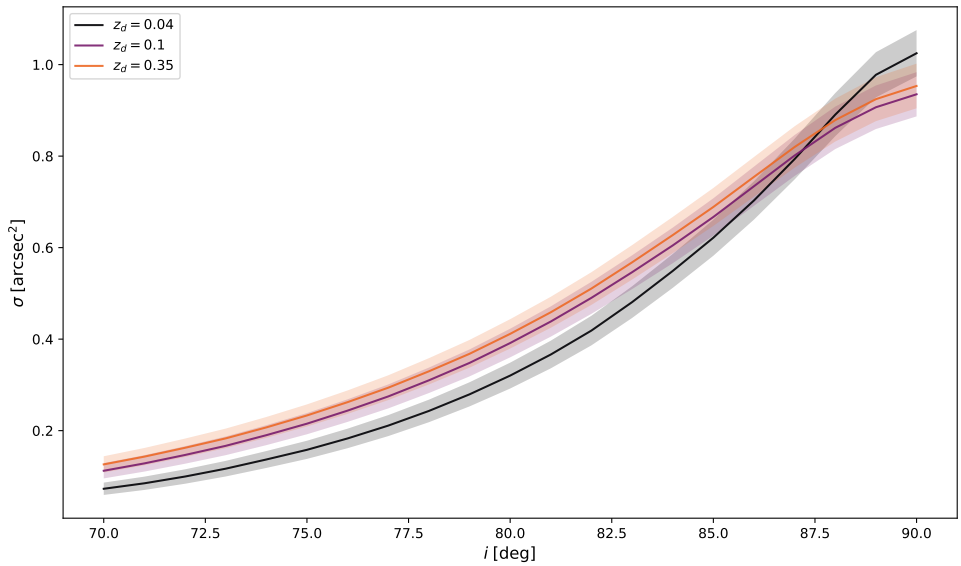

Figure 5.6: Impact of disc thickness z_d on lensing cross section σ with varying inclination angle within the MOND scenario. The other corresponding lens galaxy parameters are $M_\mathrm{d} = 10^{11}\,\mathrm{M}_\odot$, $R_\mathrm{d} = 3.5\,\mathrm{kpc}$, $M_\mathrm{b} = 10^{9}\,\mathrm{M}_\odot$, and $r_\mathrm{b} = 0.7\,\mathrm{kpc}$. The lens and source are placed at redshift $z_\mathrm{L} = 0.5$ and $z_\mathrm{S} = 2.0$, respectively. The shaded areas represent the one standard deviation uncertainties around the obtained SGL cross section curves.

5.5 Conclusions

The dark matter framework has been highly successful in describing a plethora of phenomena, ranging from astrophysical to cosmological observations. Nonetheless, the nature of dark matter still eludes the community and currently represents one of the greatest mysteries in physics. As such, alternatives to the dark matter paradigm, which are able to match a wide-variety of observations, warrant investigation. Within the landscape of alternatives to dark matter, MOND is often considered empirically as the strongest contender to the dark matter scenario. Indeed, MOND has passed numerous observational tests and also produced a variety of now confirmed predictions.

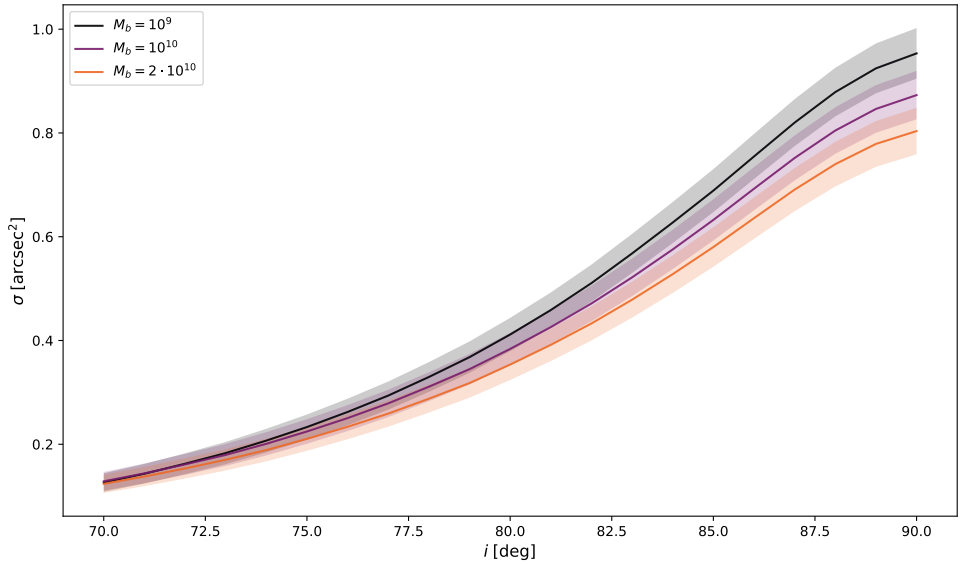

Figure 5.7: Impact of bulge mass M_b on lensing cross section σ with varying inclination angle within the MOND scenario. The other corresponding lens galaxy parameters are $M_\mathrm{d} = 10^{11}\,\mathrm{M}_\odot$, $R_\mathrm{d} = 3.5\,\mathrm{kpc}$, $z_\mathrm{d} = 0.35\,\mathrm{kpc}$, and $r_\mathrm{b} = 0.7\,\mathrm{kpc}$. The lens and source are placed at redshift $z_\mathrm{L} = 0.5$ and $z_\mathrm{S} = 2.0$, respectively. The shaded areas represent the one standard deviation uncertainties around the obtained SGL cross section curves.

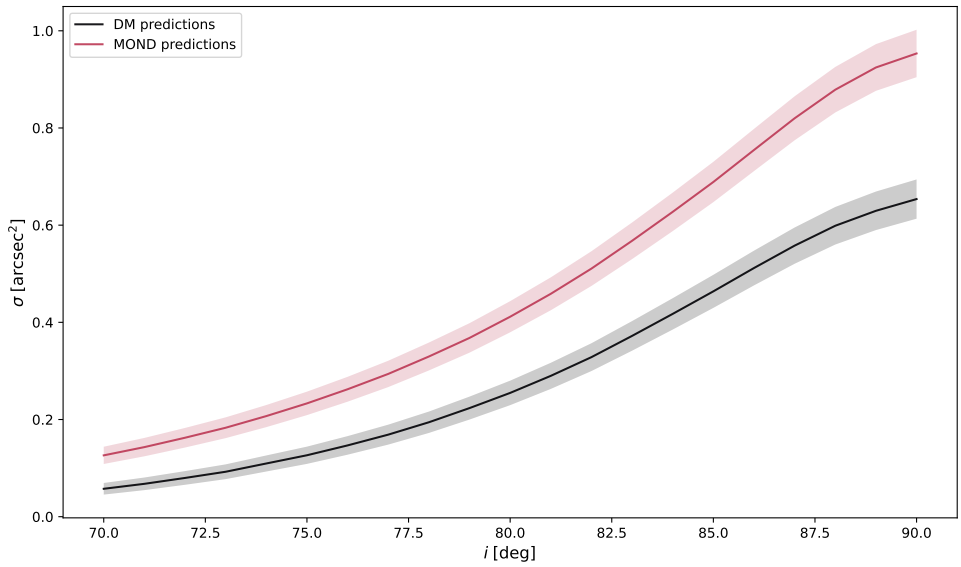

Figure 5.8: A comparison of lensing cross sections predictions with varying inclination angle for the same disc galaxy in MOND and the conventional DM scenario. The disc galaxy parameters are $M_\mathrm{d} = 10^{11}\,\mathrm{M}_\odot$, $R_\mathrm{d} = 3.5\,\mathrm{kpc}$, $z_\mathrm{d} = 0.35\,\mathrm{kpc}$, and $M_\mathrm{b} = 10^9\,\mathrm{M}_\odot$, and $r_\mathrm{b} = 0.7\,\mathrm{kpc}$. The DM halo is taken as a NSIS profile with parameters $\rho_0 = 6.36 \cdot 10^7\,\mathrm{M}_\odot/\mathrm{kpc}^3$, and $r_0 = 3.44$ kpc. The lens and source are placed at redshift $z_\mathrm{L} = 0.5$ and $z_\mathrm{S} = 2.0$, respectively. The shaded areas represent the one standard deviation uncertainties around the obtained SGL cross section curves.

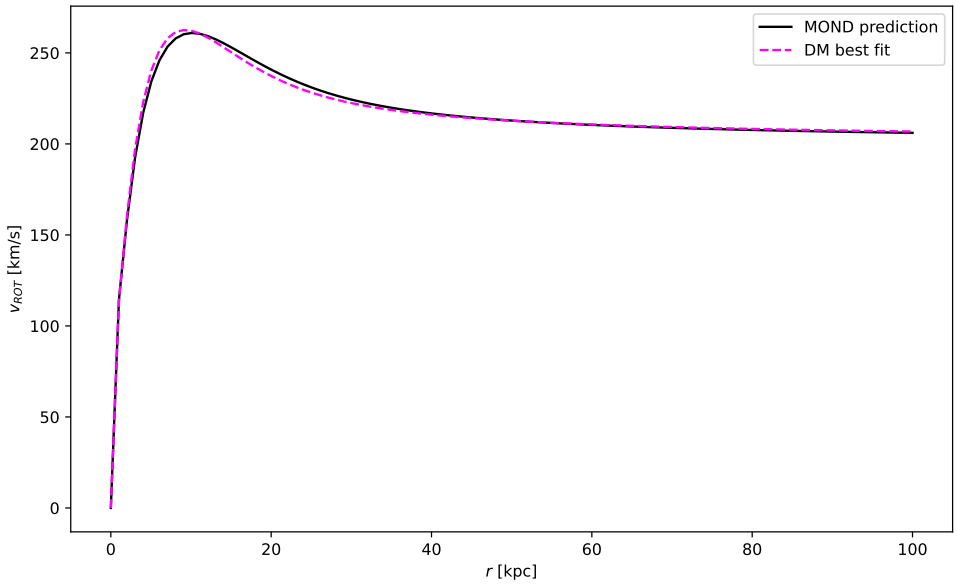

Figure 5.9: A comparison of MONDian rotation curve predictions with the best fit DM alternative. The solid blue line shows the MONDian rotation curve prediction for a disc galaxy with parameters: $M_{\rm d} = 10^{11}\,{\rm M}_{\odot}$, $R_{\rm d} = 3.5\,{\rm kpc}$, $z_{\rm d} = 0.35\,{\rm kpc}$, and $M_{\rm b} = 10^{9}\,{\rm M}_{\odot}$, and $r_{\rm b} = 0.7\,{\rm kpc}$. The dashed red line show the corresponding Newtonian fit of a DM halo, which is taken as a NSIS profile with parameters $\rho_0 = 6.36 \cdot 10^{7}\,{\rm M}_{\odot}/{\rm kpc}^3$, and $r_0 = 3.44$ kpc

.

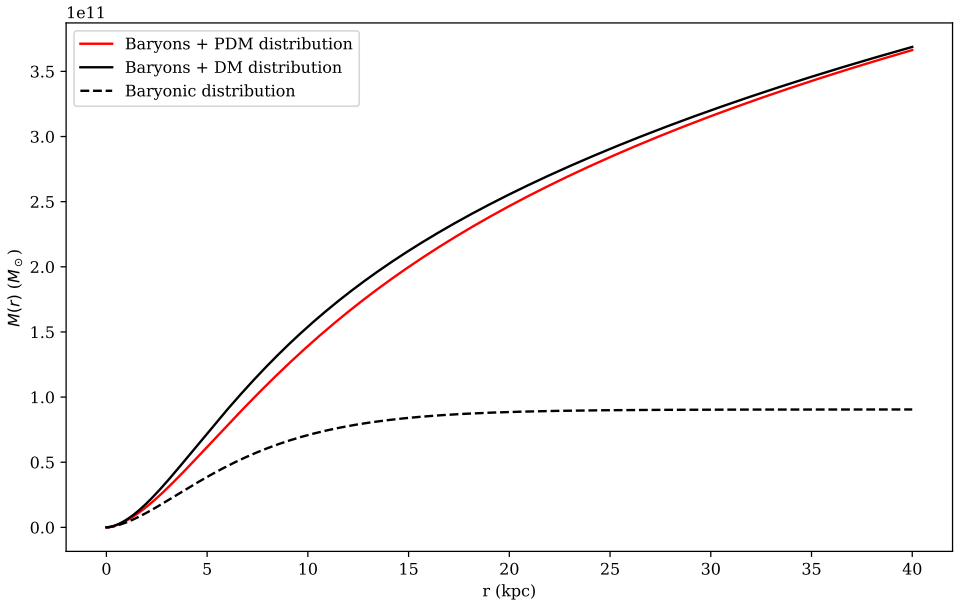

Figure 5.10: Corresponding cummulative mass profiles with radius r along the equatorial plane for a MONDian PDM distribution and DM alternative found from fitting rotation curves shown in Fig. 5.9 .

Strong gravitational lensing by galaxies is capable of investigation in both regions of high, and low Newtonian accelerations. Therefore, in principle, it represents a valuable probe for MONDian effects over the full range of the acceleration scales within galaxies. In particular, studies of disc galaxies would enable a coupling of rotation curve dynamics and strong gravitational lensing. Hence, these represent a great laboratory for investigating gravitational physics.

In this paper, we have derived the strong gravitational lensing effects of disc galaxies in MOND. In the QUMOND formulation of MOND we have employed the concept of equivalent Newtonian systems to apply the standard lensing formalism to MOND. Within this framework, we obtained the highly non-trivial distribution of phantom dark matter for disc galaxies and probed its characteristics.

We have found that disc galaxy lensing in MOND produces physically plausible values of deflection angle, magnification and shear. Furthermore, we have shown that the inclination of the disc galaxy lens w.r.t. the observer highly influences the lensing geometry. We have seen that within the MOND paradigm, the classical caustic curves' morphology and number of lensed images expected for disc lenses is readily recovered. Moreover, we have probed the impact of lens morphological and mass parameters on the strong lensing cross section and found non-trivial, and even counter-intuitive, correlations due to the onset of purely MONDian effects.

Furthermore, we have drawn comparisons between inclination effects on the lensing cross section predicted in MOND and the dark matter framework. We have found that MOND non-linearities dominate over standard Newtonian lensing effects, resulting in: **(i)** steeper inclination effects (correlated to the non-spherical phantom dark matter density profile); and **(ii)** overall larger lensing cross sections. In particular, it is noteworthy that a difference in the cross section of the obtained magnitude (which directly correlates to lensing likelihood) will still clearly impact the number of disc galaxy lenses predicted to be observed in upcoming optical surveys such as Euclid and LSST. Therefore, these future surveys will be able to distinguish the MOND and dark matter paradigms purely by disc galaxy gravitational lensing number counts.

Our results might still need careful consideration, as they are ultimately dependent on the choice of interpolating function of MOND. In this paper, we have focused on the widely used form of interpolating function in Eqn. (5.21), which has given a realisation of MOND able to pass a plethora of observational tests. We have also employed the alternative radial acceleration relation interpolating function (see Appendix B) to check the robustness of our results. We find that these interpolating functions produce similar lensing signatures, and both are distinct from the dark matter predictions. Therefore, although a different choice of interpolating function could ultimately produce different lensing effects, we believe our results will generalise to a broad range of choices. It is then exactly this (limited) dependence on the interpolating function that makes strong gravitational lensing by disc galaxies an exciting astrophysical tool to probe and constrain the full applicability of MOND.

Appendix

Code Routine

The code routine developed to obtain the results in this work is available at the GitHub repository – https://github.com/chrisharhaw/MOND_lensing.git. Here, we give a brief explanation of the logic implemented in the three main codes of the routine, i.e., `density_grid.py`, `alpha_rad_tang.py`, and `caustic_area.py`.

`density_grid.py` routine

This code generates the baryonic and PDM distribution on a (R, z) grid associated with a choice of disc galaxy parameters, and of grid boundaries and step. To calculate the PDM we implement the following steps

1. Define the Newtonian potentials for the exponential disc and the spherical Plummer bulge according to Eqs. (5.19) and (5.20).

2. Define the gradients in cylindrical coordinates of the potentials, namely

$$\vec{\nabla}\Phi_{\rm N,d} = GM_{\rm d}\left(\left[\int_0^\infty {\rm d}k \frac{J_1(Rk)k}{(1+R_{\rm d}^2k^2)^{3/2}} Z(z,k)\right]\hat{R} + \hat{z}\left[-\int_0^\infty {\rm d}k \frac{J_0(Rk)}{(1+R_{\rm d}^2k^2)^{3/2}}\frac{dZ}{dz}\right]\right), \tag{5.30}$$

$$\vec{\nabla}\Phi_{\rm N,b} = \frac{M_{\rm b}G}{(r_{\rm b}^2+R^2)^{3/2}}(R\hat{R}+z\hat{z}), \tag{5.31}$$

   where J_0 and J_1 are Bessel functions, and we have introduced the function

$$Z(z,k) := \frac{e^{-|z|k} - z_d k e^{-|z|/z_d}}{1-z_d^2k^2}. \tag{5.32}$$

3. Compute the gradient of the total Newtonian potential by direct sum of $\vec{\nabla}\Phi_{\rm N,d}$, and $\vec{\nabla}\Phi_{\rm N,b}$, i.e., $\vec{\nabla}\Phi_{\rm N} = \vec{\nabla}\Phi_{\rm N,d} + \vec{\nabla}\Phi_{\rm N,b}$.

4. Employ the definition of the PDM from Eq. (5.7) in the following equivalent form

$$\rho_{\rm ph,b} = \frac{1}{4\pi G}\frac{d\tilde{v}}{dy}\left(\vec{\nabla}y\cdot\vec{\nabla}\Phi_{\rm N}\right) + \tilde{v}(y)\rho_{\rm B}, \tag{5.33}$$

   where we compute $\vec{\nabla}y$ directly in terms of the norm of $\vec{\nabla}\Phi_{\rm N}$. Here, $\tilde{v}$ and its derivative are computed once a functional form is given.

Finally, as an output the code returns the sum of the baryon and PDM densities, multiplied by a weight factor R – accounting for part of the volume element contribution to the calculation of the deflection angle in `alpha_rad_tang.py`, and thus compensating for divergences in the PDM close to the symmetry axis. All integration of non-standard integrals is carried out using the `quad`, and `quad_vec` functions of the python package `integrate` [405]. Fig. 5.11 shows the comparsion between the PDM density

obtained with our code for a Plummer profile (with $M_b = 10^9\,\mathrm{M}_\odot$, and $r_\mathrm{b} = 0.7\,\mathrm{kpc}$), and the respective analytical prediction for the interpolating function of Eq. (5.21). We find the two to be in good agreement.

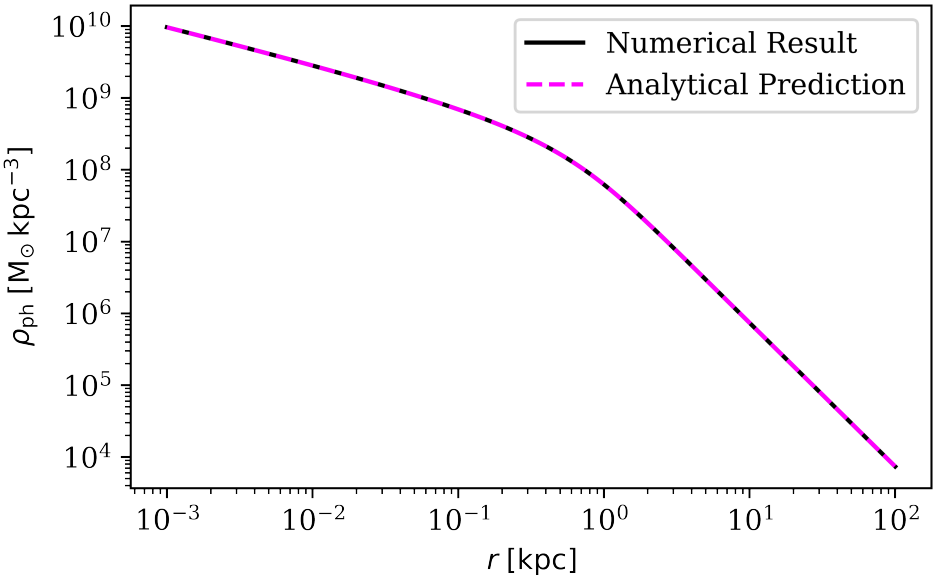

Figure 5.11: A comparison between the numerically obtained PDM (black line) and analytical prediction (dashed purple line) for a Plummer profile with $\mathrm{M}_\odot$, and $r_\mathrm{b} = 0.7\,\mathrm{kpc}$. The MOND interpolating function selected is the one displayed in Eq. (5.21).

`alpha_rad_tang.py` routine

This code loads the output of `density_grid.py` and computes the deflection angles' components. To do so, we exploit an interesting formulation of the deflection angle. From Eqs. (5.9)-(5.11) we can write

$$\vec{\hat{\alpha}}(\xi_1,\xi_2) = \frac{2G}{c^2}\int_{-\infty}^{\infty} \mathrm{d}\xi_3 \iiint \frac{\rho(\vec{r})}{|\vec{\xi}-\vec{r}|}\,\mathrm{d}^3\vec{r}\,. \tag{5.34}$$

Noting that the dependence on ξ_3 within the integral is present exclusively in the geometric term of the integrand (namely, the denominator), we swap the integration order to obtain

$$\vec{\hat{\alpha}}(\xi_1,\xi_2) = \frac{2G}{c^2}\iiint \rho(\vec{r})\mathrm{d}^3\vec{r}\int_{-\infty}^{\infty}\frac{\mathrm{d}\xi_3}{|\vec{\xi}-\vec{r}|}\,. \tag{5.35}$$

The second integral in Eq. (5.35) is readily computed to obtain the two components of the deflection angle

$$\alpha_{\xi_1} = \frac{2G}{c^2}\iiint\left(\frac{2\,(z\sin\lambda + x\cos\lambda - \xi_1)}{\xi_1^2 + (y-\xi_2)^2 + (z\sin\lambda + x\cos\lambda)^2 - 2\xi_1(z\sin\lambda + x\cos\lambda)}\right)\rho(\vec{r})\mathrm{d}^3\vec{r}\,, \tag{5.36}$$

$$\alpha_{\xi_1} = \frac{2G}{c^2}\iiint\left(\frac{y-\xi_2}{\xi_1^2 + (y-\xi_2)^2 + (z\sin\lambda + x\cos\lambda)^2 - 2\xi_1(z\sin\lambda + x\cos\lambda)}\right)\rho(\vec{r})\mathrm{d}^3\vec{r}\,, \tag{5.37}$$

where λ defines the angle between ξ_3 and the z axis of the coordinate system adapted to the disc galaxy mass distribution. Then, in this code we employ Eqs. (5.36) and (5.37) to define the components of the deflection angle. We compute these integrals by direct discretisation on a grid, whose precision can

be specified. From the deflection angle components, the code also computes the inverse magnification matrix and extracts its radial and tangential eigenvalues.

`caustic_area.py` routine

This code loads the outputs of `alpha_rad_tang.py`, i.e., the deflection angle components, and the tangential and radial eigenvalues of the inverse magnification matrix, $\lambda_{\frac{t}{r}}$. The radial and tangential critical curves can then be computed by determining the corresponding contours where $\lambda_{\frac{t}{r}} = 0$, which are traced back into caustic lines using the lens equation (5.12). Once the tangential caustic contours have been found (if they exist), the area within them is calculated. We do this for each density and inclination being investigated, then finally output these values as a `numpy` array for plotting.

The RAR interpolating function

To check the robustness of our result w.r.t. the change of the interpolating function, we consider a comparison with the RAR function [395, 396],

$$\tilde{\nu}_{\rm RAR}(y) := \frac{e^{-\sqrt{y}}}{1-e^{-\sqrt{y}}}\,. \tag{5.38}$$

We computed the RAR PDM distribution for the template disc galaxy model – namely, $M_{\rm d} = 10^{11}\,{\rm M}_{\odot}$, $R_{\rm d} = 3.5\,{\rm kpc}$, $z_{\rm d} = 0.35\,{\rm kpc}$, $M_{\rm b} = 10^{9}\,{\rm M}_{\odot}$, and $r_{\rm b} = 0.7\,{\rm kpc}$ – and find that the obtained PDM distribution is overall compatible with the one derived with the interpolating function of Eq. (5.21), henceforth referred to as $\rho_{\text{ph-RAR}}$, and $\rho_{\text{ph-S}}$, respectively. In Fig. 5.12 we show the face-on view, and side view of the PDM densities ratios, i.e., $\rho_{\text{ph-RAR}}/\rho_{\text{ph-S}}$, for the chosen template galaxy. We see that although the two PDM densities display differences, these give relative corrections only of $\mathcal{O}(1)$. Furthermore, the ratios between the two PDM densities display non-trivial morphological features, charting the different behaviour of two interpolating functions.

Finally, we have computed the SGL expected for the template galaxy whilst employing the RAR interpolation function. Fig. 5.13 shows a comparison between the inclination effects on the SGL cross section produced for the interpolating function used throughout this work, the RAR function, and the DM halo alternative. As we could expect from the ratios obtained between the two PDM distributions, the SGL effects for the two choices of interpolating functions are almost identical, and distinguishable from the DM alternative.

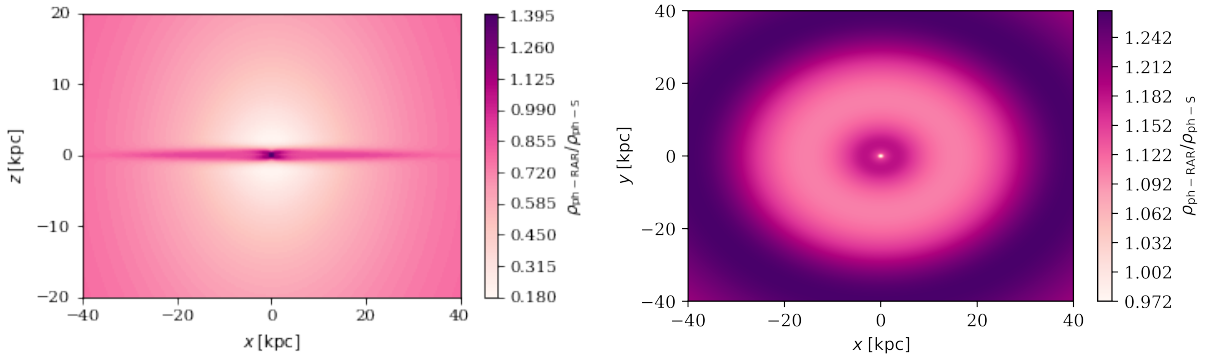

Figure 5.12: PDM densities ratio, $\rho_{\text{ph-RAR}}/\rho_{\text{ph-S}}$ on the $z-x$ plane (left panel) and on the $x-y$ plane (right panel), respectively, for a disc galaxy with $M_{\text{d}} = 10^{11}\,\text{M}_{\odot}$, $R_{\text{d}} = 3.5\,\text{kpc}$, $z_{\text{d}} = 0.35\,\text{kpc}$, $M_{\text{b}} = 10^{9}\,\text{M}_{\odot}$, and $r_{\text{b}} = 0.7\,\text{kpc}$.

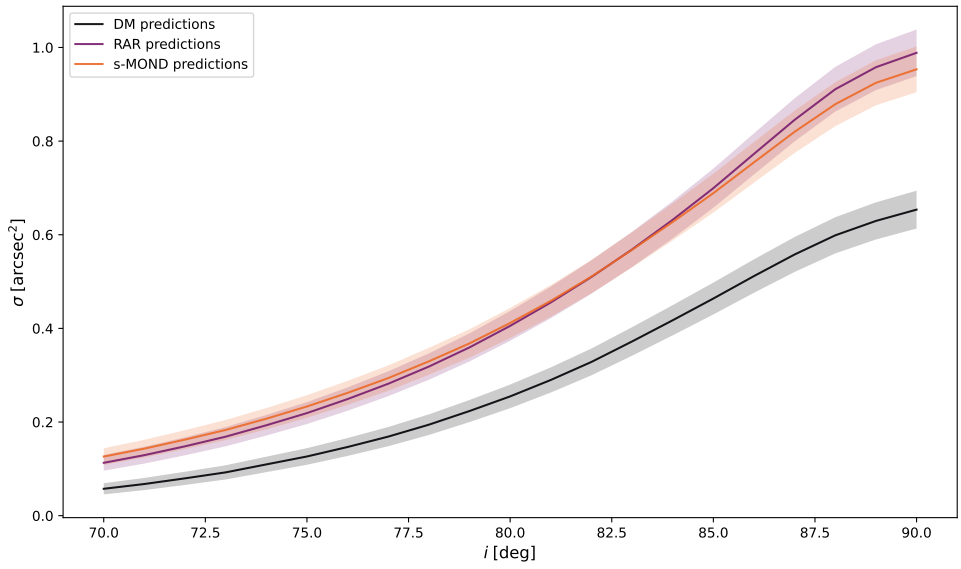

Figure 5.13: A comparison of the effects of varying inclination on the SGL cross section produced for the interpolating function used throughout this work, the RAR function, and the DM halo alternative. The disc galaxy parameters are $M_{\text{d}} = 10^{11}\,\text{M}_{\odot}$, $R_{\text{d}} = 3.5\,\text{kpc}$, $z_{\text{d}} = 0.35\,\text{kpc}$, and $M_{\text{b}} = 10^{9}\,\text{M}_{\odot}$, and $r_{\text{b}} = 0.7\,\text{kpc}$. The DM halo is taken as a NSIS profile with parameters $\rho_0 = 6.36 \cdot 10^{7}\,\text{M}_{\odot}/\text{kpc}^3$, and $r_0 = 3.44$ kpc. The lens and source are placed at redshift $z_{\text{L}} = 0.5$ and $z_{\text{S}} = 2.0$, respectively. The shaded areas represent the one standard deviation uncertainties around the obtained SGL cross section curves.

Chapter 6

Conclusions

The ΛCDM model is extremely successful and has been considered the standard cosmology for over two decades. Despite the confirmation of many ΛCDM predictions, there are underlying tensions whose statistical significance has grown as the precision and volume of cosmological data has increased. In order to investigate sources of systematic error, cosmic distance ladder independent probes are of the upmost importance. Strong gravitational lensing provides a cosmic distance ladder independent technique which can be applied to investigate the acceleration of cosmic expansion the cosmological principle, alternative cosmological models, and the nature of dark matter and dark energy. The recent advances in strong lensing observations have started to enable statistical analyses for cosmological purposes, with vastly more data expected to arrive in the next decade.

In this thesis, we have explored many of these various applications in cosmology. In Chapter 3, we investigate the use of strong lensing for statistical cosmology, using the largest catalogue of galaxy-scale lensing systems compiled to date [215]. We applied a global fit of many power-law lens models to this sample in order to perform a Bayesian comparison of the expansion histories of the standard ΛCDM and timescape cosmologies using the H_0 independent method derived from the distance ratios within each system. We found that the assumption of average spherical symmetry applied in these lens models, produced unphysical cosmological parameters in the ΛCDM model. Certain image configurations, such as quadruply imaged sources, cannot be produced with perfectly spherical mass distributions. Thus, the lens effect of the assumed average spherical lens model does not equate to the average lens effect of a collection of randomly orientated elliptical galaxies. Whilst this technique has been shown to find physical cosmological values with the addition of constraints on the luminosity density profile of lens galaxies from high resolution follow-up imagery [215], our results bring into question the global use of spherically symmetric lens models applied.

In Chapter 4, we have extended the work in the previous chapter to include time-delay systems to see if the additional constraints placed upon on the lens model would produce physical cosmological parameters. However, the inclusion of time-delay data alone was found insufficient to constrain cosmology. Despite this, time-delay cosmography using only a few lensing systems with individually fit

lens models, is capable of returning precise constraints on the Hubble constant H_0, as shown by the H0LiCOW collaboration [249], amongst others [254]. In this chapter, we have performed the first analysis of the dressed Hubble constant in the timescape model using time-delay cosmography, and found that the timescape model is statistically indistinguishable from ΛCDM with this limited data set.

Further research on the differences between fitting a lens model with average ellipticity, against the assumed averaged spherical symmetry, or individually fit lens models to each system is warranted from the work done in these chapters. The next generation of surveys predicts over 100,000 observed strong lensing systems [270]. Therefore, improving analyses that can constrain cosmology, without the need for high-resolution imagery, is of incredible use. Alternatively, time-delay cosmography has already proved able to provide powerful constraints with only a small number of systems. With the amount of data we expect to receive and the improved precision on velocity dispersions measured using adaptive optics, time delay cosmography may be able to statistically distinguish between cosmological models in the near future. Furthermore, an extension of chapter 4 and of current applications of time-delay cosmography, will be to directly test for anisotropy in the Hubble constant. A first step would be to utilise mock catalogues to determine how many lens systems are required to distinguish a non-kinematic dipole from a pure monopole in H_0.

The discussion of spherical symmetry in Chapters 3 and 4, inspired the investigation of Chapter 5 into the inclination effects of strong lensing by disc galaxies with both standard DM halos in the ΛCDM paradigm, and MOND. Whilst our results are dependent on the choice of interpolating function and formulation of MOND, we have shown that MOND is capable of producing similar lens effects in the shape of critical and caustic curves to that of DM haloes. However, MOND predicts a caustic area much larger than the DM alternative. Hence, the formulation of MOND investigated would predict far more spiral galaxies to be observed than in the standard DM paradigm. We have also found counterintuitive correlations between the effect of the disc thickness and bulge radius on the caustic area and the likelihood of strong lensing. Thus, there is a balance between Newtonian and MONDian effects that naïvely one might not expect. We conclude that the strong lensing of spiral galaxies gives an opportunity to test and compare modified theories of gravity against Newtonian physics and dark matter.

Further work to predict the number of disc galaxies lenses and their corresponding inclination distribution for the MOND and DM paradigm is ongoing. These predictions can be compared to the number of lenses observed in upcoming surveys such as LSST, in order to distinguish one theory of gravity over another or to constrain the dark matter halo profiles of spiral galaxies and the interpolating function of MOND. The combination of spiral galaxy rotation curves with lensing observations provides a powerful tool for constraining our theories of gravity. This makes searches for low mass late-type galaxies as strong gravitational lenses in the next generation of surveys incredibly exciting, as the data needed for our predictions is expected to be available over the coming decade.

Overall, this thesis highlights issues in using strong lensing for statistical cosmology and proposes

new tests of ΛCDM and MOND, in anticipation of the next decade of numerous and precise observations.

Bibliography

[1] E. Abdalla et al., "Cosmology intertwined: A review of the particle physics, astrophysics, and cosmology associated with the cosmological tensions and anomalies", Journal of High Energy Astrophysics **34**, 49–211 (2022).

[2] J. A. Acevedo Barroso et al. (Euclid collaboration), "Euclid: The Early Release Observations Lens Search Experiment", arXiv:2408.06217 (2024).

[3] P. A. Abell et al. (LSST Science and LSST Project collaborations), "LSST Science Book, Version 2.0", (2009).

[4] D. Eisenstein et al. (DESI collaboration), "The Dark Energy Spectroscopic Instrument (DESI): Science from the DESI Survey", American Astronomical Society Meeting Abstracts **225** (2015).

[5] A. G. Adame, J. Aguilar, S. Ahlen, et al. (DESI collaboration), "DESI 2024 VI: cosmological constraints from the measurements of baryon acoustic oscillations", Journal of Cosmology and Astroparticle Physics 02, 021 (2025).

[6] T. Abbott et al. (DES collaboration), "The Dark Energy Survey", arXiv:astro-ph/0510346 (2005).

[7] K. Bechtol et al. (DES collaboration), "Dark Energy Survey Year 6 Results: Photometric Data Set for Cosmology", arXiv:2501.05739 (2025).

[8] J. P. Gardner et al., "The James Webb Space Telescope", Space Science Reviews **123**, 485 (2006).

[9] D. Spergel, N. Gehrels, C. Baltay, et al., "Wide-Field InfrarRed Survey Telescope-Astrophysics Focused Telescope Assets WFIRST-AFTA 2015 Report", arXiv:1503.03757 (2015).

[10] C. Cahillane and G. Mansell, "Review of the Advanced LIGO Gravitational Wave Observatories Leading to Observing Run Four", Galaxies **10**, 36 (2022).

[11] B. Mours (VIRGO collaboration), "The VIRGO Project", in International Europhysics Conference on High-energy Physics (1993).

[12] F. Acernese et al. (Virgo collaboration), "The Virgo O3 run and the impact of the environment", Classical Quantum Gravity **39**, 235009 (2022).

[13] T. Akutsu et al. (KAGRA collaboration), "Overview of KAGRA : KAGRA science", Progress of Theoretical and Experimental Physics **2021**, 05A103 (2020).

[14] N. Feigl (IceCube collaboration), "The IceCube Upgrade: status and prospects for advances with GeV neutrinos", Proceedings of Science **ICHEP2024**, 149 (2025).

[15] Y. Suzuki, "The Super-Kamiokande experiment", European Physics Journal C **79**, 298 (2019).

[16] D. W. Hogg, D. J. Eisenstein, M. R. Blanton, et al., "Cosmic Homogeneity Demonstrated with Luminous Red Galaxies", Astrophysical Journal **624**, 54–58 (2005).

[17] M. I. Scrimgeour, T. Davis, C. Blake, et al., "The WiggleZ dark energy survey: the transition to large-scale cosmic homogeneity", Monthly Notices of the Royal Astronomical Society **425**, 116–134 (2012).

[18] P. Ntelis et al., "Exploring cosmic homogeneity with the BOSS DR12 galaxy sample", Journal of Cosmology and Astroparticle Physics 06, 019 (2017).

[19] S. Sarkar and B. Pandey, "Unravelling the cosmic web: an analysis of the Sloan Digital Sky Survey Data Release 14 with the local dimension", Monthly Notices of the Royal Astronomical Society **485**, 4743–4753 (2019).

[20] P. Sarkar, S. Majumdar, B. Pandey, et al., "The many scales to cosmic homogeneity: Use of multiple tracers from the SDSS", arXiv:1611.07915 (2016).

[21] J. K. Yadav, J. S. Bagla, and N. Khandai, "Fractal dimension as a measure of the scale of homogeneity", Monthly Notices of the Royal Astronomical Society **405**, 2009–2015 (2010).

[22] V. Springel, S. D. M. White, A. Jenkins, et al., "Simulations of the formation, evolution and clustering of galaxies and quasars", Nature **435**, 629–636 (2005).

[23] V. Springel, "The cosmological simulation code GADGET-2", Monthly Notices of the Royal Astronomical Society **364**, 1105–1134 (2005).

[24] M. J. Williams, H. J. Macpherson, D. L. Wiltshire, et al., "First investigation of void statistics in numerical relativity simulations", Monthly Notices of the Royal Astronomical Society **536**, 2645–2660 (2025).

[25] H. J. Macpherson, P. D. Lasky, and D. J. Price, "Inhomogeneous cosmology with numerical relativity", Physical Review D **95**, 064028 (2017).

[26] R. L. Munoz and M. Bruni, "Structure formation and quasispherical collapse from initial curvature perturbations with numerical relativity simulations", Physical Reviews D **107**, 123536 (2023).

[27] D. J. Fixsen, "The temperature of the cosmic microwave background", The Astrophysical Journal **707**, 916–920 (2009).

[28] N. Aghanim, Y. Akrami, M. Ashdown, et al. (Planck collaboration), "Planck 2018 results. VI. Cosmological parameters", Astronomy & Astrophysics **641**, A6 (2020).

[29] G. Hinshaw et al., "Five-Year Wilkinson Microwave Anisotropy Probe (WMAP) Observations: Data Processing, Sky Maps, and Basic Results", Astrophysical Journal Supplementary Series **180**, 225–245 (2009).

[30] R. Bernabei et al. (DAMA collaboration), "First results from DAMA/LIBRA and the combined results with DAMA/NaI", European Physics Journal C **56**, 333–355 (2008).

[31] F. Zwicky, "On the Masses of Nebulae and of Clusters of Nebulae", Astrophysical Jorunal **86**, 217 (1937).

[32] V. C. Rubin, J. Ford W. K., and N. Thonnard, "Extended rotation curves of high-luminosity spiral galaxies. IV. Systematic dynamical properties, Sa -> Sc.", Astrophysical Journal Letters **225**, L107–L111 (1978).

[33] A. Bosma, "The distribution and kinematics of neutral hydrogen in spiral galaxies of various morphological types.", PhD thesis (Groningen Univ., Groningen, The Netherlands, 1978).

[34] Y. Sofue and V. Rubin, "Rotation Curves of Spiral Galaxies", Annual Review of Astronomy and Astrophysics **39**, 137–174 (2001).

[35] P. J. E. Peebles, "Large-scale background temperature and mass fluctuations due to scale-invariant primeval perturbations", Astrophysical Journal Letters **263**, L1–L5 (1982).

[36] J. Calcino, J. Garcia-Bellido, and T. M. Davis, "Updating the MACHO fraction of the Milky Way dark halowith improved mass models", Monthly Notices of the Royal Astronomical Society **479**, 2889–2905 (2018).

[37] C. Alcock, R. A. Allsman, D. R. Alves, et al., "The MACHO Project: Microlensing Results from 5.7 Years of Large Magellanic Cloud Observations", Astrophysical Journal **542**, 281–307 (2000).

[38] F. Iocco, G. Mangano, G. Miele, et al., "Primordial Nucleosynthesis: from precision cosmology to fundamental physics", Physics Reports **472**, 1–76 (2009).

[39] K. Freese, "Status of Dark Matter in the Universe", International Journal of Modern Physics **26**, 325–355 (2017).

[40] G. Arcadi, M. Dutra, P. Ghosh, et al., "The waning of the WIMP? A review of models, searches, and constraints", European Physical Journal C **78**, 203 (2018).

[41] A. H. G. Peter, V. Gluscevic, A. M. Green, et al., "WIMP physics with ensembles of direct-detection experiments", Physics of the Dark Universe **5-6**, 45–74 (2014).

[42] T. Marrodán Undagoitia and L. Rauch, "Dark matter direct-detection experiments", Journal of Physics G **43**, 013001 (2016).

[43] L. Roszkowski, E. M. Sessolo, and S. Trojanowski, "WIMP dark matter candidates and searches—current status and future prospects", Reports on Progress in Physics **81**, 066201 (2018).

[44] L. Bergstrom, "Dark Matter Candidates", New Journal of Physics **11**, 105006 (2009).

[45] L. Di Luzio, M. Giannotti, E. Nardi, et al., "The landscape of QCD axion models", Physics Reports **870**, 1–117 (2020).

[46] E. G. M. Ferreira, "Ultra-light dark matter", Astronomy & Astrophysics Reviews **29**, 7 (2021).

[47] E. Hubble, "A Relation between Distance and Radial Velocity among Extra-Galactic Nebulae", Proceedings of the National Academy of Science **15**, 168–173 (1929).

[48] A. G. Riess, A. V. Filippenko, P. Challis, et al., "Observational Evidence from Supernovae for an Accelerating Universe and a Cosmological Constant", Astronomical Journal **116**, 1009–1038 (1998).

[49] S. Perlmutter, G. Aldering, G. Goldhaber, et al., "Measurements of Ω and Λ from 42 High-Redshift Supernovae", Astrophysical Journal **517**, 565–586 (1999).

[50] A. Einstein, "Cosmological Considerations in the General Theory of Relativity", Sitzungsberichte der Königlich Preussischen Akademie der Wissenschaften zu Berlin, 142–152 (1917).

[51] M. Li, X.-D. Li, S. Wang, et al., "Dark Energy: A Brief Review", Frontiers of Physics (Beijing) **8**, 828–846 (2013).

[52] S. Weinberg, "The Cosmological Constant Problem", Rev. Mod. Phys. **61**, 1–23 (1989).

[53] G. Miknaitis, G. Pignata, A. Rest, et al., "The ESSENCE Supernova Survey: Survey Optimization, Observations, and Supernova Photometry", Astrophysical Journal **666**, 674–693 (2007).

[54] W. M. Wood-Vasey, G. Miknaitis, C. W. Stubbs, et al., "Observational Constraints on the Nature of Dark Energy: First Cosmological Results from the ESSENCE Supernova Survey", Astrophysical Journal **666**, 694–715 (2007).

[55] D. Brout et al., "The Pantheon+ Analysis: Cosmological Constraints", Astrophysical Journal **938**, 110 (2022).

[56] S. Pandey et al. (DES collaboration), "Dark Energy Survey year 3 results: Constraints on cosmological parameters and galaxy-bias models from galaxy clustering and galaxy-galaxy lensing using the redMaGiC sample", Physical Review D **106**, 043520 (2022).

[57] A. Conley, J. Guy, M. Sullivan, et al., "Supernova Constraints and Systematic Uncertainties from the First Three Years of the Supernova Legacy Survey", Astrophysical Journal Supplement Series **192**, 1 (2011).

[58] H. Campbell, C. B. D'Andrea, R. C. Nichol, et al., "Cosmology with Photometrically Classified Type Ia Supernovae from the SDSS-II Supernova Survey", Astrophysical Journal **763**, 88 (2013).

[59] A. Rest et al., "Cosmological Constraints from Measurements of Type Ia Supernovae discovered during the first 1.5 yr of the Pan-STARRS1 Survey", Astrophysical Journal **795**, 44 (2014).

[60] A. J. Cuesta, L. Verde, A. Riess, et al., "Calibrating the cosmic distance scale ladder: the role of the sound-horizon scale and the local expansion rate as distance anchors", Monthly Notices of the Royal Astronomical Society **448**, 3463–3471 (2015).

[61] T. M. Davis, S. R. Hinton, C. Howlett, et al., "Can redshift errors bias measurements of the hubble constant?", Monthly Notices of the Royal Astronomical Society **490**, 2948–2957 (2019).

[62] J. Calcino and T. Davis, "The need for accurate redshifts in supernova cosmology", Journal of Cosmology and Astroparticle Physics 01, 038 (2017).

[63] S. Randich, G. Gilmore, L. Magrini, et al., "The gaia-eso public spectroscopic survey: implementation, data products, open cluster survey, science, and legacy", Astronomy & Astrophysics **666**, A121 (2022).

[64] M. M. Phillips, "The Absolute Magnitudes of Type IA Supernovae", Astrophysical Journal Letters **413**, L105 (1993).

[65] I. M. H. Etherington, "On the Definition of Distance in General Relativity.", Philosophical Magazine **15**, 761 (1933).

[66] J. R. Herrnstein, J. M. Moran, L. J. Greenhill, et al., "A Geometric distance to the galaxy NGC 4258 from orbital motions in a nuclear gas disk", Nature **400**, 539–541 (1999).

[67] M. J. Reid, D. W. Pesce, and A. G. Riess, "An improved distance to ngc 4258 and its implications for the hubble constant", The Astrophysical Journal Letters **886**, L27 (2019).

[68] A. G. Riess, W. Yuan, L. M. Macri, et al., "A Comprehensive Measurement of the Local Value of the Hubble Constant with 1 $kms^{-1}Mpc^{-1}$ Uncertainty from the Hubble Space Telescope and the SH0ES Team", Astrophysical Journal Letters **934**, L7 (2022).

[69] S. K. Choi, M. Hasselfield, S.-P. P. Ho, et al., "The atacama cosmology telescope: a measurement of the cosmic microwave background power spectra at 98 and 150 ghz", Journal of Cosmology and Astroparticle Physics 12, 045 (2020).

[70] K. Prabhu, S. Raghunathan, M. Millea, et al., "Testing the ΛCDM Cosmological Model with Forthcoming Measurements of the Cosmic Microwave Background with SPT-3G", arXiv:2403.17925 (2024).

[71] W. L. Freedman et al., "The Carnegie-Chicago Hubble Program. VIII. An Independent Determination of the Hubble Constant Based on the Tip of the Red Giant Branch", Astrophysical Journal **882**, 34 (2019).

[72] W. L. Freedman, B. F. Madore, T. Hoyt, et al., "Calibration of the Tip of the Red Giant Branch", Astrophysical Journal **891**, 57 (2020).

[73] W. L. Freedman and B. F. Madore, "Progress in direct measurements of the Hubble constant", Journal of Cosmology and Astroparticle Physics 11, 050 (2023).

[74] B. P. Abbott et al. (LIGO Scientific, Virgo, 1M2H, Dark Energy Camera GW-E, DES, DLT40, Las Cumbres Observatory, VINROUGE, MASTER), "A gravitational-wave standard siren measurement of the Hubble constant", Nature **551**, 85–88 (2017).

[75] S. M. Feeney, H. V. Peiris, A. R. Williamson, et al., "Prospects for resolving the Hubble constant tension with standard sirens", Physical Review Letters **122**, 061105 (2019).

[76] M. Soares-Santos et al. (DES, LIGO Scientific, Virgo collaborations), "First Measurement of the Hubble Constant from a Dark Standard Siren using the Dark Energy Survey Galaxies and the LIGO/Virgo Binary–Black-hole Merger GW170814", Astrophysical Journal Letters **876**, L7 (2019).

[77] T. M. C. Abbott et al. (DES collaboration), "Dark Energy Survey year 1 results: Cosmological constraints from galaxy clustering and weak lensing", Physcial Reviews D **98**, 043526 (2018).

[78] T. M. C. Abbott et al. (DES collaboration), "Dark Energy Survey Year 3 results: Cosmological constraints from galaxy clustering and weak lensing", Physical Review D **105**, 023520 (2022).

[79] D. W. Pesce et al., "The Megamaser Cosmology Project. XIII. Combined Hubble constant constraints", Astrophysical Journal Letters **891**, L1 (2020).

[80] E. D. Reese, J. E. Carlstrom, M. Joy, et al., "Determining the cosmic distance scale from interferometric measurements of the sunyaev-zel'dovich effect", Astrophysical Journal **581**, 53–85 (2002).

[81] M. Bonamente, M. K. Joy, S. J. LaRoque, et al., "Determination of the Cosmic Distance Scale from Sunyaev-Zel'dovich Effect and Chandra X-Ray Measurements of High-Redshift Galaxy Clusters", Astrophysical Journal **647**, 25–54 (2006).

[82] A. Kozmanyan, H. Bourdin, P. Mazzotta, et al., "Deriving the Hubble constant using Planck and XMM-Newton observations of galaxy clusters", Astronomy & Astrophysics **621**, A34 (2019).

[83] J. T. Wan, A. B. Mantz, J. Sayers, et al., "Measuring H_0 using X-ray and SZ effect observations of dynamically relaxed galaxy clusters", Monthly Notices of the Royal Astronomical Society **504**, 1062–1076 (2021).

[84] J. Melnick, R. Terlevich, and E. Terlevich, "Hii galaxies as deep cosmological probes", Monthly Notices of the Royal Astronomical Society **311**, 629 (2000).

[85] R. Chávez, E. Terlevich, R. Terlevich, et al., "Determining the Hubble constant using giant extragalactic H II regions and H II galaxies", Monthly Notices of the Royal Astronomical Society **425**, L56–L60 (2012).

[86] A. L. González-Morán, R. Chávez, E. Terlevich, et al., "Independent cosmological constraints from high-z H II galaxies: new results from VLT-KMOS data", Monthly Notices of the Royal Astronomical Society **505**, 1441–1457 (2021).

[87] S. Mukherjee, A. Krolewski, B. D. Wandelt, et al., "Cross-correlating Dark Sirens and Galaxies: Constraints on H0 from GWTC-3 of LIGO–Virgo–KAGRA", The Astrophysical Journal **975**, 189 (2024).

[88] V. Poulin, J. L. Bernal, E. D. Kovetz, et al., "Sigma-8 tension is a drag", Physical Review D **107**, 123538 (2023).

[89] A. Amon et al. (DES collaboration), "Dark Energy Survey Year 3 results: Cosmology from cosmic shear and robustness to data calibration", Physical Review D **105**, 023514 (2022).

[90] L. F. Secco et al. (DES collaboration), "Dark Energy Survey Year 3 results: Cosmology from cosmic shear and robustness to modeling uncertainty", Physical Review D **105**, 023515 (2022).

[91] Busch, J. L. vD. et al., "KiDS-1000: Cosmic shear with enhanced redshift calibration", Astronomy & Astrophysics **664**, A170 (2022).

[92] P. Simon, L. Porth, P. Burger, et al., "KiDS-1000: Detection of deviations from a purely cold dark-matter power spectrum with tomographic weak gravitational lensing", arXiv:2502.04449 (2025).

[93] T. Simon, P. Zhang, V. Poulin, et al., "Consistency of effective field theory analyses of the BOSS power spectrum", Physical Review D **107**, 123530 (2023).

[94] O. H. E. Philcox and M. M. Ivanov, "BOSS DR12 full-shape cosmology: ΛCDM constraints from the large-scale galaxy power spectrum and bispectrum monopole", Physical Review D **105**, 043517 (2022).

[95] S. Yuan, L. H. Garrison, D. J. Eisenstein, et al., "Stringent $\sigma 8$ constraints from small-scale galaxy clustering using a hybrid MCMC + emulator framework", Monthly Notices of the Royal Astronomical Society **515**, 871–896 (2022).

[96] Z. Zhai, J. L. Tinker, A. Banerjee, et al., "The Aemulus Project. V. Cosmological Constraint from Small-scale Clustering of BOSS Galaxies", Astrophysical Journal **948**, 99 (2023).

[97] P. A. R. Ade et al. (Planck collaboration), "Planck 2015 results. XXIV. Cosmology from Sunyaev-Zeldovich cluster counts", Astronomy & Astrophysics **594**, A24 (2016).

[98] A. Krolewski, S. Ferraro, and M. White, "Cosmological constraints from unWISE and Planck CMB lensing tomography", Journal of Cosmology and Astroparticle Physics 12, 028 (2021).

[99] M. White et al., "Cosmological constraints from the tomographic cross-correlation of DESI Luminous Red Galaxies and Planck CMB lensing", Journal of Cosmology and Astroparticle Physics 02, 007 (2022).

[100] S.-F. Chen, M. White, J. DeRose, et al., "Cosmological analysis of three-dimensional BOSS galaxy clustering and Planck CMB lensing cross correlations via Lagrangian perturbation theory", Journal of Cosmology and Astroparticle Physics 07, 041 (2022).

[101] T. M. C. Abbott et al. (DES and SPT collaborations), "Joint analysis of Dark Energy Survey Year 3 data and CMB lensing from SPT and Planck. III. Combined cosmological constraints", Physical Review D **107**, 023531 (2023).

[102] C. Heymans et al., "KiDS-1000 Cosmology: Multi-probe weak gravitational lensing and spectroscopic galaxy clustering constraints", Astronomy & Astrophysics **646**, A140 (2021).

[103] C. García-García, J. R. Zapatero, D. Alonso, et al., "The growth of density perturbations in the last ∼10 billion years from tomographic large-scale structure data", Journal of Cosmology and Astroparticle Physics 10, 030 (2021).

[104] E. P. Longley et al. (LSST Dark Energy Science collaboration), "A unified catalogue-level reanalysis of stage-III cosmic shear surveys", Monthly Notices of the Royal Astronomical Society **520**, 5016–5041 (2023).

[105] N. Aghanim et al. (Planck collaboration), "Planck 2018 results. I. Overview and the cosmological legacy of Planck", Astronomy & Astrophysics **641**, A1 (2020).

[106] G. F. R. Ellis and J. E. Baldwin, "On the expected anisotropy of radio source counts", Monthly Notices of the Royal Astronomical Society **206**, 377–381 (1984).

[107] N. Secrest, S. von Hausegger, M. Rameez, et al., "Forty years of the Ellis–Baldwin test", Nature Reviews Physics **7**, 68–70 (2025).

[108] J. J. Condon, W. D. Cotton, E. W. Greisen, et al., "The NRAO VLA Sky Survey", Astronomical Journal **115**, 1693–1716 (1998).

[109] T. Mauch, T. Murphy, H. J. Buttery, et al., "SUMSS: A wide-field radio imaging survey of the southern sky. 2. The Source catalogue", Monthly Notices of the Royal Astronomical Society **342**, 1117 (2003).

[110] T. Murphy, T. Mauch, A. Green, et al., "The second epoch Molonglo Galactic Plane Survey: compact source catalogue", Monthly Notices of the Royal Astronomical Society **382**, 382–392 (2007).

[111] J. Colin, R. Mohayaee, M. Rameez, et al., "High-redshift radio galaxies and divergence from the CMB dipole", Monthly Notices of the Royal Astronomical Society **471**, 1045–1055 (2017).

[112] P. K. Aluri, P. Cea, P. Chingangbam, et al., "Is the Observable Universe Consistent with the Cosmological Principle?", Classical and Quantum Gravity **40**, 094001 (2023).

[113] S. J. Nakoneczny et al., "QZO: A Catalog of 5 Million Quasars from the Zwicky Transient Facility", arXiv:2502.13054 (2025).

[114] P. R. M. Eisenhardt, F. Marocco, J. W. Fowler, et al., "The CatWISE Preliminary Catalog: Motions from WISE and NEOWISE Data", Astrophysical Journal Supplement Series **247**, 69 (2020).

[115] N. J. Secrest, S. von Hausegger, M. Rameez, et al., "A Test of the Cosmological Principle with Quasars", Astrophysical Journal Letters **908**, L51 (2021).

[116] N. J. Secrest, S. von Hausegger, M. Rameez, et al., "A Challenge to the Standard Cosmological Model", Astrophysical Journal Letters **937**, L31 (2022).

[117] E. Di Valentino, L. A. Anchordoqui, Ö. Akarsu, et al., "Snowmass2021 - letter of interest cosmology intertwined ii: the hubble constant tension", Astroparticle Physics **131**, 102605 (2021).

[118] S. W. Hawking and G. F. R. Ellis, *The Large Scale Structure of Space-Time*, Cambridge Monographs on Mathematical Physics (Cambridge University Press, 1973).

[119] W. J. Wolf, C. García-García, and P. G. Ferreira, "Robustness of Dark Energy Phenomenology Across Different Parameterizations", arXiv:2502.04929 (2025).

[120] M. Chevallier and D. Polarski, "Accelerating universes with scaling dark matter", International Journal of Modern Physics D **10**, 213–224 (2001).

[121] E. V. Linder, "Exploring the expansion history of the universe", Physical Review Letters **90**, 091301 (2003).

[122] D. Rubin et al., "Union Through UNITY: Cosmology with 2,000 SNe Using a Unified Bayesian Framework", arXiv:2311.12098 (2023).

[123] G. W. Gibbons, "Phantom matter and the cosmological constant", arXiv:hep-th/0302199 (2003).

[124] V. Poulin, T. L. Smith, T. Karwal, et al., "Early dark energy can resolve the hubble tension", Physical Review Letters **122** (2019).

[125] J. C. Hill, E. McDonough, M. W. Toomey, et al., "Early dark energy does not restore cosmological concordance", Physical Review D **102**, 043507 (2020).

[126] S. Vagnozzi, "Consistency tests of ΛCDM from the early integrated Sachs-Wolfe effect: Implications for early-time new physics and the Hubble tension", Physical Reviews D **104**, 063524 (2021).

[127] J. C. Hill, E. Calabrese, S. Aiola, et al., "Atacama cosmology telescope: constraints on prerecombination early dark energy", Physical Review D **105**, `10.1103/physrevd.105.123536` (2022).

[128] V. Poulin, T. L. Smith, and A. Bartlett, "Dark energy at early times and act data: a larger hubble constant without late-time priors", Physical Review D **104** (2021).

[129] A. La Posta, T. Louis, X. Garrido, et al., "Constraints on prerecombination early dark energy from spt-3g public data", Physical Review D **105** (2022).

[130] T. L. Smith, M. Lucca, V. Poulin, et al., "Hints of early dark energy in planck, spt, and act data: new physics or systematics?", Physical Review D **106** (2022).

[131] S. Kumar, R. C. Nunes, and S. K. Yadav, "Dark sector interaction: a remedy of the tensions between CMB and LSS data", European Physics Joural C **79**, 576 (2019).

[132] E. Di Valentino, A. Melchiorri, O. Mena, et al., "Interacting dark energy in the early 2020s: A promising solution to the H_0 and cosmic shear tensions", Physics of the Dark Universe **30**, 100666 (2020).

[133] E. Di Valentino, A. Melchiorri, O. Mena, et al., "Nonminimal dark sector physics and cosmological tensions", Physical Review D **101**, 063502 (2020).

[134] L. Giani, C. Howlett, K. Said, et al., "An effective description of Laniakea: impact on cosmology and the local determination of the Hubble constant", Journal of Cosmology and Astroparticle Physics 01, 071 (2024).

[135] M. Lucca, "Dark energy–dark matter interactions as a solution to the S8 tension", Physics of the Dark Universe **34**, 100899 (2021).

[136] T. Clifton, P. G. Ferreira, A. Padilla, et al., "Modified Gravity and Cosmology", Physical Reports **513**, 1–189 (2012).

[137] E. P. Verlinde, "On the Origin of Gravity and the Laws of Newton", Journal of High Energy Physics **04**, 029 (2011).

[138] E. P. Verlinde, "Emergent Gravity and the Dark Universe", SciPost Physics **2**, 016 (2017).

[139] T. P. Sotiriou and V. Faraoni, "$f(R)$ Theories of gravity", Reviews of Modern Physics **82**, 451–497 (2010).

[140] A. Giusti, "MOND-like fractional Laplacian theory", Physical Review D. D **101**, 124029 (2020).

[141] F. Benetti, A. Lapi, G. Gandolfi, et al., "Dark matter in fractional gravity. i. astrophysical tests on galactic scales", Astrophysical Journal **949**, 65 (2023).

[142] T. Padmanabhan and D. Kothawala, "Lanczos-Lovelock models of gravity", Physics Reports **531**, 115–171 (2013).

[143] J. W. Moffat, "Scalar–tensor–vector gravity theory", Journal of Cosmology and Astroparticle Physics 03, 004 (2006).

[144] J. W. Moffat and S. Rahvar, "The MOG weak field approximation and observational test of galaxy rotation curves", Monthly Notices of the Royal Astronomical Society **436**, 1439–1451 (2013).

[145] J. Oppenheim and Z. Weller-Davies, "Covariant path integrals for quantum fields back-reacting on classical space-time", arXiv:2302.07283 (2023).

[146] J. Oppenheim, E. Panella, and A. Pontzen, "Emergence of phantom cold dark matter from spacetime diffusion", arXiv:2407.13820 (2024).

[147] J. Magueijo and L. Smolin, "Gravity's rainbow", Classical and Quantum Gravity **21** (2004).

[148] G. F. R. Ellis, "Relativistic cosmology: its nature, aims and problems.", in General relativity and gravitation conference (1984), pp. 215–288.

[149] G. F. R. Ellis and W. Stoeger, "The 'fitting problem' in cosmology", Classical and Quantum Gravity **4**, 1697–1729 (1987).

[150] A. Krasiński, *Inhomogeneous cosmological models* (Cambridge Univ. Press, Cambridge, UK, 1997).

[151] K. Bolejko, A. Krasiński, C. Hellaby, et al., *Structures in the Universe by Exact Methods: Formation, Evolution, Interactions*, Cambridge Monographs on Mathematical Physics (Cambridge Univ. Press, Cambridge, UK, 2010).

[152] J. Plebański and A. Krasiński, *An introduction to general relativity and cosmology* (Cambridge Univ. Press, Cambridge, UK, 2006).

[153] C. W. Misner and D. H. Sharp, "Relativistic equations for adiabatic, spherically symmetric gravitational collapse", Physical Review **136**, B571 (1964).

[154] R. A. Sussman, "Quasi-local variables and inhomogeneous cosmological sources with spherical symmetry.", in Gravitation and cosmology, Vol. 1083, American Institute of Physics Conference Series (2008), pp. 228–235.

[155] G. Lemaitre, "The expanding universe", Annales de la Société Scientifique de Bruxelles **53**, 51–85 (1933).

[156] R. C. Tolman, "Effect of inhomogeneity on cosmological models", Proceedings of the National Academy of Sciences **20**, 169–176 (1934).

[157] H. Bondi, "Spherically symmetrical models in general relativity", Monthly Notices of the Royal Astronomical Society **107**, 410–425 (1947).

[158] M.-N. Célérier, K. Bolejko, and A. Krasiński, "A (giant) void is not mandatory to explain away dark energy with a Lemaitre – Tolman model", Astron. Astrophys. **518**, A21 (2010).

[159] P. Szekeres, "A class of inhomogeneous cosmological models", Communications in Mathematical Physics **41**, 55–64 (1975).

[160] P. Szekeres, "Quasispherical Gravitational Collapse", Physical Review D **12**, 2941 (1975).

[161] R. Kantowski and R. K. Sachs, "Some spatially homogeneous anisotropic relativistic cosmological models", Journal of Mathematical Physics **7**, 443 (1966).

[162] D. Eardley, E. Liang, and R. Sachs, "Velocity dominated singularities in irrotational dust cosmologies", Journal of Mathematical Physics **13**, 99–106 (1972).

[163] K. Bolejko, "Cosmological backreaction within the Szekeres model and emergence of spatial curvature", Journal of Cosmology and Astroparticle Physics 06, 025 (2017).

[164] A. Y. Kamenshchik and C. M. F. Mingarelli, "A Generalized Heckmann-Schucking cosmological solution in the presence of a negative cosmological constant", Physics Letters B **693**, 213–217 (2010).

[165] J. R. Gott, M. Juric, D. Schlegel, et al., "A map of the universe", Astrophysical Journal **624**, 463 (2005).

[166] D. L. Wiltshire, "Cosmic Structure, Averaging and Dark Energy", in *Proceedings of the XVth Brazilian School of Cosmology and Gravitation* (Cambridge Scientific Publishers, Cambridge, UK, 2014), pp. 203–244, arXiv:1311.3787.

[167] I. Zlatev, L.-M. Wang, and P. J. Steinhardt, "Quintessence, cosmic coincidence, and the cosmological constant", Physical Review Letters **82**, 896–899 (1999).

[168] C. Clarkson, G. Ellis, J. Larena, et al., "Does the growth of structure affect our dynamical models of the universe? The averaging, backreaction and fitting problems in cosmology", Reports on Progress in Physics **74**, 112901 (2011).

[169] C. Clarkson and O. Umeh, "Is backreaction really small within concordance cosmology?", Classical Quantum Gravity **28**, 164010 (2011).

[170] T. Buchert, "On average properties of inhomogeneous fluids in general relativity. 1. Dust cosmologies", General Relativity and Gravitation **32**, 105–125 (2000).

[171] T. Buchert, "On average properties of inhomogeneous fluids in general relativity II: perfect fluid cosmologies", General Relativity and Gravitation **33**, 1381–1405 (2001).

[172] T. Buchert, P. Mourier, and X. Roy, "On average properties of inhomogeneous fluids in general relativity III: general fluid cosmologies", General Relativity and Gravitation **52**, 27 (2020).

[173] T. Buchert, H. van Elst, and A. Heinesen, "The averaging problem on the past null cone in inhomogeneous dust cosmologies", General Relativity and Gravitation **55**, 7 (2023).

[174] R. L. Arnowitt, S. Deser, and C. W. Misner, "The dynamics of general relativity", in *Gravitation: An introduction to current research* (Wiley, New York, USA, 1962), pp. 203–244, Republished in *General Relativity and Gravitation* **40** (2008) 1997–2027 [arXiv:gr-qc/0405109].

[175] É. Gourgoulhon, *3+1 Formalism in General Relativity: Bases of Numerical Relativity*, Lecture Notes in Physics (Springer-Verlag, Berlin, Germany, 2007), arXiv:gr-qc/0703035.

[176] E. W. Kolb, S. Matarrese, A. Notari, et al., "The effect of inhomogeneities on the expansion rate of the universe", Physical Review D **71**, 023524 (2005).

[177] E. R. Siegel and J. N. Fry, "Effects of inhomogeneities on cosmic expansion", Astrophysical Journal Letters **628**, L1–L4 (2005).

[178] A. Ishibashi and R. M. Wald, "Can the acceleration of our universe be explained by the effects of inhomogeneities?", Classical Quantum Gravity **23**, 235–250 (2006).

[179] S. R. Green and R. M. Wald, "A new framework for analyzing the effects of small scale inhomogeneities in cosmology", Physical Reviews D **83**, 084020 (2011).

[180] S. R. Green and R. M. Wald, "How well is our universe described by an FLRW model?", Classical and Quantum Gravity **31**, 234003 (2014).

[181] T. Buchert et al., "Is there proof that backreaction of inhomogeneities is irrelevant in cosmology?", Classical Quantum Gravity **32**, 215021 (2015).

[182] T. Clifton and R. A. Sussman, "Cosmological Backreaction in Spherical and Plane Symmetric Dust-Filled Space-Times", Classical Quantum Gravity **36**, 205004 (2019).

[183] D. L. Wiltshire, "Cosmic clocks, cosmic variance and cosmic averages", New Journal of Physics **9**, 377 (2007).

[184] D. L. Wiltshire, "Exact solution to the averaging problem in cosmology", Physical Review Letters **99**, 251101 (2007).

[185] J. A. G. Duley, M. A. Nazer, and D. L. Wiltshire, "Timescape cosmology with radiation fluid", Classical and Quantum Gravity **30**, 175006 (2013).

[186] D. L. Wiltshire, "Cosmological equivalence principle and the weak-field limit", Physical Review D **78**, 084032 (2008).

[187] D. L. Wiltshire, "Average observational quantities in the timescape cosmology", Physical Review D **80**, 123512 (2009).

[188] M. Milgrom, "A modification of the Newtonian dynamics: implications for galaxy systems", Astrophysical Journal **270**, 384–389 (1983).

[189] M. Milgrom, "A Modification of the Newtonian dynamics: Implications for galaxies", Astrophysical Journal **270**, 371–383 (1983).

[190] M. Milgrom, "A modification of the Newtonian dynamics as a possible alternative to the hidden mass hypothesis.", Astrophysical Journal **270**, 365–370 (1983).

[191] B. Famaey and S. S. McGaugh, "Modified Newtonian Dynamics (MOND): Observational Phenomenology and Relativistic Extensions", Living Reviews in Relativity **15**, 10 (2012).

[192] J. D. Bekenstein, "Relativistic gravitation theory for the MOND paradigm", Physical Review D **70**, 083509 (2004), [Erratum: Physical Review D 71, 069901 (2005)].

[193] C. Skordis, "Generalizing tensor-vector-scalar cosmology", Physical Review D **77**, 123502 (2008).

[194] M. Milgrom, "Bimetric MOND gravity", Physical Review D **80**, 123536 (2009).

[195] M. Milgrom, "Cosmological fluctuation growth in bimetric MOND", Physical Review D **82**, 043523 (2010).

[196] M. Milgrom, "Matter and twin matter in bimetric MOND", Monthly Notices of the Royal Astronomical Society **405**, 1129 (2010).

[197] T. G. Zlosnik, P. G. Ferreira, and G. D. Starkman, "Modifying gravity with the aether: An alternative to dark matter", Physical Review D **75**, 044017 (2007).

[198] H. Haghi, A. E. Bazkiaei, A. H. Zonoozi, et al., "Declining rotation curves of galaxies as a test of gravitational theory", Monthly Notices of the Royal Astronomical Society **458**, 4172–4187 (2016).

[199] R. H. Sanders, "The prediction of rotation curves in gas-dominated dwarf galaxies with modified dynamics", Monthly Notices of the Royal Astronomical Society **485**, 513–521 (2019).

[200] Y. Zhu, H.-X. Ma, X.-B. Dong, et al., "How close dark matter haloes and MOND are to each other: three-dimensional tests based on Gaia DR2", Monthly Notices of the Royal Astronomical Society **519**, 4479–4498 (2023).

[201] X. Hernandez, V. Verteletskyi, L. Nasser, et al., "Statistical analysis of the gravitational anomaly in gaia wide binaries", Monthly Notices of the Royal Astronomical Society **528**, 4720–4732 (2023).

[202] K.-H. Chae, "Robust Evidence for the Breakdown of Standard Gravity at Low Acceleration from Statistically Pure Binaries Free of Hidden Companions", Astrophysical Journal **960**, 114 (2024).

[203] F. Lelli, S. S. McGaugh, J. M. Schombert, et al., "One law to rule them all: the radial acceleration relation of galaxies", Astrophysical Journal **836**, 152 (2017).

[204] T. Mistele, S. McGaugh, F. Lelli, et al., "Radial acceleration relation of galaxies with joint kinematic and weak-lensing data", Journal of Cosmology and Astroparticle Physics 04, 020 (2024).

[205] R. Scarpa, R. Falomo, and A. Treves, "On the orbital velocity of isolated galaxy pairs: II accurate MOND predictions", Monthly Notices of the Royal Astronomical Society **512**, 544–547 (2022).

[206] S. S. McGaugh, J. M. Schombert, F. Lelli, et al., "Accelerated structure formation: the early emergence of massive galaxies and clusters of galaxies", Astrophysical Journal **976**, 13 (2024).

[207] M. Milgrom, "Testing the mond paradigm of modified dynamics with galaxy-galaxy gravitational lensing", Physical Review Letters **111**, 041105 (2013).

[208] T. Mistele, S. McGaugh, F. Lelli, et al., "Indefinitely Flat Circular Velocities and the Baryonic Tully–Fisher Relation from Weak Lensing", Astrophysical Journal Letters **969**, L3 (2024).

[209] R. H. Sanders, "A Faber-Jackson relation for clusters of galaxies: implications for modified dynamics.", Astronomy & Astrophysics **284**, L31–L34 (1994).

[210] B. Famaey, L. Pizzuti, and I. D. Saltas, "On the nature of the missing mass of galaxy clusters in MOND: the view from gravitational lensing", arXiv:2410.02612 (2024).

[211] D. Walsh, R. F. Carswell, and R. J. Weymann, "0957 + 561 A, B: twin quasistellar objects or gravitational lens?", Nature **279**, 381–384 (1979).

[212] S. Refsdal, "On the possibility of determining Hubble's parameter and the masses of galaxies from the gravitational lens effect", Monthly Notices of the Royal Astronomical Society **128**, 307 (1964).

[213] I. I. Shapiro, "Fourth Test of General Relativity", Physical Review Letters **13**, 789–791 (1964).

[214] X. Huang et al., "DESI Strong Lens Foundry I: HST Observations and Modeling with GIGA-Lens", arXiv:2502.03455 (2025).

[215] Y. Chen, R. Li, Y. Shu, et al., "Assessing the effect of lens mass model in cosmological application with updated galaxy-scale strong gravitational lensing sample", Monthly Notices of the Royal Astronomical Society **488**, 3745–3758 (2019).

[216] P. L. Kelly et al., "Constraints on the Hubble constant from supernova Refsdal's reappearance", Science **380**, abh1322 (2023).

[217] M. Pascale et al., "SN H0pe: The First Measurement of H_0 from a Multiply Imaged Type Ia Supernova, Discovered by JWST", Astrophysical Journal **979**, 13 (2025).

[218] J. D. R. Pierel et al., "Lensed Type Ia Supernova "Encore" at z = 2: The First Instance of Two Multiply Imaged Supernovae in the Same Host Galaxy", Astrophysical Journal Letters **967**, L37 (2024).

[219] P. Schneider, C. S. Kochanek, and J. Wambsganss, *Gravitational lensing: strong, weak and micro*, 1st ed. (Springer, 2006).

[220] P. Schneider, J. Ehlers, and E. E. Falco, *Gravitational Lenses* (Springer-Verlag, 1992).

[221] M. Meneghetti, *Introduction to Gravitational Lensing: With Python Examples* (Springer International Publishing, 2022).

[222] P. Saha, D. Sluse, J. Wagner, et al., "Essentials of Strong Gravitational Lensing", Space Science Reviews **220**, 12 (2024).

[223] T. Treu, "Strong Lensing by Galaxies", Annual Review of Astronomy and Astrophysics **48**, 87–125 (2010).

[224] S. Birrer, M. Millon, D. Sluse, et al., "Time-Delay Cosmography: Measuring the Hubble Constant and Other Cosmological Parameters with Strong Gravitational Lensing", Space Science Reviews **220**, 48 (2024).

[225] T. Treu and A. J. Shajib, "Strong Lensing and H_0", arXiv:2307.05714 (2023).

[226] J. Prat and D. Bacon, "Weak Gravitational Lensing", arXiv:2501.07938 (2025).

[227] R. Blandford and R. Narayan, "Fermat's Principle, Caustics, and the Classification of Gravitational Lens Images", Astrophysical Journal **310**, 568 (1986).

[228] C. M. O'Riordan, L. J. Oldham, A. Nersesian, et al. (Euclid collaboration), "Euclid: A complete Einstein ring in NGC 6505", Astronomy & Astrophysics **694**, A145 (2025).

[229] W. L. Burke, "Multiple Gravitational Imaging by Distributed Masses", Astrophysical Journal Letters **244**, L1 (1981).

[230] S. Birrer, A. Amara, and A. Refregier, "The mass-sheet degeneracy and time-delay cosmography: Analysis of the strong lens RXJ1131-1231", Journal of Cosmology and Astroparticle Physics 08, 020 (2016).

[231] J.-P. Kneib and P. Natarajan, "Cluster Lenses", Astronomy and Astrophysics Review **19**, 47 (2011).

[232] A. M. Koekemoer, J. Mack, J. M. Lotz, et al., "The Hubble Space Telescope Frontier Fields Program", AAS/High Energy Astrophysics Division **16**, 105.23 (2017).

[233] A. Pagul, F. J. Sánchez, I. Davidzon, et al., "Hubble Frontier Field Clusters and Their Parallel Fields: Photometric and Photometric Redshift Catalogs", Astrophysical Journal Supplement Series **256**, 27 (2021).

[234] M. Postman, D. Coe, N. Benítez, et al., "The Cluster Lensing and Supernova Survey with Hubble: An Overview", Astrophysical Journal Supplement Series **199**, 25 (2012).

[235] J. M. Lotz, A. Koekemoer, D. Coe, et al., "The Frontier Fields: Survey Design and Initial Results", Astrophysical Journal **837**, 97 (2017).

[236] B. Salmon, D. Coe, L. Bradley, et al., "RELICS: The Reionization Lensing Cluster Survey and the Brightest High-z Galaxies", Astrophysical Journal **889**, 189 (2020).

[237] D. Coe, B. Salmon, M. Bradač, et al., "RELICS: Reionization Lensing Cluster Survey", Astrophysical Journal **884**, 85 (2019).

[238] B. Salmon, D. Coe, L. Bradley, et al., "RELICS: A Candidate z $\sim$ 10 Galaxy Strongly Lensed into a Spatially Resolved Arc", Astrophysical Journal Letters **864**, L22 (2018).

[239] C. L. Steinhardt, M. Jauzac, A. Acebron, et al., "The BUFFALO HST Survey", Astrophysical Journal Supplement Series **247**, 64 (2020).

[240] P. L. Kelly, G. Brammer, J. Selsing, et al., "SN Refsdal: Classification as a Luminous and Blue SN 1987A-like Type II Supernova", Astrophysical Journal **831**, 205 (2016).

[241] P. L. Kelly et al., "Deja Vu All Over Again: The Reappearance of Supernova Refsdal", Astrophysical Journal Letters **819**, L8 (2016).

[242] A. Goobar et al., "iPTF16geu: A multiply imaged, gravitationally lensed type Ia supernova", Science **356**, 291–295 (2017).

[243] S. A. Rodney, G. B. Brammer, J. D. R. Pierel, et al., "A gravitationally lensed supernova with an observable two-decade time delay", Nature Astronomy **5**, 1118–1125 (2021).

[244] J. D. R. Pierel, B. L. Frye, M. Pascale, et al., "JWST Photometric Time-delay and Magnification Measurements for the Triply Imaged Type Ia "SN H0pe" at z = 1.78", Astrophysical Journal **967**, 50 (2024).

[245] C. Grillo, L. Pagano, P. Rosati, et al., "Cosmography with supernova Refsdal through time-delay cluster lensing: Independent measurements of the Hubble constant and geometry of the Universe", Astronomy & Astrophysics **684**, L23 (2024).

[246] S. H. Suyu et al., "HOLISMOKES – I. Highly Optimised Lensing Investigations of Supernovae, Microlensing Objects, and Kinematics of Ellipticals and Spirals", Astronomy & Astrophysics **644**, A162 (2020).

[247] F. Courbin, A. Eigenbrod, C. Vuissoz, et al., "COSMOGRAIL: the COSmological MOnitoring of GRAvItational Lenses", in Gravitational lensing impact on cosmology, Vol. 225, IAU Symposium (2005), pp. 297–303.

[248] M. Millon, F. Courbin, V. Bonvin, et al., "COSMOGRAIL: XIX. Time delays in 18 strongly lensed quasars from 15 years of optical monitoring", Astronomy & Astrophysics **640**, A105 (2020).

[249] K. C. Wong, S. H. Suyu, G. C.-F. Chen, et al., "H0LiCOW XIII. A 2.4% measurement of H_0 from lensed quasars: 5.3σ tension between early and late-Universe probes", Monthly Notices of the Royal Astronomical Society **498**, 1420–1439 (2020).

[250] S. H. Suyu, V. Bonvin, F. Courbin, et al., "H0LiCOW I. H_0 Lenses in COSMOGRAIL's Wellspring: Program Overview", Monthly Notices of the Royal Astronomical Society **468**, 2590–2604 (2017).

[251] C. E. Rusu, K. C. Wong, V. Bonvin, et al., "H0LiCOW XII. Lens mass model of WFI2033-4723 and blind measurement of its time-delay distance and H_0", Monthly Notices of the Royal Astronomical Society **498**, 1440–1468 (2019).

[252] G. C.-F. Chen, C. D. Fassnacht, S. H. Suyu, et al., "A SHARP view of H0LiCOW: H_0 from three time-delay gravitational lens systems with adaptive optics imaging", Monthly Notices of the Royal Astronomical Society **490**, 1743–1773 (2019).

[253] S. Birrer, T. Treu, C. E. Rusu, et al., "H0LiCOW - IX. Cosmographic analysis of the doubly imaged quasar SDSS 1206+4332 and a new measurement of the Hubble constant", Monthly Notices of the Royal Astronomical Society **484**, 4726–4753 (2019).

[254] C. Lemon, M. W. Auger, R. McMahon, et al., "The STRong lensing Insights into the Dark Energy Survey (STRIDES) 2017/2018 follow-up campaign: discovery of 10 lensed quasars and 10 quasar pairs", Monthly Notices of the Royal Astronomical Society **494**, 3491–3511 (2020).

[255] A. J. Shajib, S. Birrer, T. Treu, et al., "STRIDES: a 3.9 per cent measurement of the Hubble constant from the strong lens system DES J0408-5354", Monthly Notices of the Royal Astronomical Society **494**, 6072–6102 (2020).

[256] M. Millon, A. Galan, F. Courbin, et al., "TDCOSMO. I. An exploration of systematic uncertainties in the inference of H_0 from time-delay cosmography", Astronomy & Astrophysics **639**, A101 (2020).

[257] S. Birrer, A. J. Shajib, A. Galan, et al., "TDCOSMO. IV. Hierarchical time-delay cosmography - joint inference of the Hubble constant and galaxy density profiles", Astronomy & Astrophysics **643**, A165 (2020).

[258] G. C. Chen, C. D. Fassnacht, S. H. Suyu, et al., "TDCOSMO. VI. Distance measurements in time-delay cosmography under the mass-sheet transformation", Astronomy & Astrophysics **652**, A7 (2021).

[259] A. J. Shajib, P. Mozumdar, G. C. .-. Chen, et al., "TDCOSMO. XII. Improved Hubble constant measurement from lensing time delays using spatially resolved stellar kinematics of the lens galaxy", Astronomy & Astrophysics **673**, A9 (2023).

[260] D. J. Lagattuta, M. W. Auger, and C. D. Fassnacht, "Adaptive Optics Observations of B0128+437: A Low-mass, High-redshift Gravitational Lens", Astrophysical Journal Letters **716**, L185–L189 (2010).

[261] C. Y. Tan, A. J. Shajib, S. Birrer, et al., "Project Dinos I: A joint lensing-dynamics constraint on the deviation from the power law in the mass profile of massive ellipticals", Monthly Notices of the Royal Astronomical Society **530**, 1474–1505 (2024).

[262] R. Kormann, P. Schneider, and M. Bartelmann, "Isothermal elliptical gravitational lens models.", Astronomy & Astrophysics **284**, 285–299 (1994).

[263] J. F. Navarro, V. R. Eke, and C. S. Frenk, "The cores of dwarf galaxy haloes", Monthly Notices of the Royal Astronomical Society **283**, L72–L78 (1996).

[264] J. F. Navarro, V. R. Eke, and C. S. Frenk, "The cores of dwarf galaxy haloes", Monthly Notices of the Royal Astronomical Society **283**, L72–L78 (1996).

[265] S. Birrer and A. Amara, "lenstronomy: Multi-purpose gravitational lens modelling software package", Physics of the Dark Universe **22**, 189–201 (2018).

[266] A. Burkert, "The Structure of Dark Matter Halos in Dwarf Galaxies", Astrophysical Journal Letters **447**, L25–L28 (1995).

[267] P. Salucci, "The distribution of dark matter in galaxies", Annual Reviews of Astronomy and Astrophysics **27** (2019).

[268] A. A. Dutton, B. J. Brewer, P. J. Marshall, et al., "The SWELLS survey – II. Breaking the disc–halo degeneracy in the spiral galaxy gravitational lens SDSS J2141-0001*", Monthly Notices of the Royal Astronomical Society **417**, 1621–1642 (2011).

[269] B. J. Brewer, P. J. Marshall, M. W. Auger, et al., "The SWELLS survey - VI. Hierarchical inference of the initial mass functions of bulges and discs", Monthly Notices of the Royal Astronomical Society **437**, 1950–1961 (2014).

[270] T. E. Collett, "The population of galaxy–galaxy strong lenses in forthcoming optical imaging surveys", Astrophysical Journal **811**, 20 (2015).

[271] T. Buchert, A. A. Coley, H. Kleinert, et al., "Observational Challenges for the Standard FLRW Model", International Journal of Modern Physics D **25**, 1630007 (2016).

[272] P. J. E. Peebles, "Anomalies in Physical Cosmology", Annals of Physics **447**, 169159 (2022).

[273] S. Cao, M. Biesiada, R. Gavazzi, et al., "Cosmology with Strong Lensing Systems", Astrophysical Journal **806**, 185 (2015).

[274] S. Räsänen, K. Bolejko, and A. Finoguenov, "New test of the FLRW metric using the distance sum rule", Physical Review Letters **115**, 101301 (2015).

[275] K. Liao, Z. Li, G.-J. Wang, et al., "Test of the FLRW metric and curvature with strong lens time delays", Astrophysical Journal **839**, 70 (2017).

[276] J. Qi, S. Cao, M. Biesiada, et al., "Strongly gravitationally lensed type Ia supernovae: Direct test of the Friedman-Lemaître-Robertson-Walker metric", Physical Review D **100**, 023530 (2019).

[277] V. F. Cardone, E. Piedipalumbo, and P. Scudellaro, "Cosmological parameters from lenses distance ratio", Monthly Notices of the Royal Astronomical Society **455**, 831–837 (2016).

[278] A. G. Riess, G. S. Anand, W. Yuan, et al., "Crowded No More: The Accuracy of the Hubble Constant Tested with High Resolution Observations of Cepheids by JWST", arXiv:2307.15806 (2023).

[279] D. J. Eisenstein, I. Zehavi, D. W. Hogg, et al., "Detection of the Baryon Acoustic Peak in the Large-Scale Correlation Function of SDSS Luminous Red Galaxies", Astrophysical Journal **633**, 560–574 (2005).

[280] F. Sylos Labini, N. L. Vasilyev, L. Pietronero, et al., "Absence of self-averaging and of homogeneity in the large-scale galaxy distribution", EPL (Europhysics Letters) **86**, 49001 (2009).

[281] D. L. Wiltshire, "From time to timescape - Einstein's unfinished revolution", International Journal of Modern Physics D **18**, 2121–2134 (2009).

[282] B. M. Leith, S. C. C. Ng, and D. L. Wiltshire, "Gravitational energy as dark energy: concordance of cosmological tests", Astrophysical Journal **672**, L91–L94 (2007).

[283] P. R. Smale and D. L. Wiltshire, "Supernova tests of the timescape cosmology", Monthly Notices of the Royal Astronomical Society **413**, 367–385 (2011).

[284] L. H. Dam, A. Heinesen, and D. L. Wiltshire, "Apparent cosmic acceleration from type Ia supernovae", Monthly Notices of the Royal Astronomical Society **472**, 835–851 (2017).

[285] Z. G. Lane, A. Seifert, R. Ridden-Harper, et al., "Cosmological foundations revisited with pantheon+", Monthly Notices of the Royal Astronomical Society **536**, 1752–1777 (2025).

[286] J. Larena, J.-M. Alimi, T. Buchert, et al., "Testing backreaction effects with observations", Physical Review D **79**, 083011 (2009).

[287] T. Treu and L. Koopmans, "The internal structure and formation of early-type galaxies: the gravitational–lens system MG2016+112 at z=1.004", Astrophysical Journal **575**, 87–94 (2002).

[288] T. Treu and L. V. E. Koopmans, "Massive Dark-matter halos and Evolution of Early-type Galaxies to z=1", Astrophysical Journal **611**, 739–760 (2004).

[289] L. V. E. Koopmans and T. Treu, "The stellar velocity dispersion of the lens galaxy in MG2016+112 at z=1.004", Astrophysical Journal **568**, L5–L8 (2002).

[290] L. V. E. Koopmans and T. Treu, "The Structure and Dynamics of Luminous and Dark Matter in the Early-Type Lens Galaxy of 0047-281 at z=0.485", Astrophysical Journal **583**, 606–615 (2003).

[291] A. J. Ruff, R. Gavazzi, P. J. Marshall, et al., "The SL2S Galaxy-scale Lens Sample. II. Cosmic evolution of dark and luminous mass in early-type galaxies", Astrophysical Journal **727**, 96 (2011).

[292] A. Sonnenfeld, R. Gavazzi, S. H. Suyu, et al., "The SL2S Galaxy-scale Lens Sample. III. Lens Models, Surface Photometry and Stellar Masses for the final sample", Astrophysical Journal **777**, 97 (2013).

[293] A. Sonnenfeld, T. Treu, R. Gavazzi, et al., "The SL2S Galaxy-scale Lens Sample. IV. The dependence of the total mass density profile of early-type galaxies on redshift, stellar mass, and size", Astrophysical Journal **777**, 98 (2013).

[294] A. Sonnenfeld, T. Treu, P. J. Marshall, et al., "The SL2S Galaxy-scale Lens Sample. V. Dark Matter Halos and Stellar IMF of Massive Early-type Galaxies out to Redshift 0.8", Astrophysical Journal **800**, 94 (2015).

[295] A. S. Bolton, S. Burles, L. V. E. Koopmans, et al., "The Sloan Lens ACS Survey. V. The Full ACS Strong-Lens Sample", Astrophysical Journal **682**, 964–984 (2008).

[296] M. W. Auger, T. Treu, A. S. Bolton, et al., "The Sloan Lens ACS Survey. IX. Colors, Lensing and Stellar Masses of Early-type Galaxies", Astrophysical Journal **705**, 1099–1115 (2009).

[297] M. W. Auger, T. Treu, A. S. Bolton, et al., "The Sloan Lens ACS Survey. X. Stellar, Dynamical, and Total Mass Correlations of Massive Early-type Galaxies", Astrophysical Journal **724**, 511–525 (2010).

[298] Y. Shu, J. R. Brownstein, A. S. Bolton, et al., "The Sloan Lens ACS Survey. XIII. Discovery of 40 New Galaxy-Scale Strong Lenses", Astrophysical Journal **851**, 48 (2017).

[299] Y. Shu, A. S. Bolton, J. R. Brownstein, et al., "The Sloan Lens ACS Survey. XII. Extending Strong Lensing to Lower Masses", Astrophysical Journal **803**, 71 (2015).

[300] J. R. Brownstein, A. S. Bolton, D. J. Schlegel, et al., "The BOSS Emission-Line Lens Survey (BELLS). I. A large spectroscopically selected sample of Lens Galaxies at redshift ~ 0.5", Astrophysical Journal **744**, 41 (2012).

[301] Y. Shu, A. S. Bolton, C. S. Kochanek, et al., "The BOSS Emission-Line Lens Survey. III. : Strong Lensing of Lyα Emitters by Individual Galaxies", Astrophysical Journal **824**, 86 (2016).

[302] Y. Shu, A. S. Bolton, S. Mao, et al., "The BOSS Emission-Line Lens Survey. IV. : Smooth Lens Models for the BELLS GALLERY Sample", Astrophysical Journal **833**, 264 (2016).

[303] I. Jorgensen, M. Franx, and P. Kjaergaard, "Spectroscopy for E and S0 galaxies in nine clusters", Monthly Notices of the Royal Astronomical Society **276**, 1341–1364 (1995).

[304] M. Cappellari, R. Bacon, M. Bureau, et al., "The SAURON project - IV. The mass-to-light ratio, the virial mass estimator and the fundamental plane of elliptical and lenticular galaxies", Monthly Notices of the Royal Astronomical Society **366**, 1126–1150 (2006).

[305] D. Mehlert, D. Thomas, R. P. Saglia, et al., "Spatially resolved spectroscopy of Coma cluster early-type galaxies - III. The stellar population gradients", Astronomy & Astrophysics **407**, 423–435 (2003).

[306] M. Bernardi, R. K. Sheth, J. Annis, et al., "Early-Type Galaxies in the Sloan Digital Sky Survey. I. The Sample", Astronomical Journal **125**, 1817 (2003).

[307] J. F. Navarro, C. S. Frenk, and S. D. M. White, "The Structure of Cold Dark Matter Halos", Astrophysical Journal **462**, 563 (1996).

[308] J. Wagner, "Self-gravitating dark matter gets in shape", International Journal of Modern Physics D **29**, 2043017 (2020).

[309] L. V. E. Koopmans, "Gravitational Lensing & Stellar Dynamics", EAS Publications Series **20**, 161–166 (2006).

[310] R. Trotta, "Bayesian Methods in Cosmology", arXiv:1701.01467 (2017).

[311] A. Aghamousa and A. Shafieloo, "Nonparametric test of consistency between cosmological models and multiband CMB measurements", Journal of Cosmology and Astroparticle Physics **06**, 003 (2015).

[312] S. Alam, M. Ata, S. Bailey, et al., "The clustering of galaxies in the completed SDSS-III Baryon Oscillation Spectroscopic Survey: cosmological analysis of the DR12 galaxy sample", Monthly Notices of the Royal Astronomical Society **470**, 2617–2652 (2017).

[313] T. Delubac, J. E. Bautista, N. G. Busca, et al., "Baryon Acoustic Oscillations in the Ly{\alpha} forest of BOSS DR11 quasars", Astronomy & Astrophysics **574**, A59 (2015).

[314] R. E. Kass and A. E. Raftery, "Bayes Factors", Journal of the American Statistical Association **90**, 773–795 (1995).

[315] R. Trotta, "Applications of Bayesian model selection to cosmological parameters", Monthly Notices of the Royal Astronomical Society **378**, 72–82 (2007).

[316] E. Di Valentino, O. Mena, S. Pan, et al., "In the realm of the hubble tension—a review of solutions", Classical and Quantum Gravity **38**, 153001 (2021).

[317] F. Melia, J.-J. Wei, and X.-F. Wu, "Model selection using time-delay lenses", Monthly Notices of the Royal Astronomical Society **519**, 2528–2534 (2022).

[318] S. H. Suyu, "Cosmography from two-image lens systems: overcoming the lens profile slope degeneracy", Monthly Notices of the Royal Astronomical Society **426**, 868–879 (2012).

[319] D. Rusin, C. S. Kochanek, and C. R. Keeton, "Self-similar Models for the Mass Profiles of Early-Type Lens Galaxies", Astrophysical Journal **595**, 29–42 (2003).

[320] S. H. Suyu, S. W. Hensel, J. P. McKean, et al., "Disentangling baryons and dark matter in the spiral gravitational lens b1933+503", Astrophysical Journal **750**, 10 (2012).

[321] J. Buchner, A. Georgakakis, K. Nandra, et al., "X-ray spectral modelling of the AGN obscuring region in the CDFS: Bayesian model selection and catalogue", Astronomy & Astrophysics **564**, A125 (2014).

[322] W. Sheu, A. J. Shajib, T. Treu, et al., "Project Dinos II: Redshift evolution of dark and luminous matter density profiles in strong-lensing elliptical galaxies across $0.1 < z < 0.9$", arXiv:2408.10316 (2024).

[323] C. D. Fassnacht, T. J. Pearson, A. C. S. Readhead, et al., "A Determination of H_0 with the CLASS Gravitational Lens B1608+656. I. Time Delay Measurements with the VLA", Astrophysical Journal **527**, 498–512 (1999).

[324] C. D. Fassnacht, E. Xanthopoulos, L. V. E. Koopmans, et al., "A Determination of H_0 with the CLASS Gravitational Lens B1608+656. III. A Significant Improvement in the Precision of the Time Delay Measurements", Astrophysical Journal **581**, 823–835 (2002).

[325] S. H. Suyu, P. J. Marshall, R. D. Blandford, et al., "Dissecting the Gravitational Lens B1608+656. I. Lens Potential Reconstruction", Astrophysical Journal **691**, 277–298 (2009).

[326] S. T. Myers, C. D. Fassnacht, S. G. Djorgovski, et al., "1608+656: A Quadruple-Lens System Found in the CLASS Gravitational Lens Survey", Astrophysical Journal Letters **447**, L5 (1995).

[327] C. D. Fassnacht, D. S. Womble, G. Neugebauer, et al., "1608+656: A Gravitationally Lensed Poststarburst Radio Galaxy", Astrophysical Journal Letters **460**, L103 (1996).

[328] I. Jee, S. H. Suyu, E. Komatsu, et al., "A measurement of the Hubble constant from angular diameter distances to two gravitational lenses", Science **365**, 1134–1138 (2019).

[329] L. Wisotzki, P. L. Schechter, H. V. Bradt, et al., "HE 0435-1223: A wide separation quadruple QSO and gravitational lens", Astronomy & Astrophysics **395**, 17–23 (2002).

[330] A. Eigenbrod, F. Courbin, G. Meylan, et al., "COSMOGRAIL: the COSmological MOnitoring of GRAvItational Lenses. III. Redshift of the lensing galaxy in eight gravitationally lensed quasars", Astronomy & Astrophysics **451**, 759–766 (2006).

[331] D. Sluse, D. Hutsemékers, F. Courbin, et al., "Microlensing of the broad line region in 17 lensed quasars", Astronomy & Astrophysics **544**, A62 (2012).

[332] R. J. Weymann, D. Latham, J. R. P. Angel, et al., "The triple QSO PG1115 + 08: another probable gravitational lens", Nature **285**, 641–643 (1980).

[333] J. L. Tonry, "Redshifts of the Gravitational Lenses B1422+231 and PG 1115+080", Astronomical Journal **115**, 1–5 (1998).

[334] C. A. Christian, D. Crabtree, and P. Waddell, "Detection of the Lensing Galaxy in PG 1115+080", Astrophysical Journal **312**, 45 (1987).

[335] D. Sluse, J. Surdej, J.-F. Claeskens, et al., "A quadruply imaged quasar with an optical einstein ring candidate: 1rxs-j113155.4–123155", Astronomy & Astrophysics **406**, L43–L46 (2003).

[336] D. Sluse, J.-F. Claeskens, D. Hutsemékers, et al., "Multi-wavelength study of the gravitational lens system RXS J1131-1231. III. Long slit spectroscopy: micro-lensing probes the QSO structure", Astronomy & Astrophysics **468**, 885–901 (2007).

[337] S. H. Suyu, T. Treu, S. Hilbert, et al., "Cosmology from Gravitational Lens Time Delays and Planck Data", Astrophysical Journal Letters **788**, L35 (2014).

[338] M. Oguri et al. (SDSS collaboration), "Discovery of Two Gravitationally Lensed Quasars with Image Separations of 3 Arcseconds from the Sloan Digital Sky Survey", Astrophysical Journal **622**, 106–115 (2005).

[339] A. Agnello, C. Grillo, T. Jones, et al., "Discovery and first models of the quadruply lensed quasar SDSS J1433+6007", Monthly Notices of the Royal Astronomical Society **474**, 3391–3396 (2018).

[340] N. D. Morgan, J. A. R. Caldwell, P. L. Schechter, et al., "WFI J2026-4536 and WFI J2033-4723: Two New Quadruple Gravitational Lenses", American Astronomical Society **127**, 2617–2630 (2004).

[341] C. McCully, C. R. Keeton, K. C. Wong, et al., "A new hybrid framework to efficiently model lines of sight to gravitational lenses", Monthly Notices of the Royal Astronomical Society **443**, 3631–3642 (2014).

[342] S. Hilbert, J. Hartlap, S. D. M. White, et al., "Ray-tracing through the Millennium Simulation: Born corrections and lens-lens coupling in cosmic shear and galaxy-galaxy lensing", Astronomy & Astrophysics **499**, 31–43 (2009).

[343] M. J. Williams, "Numerical simulations in relativistic cosmology", PhD thesis (University of Canterbury, New Zealand, 2024).

[344] S. Cao, J. Qi, Z. Cao, et al., "Direct test of the FLRW metric from strongly lensed gravitational wave observations", Scientific Reports **9**, 11608 (2019).

[345] R. F. L. Holanda, V. C. Busti, and J. S. Alcaniz, "Probing the cosmic distance duality with strong gravitational lensing and supernovae Ia data", Journal of Cosmology and Astroparticle Physics 02, 054 (2016).

[346] D. Kumar, D. Jain, S. Mahajan, et al., "Constraining Cosmological and Galaxy Parameters using Strong Gravitational Lensing Systems", Physical Review D **103**, 063511 (2021).

[347] T. Li, T. E. Collett, C. M. Krawczyk, et al., "Cosmology from large populations of galaxy–galaxy strong gravitational lenses", Monthly Notices of the Royal Astronomical Society **527**, 5311–5323 (2023).

[348] T. Liu, S. Cao, J. Zhang, et al., "Testing the cosmic curvature at high redshifts: the combination of LSST strong lensing systems and quasars as new standard candles", Monthly Notices of the Royal Astronomical Society **496**, 708–717 (2020).

[349] J.-Z. Qi, S. Cao, S. Zhang, et al., "The distance sum rule from strong lensing systems and quasars - test of cosmic curvature and beyond", Monthly Notices of the Royal Astronomical Society **483**, 1104–1113 (2019).

[350] B. Wang, J.-Z. Qi, J.-F. Zhang, et al., "Cosmological model-independent constraints on spatial curvature from strong gravitational lensing and type Ia supernova observations", Astrophysical Journal **898**, 100 (2020).

[351] H. Zhou and Z.-X. Li, "Model-independent Estimations for the Cosmic Curvature from the Latest Strong Gravitational Lensing Systems", Astrophysical Journal **889**, 186 (2020).

[352] A. Seifert, Z. G. Lane, M. Galoppo, et al., "Supernovae evidence for foundational change to cosmological models", Monthly Notices of the Royal Astronomical Society **537**, L55–L60 (2025).

[353] M. Bartelmann, "Gravitational lensing", Classical and Quantum Gravity **27**, 233001 (2010).

[354] J. Liu, X. Chen, and X. Ji, "Current status of direct dark matter detection experiments", Nature Physics **13**, 212–216 (2017).

[355] Y. e. a. Meng (PandaX-4T Collaboration), "Dark matter search results from the pandax-4t commissioning run", Physical Review Letters **127**, 261802 (2021).

[356] C. Blanco and R. K. Leane, "Search for dark matter ionization on the night side of jupiter with cassini", Physical Review Letters **132**, 261002 (2024).

[357] G. Bertone and D. Hooper, "History of dark matter", Reviews of Modern Physics **90**, 045002 (2018).

[358] S. Profumo, L. Giani, and O. F. Piattella, "An Introduction to Particle Dark Matter", Universe **5**, 213 (2019).

[359] D. Astesiano, S. L. Cacciatori, V. Gorini, et al., "Towards a full general relativistic approach to galaxies", European Physical Journal C **82**, 554 (2022).

[360] W. Beordo, M. Crosta, M. Lattanzi, et al., "Geometry-driven and dark-matter-sustained Milky Way rotation curves with Gaia DR3", Monthly Notices of the Royal Astronomical Society **529**, 4681–4698 (2024).

[361] M. Galoppo and D. L. Wiltshire, "Exact solutions for differentially rotating galaxies in general relativity", arXiv:2406.14157 (2024).

[362] M. Galoppo, F. Re, and D. L. Wiltshire, "Quasilocal Newtonian limit of general relativity and galactic dynamics", arXiv:2408.00358 (2024).

[363] C. M. Trott, T. Treu, L. V. E. Koopmans, et al., "Stars and dark matter in the spiral gravitational lens 2237+0305", Monthly Notices of the Royal Astronomical Society **401**, 1540–1551 (2010).

[364] I. Banik and H. Zhao, "From Galactic Bars to the Hubble Tension: Weighing Up the Astrophysical Evidence for Milgromian Gravity", Symmetry **14**, 1331 (2022).

[365] J. Bekenstein and M. Milgrom, "Does the missing mass problem signal the breakdown of Newtonian gravity?", Astrophysical Journal **286**, 7–14 (1984).

[366] M. Milgrom, "Quasi-linear formulation of MOND", Monthly Notices of the Royal Astronomical Society **403**, 886–895 (2010).

[367] M. Bílek, H. Zhao, B. Famaey, et al., "Evolution of globular-cluster systems of ultra-diffuse galaxies due to dynamical friction in mond gravity", Astronomy & Astrophysics **653**, A170 (2021).

[368] P. Kroupa, E. Gjergo, E. Asencio, et al., *The many tensions with dark-matter based models and implications on the nature of the Universe*, 2023.

[369] M. Milgrom, "Can the Hidden Mass Be Negative?", Astrophysical Journal **306**, 9 (1986).

[370] L. Ciotti, P. Londrillo, and C. Nipoti, "Axisymmetric and triaxial mond density-potential pairs", Astrophysical Journal **640**, 741 (2006).

[371] X. Wu, B. Famaey, G. Gentile, et al., "Milky Way potentials in cold dark matter and MOdified Newtonian Dynamics. Is the Large Magellanic Cloud on a bound orbit?", Monthly Notices of the Royal Astronomical Society **386**, 2199–2208 (2008).

[372] L. Ciotti, H. Zhao, and P. T. de Zeeuw, "Separable triaxial potential–density pairs in modified Newtonian dynamics", Monthly Notices of the Royal Astronomical Society **422**, 2058–2071 (2012).

[373] C.-M. Ko, "On the problem of deformed spherical systems in modified newtonian dynamics", Astrophysical Journal **821**, 111 (2016).

[374] D. J. Mortlock and E. L. Turner, "Gravitational lensing in modified Newtonian dynamics", Monthly Notices of the Royal Astronomical Society **327**, 557–566 (2001).

[375] M. Milgrom, "The a_0 – cosmology connection in MOND", arXiv:2001.09729, `10.48550/arXiv.2001.09729` (2020).

[376] J. A. A. Barroso et al., "Euclid: the early release observations lens search experiment", arXiv:2408.06217 (2024).

[377] O. Tihhonova, F. Courbin, D. Harvey, et al., "H0LiCOW VIII. A weak-lensing measurement of the external convergence in the field of the lensed quasar HE0435-1223", Monthly Notices of the Royal Astronomical Society **477**, 5657–5669 (2018).

[378] P. Wells, C. D. Fassnacht, and C. E. Rusu, "TDCOSMO: XIV. Practical techniques for estimating external convergence of strong gravitational lens systems and applications to the SDSS J0924+0219 system", Astronomy & Astrophysics **676**, A95 (2023).

[379] C. R. Keeton and C. S. Kochanek, "Gravitational Lensing by Spiral Galaxies", Astrophysical Journal **495**, 157–169 (1998).

[380] M. Meneghetti, A. Ragagnin, S. Borgani, et al., "The probability of galaxy-galaxy strong lensing events in hydrodynamical simulations of galaxy clusters", Astronomy & Astrophysics **668**, A188 (2022).

[381] E. Pouliasis, P. D. Matteo, and M. Haywood, "A Milky Way with a massive, centrally concentrated thick disc: new Galactic mass models for orbit computations", Astronomy & Astrophysics **598**, A66 (2017).

[382] J. Binney and S. Tremaine, *Galactic Dynamics: Second Edition* (Princeton University Press, 2008).

[383] P. C. van der Kruit and L. Searle, "Surface photometry of edge-on spiral galaxies. I - A model for the three-dimensional distribution of light in galactic disks.", Astronomy & Astrophysics **95**, 105–115 (1981).

[384] P. C. van der Kruit and L. Searle, "Surface photometry of edge-on spiral galaxies.", Astronomy & Astrophysics **110**, 61–78 (1982).

[385] L. Mestel, "On the Galactic Law of Rotation", Monthly Notices of the Royal Astronomical Society **126**, 553–575 (1963).

[386] G. G. Kuzmin, "Constraining the NFW potential with observations and modelling of low surface brightness galaxy velocity fields", Astron. Zh. **33** (1956).

[387] Y. Wang and E. L. Turner, "Caustics, critical curves and cross-sections for gravitational lensing by disc galaxies", Monthly Notices of the Royal Astronomical Society **292**, 863–870 (1997).

[388] O. Möller and A. W. Blain, "Strong gravitational lensing by spiral galaxies", Monthly Notices of the Royal Astronomical Society **299**, 845–850 (1998).

[389] H. Y. Shan, M. Feix, B. Famaey, et al., "An analytic model for non-spherical lenses in covariant modified newtonian dynamics", Monthly Notices of the Royal Astronomical Society **387**, 1303–1312 (2008).

[390] P. Lang et al., "Bulge growth and quenching since z = 2.5 in candels/3b-hst", Astrophysical Journal **788**, 11 (2014).

[391] R. J. Allen et al., "The size evolution of star-forming galaxies since z = 7 using zfourge", Astrophysical Journal Letters **834**, L11 (2017).

[392] J. C. Forbes and A. Loeb, "Evaporation of planetary atmospheres due to XUV illumination by quasars", Monthly Notices of the Royal Astronomical Society **479**, 171–182 (2018).

[393] G. N. Candlish, R. Smith, and M. Fellhauer, "RAyMOND: an N-body and hydrodynamics code for MOND", Monthly Notices of the Royal Astronomical Society **446**, 1060–1070 (2014).

[394] F. Lüghausen, B. Famaey, and P. Kroupa, "Phantom of RAMSES (POR): A new Milgromian dynamics N-body code", Canadian Journal of Physics **93**, 232–241 (2015).

[395] S. McGaugh, F. Lelli, and J. Schombert, "Radial Acceleration Relation in Rotationally Supported Galaxies", Physical Review Letters **117**, 201101 (2016).

[396] R. Stiskalek and H. Desmond, "On the fundamentality of the radial acceleration relation for late-type galaxy dynamics", Monthly Notices of the Royal Astronomical Society **525**, 6130–6145 (2023).

[397] F. Re and P. Di Cintio, "Structure of the equivalent Newtonian systems in MOND N-body simulations. Density profiles and the core-cusp problem", Astronomy & Astrophysics **678**, A110 (2023).

[398] P. Di Cintio, F. Re, and C. Chiari, "Dynamical friction in the quasi-linear formulation of modified Newtonian dynamics (QuMOND)", Astronomy & Astrophysics **689**, A150 (2024).

[399] R. H. Sanders and D. D. Land, "MOND and the More Fundamental Plane", Monthly Notices of the Royal Astronomical Society **389**, 701 (2008).

[400] G. Orban de Xivry and P. Marshall, "An atlas of predicted exotic gravitational lenses", Monthly Notices of the Royal Astronomical Society **399**, 2–20 (2009).

[401] I. Banik, M. Milgrom, and H. Zhao, "Toomre stability of disk galaxies in quasi-linear MOND", arXiv e-prints, arXiv:1808.10545 (2018).

[402] M. Persic and P. Salucci, "Mass Decomposition of Spiral Galaxies from Disc Kinematics", Monthly Notices of the Royal Astronomical Society **245**, 577 (1990).

[403] M. Persic, P. Salucci, and F. Stel, "The universal rotation curve of spiral galaxies — I. The dark matter connection", Monthly Notices of the Royal Astronomical Society **281**, 27–47 (1996).

[404] P. Salucci and A. Burkert, "L9 Dark Matter Scaling Relations", Astrophysical Journal Letters **537**, L9–L12 (2000).

[405] P. Virtanen et al., "SciPy 1.0: Fundamental Algorithms for Scientific Computing in Python", Nature Methods **17**, 261–272 (2020).